Engineering Ionic Liquid EDLCs: Influence of Cation Type, Carbon Structure and Increased Operation Temperature

By:

Asa Noofeli

A thesis submitted in partial fulfilment of the requirements for the degree of
Doctor of Philosophy

The University of Sheffield
Faculty of Engineering
Department of Chemical & Biological Engineering

02/05/2016

Declaration of Authors Right

Unless otherwise stated, this thesis is the original work of author.

Asa Noofeli

Acknowledgement

I would like to express my best gratitude to my supervisor, Professor Peter Hall, for the opportunity to undertake this project and his valuable guidance and support over years. Thanks are also extended to Dr Anthony Rennie for his continued encouragement, supervision and valuable stimulating discussions throughout.

I am also grateful to Dr Mojtaba Mirzaeian at the University of West of Scotland for valuable advise on electrolytes selection and general aspects of this research. I would also like to thank Dr Fiona Sillars for facilitating access to Advanced Material Research Laboratories (AMRL center) of the University of Strathclyde at the early stages of this work. Appreciations are also extended to Professor Roberto Torresi at the University of Sao-Paulo for repeating Viscometry measurements at various temperatures.

I also appreciate and acknowledge the support and advise from the technical laboratory and workshop staff; Mr. Keith Penny, Mr. Mark Jones, Mr. Usman Younis, Mr. Oz Mcfarlane and Mr. Mark Mcintosh.
Thanks are also given to my fellow PhD researchers and friends across the faculty I shared time with for making my time at Sheffield enjoyable.

Last but not least I would like to thank my parents for their great support and love during the course of this work. Without them the completion of this work would have not been possible.

Contents:

List of Figures:

List of Tables:

List of Abbreviations

AC- Activated Carbon

AC- Alternating Current

BET- Brunauer Emmett Teller

CC- Constant Current

CCA- Climate Change Act

CE- Counter Electrode

DBL- Double Layer

DFT- Density Functional Theory

DSC- Differential Scanning Calorimetry

EC- Electrochemical Capacitor

EDLC- Electrochemical Double Layer Capacitors

EERA- European Energy Research Alliance

EIS- Electrochemical Impedance Spectroscopy

ESR- Equivalent Series Resistance

ESW- Electrochemical Stability Window

EV- Electric Vehicle

GC- Galvanostatic Cycling

HEV- Hybrid Electric Vehicle

IHP- Inner Helmholtz Plane

IL- Ionic Liquid

IPCC- Intergovernmental Panel on Climate Change

IUPAC- International Union of Pure and Applied Chemistry

KWW- Kohlrausch William Watts

MWCNT- Multi Walled Carbon Nanotubes

OHP- Outer Helmholtz Plane

RC- Randle’s Circuit

RE- Reference Electrode

RTIL- Room Temperature Ionic Liquids

SMES- Superconducting Magnetic Energy Storage

SWCNT- Single Walled Carbon Nanotubes

UNFCCC- United Nations Framework Convention on Climate Change

UNFPA- United Nations Population Fund
UPS- Uninterruptable Power Supplies
WE- Working Electrode

Abstract

Development of safe, robust and reliable electrochemical energy conversion systems with high energy and power densities can be a response to the universal demand for a clean transport industry free from any fossil fuels derivatives.

Electrochemical Double Layer Capacitors (EDLCs) are potential candidates that not only provide short pulses of energy at high powers but also deliver stable charge-discharge cycles in excess of 10^6 cycles. Correspondingly when used in conjugation with a battery stack in an electric vehicle can assist the battery when power boosts are required and therefore extending the battery lifetime. In literature studies these devices are commonly referred to as Electrochemical Capacitors (ECs) and supercapacitors. Commercially available EDLCs are based on aqueous or organic electrolytes that can safely operate in limited potentials. However the room temperature ionic liquids (RTILs) are promising alternatives to replace the current electrolytes as they demonstrate significantly higher and safer operating potentials, thus improving specific energy density.

This study identified that the physiochemical properties, operating potential and the cation volume of the Ionic Liquids (ILs), as well as the pore size distribution of the carbon materials influencing the capacitance performance. Hence a systematic study of nine different ionic liquids with varying chain lengths and linkages from four classes of pyrrolidinium, sulfonium, ammonium and phosphonium RTILs was performed.

The utilized IL cations in this study are the following: 1-methyl-1-propylpyrrolidinium [Pyr_{13}], 1-butyl-1-methylpyrrolidinium [Pyr_{14}], diethyl-methylsulfonium [S_{221}], triethylsulfonium [S_{222}], butyltrimethylammonium [N_{1114}], butyltriethylammonium [N_{2224}], N,N-diethyl-N-methyl-N-(2methoxy-ethyl)ammonium [$N_{122(2O1)}$], pentyltriethylphosphonium [P_{2225}] and (2methoxy-ethyl)triethylphosphonium [$P_{222(2O1)}$)] that are combined with a bis(trifluoro-methane)sulfonimide [NTf_2] anion.

The characterization of the utilized ILs was performed using Karl Fischer measurements, Differential Scanning Calorimetry, rheology, density and conductivity measurements and two/three electrode stability potential measurements. Through these measurements it was found that sulfonium and

non-ether ammonium ionic liquids provide the lowest and highest viscosities at 33-40 mPa.s and 105-150 mPa.s, respectively. This trend is also observed for the conductivity measurements at 6.6 and 7.3 mS cm^{-1} for $[S_{221}][Tf_2N]$ and $[S_{222}]$-$[Tf_2N]$ whereas values of 2.1 and 1.3 mS cm^{-1} were attained for non-ether N-ILs, i.e. $[N_{1114}][Tf_2N]$ and $[N_{2224}][Tf_2N]$. These trends were maintained at higher operating temperatures with significant drop in the value of viscosity and increase in conductivity.

The effect of pore size distribution was also investigated by combining each liquid with four different activated carbons produced in-situ where the pore characteristics of the produced carbons was controlled with varying the precursors quantities. AC200, AC250, AC300 and AC350 carbons were produced with the total pore volumes of 0.48, 0.53, 0.62 and 0.67 cm^3 g^{-1} containing mesopore volumes of 56%, 58%, 62% and 64%, respectively. These characterizations were obtained through nitrogen adsorption/desorption at 77K.

The temperature elevation approach was also used at 25°C, 40°C, 60°C and 80°C in order to study the effect of temperature on ILs physiochemical properties and capacitance response of the produced cells. The capacitance response was investigated with Galvanostatic cycling (GC) at a wide range of discharge densities. Electrochemical Impedance Spectroscopy (EIS) was also used to determine the capacitance performance at 0.01 Hz and monitor the solution, ionic and equivalent series resistances variation with pore size distribution and temperature. No clear consistency or trend was observed for capacitances determined from the EIS method indicating that frequency of 0.01 Hz may be slightly high for capacitance determination using this method. However highest ionic and equivalent series resistances were obtained from narrowest pores, i.e. AC200 and AC250, which was clearly supported by reduction in specific capacitance using GC method when compared against wider pore carbons, i.e. AC300 and AC350.

This study has identified that the increase in alkyl side chain length of the cation difficult the IL movement and reduces the transport and electronic properties with the exception of $[S_{222}][Tf_2N]$ where extra CH_2 in this IL causes symmetric shielding of charge hindering specific capacitance by 35% when compared against

$[S_{221}][Tf_2N]$ from 55.8 Fg^{-1} to 36.2 Fg^{-1} considering that better physiochemical characteristics were reported for the former liquid. Comparatively incorporation of methoxyethyl into the side chain introduces an electronegative region on the cation reducing the positive charge on this species and increases the cation flexibility. However this is done at the expense of reduced operating potential. When these ILs are paired with different activated carbon, wider pore AC300 and AC350 demonstrated to display higher capacitance performance in comparison to narrow pore ACs due to the provision of larger pathways for ion transport and double layer formation. As stated, sulfonium based ILs are shown to produce the largest capacitance performance due to provision of the best physiochemical properties whereas the least capacitance performance was obtained for phosphonium based ILs. Although reasonably good physiochemical properties displayed for $[P_{222(2O1)}][NTf_2]$ and reasonably high operating potential for $[P_{2225}][NTf_2]$ but due to the large volume of the cation, these species are most likely to access a large fraction of surface due to their dimension. However in the case of the methoxyethyl incorporated $[N_{122(2O1)}][NTf_2]$ IL an improvement in capacitance performance was obtained in compare to the non-ether constituent where the cation size is much smaller than the $[P_{222(2O1)}][NTf_2]$ IL cation.

From the temperature elevation approach it was found that although solution resistance is reduced due to the improved conductivity but a substantial increase in the ionic and solution resistances was experienced mainly due to the accumulation of resistances and increase in the system energy. In other words, the increase of the total impedance of the cell due to temperature was found to reduce the performance significantly in terms of specific energy and specific power. At 25°C operation and low discharge current, relatively small cation $[N_{1114}][NTf_2]$ liquid exhibits the highest specific energy and power at 51.17 Wh kg^{-1} and 740 W kg^{-1}, respectively, where ether incorporated $[P_{222(2O1)}][NTf_2]$ produces the least performance in the order of 19.7 Wh kg^{-1} and 645 W kg^{-1}. As temperature increases, a significant decrease in these values and other studied liquids were observed with the exception of large cation $[P_{2225}][NTf_2]$ liquid where specific energy increased by 16% from 31 to 36.1 Wh kg^{-1} as temperature increases from 25°C to 80°C. However a marginal 2.4% decrease in power was still observed.

1 Introduction

1.1 Population, climate change and decelerating policies

Climate change, the major challenge scientists are facing, is mainly caused by growing concentration of greenhouse gases in the atmosphere. Assessments and studies performed by Intergovernmental Panel on Climate Change (IPCC) illustrate that the prime driver for production of these gases is mostly caused by human activities, e.g. fossil fuels combustion and cement production, where vast quantities of CO_2 are released to the environment on a daily basis [1, 2].

On the other hand, global population studies carried by United Nations Population Fund (UNFPA), show that the overall world's population is growing which is not in favour of reducing energy consumption. As an example, in the 2012 Revision carried by the same body, it is estimated that by year 2050 the developing world population will increase by 28% from 5.9 billion to 8.2 billion [3].

According to the same document, a projection of up to two-fold increase is estimated for the least developed countries. At the same time the prospects for developed countries show a low population increase or in some countries a descending trend. Even though the improved health care and life standards in the developed countries have increased the life expectancy of its population, the rapid increase in population from the developing world has led to an overall global population growth.

A growing population demands more energy as a consequence energy costs will increase. Thus various policies and technologies are emerging as a response against the climate change and the energy demand.

Among the UK's national laws and policies are the "Climate Change Act 2008", "CRC Energy Efficiency Scheme Order 2010" and "The Energy Act 2013" where national measures are set to meet the emission target cuts by 2050 through emissions trading schemes for large organizations to improve energy efficiency and encourage companies to invest in low carbon technologies by stabilizing incentives with long-term contracts [4]. These policies are emerged for both short/long-term runs.

It is worth highlighting that the climate change combat is an international debate and it is the concern of many countries all over the globe. Many agreements and plans are set internationally mainly through the United Nations (UN) and the European Union (EU). For instance the “United Nations Framework Convention on Climate Change” (UNFCCC) and the “European Strategic Energy Technology Plan” (SET-Plan) are common examples. The former provides a strong platform for global actions through 25 articles and the latter is mainly set as a response against the climate change challenge in order to meet the set targets for emission cuts. Accordingly for EU to work attentively towards the SET-Plan, it brings together more than 150 research centers, organizations and universities in a European Energy Research Alliance (EERA) assembly to actively interact and work together through various joint or individual research programs [5].

The UK government is one of the participants in many of the above programs. In order to meet the short-term and long-term targets, the government expects 40% of the electricity generation from low carbon sources, such as 30% from renewable energy and the remainder from nuclear plants and clean coal by year 2020 [6]. There are also long term plans in place to lower emissions even further. For example one of the principal associated targets in the “Climate Change Act” is to make a 80% cut in greenhouse emissions by the year 2050 [7].
Parallel to these policies new markets are developing along side to identify alternatives and exploit more efficient sources of energy.

1.2 Electrification of the transport system

The UK transport system is heavily dependent on fossil fuel’s derivative products such as petrol and diesel. Approximately one quarter of the total CO_2 emissions belongs to the road transportation produced by fossil fuels [8]. A three-fold increase for this figure is estimated by 2050 if no serious actions take place today. With the current figure, transport becomes the second largest sector after power industry for greenhouse gas emissions.

With the global population growth on one side and demand for more energy on the other, it is important to decelerate climate change but enable greater mobility at the same time. In order to achieve this a major shift from fossil fuels derivative to low CO_2 fuels is required. Moreover technologies that improve vehicle efficiency must also be considered.

In order to minimize the CO_2 footprint and keep up with the CO_2 emission cut targets government of many countries turned to electrification for sustainable road transport. This requires the development of hybrid electric vehicles (HEVs) and electric vehicles (EVs) on the large scale. Pure EVs are considered to be the cleanest choice for transport if they are fuelled from renewable sources, such as solar or wind. Although big brands such as Chevrolet, Renault, Jaguar and few others have introduced several experimental models of electric powered vehicles, but they suffer from prolonged charging time and high costs. Another important challenge towards attaining a sustainable transport system is the low efficiency and limited ability of the magnetic or electrical field to store large capacities of electric energy which in turn leads to limited driving range. For these reasons there are still room for further improvements on these devices.

In order to tackle these unfavourable concerns, the development of robust and reliable energy storage technologies is essential. However no sole system can satisfy all needs, therefore various energy storage systems have been emerged to suit specific demands.

1.3 Electrical energy storage: An overview

Development of various energy storage technologies requires the transformation of electrical energy into other forms of energy. As observed from Figure 1.1 there are many different storage technologies available but what makes a technology adequate for an application is the requirements needed to satisfy the demand.

This image has been removed due to the copyright

Figure 1.1 Discharge time vs. rated power for various storage systems. Adapted from [9]

The electrical storage systems are mainly classified into five main categories of electrochemical, chemical, magnetic, mechanical and other storages including nuclear energy, clean fuels and renewables. The main technologies associated with each mentioned category are discussed in the following subsections. It is worth highlighting that most of the introduced systems in these sections are mainly utilized for the purpose of power delivery.

1.3.1 Electrochemical storage

In recent years, there has been a growing interest in developing more efficient energy storage systems through the use of the electrochemical route where electrochemical cells (batteries) and supercapacitors are at the forefront of these studies.

The electrical energy storage in these devices occurs through two distinct modes of indirect and direct. In the indirect mode, which occurs in batteries, a faradaic oxidation or reduction reaction is required to release a charge across the voltage difference of the positive and negative electrodes in order to allow for energy storage. In the direct mode, such as conventional capacitors, the charge is stored in a non-faradaic manner where the energy storage takes place electrostatically as positive and negative charges on the plates of the capacitor [10].

The efficiency of these modes is substantially greater than fuel combustion systems, i.e. 99.9% efficiency. Additionally, they are usually reversible and involve with direct conversion of chemical energy to Gibbs free energy [10].

The fundamental operation of supercapacitors is similar to conventional capacitors with a difference that supercapacitors utilize porous material as the electrode structure to host the charges in place of the dielectric plates.

Due to the contrast in nature of charge storage mechanism in batteries and supercapacitors, the amount of stored energy per units of volume is only 10% of a conventional battery. However what makes supercapacitors an attractive choice to explore is the rate at which they deliver the power that is 10-100 times greater than a conventional battery. In turn this allows for much shorter charging and discharging cycle times compared to different types of batteries. This is clearly shown in Figure 1.1.

The quick charge/discharge cycling nature of supercapacitors allows for their utilization in where short duration pulses of power boost are required. A simple example of such applications is in EVs where the use of a supercapacitor, alongside a battery, improves the efficiency of the driving cycles and prolongs the battery life through regenerative braking and acceleration. Explicitly, a supercapacitor contributes to the load share and reduces the duty cycle on a battery by providing pulses of power in order to assist the battery and increase its lifetime.

1.3.2 Chemical storage

Hydrogen is a secondary source of energy. This means that it must be produced from a primary source via a chemical process. Hence hydrogen storage is categorized as a chemical storage. The external storage of hydrogen is particularly useful when there is a large surplus in supply in comparison to the demand. This usually occurs when intermittent sources of energy are connected to the grid. At this point the surplus energy is converted to hydrogen through electrolysis. In turn, the produced hydrogen can be fed to a fuel cell for conversion back to electricity at periods of peak demand. Alternatively hydrogen can also be compressed and utilized as a fuel to hydrogen powered vehicles. However the associated energy efficiency of these vehicles are much lower in comparison to conventional battery/supercapacitor system discussed in section 1.3.1. This is due to the energy losses while compressing the gas, which hinders the amount of stored energy per unit of volume. Accordingly an efficient and safe storage method of hydrogen is still counts as a major challenge.

1.3.3 Magnetic storage

The storage of electrical energy through this route is done with a relatively novel technology of Superconducting Magnetic Energy Storage (SMES). The SMES stores the surplus electricity supplied from grid in a magnetic field, which is comprised of a cryogenically cooled superconducting coil.

The storage efficiency with SMES is at the maximum with near zero energy losses. This means that when the magnetic charge storage through the coil is complete, there will be no decay or leakage of current with time allowing for indefinite charge storage [11]. At discharge the power delivery can occur instantaneously in a single cycle to recover possible sudden losses in line power. Delivery at this manner helps to preserve the reliability of the grid especially when intermittent energy sources are connected to it. These sources of energy will be discussed in section 1.3.5.3.

1.3.4 Mechanical storage

Hydroelectricity, pumped storage and flywheels are the common examples of mechanical energy storage. Production of the hydroelectricity requires hydraulic dams with reservoirs. Hydroelectricity is usually used when there is a big gap between the supply and demand of electricity or when demand is at its maximum. To fulfil this gap, the stored water in the reservoir is released on hydroelectric turbines that are connected to generators. Hydroelectricity storage is usually used in conjugation with the pumped storage. At low demand or off-peak periods the pumped storage can be utilized to recreate the hydrostatic head, for future hydroelectricity generation, by using a pump-back approach and pumping the water back to the hydraulic dam. At pure pumped storage plants, water is only shifted between a lower reservoir and a higher one.

On the other hand are the flywheels that comprised of an accelerating rotor, which produces rotational kinetic energy with minimum friction and >96% efficiency [12]. According to the law of conservation of energy an isolated object in motion remains in motion hence the produced energy is considered as active energy and remains in the system unless acted upon. Therefore by removing the energy from the system, the rotating speed of the rotor is reduced.

1.3.5 Energy generation from other sources

1.3.5.1 Nuclear energy

In conventional electricity generating nuclear power plants only around 35% of the generated heat is obtained in the form of electrical energy [13]. Despite the inefficient conversion rate and waste disposal complexity of nuclear fission products, this technique remains attractive until today as it generates a constant power output. However, the emission cut targets and low efficiency of the process and recurrence of disasters such as Forsmark and Fukushima in recent years on the other side have reduced the number of European countries who are heavily dependent on the nuclear power, e.g. Germany, to invest in other sources of clean energy.

1.3.5.2 Clean fuels

Biofuel and biodiesel are common examples of the clean fuels. They count as an important step towards shifting away from the fossil fuels and move closer towards the discussed emission cut targets.

Biofuels are widely used in Brazil and US. As the name states they are produced from biological materials such as plants and living organisms. In fact the nature of the required raw materials to produce biofuels has created a competition between food stock against clean fuels. For this reason, there are many moral objections against biofuels in general. Biodiesel is the most common biofuel in Europe and considered as an oxygenated fuel due to the greater presence of H_2 and O_2 species compared to its carbon content. Although this property improves combustion but for biodiesel production most European countries import the raw materials e.g. wood from overseas [14] which increases the production costs.

1.3.5.3 Renewable energy sources

The renewable energy storage is accounted as a modern era in storage technologies. The renewables (e.g. wind, wave, and solar energy) can all be converted into electrical energy but, similar to the nuclear energy, the conversion is fairly inefficient and leads to significant energy losses.

These sources of energy generate electricity intermittently and produce fluctuating power output. This in turn poses problems for the current system of electricity delivery, where the time dependence of the energy supply must follow the time dependence of energy demand. This means that the production of energy must precisely fit with demand, which in reality is impractical.

In order to boost the overall efficiency, while generating stable power outputs, various storage systems are needed to operate over various time scales. For example at larger time scales, systems that provide more energy and over shorter time scales systems that provide more power may be used.

Accordingly, there is no single energy storage system that can satisfy all energy needs hence different storage devices have been explored and developed. Also as more and more renewable sources are connected to the grid, managing them becomes more challenging. Thus development of efficient energy storage technologies where they can shift the demands to a time period that better matches the supply is necessary.

1.4 High power electrical storage

All the stated energy storage systems are created to balance the supply of energy with the demand for it. As already discussed and illustrated in Figure 1.1, there are various technologies in place to provide power at large and small scales over short and long time scales. For instance the power delivery through some of the described storage technologies (such as magnetic, mechanical and renewables) occurs at large scales when there is a shortage in the grid. On the other hand is the electrochemical storage where there is a trade-off between the stored energy and delivered power for the main technologies exist in this category, i.e. batteries and capacitors. This trade-off is clearly described by the use of a Ragone plot, illustrated in Figure 1.2, where capacitors and batteries are expressed in terms of their specific power and energy.

This image has been removed due to the copyright

Figure 1.2 Ragone plot (Specific power vs. specific energy) for various energy storage systems. Adapted from [15]

As shown above, conventional capacitors have relatively high specific power and low specific energy in comparison to various types of batteries. This means that although a battery is capable of storing more energy than conventional capacitors but, unlike capacitors, batteries are unable to deliver the energy very quickly accordingly their specific power is low. Conversely, capacitors store less energy per unit volume but they can deliver the energy rapidly hence their specific power is high.

Accordingly electrochemical capacitors have attracted a great attention as they bridge the gap between low power, high energy batteries and conventional high power, low energy capacitors. Hence electrochemical capacitors display higher specific energy than capacitors and higher specific power than batteries.

Thus electrochemical capacitors are proposed as an alternative solution for many power application and not only EVs.

1.5 Capacitors: A historical development

Generally speaking capacitors are nothing more than an insulator between two conductors. However the evolution of current capacitors as one of the simplest energy storage devices has gone through complex processes of technical development.

The origin of electrical storage at the surface was first discovered by Thales in 6th century BC through rubbing amber. However there were no clear knowledge and understanding of the process until the mid 18th century when the “static electricity” and “electrical machines”, such as Electrophorus, Wimshurst and Leyden jars, were introduced [10].

With the discovery of Von Kleist in mid 17th century, about isolating electricity in a glass bottle from an external electric machine, Van Musschenbroek discovery of the Leyden jar and Volta pile by Volta in early 18th century a major breakthrough was made in this field.

Von Kleist’s discovery was involved with a partially water filled glass bottle that was sealed with a stopper on top and a nail through it in a way that it was in contact with water. It was found that a small amount of charge is stored when he attached the nail terminal to an external static device while holding the jar in his hand. It was also found that the charges will reunite and find a pathway to drift as he experienced a what we know today as a “shock” in his hand when he tried to remove the nail from the jar, i.e. everything was grounded [16].

The Leyden jar discovery by Van Musschenbroek was very similar to Von Kleist’s with an exception of using wrapped Lead foil inside and outside of the jar’s walls and bottom, Figure 1.3. The nail was replaced with a brass rod that was attached to a loose wire from the bottom, which lay over the inner Lead foil. He repeated the same experiment for charging as Kleist’s. The original thought was that charge storage takes place in the water but with later studies over the years, it was found that the positive and negative charges gather at the Lead foil and remain at equilibrium due to presence of the insulation, i.e. glass, in between the charges until a point where the external foil comes in contact with any external conductor. According to this proposition Leyden jar was also referred to as electric condenser as it was able to “condense” charges at the surface of the foil [10].

This image has been removed due to the copyright

Figure 1.3 Schematic of the Leyden jar. Adapted from [16]

In the enlightenment years in Europe and elsewhere, significant studies, experiments and contributions were made to the capacitor technology by different thinkers of the time, e.g. Benjamin Franklin and Michael Faraday are among the most important ones. Although over 250 years of evolution of capacitors have directed us to the place we are today but the technology developed much faster after the invention of vacuum tubes in 1920.

1.6 Applications of Electrochemical Capacitors

There are many applications associated with the use of ECs. As stated, the wide range applicability of these devices however started with the invention of vacuum tubes. The vacuum tubes were used along with amplifiers for sensible radio technology resulting in introduction of first ever AC powered radio.

Hall et al. classify today's application of ECs into three main categories of: power capture and supply, power quality applications and backup and low maintenance applications [17].

1.6.1 Power capture and supply

The electrostatic nature of the charge storage in ECs allows for many stable and fast charge-discharge cycles. This property of ECs coupled with their long cycle lives is particularly suitable for use in hybrid electric systems. For instance in seaport cranes, forklifts and elevators, the EC takes in the energy that would otherwise be lost through the repetitive movements in the form of heat losses [18]. The most common use of this type of application is in transportation ranging from HEV to city buses and even garbage trucks [19].

Although ECs are widely considered as a energy solution when high power demands are in place but for the aforementioned applications that are ranging from industrial platforms to transportation ECs need to be used in conjugation with a primary source of energy, e.g. diesel engine, battery or even fuel cell, depending on the application. In this scenario not only the energy losses and emissions to the environment reduces but participation of EC help to reduce the load on the primary energy supply hindering the lower fuel consumption rates.

A simple example of this is electric vehicles where energy supplied by the energy storage pack is partially recovered through regenerative braking and acceleration.

The power variation or change of speed is clearly seen from Figure 1.4 for a typical urban driving cycle with a battery storage system. The battery model pack and description of the internal system is given in [20]. The positive part of the plot represents the power requested by the battery pack and the negative part represents the battery charge through regenerative braking. The solid line profile is original recorded power data for the George square drive. The dotted lines though are indicative of different conditions applied for regenerative braking [21], that is a method of braking in which energy extracted from the parts braked, to be stored and reused.

This image has been removed due to the copyright

Figure 1.4 Power profile in the storage system of the Cobra at various regenerative braking. Adapted from [21]

The variation in power demand means inconsistent load on the battery pack. This is evident from above and may cause by presence of obstacles on the way, e.g. hills, speed bumps, etc., as well as manoeuvres such as accelerating, hill climbing or overtaking other cars. In this case, an EC pack must be in place to cater for high power peaks and assist a battery by converting the vehicles momentum back to electrical energy and absorbing the generated power during braking. The recovered electrical energy can in turn be used to charge the battery.

Thus the use of an EC alongside with a battery can improve the efficiency of the driving cycles. Explicitly, an EC contributes to the load share and improves the battery's lifetime by reducing the sludging rate of the positive active mass, caused by high discharge currents [22, 23], resulting in an overall reduction in the temperature of the battery [24]. In the described manner the duty cycle on a battery is reduced by provision of power pulses in order to assist the battery and increase its lifetime.

1.6.2 Power quality applications

The main purpose of these types of applications is in large-scale commercial and industrial platforms where provision of uninterruptable power supplies (UPS) is mandatory. UPS is commonly used to provide instantaneous power protection when experiencing interruptions in the system such as power shortage or voltage spikes. In fact they act as a “bridge” power until the point where the primary or a replacement power supply is restored [19]. This is done by providing energy from another energy source, e.g. an EC system. For instance in a 42V PowerNet bus, containing a battery and an EC module, maximum load occurs when vehicle’s undertakes low speed manoeuvres such as parking. In this situation the module is near stationary condition causing deficiency in alternator outputs and poor voltage regulations. Design and presence of a supplementary energy source is necessary here to assist with the alternator performance. This is delivered by an EC as a UPS system to contribute to voltage regulation when the primary energy module is at low performance conditions [25].

It is worth mentioning that the UPS system remains in use for a short period of time only until an emergency power system is connected. If there is no secondary source in place, an UPS system assists with equipment’s controlled and safe shut down during that short period of time.

1.6.3 Backup and low maintenance applications

One of the earliest commercial application successes of supercapacitors dates back to the late 1970s where they were employed as power provider for computer memory backup [26]. Nowadays small-scale ECs are used in many cordless handheld electronic devices ranging from mobile phones to cameras, laptops and wireless sensors. In these devices the EDLC is combined with a battery in a parallel arrangement as backup energy storage to supply short power pulses when for example the main energy storage is changed [17]. Also in the paired mode, the ability of ECs to perform reasonably well at low temperature counterbalances the poor performance of the batteries at similar temperatures. This means the necessity for servicing is reduced. Moreover shorter charging times and longer lifetime of supercapacitors counts as a bonus towards their applicability in regions where servicing the device is rather difficult to be performed at short and regular time intervals, e.g. rough mountain areas and oceans.

Supercapacitors are also used in both portable and stationary applications as a high power backup storage in utility sectors and industrial platforms. As an example, they are progressively being used in wind turbine pitching systems as emergency backup and also to supply power boost to the motor when the load is large [17]. Effectively this reduces the damage caused by high-speed winds and boosts the overall efficiency of the turbine. This consequently reduces the potential maintenance and servicing costs at offshore operations.

1.7 Outline of this work

Due to the excellent power performance properties of EDLCs in comparison to batteries, these devices are counted as attractive options to be adopted alongside a battery in electric vehicles. However, the need for improved energy performance to satisfy the requirement for EVs and many other discussed systems, ranging from portable electronics to hybrid vehicles and large industrial equipment, is still in place. In order to achieve this, it is essential to advance the existing knowledge and understanding of the electrochemical processes at greater details and also develop new materials to boost EDLC performance.

In this work, Ionic Liquids are explored as an alternative option in place of the currently employed electrolytes in commercially available EDLCs. Various electrolytes from major classes of ionic liquids were selected and paired with controlled porosity activated carbons.

Chapter 2 provides the necessary background knowledge about supercapacitors in order to gain better understanding of the storage mechanisms and get familiarized with materials of construction. Chapter 3 identifies the core objectives of this study and highlights the reasoning behind selecting those objectives. In Chapter 4 a background of different used techniques along with existing theories are provided. Chapter 5 provides a step-by-step description of material preparation and cell construction along with the used parameters of different techniques. The findings are then fully discussed and conclusions are drawn in chapters 6 and 7, respectively.

2 Literature Review

2.1 Capacitance

As previously discussed, storage of electrical energy is necessary for many day-to-day applications from simple electronics to power systems and electric vehicles. The capability of these devices to maintain the stored charge, i.e. capacitance, is measured in terms of the stored charge when a potential is applied. This is described by equation 2.1 where capacitance does not change with voltage and C represents capacitance (in units of Farads), q represents charge (in units of coulombs) and V represents the voltage (in units of volts).

$$C = \frac{dq}{dV} = \frac{q}{V}$$

equation 2.1

Among the most common and simplest energy storage devices is the parallel-plate capacitor, shown in Figure 2.1. In this arrangement two conductive materials are separated by an insulator, which is commonly referred to as dielectric media.

This image has been removed due to the copyright

Figure 2.1 Parallel plate capacitor

When a potential is applied across the plates, electrons accumulate on the surface of one plate resulting in electron deficiency in the opposing one. Although each plate experience equal but opposite charges but the presence of unequal electron counts at the plates creates an electric field. The strength of this electrostatic field varies inversely with the distance separating the two plates [10]. Also due to the nature of the charge storage that is electrostatically, capacitors have up to 10^6

cycle lives. The capacitance of a traditional parallel plate capacitor is determined by equation 2.2 where ε_0 is the permittivity of free space (8.854×10^{-12} F m^{-1}), ε_r is the relative dielectric constant of the interface, A is the surface area of both plates (m^2) and d is distance between the two plates (m).

$$C = \varepsilon_0 \varepsilon_r \frac{A}{d}$$

equation 2.2

Direct proportionality of the capacitance with plate surface area indicates that plates with high specific surface area are attractive choices for these capacitors.

2.2 Energy density and Power density

Energy density and Power density are also the two major attributes of any storage device. Energy density or volumetric energy density is defined as the amount of energy stored per unit volume and can be calculated by considering the work done during charge through moving a charge from one plate to the opposite one against the electric field. This energy density is found to be directly proportional to capacitance and voltage squared as illustrated in equation 2.3. Specific energy density or gravimetric energy density is the amount of stored energy per unit mass.

$$E_{max} = \int_0^V q dV = \int_0^V CV dV = C \int_0^V V dV = \frac{1}{2} CV^2$$

equation 2.3

On the other hand, power density is the amount of spent energy per unit of time that is again directly proportional to the voltage square and inversely to the device’s resistance (R), equation 2.4. Please refer to Appendix 1 for derivation of this equation.

$$P_{max} = \frac{V^2}{4R}$$

equation 2.4

The resistance (R) is in fact the Equivalent Series Resistance (ESR) derived from the device's internal components, such as the electrodes, current collectors, etc.

Due to the indirect proportional property of power density and ESR, obtaining high power densities requires the reduction of ESR. In recent years, significant research studies have been focused on diminishing the effect of ESR through pretreatment of current collectors, maximizing the contact between the electrodes and the current collector by chemically bonding it to the surface, etc. [27, 28]. Also as quadratic relation holds between operating voltage and Energy and Power densities, it is clear that by increasing operating voltage the values of both characteristics increases.

Other specifications such as mass and dimension of the device can significantly influence the costs and its suitability for a particular application. Accordingly, energy density and power density are usually expressed by normalizing the absolute energy and power, equation 2.3 and equation 2.4 per unit volume or unit mass.

Although presence of aforementioned specifications in a storage system is desired for many applications but no sole energy storage system can satisfy all requirements. Depending on the required property, energy and power could be utilized separately. For instance a capacitor and a battery can be used separately in applications where peak power pulses and significant amounts of energy are needed respectively [29]. Or in cases where both properties are needed, a capacitor can be used to assist a battery for supplying peak powers and recharge again through the use of the same battery.

2.3 Electrochemical capacitors classifications

There are several types of capacitors available commercially; Electrochemical capacitors (ECs) and Hybrid capacitors. Depending on the desired functionality, different types are utilized.

Electrochemical capacitors themselves are divided into two main types that are distinguishable from each other by their nature of charge storage mechanism and active materials of choice. A brief description of operation theory and design material of each system will be given here. Basing on these definitions below is the taxonomy of subclasses of ECs and classification of the active materials for each subclass.

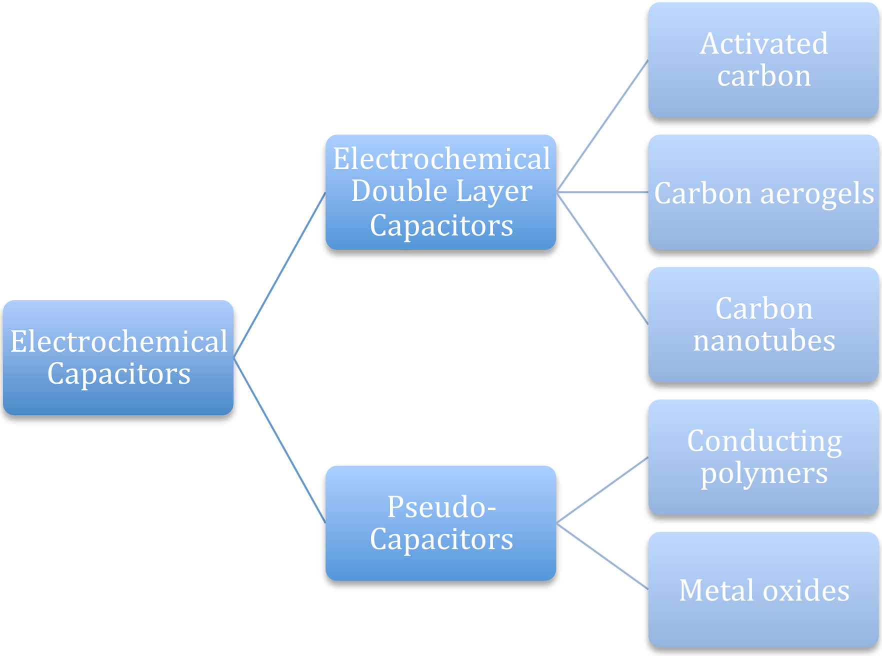

Figure 2.2 Taxonomy of Electrochemical Capacitors

In general ECs store energy by ion adsorption and fast surface redox reaction.

The first phenomenon occurs in the Electrochemical Double Layer Capacitors (EDLCs) and the latter occurs in Pseudo-capacitors [30]. The active materials used for EDLCs are from porous low cost carbon material and usually contain a high surface area. These materials are also easier to fabricate compared to Pseudo-capacitor's active materials [31].

Identifying and investigating components for pseudo-capacitors is beyond the scope of this project, therefore the attention is mainly focused on the active materials for EDLCs, see section 2.4. The nature of the utilized conducting medium too, plays an important part on the design of an EDLC. The relevant importance and different classes will be investigated in section 2.5.

In order to have a better understanding of materials, fundamental of charge storage in EDLCs and differences with pseudo capacitors are highlighted and discussed.

2.3.1 Electrochemical Double Layer Capacitors (EDLCs)

EDLCs are frequently referred to as supercapacitors and ultra-capacitors in literature. For the purpose of energy storage, as the name states, these devices employ an electrochemical double layer of charge influenced by high porosity materials as active electrodes. This chapter looks at different models that are developed for EDLCs and various compartments used for the cell fabrication.

2.3.1.1 Development of double layer models [10]

Several models have been utilized to describe the actual structure of the double layer. Helmholtz proposed the earliest mathematical model of double-layer in 1853. The model contains several layers where the thickness of each layer is dependent on the solvated ions and chemically absorbed ions to the charged electrode surface, Figure 2.3. The Helmholtz model was based on the traditional plate capacitor where the thickness associated with chemically absorbed ions is known as the inner Helmholtz plane (IHP) and the thickness characterizes the solvated ions is described as outer Helmholtz plane (OHP).

The intention of the model was first to introduce the separation of negative and positive charges at the interface of the colloidal particles with an electrolyte, which then later extended for electrode/ electrolyte interfaces where it assumes that the excess positive and negative charges present on the electrode surface have to be encountered by a layer of anions or cations that were adsorbed at the surface with no concentration gradient between the electrolyte and the adsorbed ions [10].

This is illustrated in Figure 2.3 where $\underline{\Psi}$ is the electrical potential and $\underline{d}$ is the interface where two opposite charges are separated from each other.

This image has been removed due to the copyright

Figure 2.3 Helmholtz model (1853)

The Gouy-Chapman model improves the Helmholtz model by considering thermal oscillations resulted from concentration gradient at the electrode surface, which can consequently disorder the structure of double-layer. Accordingly the model defines the double layer as an area in equilibrium (electrostatic wise) rather than rigid and ordered arrangement of ions as described by Helmholtz. Additionally the linear electrical potential drop described by Helmholtz also exists in the Gouy-Chapman model but it no longer is linear and as shown in Figure 2.4 an extra potential decay extends the potential drop into the diffuse layer. The proposed structure overestimates the double layer capacitance as the ions are accounted as point charges and they cannot be. Accordingly the model understates the double layer structure and fails to predict experimental results.

This image has been removed due to the copyright

Figure 2.4 Gouy-chapman model (1910)

Later on Gouy model was improved by another model proposed by Stern, shown in Figure 2.5. The Stern model combines the two mentioned models together and it assumes that the ions closest to the electrode are ordered at IHP and ions that are described by the Gouy model are outside of the ordered ions zone, i.e. OHP layer. Accordingly the potential decay is a linear drop in the ordered zone followed by a further decay into the diffuse layer, analogous to Gouy model.

This image has been removed due to the copyright

Figure 2.5 Stern model (1924)

Accordingly, the model comprehends the double layer capacitance, C_{dl}, as the sum of capacitive contributions of the Helmholtz layer and the diffuse layer, C_H and C_d respectively, shown in equation 2.5.

$$\frac{1}{C_{dl}} = \frac{1}{C_H} + \frac{1}{C_d}$$

equation 2.5

However in order to apply the Stern model as the proposed model for EDLCs, a determination of the Helmholtz layer thickness is required. This is rather difficult to determine as the size of ions and degree of their solvation influences the thickness.

Almost a century after proposition of Helmholtz model, Grahame model of the double layer was introduced in 1947. In this model the IHP and OHP described by Helmholtz are utilized to characterize the interaction differences between the cations and anions towards the charged surfaces. This is illustrated in Figure 2.6.

This image has been removed due to the copyright

Figure 2.6 Ion adsorption in Grahame model. Adapted from [32]

The IHP in this model is defined as the closest distance between the positively charged surface and the absorbed anion at the surface. However in the OHP, due to greater degrees of solvation, the molecules from the solvent are also involved and influence the distance between the negatively charged surface and the cation. Although the cations are smaller than the anions for some electrolytes but the anion is usually reserved in the unsolvated state at the positively charged surface whereas the cation is not in an analogous state electrostatically. In fact the cations are surrounded by solvated ions resulting in presence of bigger distance from the negatively charged surface to the cation radius, i.e. OHP. Accordingly the obtained value of capacitance at the negatively charged surface is halved when compared to the opposite charged surface. In the Grahame model the diffuse layer is described as the area beyond OHP with similar potential drop trends as the Stern model.

2.3.1.2 EDLC components

As linearity holds between the charge stored and the surface area of the electrode, see equation 2.2, a porous carbon with high surface area should also fit in this context in order to yield in production of high capacitance.

However as will be investigated later, the specific capacitance is not entirely limited to the surface area and other carbon attributes such as distribution of pore sizes (i.e. mesopore and micropore) also contribute to the capacitance. In an EDLC arrangement there are two porous carbon electrodes that are attached to current collectors. As illustrated from Figure 2.7, these electrodes are facing one another from the active sides and parted with an electronic insulator but ionically conducting separator that is soaked with an electrolyte.

The separator is an important compartment as its thickness influences certain behaviours of an EDLC. For instance, a very thin separator allows for short-circuit where the charge is transferred across it whereas a very thick separator increases the ESR and reduces the performance as a result.

As mentioned previously, the electrochemical double layer exists at the interface between electrode and the electrolyte inside the pores of the electrode. Therefore in the carbon electrode, both the ionic conduction (provided by the electrolyte around the carbon sites) and the electronic conduction (inside the carbon particle) contribute to electrical charge transport. The current collectors, on the other hand, only contribute to the electronic conduction of the charge transport and could be made from different materials.

This image has been removed due to copyright

Figure 2.7 Schematic of an EDLC compartments

Analogous to conventional capacitors, the electrochemical double layer is created when voltage is applied across the cell and charge accumulates on the surface of the electrode. Following the phenomenon of unlike charges attract, the ions at the electrolyte diffuse through the separator and into the electrode pores where carries an opposite charge. Hence double layers of opposite charges are created at each electrode [29, 33]. Ion concentrations can be utilized to aid with characterizing the double layer as the layer exists at the electrode/ electrolyte interface. In other words, the storage of charge is carried at the double layer through reversible ion adsorption from the electrolyte to the electrode surface, illustrated from Figure 2.8.

This image has been removed due to the copyright

Figure 2.8 Schematic of an EDLC. Adapted from [29]

The bulk properties of the electrode and the electrolyte are different compared to the time when they are utilized together at the interface. However the double layer generally assumes ideal polarization, i.e. no charge is transferred between the electrode and the conducting medium. Thus, at ideal conditions there are no chemical changes associated with the non-faradaic behaviour of the supercapacitor. Due to this reason the storage of charge in these devices is highly reversible which allows for many stable charge-discharge cycles. This attribute of EDLCs makes them an attractive option in environments where servicing the device is rather difficult, e.g. rough mountain areas [29].

As mentioned earlier, the linear relation of capacitance with surface area direct us towards treating the EDL as a very big plate capacitor that is influenced by the high surface carbon material to improve the performance.

However there are some disadvantages associated with this. Among the important ones is the difficulty of current access to inner areas of the porous carbon electrode caused by distribution of ohmic resistance of present electrolyte in the pores. As a result self-discharge processes or leakage current are encouraged. Another important parameter influencing the self-discharge rate is the transfer of the ions from the electrode surface to the bulk solution when no charging current is applied. From ions point of view, to overcome this problem prolonged potentiostatic holding times are required to allow ions migrating into the pores that are least accessible.

Typically this is the case for many supercapacitors, i.e. non-ideality holds. Though the degree of self-discharge is dependent on the system's electrochemistry, types of construction materials and levels of their purities.

Conway classifies and recognizes the self-discharge through three different mechanisms [10]; 1) Activation-controlled faradaic processes of species at high concentration, e.g. when the cell is charged beyond its electrochemical stability limit. Or activation-controlled faradaic processes of species attached to the surface of the electrode through oxidation or reduction, 2) Presence of impurities at the electrode or the electrolyte which consequently become oxidisable or reducible over the electrochemical voltage window leading to the non ideal polarization behaviour of the device, and 3) Faulty in construction which may lead to short-circuiting.

The contact resistance between the particles forming the carbon matrix causes another disadvantage. That is "*when a porous, electrolyte-containing matrix is addressed by a charging current, or a change in potential that drives such a current, the available electrode area in the matrix is not charged nor discharged simultaneously at a uniform rate through the matrix" [10]* leading to reduced performance.

Fundamental expectations from an EDLC to meet the essential criteria for energy storage are high cycle lives, excellent cyclability and substantial power density. These attributes are depending on number of factors including carbon electrode characteristics and the electrolyte type. In sections 2.4 and 2.5 a study of different carbon and electrolyte materials for use in EDLCs will be implemented.

2.3.2 Pseudo-capacitors

The second group of ECs is Pseudo-capacitors, commonly referred to as redox supercapacitors as well. For the purpose of charge storage, they utilize a completely different mechanism than EDLCs, which involves surface reactions and transfer of charge across the double layer [26], i.e. same as a battery. The exhibited capacitance by such arrangement is known as pseudo-capacitance.

Owing to Faradaic reactivity of surface oxygen functionalities, it is now known that around 1-5% of the obtained capacitance by an EDLC is exhibited from pseudo-capacitance. This is largely depends upon the preparation conditions of the carbon materials and the electrolyte synthesis [10]. Similarly, the pseudo-capacitors also exhibit some electrostatic double layer behaviour relevant to their electrochemically accessible sites.

2.4 Electrode materials

As stated in section 2.3.1, progress and broader adoption of EDLCs depends upon the development of new materials. In sections 2.4 and 2.5 an overview of the main classes of electrode and electrolyte materials will be discussed for use in these devices.

A great portion of research carried on EDLCs, and continuous to date, is based on the carbon. Carbon is a unique element that exists in several allotropic forms including fullerenes, graphite and nanotubes with different morphologies and physical forms (including fibres, powders, composites and foams). Mostly they are easy to fabricate, stable over a wide temperature range, chemically stable at highly acidic and basic conditions and most importantly they are low cost and readily available [34].

In order to achieve the maximum possible performance, high capacitance and minimum self-discharge rates, the carbon materials used in EDLCs must satisfy the following conditions:

1. High specific surface areas [10]
2. High degree of intra/interparticle conductivity within its structure
3. High degree of graphitization and porosity
4. Good electrolyte accessibility to intrapore surfaces i.e. good polarisability
5. Low ESR

Also Low surface functionalities of carbon materials is desirable as this may contributes to some degrees of self-discharge. Accordingly, the preferred choice of carbon must be free from any impurities such as Iron species, peroxides etc. Also the quinonoid structures must be reduced at the surface in order to minimize the effects of self-discharge.

2.4.1 Activated carbon

Activated carbons are commonly used as electrode materials in EDLCs due to their ability to provide a high surface area as well as being lower in cost and easy to manufacture in compare with other types of carbons. Activated carbons can be produced from many materials. They are usually fabricated by the carbonization of many natural feedstock and biomass precursors, such as wood, agricultural waste and coal, to produce char.

It is essential to carry an activation step in order to introduce and add pore volume to the carbonization product. The product can be activated via two approaches of physical and chemical activation. In the physical method the carbonization step is followed by the gasification of the product with an oxidizing gas at various temperatures. While in the latter activation method the carbonization is followed by thermal decomposition of the precursor saturated with chemicals such as KOH, HNO_3 etc. The purpose of both activation steps is to remove the remaining disordered carbon from the structure and add additional to the structure [17].

Also, due to presence of residual valences on the surface, most carbons that are exposed to air contain some degrees of absorbed oxygen which yields to different O-based surface functionalities such as hydroxyl, peroxyl, ketonic and quinonoid

[10]. Again, owing to the high temperature treatment of activation step, a large variety of materials, including carbon and mentioned functionalities, can be converted into activated carbons. By adjusting the process conditions such as activation temperature, activation time and concentration of the utilized reagents, the final properties of the activated carbon e.g. specific surface area and porosity can vary significantly [35]. Thus, by controlling the activation parameters opens an opportunity of obtaining carbon materials with a widespread range of porosities suitable for a desired application. The composed range can contain micropores, mesopores and even macropores with the pore size distribution of <20 Å, 20-500 Å and >500 Å respectively [31, 36]. Production of diverse particle sizes is simultaneously beneficial and detrimental towards the overall goal for many researchers that is attaining the highest capacitance possible.

Sillars and colleagues [37] investigated the effect of activated carbon pore size on the performance of ionic liquid based ECs. They found a capacitance of 210 F/g under Galvanostatic charge-discharge of 2mA cm^{-2} for EC cell containing activated carbons with average pore diameter of 3.5 nm and $EMImBF_4$ electrolyte. They also identified that the most suitable average pore diameter to achieve an optimum capacitance differs from the suitable average pore diameter required to obtain the optimum rate capability, i.e. 6.5 nm for the mentioned system. Clearly, obtaining higher power density is tightly linked with larger pore sizes whereas the smaller pore sizes correlate with higher energy density. Nonetheless, the smaller pore sizes may result in reduced capacitance, as the ions of the electrolyte may not migrate through the pores due to their bigger size in compare to the pore diameter. Thus research on activated carbons is mainly focused on controlling the pore size distribution to 1) achieve an optimal pore size for a given ion and 2) obtain a general relation to the EDLCs performance [31, 34, 36].

2.4.2 Carbon aerogels

Owing to high surface area, good electrical conductivity and low density, carbon aerogels are another promising carbon to be utilized in EDLCs. They also have the ability to bond chemically to the current collector due to the monolithic 3-dimensional mesoporous structure of conductive carbon nanoparticles. Thus carbon aerogels diminish the ESR effect further and require a lower degree of additional binding agent [38, 39].

These carbons are usually synthesized as a result of sol-gel polymerization of Resorcinol (R) and Formaldehyde (F) together in presence of a sodium carbonate catalyst (C) followed by carbonization of the RF aerogels.

There are number of papers available in literature on the synthesis procedure and various factors affecting the finish structure and the gel composition [40-42]. For instance Mirzaeian et al. investigated the effect of resorcinol and catalyst ratio with the mesoporosity of the obtained gel. They found that mesoporosity increases with increase in R/C ratio [41]. They also concluded that process conditions such as reaction time and temperature during activation and carbonization processes could significantly alter the properties of the porous carbon aerogel. For example, during carbonization they observed that the carbonization temperature affects the microstructure of the aerogel. Escribano and colleagues reported that the corresponding specific capacitance of carbon aerogels produced at beyond 900°C is significantly reduced [43]. Further investigations by them led to the assumption that this phenomena happens "*due to formation of micropores and shrinkage of the gel structure after a certain temperature*" [42]. There are also other factors affecting the carbon structure such as catalyst concentration and dilution, which control the particle size distribution and density of the material respectively.

2.4.3 Carbon nanotubes (CNTs)

Chemically stable carbon nanotubes were first discovered in 1985 by rearranging the carbon atoms through vaporization of graphite using laser pulses to create C_{60} molecules [32]. Carbon electrodes produced from this method contain open and accessible mesopores arrangement that has a very unique structure. There are two main structures known for the carbon nanotubes: Single Walled Carbon Nanotubes (SWCNT) and Multi-Wall Carbon Nanotubes (MWCNT). SWCNT is a single graphene sheet wrapped up to form a nanometer diameter cylinder whose end can be capped with a fullerene structure [17, 44]. On the other hand are the MWCNTs, where they consist of several graphene cylinders positioned around the same axis. Figure 2.9 compares the physical structure of SWCNT and MWCNT.

This image has been removed due to the copyright

Figure 2.9 (a) single sheet of CNTs, (b) single walled CNT and (c) multi wall CNT

Owing to high conductivity (5x10^{5} S m^{-1}) [45], low resistivity, high surface area, accessible pore network and great stability of CNTs, there has been an increasing interest in employing such carbons in EDLCs [31, 46]. However due to high production costs, the use of CNTs is limited to conductivity enhancer and not the main active electrode component. Chen and colleagues reported a significant reduction in ESR from 45Ω to 2.5Ω when they replaced the conductivity enhancer (acetylene black) with equal mass of MWCNTs [47].

Empirical evidences suggest that although capacitance is strongly dependent on the surface area but there are other factors influencing the capacitance of the device (especially in the case of activated carbons where a widespread range of pore sizes are available) [36]. This argument is initiated by the size of the electrolyte ions, which could be too large to fit in the micropores or too small to some degree to fit in the narrower range of mesopore volume distribution. Hence some of the pore volume remains vacant and does not contribute towards energy storage. Therefore, designing EDLCs requires the extensive study of the carbon pore size distribution as well as the suitable electrolyte.

In the next chapter, the possibility of employing different electrolytes is investigated and major benefits and drawbacks are highlighted.

2.5 Electrolyte materials

The type of electrolyte used in an EDLC cell has a remarkable effect on the amount of stored energy, i.e. energy density, and relative effectiveness of how quickly the energy could be delivered, i.e. power density. At elevated potential, the voltage of a given cell is limited by decomposition of the utilized electrolyte. This voltage is known as the Electrochemical Stability Window (ESW). Theoretically as the ESW value of an electrolyte increases, the overall cell voltage becomes larger leading to improved energy and power density outputs. In practice the value of ESW of an electrolyte differs from its operating voltage. In fact the operating voltage of an electrolyte is the maximum voltage at which it can operate safely and does not decompose. This voltage is usually utilized for standard electrochemical analyses and beyond this voltage the electrolyte decomposes.

Current commercial EDLCs operate by employing aqueous or organic electrolytes. However the operating voltage of such devices are very small and the electrolyte decomposes if greater voltages are applied. The corresponding stability voltage window of an aqueous electrolyte is 0.9 -1.229 V and the equivalent value for an organic electrolyte is 2.5 - 2.7 V [17, 30]. On the other hand, there are Room Temperature Ionic Liquids (RTILs), which they have been proposed as an alternative electrolyte for use in both EDLCs and batteries. RTILs have been shown to be stable at greater voltages [37] than conventional organic electrolytes, i.e. 3 - 3.5 V and beyond [17].

To sum up, the type of the conducting medium plays an important part in the performance characteristics of the cell. Therefore, a careful selection of a suitable electrolyte to fulfill and satisfy a greater operating voltage is essential. Sections 2.5.1, 2.5.2 and 2.5.3 look at the prospect of employing aqueous, organic and RTILs, respectively, in EDLC cells.

2.5.1 Aqueous based electrolytes

Aqueous electrolytes have predominantly lower pore size requirements compared to organic electrolytes, as the ions are smaller in size. The relative Equivalent Series Resistance (ESR) of such electrolytes is also lower compared to organic based electrolytes e.g. acetonitrile. Thus the power density of an EC device utilizing an aqueous electrolyte is more likely to be closer to its theoretical limits. However, the aqueous electrolytes contain considerably lower ESW i.e. the stability voltage limit is significantly lower than that of the organic liquids. Therefore parameters such as ESR, operating voltage and capacitance must be taken into consideration when selecting an electrolyte. These considerations and trade-offs are of course strongly dependent on the anticipated application of the supercapacitor [10, 31].

Moreover, the use of acids such as H_2SO_4 and KOH [10] as an electrolyte for EDLCs, necessitates the use of some cell compartments to be manufactured from gold, platinum or even a conductive rubber in order to overcome corrosion problems [48].

Owing to high conductivity, relatively low cost and ease of manufacturing the use of aqueous electrolytes remains attractive. However to reduce ESR and increase the output power it is essential to utilize concentrated electrolyte mediums, preferably at or in excess of 1 molar concentration, which is hazardous and costly in terms of corrosion prevention. Utilizing strong acidic mediums also induces the problem of increased rate of self-discharge in supercapacitors [10].

Due to the very low attainable energy densities by aqueous electrolytes, they are unlikely to be employed in commercial devices. However, they continuing to provide systems for better understanding of the underlying mechanisms at the laboratory scale.

2.5.2 Organic based electrolytes

As stated previously, organic based electrolytes allow for higher operational voltages up to 2.7V. Accordingly the increased operating voltage allows for higher energy densities.

Salts are also added to the organic liquids to ensure maximum ion mobility to the carbon electrode. The two extensively used organic electrolyte solvents are propylene carbonate (PC) and acetonitrile (ACN). Due to flammability and toxicity of ACN, the most commercially used organic electrolytes utilize PC as a solvent [30]. For instance, the most commonly encountered organic electrolyte consists of a solution of tetraethylammonium tetrafluoroborate (TEA BF_4) in PC with theoretical voltage stability as high as 4 V [32].

Although the organic based electrolytes allow for greater operating potential, but they suffer from lower conductivity and higher viscosity compared to aqueous electrolytes. Accordingly, the relevant ESR is significantly higher than that provided by aqueous electrolytes. This is due to the presence of a bigger fraction of unused sites caused by higher viscosity hindering full wettability of the pores in the electrode. Reduced utilized surface area means that the capacitance is correspondingly reduced which accordingly the power density is also reduced [17].

Additionally, the employed salts are hygroscopic and moisture renders the electrolyte stability therefore the organic electrolytes must be handled in H_2O/O_2 deficient environment to ensure operation at higher voltages and also to prevent formation of H_2 and O_2 gases at greater voltages than that of decomposition of water (i.e. 1.23V). Consequently, employing an organic electrolyte requires more attention in terms of handling and fabrication, which leads to additional costs.

Table 2.1 summarizes some of the important properties and attributes of aqueous and organic based electrolytes [49].

Table 2.1 Aqueous vs. organic electrolytes for use in EDLCs

Property	Aqueous electrolyte	Organic electrolyte
Operating voltage (V)	0.9 - 1.229	2.5 – 2.7
Conductivity (S cm^{-1})	1 – 7 for H_2SO_4	0.02 – 0.6 for $TEABF_4$ in PC
Max. Capacitance (F g^{-1})	250 - 300	150 -200
Attributes	Easy to fabricate, less expensive in compare to organic electrolytes, green solvent	Fabrication must carried under inert atmosphere, expensive, not eco-friendly

2.5.3 Room Temperature Ionic Liquid electrolytes (RTILs)

Ionic Liquids (ILs) are essentially salts that display a relatively low melting point (at or below room temperature). Therefore, they are also called room temperature ionic liquids (RTILs) or molten salts. These liquids are generally classified into two generations of eutectics and discrete anion electrolytes [50]. The former is mainly comprised of Lewis or Brønsted acids that complexes the halide anion structure in order to create different ionic structures [51]. On the other hand is the discrete anion generation where liquids of this type are usually hydrophilic and oppose hygroscopic properties. This attribute is sometime detrimental to some extent as it may influence the viscosity and the conductivity values [52-54]. Therefore, analogous to organic electrolytes, ionic liquids are also handled in an O_2/H_2O deficient environment.

As stated earlier, employing ILs is not only advantageous in terms of provision of large electrochemical stability window but it also offers the following excellent properties [55-57]:

- Chemically stable at elevated temperatures sometimes up to 200°C
- Remain at the liquid state for a range of temperatures, even >120°C
- Low melting point due to the asymmetric structure, typically lower than ambient temperature allowing for operation at wide range of temperatures
- Reasonable ionic conductivity
- Negligible vapour pressure
- Green solvents, low toxicity
- Non flammability

These phenomenon properties of ILs tied with the provision of high ESW voltages allow for growing applicability of these mediums in high temperature applications. Additionally, since the start of research in this field a substantial variety of different constituents of asymmetric cations and anions known to this date with different alkyl chain length and linkages altering the physicochemical properties of the ILs. As a result a projection of above one billion synthesized ILs is estimated [58]. Nonetheless, a careful choice of the cation and anions allow for designing liquids with ionic conductivity of greater 30 mS cm^{-1} and stability potential window higher that 4V at the room temperature [59, 60].

Despite all desirable qualities of ILs, the viscosity of these mediums is greater and contains lower ionic conductivity in comparison to other types of electrolytes [61, 62]. The high viscosity of the ionic liquids possesses the similar surface wettability problem as discussed in *section 2.5.2* for organic electrolytes.

There are two ways to tackle this problem: first is to add lithium salts to the ILs to reduce the viscosity which influences the capacitance retention and second is to operate at elevated temperatures. Operation at higher temperatures not only reduces the viscosity and increases the wettability but also theoretically should lower the ionic and ESR resistance resulting in enhanced performance. Contrariwise, operation at very low temperatures may also be problematic as the melting temperatures of some ionic liquids only slightly exceeds 273K [63]. A significant sum of studies on ionic liquids is based on the cation systems shown in Figure 2.10. As already mentioned, the functionalities of derivatives obtained from these cations can potentially be modified through alkyl chain length, chirality or even branching. The common anions used are generally carry delocalized charge and can range from simple halides (e.g. chloride, bromide and iodide) to larger and more flexible fluorinated anions; hexafluorophosphate $[PF_6]^-$, tetrafluoroborate $[BF_4]^-$ and bis(trifluoromethylsulfonamide) $[(CF_3SO_2)N]^-$. The anionic component of the ionic liquid controls the electrolyte reactivity with water and the degree of its hydrophobicity [64].

This image has been removed due to the copyright

Figure 2.10 Chemical structures of some commonly used cations; a) Imidazolium, b) pyrrolidinium, c) pyrodinium, d) ammonium, e) phosphonium and f) sulfonium

Although combinations of above cation and anion species allow for production of numerous electrolytes, however some of the obtained electrolytes may not remain liquid at the room temperature. Most of the ILs have greater melting temperatures than ambient, i.e. 273K, making the operation at lower temperatures extremely challenging [63]. Additionally, the low associated ionic conductivity of ILs at room temperature, limits their optimal usage to high temperature applications mostly. For instance, it has been shown by Largeot and colleagues that operation at 60°C for a carbide derived carbon and 1-ethyl-3-methylimidazolium bis(trifluoromethylsulfonamide) [EMIm TFSI] electrolyte can increase the ionic conductivity and improve the capacitance to 160 F g^{-1} [65].

It is also reported that the possibility of synthesizing diverse ILs opens up the opportunity of designing electrolytes with high ESW and ionic conductivities up to 40 mS cm^{-1} [59, 66].

On the other hand, addition of organic solvent or various lithium salts can significantly lower the viscosity, enhance ionic mobility and in turn improve the performance.

For instance, Abdallah and coleagues investigated the use of ILs in association with acetonitrile (CAN) and γ-butyrolactone (GBL) in order to lower the viscosity, enhance the conductivity and suppress the high flammability tendencies of the solvents. They found that the IL BMIm-BF_4 and IL TMPA-TFSI consist of ionic conductivities around 43 mS cm^{-2} when used along with ACN solvent at room temperature [67]. Although good transport properties, reasonable performance (85.9 F g^{-1} with ESW of 5.5 V [67]) and low flash point are attainable specially for the TMPA-TFSI in ACN electrolyte but the ACN solvent still present high toxicity properties. Despite the toxicity challenge, the above system seems promising.

In another study the conductivity of a eutectic liquid consisting a salt of Brønsted acid-base mixture, α-picoline and trifluoroacetic acid, was measured. It was found that the conductivity of the mentioned acid-base mixtures increases by one fold compared with constructing species [68]. The use of binary mixtures has been reported repeatedly in literature as a method to reduce the viscosity of various ILs

[69-73]. However depending on the additive nature, when the binary mixture is used in supercapacitors, it may introduce charge retention problems in the system.

As stated previously, EDLCs bridge the gap between the high-power capacitors and high-energy batteries. An EDLC possesses greater power density and lower energy density in comparison to batteries; hence a major challenge here is to boost the energy density. Since energy density and power density (equation 2.3 and 2.4) increase quadratically in relation with operating voltage [74], it is clear that maximizing the operating voltage will yield in improvement of the power density and energy density simultaneously.

Due to the excellent voltage provision property of RTILs in comparison to molecular electrolytes, ILs have become a potential candidate for use in EDLCs subsequently significant amount of research is focused in this field [75-81]. An in depth insight of some important properties of RTILs will be underscored and discussed in section 2.6.

2.6 Ionic liquids at molecular level

There are several different molecular properties known comprehensively that can significantly influence the bulk properties of the IL of choice. These molecular properties are described in greater details here.

2.6.1 Molecular motion and ionic interactions of ILs

Svanté Arrhenius introduced one of the earliest theorems about interionic interactions in 1887. More precisely he proposed the idea of partial dissociation of a solute into its positive and negative constituents. Respectively the motion of these constituents in solute was described as chaotic. However the interionic interactions in an electrolyte solution were thought to be independent of their ionic motion and distribution [82]. Although this concept is held true for dilute solutions of weak electrolytes but cannot be applied to strong electrolytes as the interionic electrostatic force is large and must be considered.

Later on in 1923, the presented theory by Peter Debye and Erich Hückel about the interionic interactions has built the foundation of work in this field. This theorem is now commonly known as the Debye-Hückel theory and describes the strong electrolytes as highly dissociative [82]. This means that the concentration of constituent ions is higher compared to dilute electrolyte solutions resulting in a more packed ions population in a given volume. Hence the dimension of the ions and distribution of charges are important in molecular interactions.

Generally the summation of all intermolecular interactions within the solvent and any potential solute that may exist in the solution is known as the polarity.

Though any interactions that led to the chemical transformation of the solute are disregarded from this definition [83].

The intermolecular interactions in common salts are characterized and controlled by the coulomb forces present in between the net charges of the ions as well as several interacting components [84] displayed in equation 2.6 and equation 2.7.

In molecular salts however the coulombic forces are more moderate due to the bulkier dimensions and inhomogeneous charge distribution especially on the cation constituents allowing for directional and shorter interactions [85]. Weingärtner [85] characterizes the molecular salts' interactions in the following manner:

$$U(r,\Omega) = U_{es}(r,\Omega) + U_{ind}(r,\Omega) + U_{vdW}(r,\Omega)$$

equation 2.6

Where

r = distance between the ions
Ω= set of angles

The interaction potential, U(r,Ω), encompasses of the sum of the electrostatic (U_{es}), inductive (U_{ind}) and Van der Waals (U_{vdW}) interactions. As it clearly is signified from the formulation, the interaction potential is dependent on r and Ω for reciprocal orientations. The U_{es} interaction itself can be divided into the following sub interactions:

$$U_{es}(r,\Omega) = U_{ion-ion}(r) + U_{ion-dipole}(r,\Omega) + U_{dipole-dipole}(r,\Omega) + U_{ion-quadrupole}(r,\Omega) + \cdots$$

equation 2.7

Although there are substantial references in literature about ongoing research on exploring ILs, but the fundamental physics of their solvation is poorly understood. Accordingly the screening of interactions of ILs was only introduced and explained in 2007 through a mathematical model [86].

On the other hand, the screening of interactions of common salts has been around for a relatively long time. In molecular liquids the applied electric field is screened at the conductor surface fairly easily without changing the electrostatic potential inside the bulk [86]. Remembering, in the solvation scenarios the dipole moment of a specific molecule is screened through the use of solvent ions near the solute [87].

Note: *the molecular dipole moment occurs as a result of the non-uniform distribution of charges in individual atoms. For a pair of opposite charges the dipole moment (P) is measured by magnitude of charges (q) multiply by the distance between the charges (d).*

$$P = q \times d$$

equation 2.8

Though ILs are entirely comprised of ions and ions do not have a precise and well-defined dipole moment [86]. Additionally, the interactions between the Coulombic and van der Waals interactions in ILs results in the nano-scale phase separation into polar and non-polar regions. This phenomena leads to the creation of high charge density in the non-polar areas [88] where interactions of potential molecular solutes within their distinct environment can be monitored from these specific sites in the IL.

Correspondingly in dealing with an applied electric field, the ILs interact differently in comparison to dielectric materials due to their ionic nature and therefore extra complexities implies.

When charging and discharging an IL-based EDLC, the ions travel into and out from the respective porous electrode. With this definition the diffusive dynamics are introduced in the system. It is worth mentioning that the rate of the molecular motion is not constant and can vary from femtoseconds to nanoseconds. The molecular motion at the femtoseconds scale is characterized as ultrafast and the motion at the nanoseconds scale is classified as the diffusive regime [85].

Nevertheless the motion of ILs is not entirely limited to these rates at all conditions. For instance Ito and colleague report that at the super-cooled state the diffusive behaviour can fluctuate to the scale of seconds or even longer [89]. In molecular liquids the diffusive behaviour, e.g. molecular relaxation, is simpler and is characterized by "Debye relaxation time", disclosed in equation 2.9.

$$\Phi(t) = \exp\left(-t/\tau_D\right)$$

equation 2.9

Where

$\Phi(t)$ = time correlation function
τ_D = Debye relaxation time

Though ILs respond differently to the diffusive dynamics in comparison to molecular liquids. The behaviour of ILs has repeatedly compared to the glassy dynamics [90-95] as they possess a broad distribution of diffusive processes. Accordingly they seize a non-exponential behaviour pattern where the diffusive processes can be explained through the use of the Kohlrausch William Watts (KWW) equation, equation 2.10.

$$\Phi(t) = \exp\left[\left(-t/\tau_{KWW}\right)^{\beta}\right]$$

equation 2.10

Where τ_{KWW} is the KWW relaxation time parameter and β is the stretched exponential factor, $0 < \beta < 1$.

Regardless of the liquid type, some information about the reorientation motion of the ions can be gained through the relaxation time [85]. Accordingly it is indicated that the direct proportionality between reorientation time (τ_r) and η/T must hold, even at simplest hydrodynamic models. Seemingly the mentioned proportionality also holds at temperature elevation [96]

To study the molecular dynamics there are countless papers available in literature on various techniques. Although the focus of this thesis is to study the EDLC performance but it is necessary to have a background understanding of the possible involved dynamics in order to gain better understandings of physiochemical properties.

2.6.2 Ion diffusion and physiochemical properties of Ionic Liquids

The physicochemical properties of an electrolyte are important matters when it comes to energy storage. Ionic conductivity and viscosity are among the important examples, which are closely related to the ions diffusion. For instance although ILs are entirely comprised of ions but not all ions act as charge carriers and contribute to the ionic conductivity. This is largely depends upon the mobility of the ions, dictated by the viscosity, resulting from the IL structure, dimension and molecular weight [97, 98].

Due to the more viscous nature of the ILs in comparison to molecular liquids, they possess greater diffusion coefficients in the orders of 10^{-11} m^2s^{-1}. This figure tends to be lower when dealing with molecular liquids, i.e. 10^{-9}-10^{-10} m^2s^{-1} [99-101]. Frequently, the relation between diffusion and viscosity is described by Stokes-Einstein (SE) equation [85, 102, 103], equation 2.11.

$$D = \frac{k_B T}{\xi \pi \eta r}$$

equation 2.11

Where

k_B = Boltzmann constant for given geometry diffusion (i.e. sphere)
ξ = Coupling factor ranging from, $4 < \xi < 6$
η = viscosity
r = radius of the diffusing species

The Stokes-Einstein equation holds for many electrolytes including molecular liquids and some ILs that the size of the diffusing particle is close to those dispersed in the solvent. In this case the diffusing particle resembles the model that the macroscopic species move into a compressible bed. Accordingly in scenarios where there is a large difference in size between the diffusing particle and the bulk IL, the inverse relation between diffusion (D) and viscosity (η) no longer holds [104-107].

Various studies are performed on the self-diffusion behaviour at elevated temperatures at which significant changes in diffusion was observed [108, 109]. In this case the IL no longer behaves according to the Stokes-Einstein equation. Instead it only obeys a fraction of stokes-Einstein equation in the form of the equation 2.12, which is mostly recognized for glassy dynamics [108].

$$D \propto \left({}^{T}\!/_{\eta}\right)^{m}$$

equation 2.12

The limit for exponent (m) is similar to that of KWW factor for non-exponential pattern in diffusivity equation, i.e. m<1.

The self-diffusion coefficient is related to the molar conductance ($\Lambda = \sigma / C$) by equation 2.13, which is commonly known as the Nernst-Einstein (NE) equation [85].

$$\Lambda_{NE} = {}^{F^2}\!/_{RT}\,(D^{+} + D^{-})$$

equation 2.13

Where

σ = electrical conductivity
C = molar concentration of the salt
F = Faraday constant
D^+ = diffusion coefficient of the cation species
D^- = diffusion coefficient of the anion species

Basing on the assumption that the ions motions are independent from another, i.e. σ has negligible effect, the above equation for conductance is then accurate. Accordingly Λ becomes smaller than Λ_{NE} due to the paired cationic and anionic motion of the species in a electrically neutral arrangement where they contribute to the diffusion only and not conductance [85]. Hence due to the ion pairing in the liquid phase only about 50% of the ions participate in conductance [99-101].

This is commonly encompassed for many ILs.

In general ionic liquids with low viscosity display reasonable values of conductivity, usually in the orders of 10^{-2} S cm^{-1}. This figure increases even further when operating at high temperatures. Arrhenius law explains the temperature dependence behaviour of the conductivity as follow [50, 110].

$$\sigma = \sigma_{\infty} . e^{(\frac{-E_a}{K_B T})}$$

equation 2.14

Where

σ_{∞} = hypothetical maximum electrical conductivity at infinite temperature
E_a = activation energy required for electrical conductivity
K_B = Boltzmann constant

Electrical conductivity is among the important properties required for energy storage systems including supercapacitors. From the above equation it is clear that the electrical conductivity is a function of temperature. Albeit temperature elevation influences the values of conductivity but it is not the sole determinant variant. In fact the cation and anion size and dimension are also influence the electrical conductivity.

For instance in an study performed by Vila and colleagues they showed that the conductivity diminishes as the alkyl chain length of the cation becomes longer [109]. This is a well-expected trend as the size of the alkyl chain length influences the free motion and mobility of the cation. Although in some cases the effect of the anion size follows the described behaviour as the cation but this is not the case at all times. For example, in another study Vila and colleagues observed a direct relation between increase in anion size ($Cl^- < Br^- < BF_4^-$) and electrical conductivity [109]. Some aluminium halide salts were also reported to follow the same behaviour [111]. This is explained through greater mobility of the anion while the surface charge density is reduced.

On the other hand are the bigger size anions, e.g. PF_6^- < ethyl sulfate$^-$ < tosylate$^-$, where the inverse proportionality with the electrical conductivity holds. Thus the dual effect of the anion size on conductivity is dedicated to 1) reduction in the surface electrical charge density and 2) influence of the anion size on the dynamical movement [112].

Regardless of the described conditions, if the plot of Ln(σ) vs. temperature is a linear decay then the Arrhenius behaviour holds.

However some obtained experimental data for ionic liquids show a nonlinear decay with temperature [50, 63, 99, 109, 113, 114]. In this case Vogel-Tamman-

Fulcher equation, equation 2.15, is used instead to describe the variation where T_g is the ideal glass transition temperature and is usually fitted for experimental data.

$$\sigma = \sigma_{\infty} e^{-\frac{E_a}{k_B(T-T_g)}}$$

equation 2.15

Since ILs are entirely comprised of ions, the general understanding is that they should contain high conductivities. Although this holds for many ILs but as already stated conductivity is largely dependent on the number of the charge carriers and the ions mobility [104]. These attributes themselves are described through another physiochemical property called viscosity. Hence electrical conductivity and viscosity are strongly related to one another. Owing to this quality the behaviour of both entity is interlinked. For most ILs the conductivity relation seems to be inversely proportional to the viscosity [104]. Consequently at higher temperatures, the electrical conductivity increases due to greater ion mobility caused by reduced viscosity [113]. Analogous to electrical conductivity at some cases, e.g. distillable ILs, the viscosity follows the Arrhenius behaviour [115] (equation 2.16) and in other cases follows the Vogel-Tamman-Fulcher relationship (equation 2.17) [116]. The former is reported for aprotic ILs over a wide range of temperatures and the latter is mainly reported for ILs with symmetric cations or cations that contain functional groups.

$$\eta = \eta_{\infty} e^{(\frac{E_a}{RT})}$$

equation 2.16

Where

η_{∞} = hypothetical maximum viscosity at infinite temperature
E_a = activation energy

$$\eta = A\, e^{\frac{\check{D}\, T_g}{(T-T_g)}}$$

equation 2.17

Where A is an adjustable parameter in units of mPa s, Ď is indirectly proportional to the liquid's fragility and T_g is the glass transition temperature where the viscosity reaches a high value in the orders of 10^{13} Poise at this temperature [116].

The product of the exponential function in the denominator, i.e. Ď x T_g, is commonly referred to as adjustable parameter B and has units of Kelvin.

There are also reports on ILs that do not obey the either relation [117].

As already discussed, there is a relation between electrical conductivity and the viscosity. To visualize this relation a Walden plot, σ vs. log(η), is used to provide good information about the ionicity. Dilute solution of KCL is used as an indication of a fully dissociated system where it creates a solid line profile known as Walden line. In a fully dissociated state the ions have equal mobility, therefore presence of acidity or basicity causes deviation from the Walden line [97].

3 Objectives

In spite of creation of numerous ionic liquid combinations, a systematic study of these electrolytes becomes rather difficult and demanding. This project aims to perform a systematic study of various ionic liquids in an EDLC arrangement in a clear and well-defined framework. This is implemented through creating various combinations of Carbon-IL cells in the laboratory. The overall performance of the manufactured cells was then studied using Galvanostatic and impedance measurements. A range of individual physical property measurements was also precisely performed for both ILs and carbon materials.

In order to accomplish the above objectives, four activated Xerogel-based carbons were produced in the laboratory as porous electrode materials and nine different liquids from different classes of ILs were selected as electrolytes.

By varying the relative fractions of resorcinol to catalyst when producing the aerogels and keeping the ratios of other precursors and processing conditions such as carbonization or activation temperature and time fixed, a range of carbons with different pore characteristics and surface areas was produced. The chosen ionic liquids are from the pyrrolidinium, sulfonium, ammonium and phosphonium groups. Although cationic component of selected ILs are from these classes but the anionic component, i.e. Tf_2N, kept the same for all combinations as the variation in type of the anionic constituent can influence the hydrophobicity and physiochemical properties of the IL. In fact these electrolytes mainly differ from one another by the alkyl chain length of the cationic component and inclusion of functional groups in ammonium and phosphonium based liquids.

Albeit the priority for choosing ILs is given to the liquids with low viscosities but not all chosen electrolytes offer this property optimally at room temperature. As discussed in the previous section, the high viscosity of ILs is one of the major challenges towards utilization in storage devices due to limited ion mobility hindering the performance. Even though the viscosity can be reduced by addition of small amounts of organic solvents [118, 119], addition at traces level can lead to a major fluctuations in the values of diffusion coefficient [104] and electrochemical stability. However, due to the dependence of the diffusion coefficient and viscosity on temperature, temperature elevation was employed to alter the viscosity over various temperatures (from 25°C, 40°C, 60°C and 80°C). This operation temperature range is specifically selected to identify a maximum operating temperature that various cell combinations remain stable without any significant voltage drops and also to identify the potential combinations that can be explored for future use in place or conjugation with fuel cells that operate in 80°C. Accordingly this operation temperature was selected as a maxima for the studied range where safe operation must be ensured in the light to be used with fuel cells in future.

At a further attempt to reduce the viscosity, the effect of presence of presence of an ether linkage was also investigated for the Ammonium based and Phosphonium based ILs where greater values of viscosities were recorded at room temperature.

4 Theory

This chapter briefly describes the background to techniques used in order to determine the physical properties of the manufactured carbons (i.e. surface area and pore characteristics) and physiochemical characterizations of the chosen electrolytes (i.e. viscometry, thermal properties measurements, water content and conductivity).

The surface area and pore characteristic properties of the fabricated carbons were determined through the use of BET. The physiochemical properties of the ILs were determined using rheology, differential scanning calorimetry, water content and conductivity

4.1 Physical state characterization

4.1.1 Gas adsorption-desorption

Gas adsorption is commonly used to determine structural properties, pore characteristics and relevant surface area of a porous solid material, e.g. activated carbons. Through this method, adsorption always takes place at the solid surface where it is directly exposed to a gas that is thermodynamically below its critical temperature. It is very common to refer to the adsorbed gas and the solid surface as the “adsorbate” and “adsorbent”, respectively [120].

Depending on the system of study and nature of the material, various inert gases such as N_2, Kr, Ar, H_2, CO and CO_2 can be selected as the adsorbate [121]. In this study however, nitrogen gas is utilized in order to probe even the smallest micropores accurately whereas utilization of other gases for our purpose can lead to partial measurements of the adsorption isotherms.

Gas adsorption can occur via a chemical or physical route.

In chemical adsorption, or chemisorption, an electron is transferred from the adsorbate to the adsorbent surface, which is usually associated with large interaction potential (E_P) as a chemical reaction is required to overcome the activation energy barrier in order to create a platform for adsorption to occur. This results in high heats of adsorption, which in turn causes only one layer of molecules to be adsorbed to the surface of the adsorbent. Accordingly, chemisorption usually occurs at higher temperatures than the adsorbate critical temperature and is irreversible, i.e. no desorption occurs.

In physical route, or physisorption, the adsorption solely occurs through van der Waal's forces at very low diffusion rates [122]. Hence the heat of adsorption is much smaller compared to that of chemisorption. This in turn allows for multiple layers of molecules to be absorbed on the adsorbent surface. Also physisorption is a reversible adsorption process, i.e. desorption occurs.

Moreover low diffusion rates means prolonged adsorption times and as already stated no surface altering chemical reactions occurring as associated with chemisorption. Hence physisorption technique is selected for studying the solid carbon samples.

Regardless of the adsorption method, an isotherm is always produced which characterizes the porous solid by measuring the amount of adsorbate onto the adsorbent surface over a range of pressures. Hence the amount of adsorbed gas is not only a function of interaction potential but pressure (P) and absolute temperature (T) also have an affect [123]:

$$W = f\,(E_P, P, T)$$

equation 4.1

During physisorption with N_2 the temperature is kept constant at 77K, so above statement simplifies to:

$$W = f\,(E_P, P)$$

equation 4.2

In order to obtain useful information about surface area and pore characteristics, there are various methods of isotherm interpretation proposed and are available in literature. Among these methods are Brunauer-Emmett-Teller (BET) method [124] to determine the surface area, Barret-Joyner-Halenda (BJH) method [125] to determine pore size distribution, density functional theory (DFT) method to determine the mesopore volume and finally the t-plot method to determine the micropore volume [126]. The surface area and pore size distribution can also be determined through the DFT method as a quick check to ensure consistency with the attained trends from BET and BJH.

The initial step to interpret any isotherms is to determine the nature of adsorption processes which is classified by IUPAC into six main type isotherms [127], shown in Figure 4.1.

This image has been removed due to the copyright

Figure 4.1 Various types of physisorption isotherms. Adapted from [127]

As shown in Figure 4.1, different types of isotherms display a unique and individual shape that is associated with the operational temperature and interaction nature of the adsorbate and the adsorbent together.

In type I isotherms, a rapid adsorption is experienced at the low relative pressures followed by a constant adsorption at increased relative pressures. Afterwards, the profile either reaches a limit for the volume adsorbed or reaches a saturated vapour pressure. Although the reversibility holds for both scenarios, the desorption isotherm for the latter scenario may lie above the adsorption isotherm. The type I isotherm is mainly observed for adsorbents with microprosity whose pore dimension is slightly larger than the adsorbate molecular dimension. Accordingly the adsorption process carries on until a point where a molecular monolayer of pure adsorbate is present at the adsorbent surface. Hence this point resembles a complete filling of micropores with the adsorbate.

In type II, III, IV and V isotherms, a limit for completion of the monolayer is not achieved. Hence determination of this point is arbitrary and it mainly assumed to be present at the inflexion points on the isotherm, represented by letter ‘B’.

Unlike type I, the type II isotherms do not exhibit any saturation limit. They are mainly obtained either for non-porous or wide porosity range adsorbents where infinite monolayers and multilayers can potentially form. It can be interpreted that after point ‘B’, where monolayers are all formed, completion of other layers on top are continued.

Type III isotherms occur when the attraction force holding the adsorbate molecules together is greater than the force between the adsorbate and the adsorbent. In this scenario the volume of the adsorbed gas increases significantly once the monolayer is formed. This in turn leads to formation of a convex shaped isotherm. Similar to type II isotherm, the type III isotherm is particularly obtained when the solid sample is non-porous [128].

Type IV isotherms are in fact very similar to the type II isotherms but with the formation of finite multilayers instead of the infinite ones. This leads to complete filling of the capillaries in the mesopores where relatively strong interactions between the adsorbate and the adsorbent are present.

Type V isotherms are similar to the type III isotherms where the interactions of adsorbate and adsorbent are weak. Type V isotherms are very similar to type IV in terms of the profile shape and similarly are associated with mesopore filling.

Additionally, the desorption isotherms for both types IV and V is in disagreement with their adsorption profile in terms of not following the same path. Accordingly a gap is created between the adsorption and desorption isotherms that at lower relative pressures closes itself up. This leads to establishment of adsorption hysteresis, which are illustrated in Figure 4.2.

Type VI isotherm are represented by steps-rise multilayer adsorption profile which are associated with monolayer adsorption for each step. The overall shape of the profile and sharpness of the steps are strongly dependent on the system of study and the adsorption temperature. It is worth noting that these profiles are not very common.

As already mentioned, the nature of the type IV and V isotherm profiles lead to creation of adsorption hysteresis loops where they are usually related with the capillary condensation in the mesopore volume. These hysteresis loops are characterized into four main types as shown in Figure 4.2.

This image has been removed due to the copyright

Figure 4.2 Various types of hysteresis loops. Adapted from [127]

Regardless of the type of the hysteresis loop, a common trend is attained for most desorption profiles: that is characterized with a steep region of branching followed by a gentler closing point. Among the illustrated hysteresis loops, the H1 and H4 are the two extreme cases where in former the adsorption and desorption isotherms are generated vertically and almost parallel to one another over a significant range of adsorbed gas. This scenario occurs oppositely for the H4 type loops where the adsorption and desorption isotherms similarly remain almost parallel with respect to each other but over a appreciable range of relative pressures and in the horizontal direction. The H1 and H4 hysteresis loops are attained for agglomerates of relatively uniform spheres and narrow slit shaped micropores, respectively.

The types H2 and H3 loops are mainly recognized as intermediate profiles between the extreme H1 and H4 classes. The H2 types are attained for more than one distinct pore structure, thus interpretation of these type loops are rather difficult. This has been explained through the mechanism differences between condensation and evaporation, which are occurring in "ink bottle" pores. These types of pores are composed of wide bodies and narrow necks. Finally the H3 loops are attained for plate-shaped aggregates.

4.1.1.1 Langmuir theory

Various isotherm kinetic theories and equations have been developed. Most of these equations applied to a small range pressures consequently they are invalid when applied to real experimental data, i.e. a wider range of relative pressures. In the next sub-sections the utilized methods to interpret the data will be discussed.

For the purpose of the surface area determination, the succession of these equations is strongly dependent on their prediction of the adsorbate molecules onto the surface to create a monolayer of molecules. The Langmuir theory is one of the pioneer theorems for surface area determination and similarly obeys the same adsorption manner. As described in section 4.1.1 the adsorption of a single molecular layer onto the surface is associated with the type I isotherms where a maximum adsorbed amount is approached and is associated with the micropore filling.

In order to derive the theory, the following assumptions have been made:

1. Monolayer of molecules formed on energetically uniform surface
2. The rate of the adsorption and desorption are equal
3. No further adsorption beyond formation of the monolayer occurs
4. No variation in porosity. This means that all pore sites on the surface are alike and a single adsorbate molecule could be adsorbed to the surface at most as the adsorbate residence from the neighbouring sites have an influence

However due to the oversimplifying assumptions, the Langmuir model fails to describe the surface area for mesoporous materials with type II and IV isotherms.

4.1.1.2 BET theory

The limitation for describing the mesoporous materials through Langmuir theory led to development of another theory called Brunauer, Emmett and Tellerthat (BET) theory that is in fact the extension of the Langmuir but is able to explain the multilayer adsorption. Derivation of this theory for multilayer adsorption also requires making number of assumptions that are underlined as follow:

1. Infinite layers of adsorbate molecules are physically adsorbed to the surface
2. Langmuir theory applies to every layer with no interactions between the layers
3. Energetically uniform surface. Hence there are no interactions whatsoever between the neighbouring molecules leading to no interactions between the adsorbed layers

This image has been removed due to copyright

Figure 4.3 pores filling with increase in relative pressures

The resulting BET equation is expressed by the following equation and the total surface area can be calculated through dividing the (c-1)/v_mc term by sample weight.

$$\frac{1}{v(\frac{P_0}{P}-1)}=\frac{1}{v_m c}+\frac{c-1}{v_m c}(\frac{P}{P_0})$$

Where P and P_0 are equilibrium and saturation pressure of adsorbate at the temperature of adsorption, v is the adsorbed gas quantity and v_m is the monolayer adsorbed gas quantity. c represents the BET constant that is expressed by:

$$c = \exp\left(\frac{E_I - E_L}{RT}\right)$$

Where E_I and E_L are the heat of adsorption for the first and second or higher layers. E_L is equal to the heat of condensation for the adsorbate.

4.1.2 Rheology

Viscosity is important for many applications especially for electrolytes in energy storage systems as this property controls the ions motion towards a charged electrode surface. As discussed previously viscosity is accounted as one of the main contributing factors for determining the rate of mass transport.

Hence for precise measurements at varying temperatures in an O_2/H_2O deficient environment, the electrolyte samples were transferred to Universidad de São Paulo for analysis.

4.1.3 Differential scanning calorimetry

Differential Scanning Calorimetry (DSC) is a thermo analytical technique used to quantitatively determine the physical transitions and chemical reactions of solid and liquid samples. Through this technique information about melting point, glass transition, enthalpy of fusion, crystallization behaviour, reaction enthalpies, reaction kinetics, specific heat capacities and many other characteristics can be extracted depending on the nature of the sample.

In the course of this work the DSC is only used to determine the melting point (T_m) of the electrolytes.

For the purpose of energy storage in supercapacitors, the range at which the utilized ionic liquids remain in the liquid state is very important. This is exceptionally important for us, as temperature elevation runs were also proposed as a solution to reduce the electrolyte’s viscosity and improve performance. Hence determination of T_m through DSC is essential in order to ensure the liquid range is in fact holds for the utilized operating temperature range, i.e. 25°C - 80°C.

The DSC test measures the heat flow into and out of the sample while heating, cooling or at constant temperature conditions. A DSC instrument is mainly comprised of ceramic sensors, a small silver furnace, temperature sensors and cooling attachment compartments. Below is a simplified cross-sectional view of a DSC measuring cell. The FRS5 and Pt100 sensors measure the difference of heat flows through the sample and furnace temperature (T_c) respectively.

This image has been removed due to the copyright

Figure 4.4 left: x-section representation of a DSC unit, right: magnified section of the sample pan

The generated heat from the silver furnace flows upward towards the sample and reference crucibles. In this process the heat flows across the silver plate just above the furnace then through the glass ceramic interface disk and the FRS5 sensor. The heat then flows in two thermocouples arranged in series and located just beneath the sample crucible and to the sample. The purpose of the radial thermocouples is to measure the difference between the two heat flows represented by temperatures T_s and T_d on Figure 4.4. It also adds extra calorimetry sensitivity that is defined by [$S = V / \Delta T$]. From Ohm's law the heat flow on the sample side is given by:

$$\phi_s = \frac{T_s - T_c}{R_{th}}$$

equation 4.3

Owing to the symmetrical thermocouples arrangement, the thermal resistances for both sample and reference sides are the same. Analogously above equation holds for the heat flow through the reference crucible (ϕ_r) too. Hence the corresponding DSC signal to the sample can be obtained as ϕ_s - ϕ_r, **equation** 4.4

$$\phi = \frac{T_s - T_r}{R_{th}}$$

equation 4.4

Since T_s and T_r are determined by the thermocouples, it is compulsory to consider the sensitivity ratios. Hence above equation of heat flow is simplified to the following:

$$\phi = \frac{V/_S}{R_{th}} = \frac{V}{E}$$

equation 4.5

Where V is the thermoelectric voltage and E is the product of sensitivity and R_{th} commonly known as calorimetric sensitivity of a sensor. Various transition temperature profiles could be obtained depending on the materials properties but usually the melting peaks are triangular shaped and endothermic in nature as the heat is adsorbed to breakdown the crystallization energy.

4.1.4 Water content measurement [129]

In analytical chemistry, Karl Fischer titration method is used as a common technique to determine the traces of water content available in the electrolyte samples. This measurement is in particular very important when dealing with ILs as presence of considerable amount of moisture content reduces the operating potential and hindering the performance at the same time. There are volumetric and coulometric titration procedures where the latter is selected for measuring the water content. The instrument itself is consists of a titration vessel, which is comprised of two main compartments of: anode solution which is usually a mixture of an alcohol (methanol), a basic solution (imidazole) with sulfur dioxide and iodine and a small cathode that is immersed in the anode solution. These two compartments are separated with an ion-permeable diaphragm. Below are the general reactions occurring when a water-containing sample is added to the vessel.

$$CH_3OH + SO_2 + RN \rightarrow [RNH]SO_3CH_3$$

equation 4.6

$$H_2O + I_2 + [RNH]SO_3CH_3 + 2RN \rightarrow [RNH]SO_4CH_3 + 2[RNH]I^-$$

equation 4.7

From above equations it is clear that sulfur dioxide oxidizes via two steps of 1) reaction with the hydroxyl bond on methanol and 2) present water contents in the sample electrolyte in presence of I_2. Hence the overall reaction consumes one mole of water with one mole of iodine, i.e. 1:1 ratio. The endpoint of the reaction is determined through a controlled current potentiometry with using two electrodes. Hence this method is commonly referred to in literature as the bi-potentiometric method. The two mentioned electrodes are potentially working electrodes and an indicator electrode where the current is detained constant between them. Towards the end of the reaction, there are more I^- than I_2 hence a sudden voltage drop occurs due to the presence of remaining I_2 in the anode solution. At this point the indicator electrode detects the voltage drop and the reaction ends. The interpretation of the results to determine the water content in the electrolyte sample is done through obtaining the amount of utilized charge to reach the endpoint and reproduce I_2.

4.1.5 Conductivity analysis

The conductivity of an electrolyte is usually determined through voltammetric experiments where the utilization of large quantities of electrolyte is not very economical, especially as temperature elevation must also be considered.

In voltammetric experiments, the value of conductivity is usually determined by the ohmic drop measured upon a changing current [130]. The impedance method was used for determination of this resistance. Please refer to section 4.2.4 for more information on this technique.

The value of conductivity was determined through equation 4.8 where κ is the cell constant units and R is the resistance determined from the Nyquist plot. The cell constant itself can either be determined via equation 4.9 or through the use of a calibration solution with a known conductivity. Prior to each IL conductivity runs, and impedance measurement was performed with the calibration solution to correct for the cell constant.

$$\tau = \frac{\kappa}{R}$$

equation 4.8

$$\kappa = \frac{L}{A_{elec}}$$

equation 4.9

Where A_{elec} is the surface area of the active working electrode and L is the distance parting the two electrodes.

4.2 Electrochemical characterization

4.2.1 Two-electrode (2e) and three-electrode (3e) measurements

Electrolytes in general account as a crucial component of any electrochemical system. Among all the physiochemical properties, the electrochemical stability window (ESW) is the most indispensible one as it defines the maximum potential range that the electrolyte remains inert towards electrolysis that is involves electronation and de-electronation processes. In other words ESW is the potential difference between the onset of oxidation and reduction reactions that occur at the positively charged and negatively charged electrodes, respectively [104, 131]. Voltammetry experiments are generally used to determine the ESW for most electrolytes. See section 4.2.2 for background details on linear sweep voltammetry. This is usually done using a potentiostat where it regulates the potential difference between the working electrode (WE) and the reference electrode (RE) implemented by introduction of current in the system via an auxiliary electrode, commonly referred to as counter electrode (CE). When the potential difference is greater and beyond than that of the stability window, then the electrolyte decomposes [132] and is observed as a sharp increase in current. This is clearly demonstrated in Figure 4.5.

This image has been removed due to the copyright

Figure 4.5 Variation of potential at varying current. Adapted from [10]

The main interactions are occurring at the working electrode. If the dominant interaction is oxidizing the electrode is anodic, or vice versa if it is reducing then the working electrode is cathodic. On the other hand the reference electrode has the important role of separating the oxidation and reduction processes. The reference electrode can be utilized into two arrangements of 2-electrode and 3-electrode cells.

Although the cyclic voltammetry method is fairly simple to perform for these type of measurements but various factors may influence the stability range of an electrolyte, regardless of the selected system. Among these factors are the voltammetric parameters such as potential scan rate and the cut-off current as well as electrodes materials, impurities and cations/anions dimensions and nature [105, 133].

The selection of potential scan rate and the cut-off current values are fairly arbitrary and the selected limits must be determined through available literature.

On the other hand, presence of impurities, such O_2 and H_2O, in the ILs is accounted as one of the major limitations in determination of the ESW value. This is largely due to the hygroscopic nature of these mediums. In other words presence of aforementioned elements causes different levels of dryness, which consequently results in an inconsistency of the reported literature values for a specific electrolyte [134]. For this reason, the ILs must be dried and kept in a nitrogen or argon filled atmosphere environment.

As already stated the effect of ions dimensions and nature is also significant for ESW determination. In general pyrrolidinium, phosphonium and ammonium based cations results in wider stability windows compared to the imidazolium-based cations [56, 135, 136]. However this is strongly reliant on the selected anion too. The $[NTf_2]^-$ and $[FAP]^-$ anions are more resistant towards oxidation, imposing a wider range of ESW compared to $[BF_4]^-$ and $[PF_6]^-$ anions. Albeit individual properties of the cation and anion may seem desirable but those properties may no longer remain the same when serve as a conjugated IL molecule. Hence it is important to determine the ESW of the IL and not entirely rely on the information about individual species.

The alkyl chain length and functionalized branching groups on the cation are also effect the ESW value. For instance when the alkyl chain length on the cation is extended, wider stability windows are detected. However this trend is reverse when for example a functionalized ether-linkage is added to the cation structure [137].

Finally the last important factor influencing the ESW is materials at which the aforementioned electrodes are produced from. For instance the material of choice for WE is a wide range from tungsten to gold and glassy carbon [63]. Accordingly the choice must correlate with the actual electrode/electrolyte system of choice.

Since carbon is the main utilized element for constructing the electrodes therefore a glassy carbon WE was employed.

4.2.2 Linear sweep voltammetry

Linear sweep voltammetry is known as a fundamental method for studying the current potential dependence of a system where a quick screening procedure is utilized to pinpoint feasible system materials. The linear sweep voltammetry is also referred to as cyclic voltammetry when applied in repetitive manner.

There are many applications recognized for this method. For instance kinetic investigations, such as pioneer studies on diffusion-controlled processes [138, 139], are among the important ones. Kinetic information can be extracted via interpretation of the voltammogram. This is beyond the required application of this method, hence no further information is provided here. Please refer to [140] if more information is required.

The linear sweep voltammetry is only used in this study to determine the limits of the decomposition potential, hence with the aid of literature study a bigger range potential is applied to accurately determine the decomposition potential of the electrolyte.

Via this method the change in potential with time (dE/dt) is scanned with a constant scan (or sweep) rate from potential E_1 to potential E_2, known as the potential difference ΔE, and the response is recorded [10, 140]. This method was utilized for determination of both operating and ESW voltages.

4.2.3 Galvanostatic cycling

There are number of diverse techniques recognized to characterize the supercapacitors. For instance Galvanostatic cycling (GC) as large amplitude technique [141-145] and EIS as small amplitude technique [146-151] have been extensively utilized to do the job experimentally. On the other hand there has been some studies and developments on the computational simulations [152-155].

However the focus in this study is to characterize the capacitors via experimental route. Accordingly GC and EIS methods are discussed in greater details.

The Galvanostatic cycling, also known as constant current cycling (CC), is a direct current (DC) measurement and describes the capacitance by monitoring the voltage response when various currents are applied.

On a more general basis, the CC cycling is utilized to determine the discharge capacity and the cycle life of the system due to the simpler electrical control arrangement when compared to the other method. As the name states CC cycling works by applying a constant current and monitoring the potential response (ΔE) that was developed across the system over a specific time (Δt), as illustrated in the following equations [10]:

$$C = \frac{\Delta q}{\Delta E}$$

equation 4.10

And

$$\Delta q = \int I.dt$$

equation 4.11

Substituting Δq in equation of capacitance, gives:

$$C = \int I.\frac{dt}{\Delta E} = I\frac{\Delta t}{\Delta E}$$

equation 4.12

The potential difference increases linearly with time as more and more charge accumulates at the interface. Hence a linear profile that corresponds to ideal charging is attained. Though this condition only hold true for ideally polarizable electrodes where no rate limiting processes are occurring, i.e. current passes the charge across the interface with no interruptions caused by these processes. Since the chosen electrodes in this study, i.e. porous carbon, are not ideally polarizable in general then the potential difference usually deviates from the ideal profile, which is known to have a linear dependence on time. This is clearly illustrated in Figure 4.6.

This image has been removed due to the copyright

Figure 4.6 CC charging for an ideally and non-ideally polarized electrode.
Adapted from [10]

Most EDLCs are 2-terminal system with potentially no reference electrode. Please refer to section 4.2.1 for more information. Hence an overall evaluation of the 2-terminal system will be obtained by considering an individual terminal capacitance and multiplying it by two. Although in producing EC cells, electrodes with similar mass are selected but within this selection the electrode with lower active mass is usually chosen for the calculations to ensure exaggerations in presence of the active carbon mass is minimized.

The value of equivalent series resistance (ESR) can also be determined from when the current direction is reversed from charge to discharge. Usually the current reversal point is associated with a potential drop (ΔE_{iR}) at the beginning of the discharge profile. This potential drop is commonly referred to as the internal resistance (iR) and displayed in Figure 4.7.

This image has been removed due to the copyright

Figure 4.7 a) configuration of an EDLC and b) potential profile across the same EDLC on discharge. Adapted from [10]

The Galvanostatic profile of above schematic is represented as follow:

This image has been removed due to the copyright

Figure 4.8 observed iR drop on the discharge profile of a Galvanostatic cycling procedure. Adapted from [32]

Accordingly above values can be utilized to calculate the ESR using the Ohm's law:

$$ESR = \frac{\Delta E_{iR}}{I}$$

equation 4.13

It is worth mentioning that the rate of the charge and discharge is fairly important and is influential on the amount of stored energy. For instance, at lower charge/discharge rates, more energy is stored and vice-versa at higher rates less energy is stored. Hence it is essential to perform the GC measurements at varying discharge rates.

4.2.4 Electrochemical impedance spectroscopy [EIS] [10, 102]

Ohm's Law describes the resistance as a constant measure where it creates opposition to the passage of current when voltage is applied, denoted as R=V/I. This relation can solely be applied to 'ideal resistors', which 1) assumes an in phase flow of current and voltage in the resistor, 2) neglects the effect of frequency on resistance and 3) follows the Ohm's Law at all circumstances regardless of the current and voltage levels.

However for real circuit elements the story is different and a more complex behaviour is anticipated. This behaviour is described by electrochemical impedance spectroscopy (EIS) where there are conceptual similarities to resistance but with a broader range of applicability to circuit elements and no simplifying factors.

Unlike Galvanostatic cycling, EIS is an alternating current (AC) technique and is used to characterize the capacitive and resistive behaviour of the produced EDLC cells.

This is done by applying an AC potential and monitoring the current response where resistances are become isolated as a function of frequency.

Analogous to Ohm's Law, the impedance is also represented as a fraction of potential and current for a given frequency, equation 2.14

$$Z(\omega) = \frac{E(t)}{I(t)}$$

equation 4.14

In a purely sinusoidal potential, E(t) is the time variant potential show equation 2.15 and I(t) is the current response that is lagged by phase angle , ϕ, is expressed by equation 4.16.

$$E(t) = E_0 \sin(\omega t)$$

equation 4.15

$$I(t) = I_0 \sin(\omega t + \phi)$$

equation 4.16

Where ω is the angular frequency calculated by 2πf. If the potential and response current is considered as a rotating vector, as shown in Figure 4.9, then its length is the amplitude E and ω is the frequency of rotation. The frequency of the potential and current response is usually the same, however this is not the case for the resistance. In fact other resistances than ohmic may influence the shape by imposing a certain phase angle and causing the response to be out of phase.

This image has been removed due to the copyright

Figure 4.9: Rotating vector diagram for an alternating voltage signal and alternating current response. Adopted from [102]

Hence the observed potential and alternating current at any time can be considered as the component of rotating vector diagram.

It is worth discussing that the impedance may contain capacitive elements, inductive elements or even ohmic resistances. These elements and their respective dependence on frequency are shown in the following table:

Table 4.1 Various elements of equivalent circuits. Adapted from [10]

	Current vs. potential	**Z’=**
Resistor R (Z_R)	E = IR	R
Capacitor C (Z_C)	I = C dE/dt	∞
Inductor L (Z_L)	E = L di/dt	-

As shown on the above table, the current response for a '*capacitor'* is determined by multiplication of the capacitance by the derivative of the excitation potential signal. The time variant potential, expressed in equation 4.15, could also be expressed in the following form for the same circuit element:

$$E(t) = E_0 \cos(\omega t + \phi)$$

equation 4.17

The substitution of derivative of the rearranged expression of time variant potential in the current response equation of the capacitors, gives:

$$I(t) = C[-\omega E_0 \sin(\omega t + \phi)]$$

equation 4.18

This expression can also be expressed in the following form:

$$I(t) = C[\omega E_0 \cos(\omega t + \phi + {}^{\pi}/_{2})]$$

equation 4.19

As stated earlier, the excitation potential and the alternating current response could be expressed in terms of the rotating vector diagram. By using the given information and Euler's mathematical relationship of the base of the natural logarithm, i.e. exponential function, equation 4.17 and equation 4.19 can be simplified to the following equations respectively. Note that j is √-1.

$$E = E_0 e^{j\phi}$$

equation 4.20

$$I = C\omega E_0 e^{j(\phi + {}^{\pi}/_{2})} = C\omega E_0 (e^{j\phi}. e^{j{}^{\pi}/_{2}}) = C\omega j E_0 e^{j\phi}$$

equation 4.21

The current response is simplified even further by equalizing the ($e^{j\pi/2}$) function to j as –π/2 is defined as the phase shift between the potential and current in an ideal capacitor. This part is commonly referred to as the imaginary component. According to equation 4.14 the impedance for capacitors is derived and expressed in equation 4.22.

$$Z_C = \frac{E_0 e^{j\phi}}{C\omega j E_0 e^{j\phi}} = \frac{1}{C\omega j} = \frac{-j}{C\omega}$$

equation 4.22

In theory, by utilizing the EIS method for capacitance measurements, the pseudo capacitance of the electrode is distinguished from the double layer capacitance over a specified range of frequencies [10]. Accordingly direct information about the resistances and device performance could be extracted from this measurement. The Z_C expression is representable on the Nyquist plot and the determined capacitance here is known as the equivalent series capacitance (C_{ESC}), which is usually frequency dependent [156]. This means that C_{ESC} would no longer see the system as an isolated DBL capacitor hence the equation of capacitance, i.e. dependence on surface area, as defined in section 2.1 is not equal to the C_{ESC}:

$$C_{ESC} \neq \frac{e_0 e_r A}{d}$$

equation 4.23

In fact the C_{ESC} follows the system response as a whole accordingly determination of capacitance via both methods is important. The determination of the cell capacitance via impedance at the lowest frequency, Z_{im}, is done through the following equation:

$$C = \frac{1}{2\pi\omega Z_{im}}$$

equation 4.24

To characterize supercapacitors via EIS, an equivalent circuit is required to interpret the data. However, in spite of extensive efforts in this field no single circuit model has been established to mimic and rationalize the entire system behaviour as a whole [156].

The classical interpretation of the response is based on the transmission line model where the structure of the porous medium is assumed to be cylindrical in shape [157, 158]. In this model, the charge enters the electrode pores progressively [10, 159] and the pore structure itself is described by a series of RC circuit components that are connected in parallel and are present along the length of the pore as shown below.

This image has been removed due to the copyright

Figure 4.10 The transmission line model of a carbon pore. Adapted from [156]

The resistor in this model represent the electrolyte diffusion into the electrode pore and the capacitor accounts for local charge storage through electrolyte’s polarization at the pore surface.

However the transmission line model only works for porous materials that are identical and uniform in structure. Accordingly modifications to the circuit model are necessary as the selected carbon material for this study is produced via pyrolysis at high temperature, i.e. wide pore size distribution and irregular particle sizes. Additionally utilization of ionic liquids as electrolytes imposes extra complexity into the system due to the purely ionic nature of these materials.

Considering above limitations, the proposed circuit for the utilized system is shown in Figure 4.11:

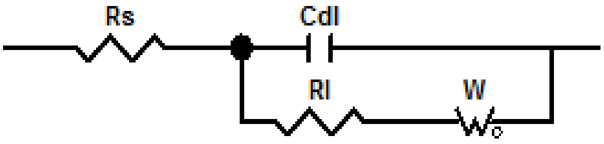

Figure 4.11 the equivalent circuit for the employed porous system

This circuit is commonly known as the Randle’s circuit and is used to describe the impedance behaviour of an EDLC system [10, 33, 146, 160, 161]. In this model there are variety of components; capacitor (C_{dl}), ionic resistance (R_I), solution resistance (R_S) and Warburg (W) resistance. Every single component in this arrangement represents and simulates a unique behaviour of an EDLC cell.

The development of the Randle’s circuit from a single capacitor circuit, i.e. an ideal capacitor, followed by the introduction of other involved resistances along with the graphical representation of impedance response on the complex plane of Nyquist plots is expressed in the following figure.

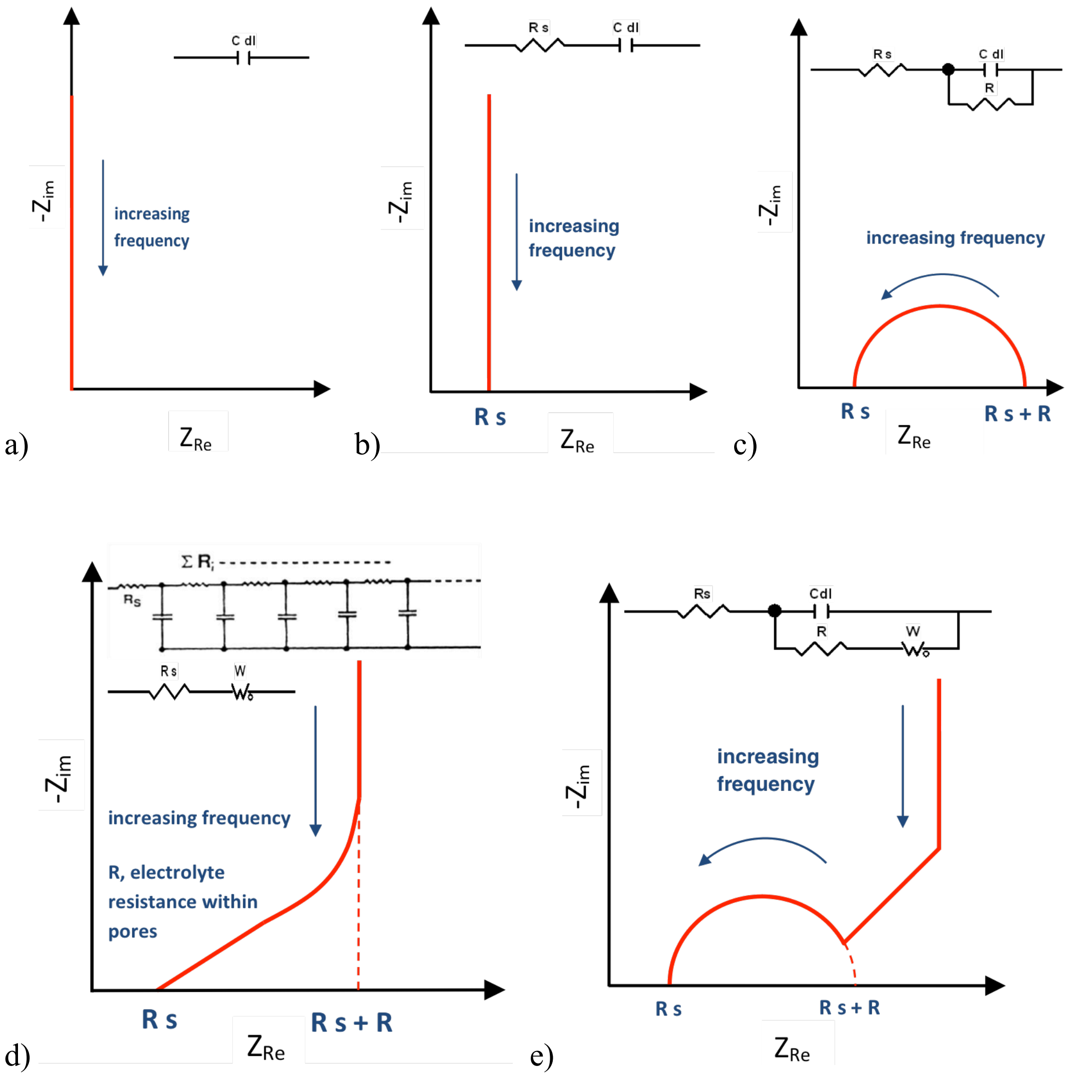

Figure 4.12 An equivalent circuit and Nyquist plot for a) an ideal capacitor, b) a solution resistor and a capacitor in series, c) circuit represented in b with addition of leakage resistance in parallel, d) a porous medium with electrolyte in the pores and e) Randle's circuit for porous electrode systems

The plots presented in Figure 4.12 are adopted from [32] and briefly edited. The Nyquist plot for a capacitor, shown in Figure 4.12 a), exhibits a pure imaginary component at all frequencies hence the plot is a single vertical line lies on the imaginary axis with zero real impedance. This vertical line shifts along the x-axis, as shown in Figure 4.12 b), when a resistor is introduced in series with the ideal capacitor. This frequency response now contains real component as well as an imaginary one and is induced by the electrolyte. Hence this resistance is commonly referred to as the solution resistance (R_S) and its value is determined through the response intercept with the real impedance axis. The representation of the leakage resistance on the described circuit in Figure 4.12 b) is done through the addition of an extra resistor in parallel to the capacitor. If the value of the leakage resistance is high, then a frequency response similar to Figure 4.12 b) is expected, otherwise the generated response is semicircle in shape with both real and imaginary components as shown in Figure 6.12 c). The highest attainable real impedance occurs at the x-axis where the imaginary component is approaching zero. The resistance at this point is comprised of the summation of two resistances; R_S and ionic or polarization resistance (R_I) that is described as the diameter of the semicircle. As the frequency is increasing, another resistance component can be determined. This resistance is in fact the real component of the impedance measured at 1kHz and commonly identified as the equivalent series resistance (ESR) where it is important for improvements on the system design and optimization of the power density [10]. The measurement at 1kHz frequency is particularly advantageous as the frame reference for some instruments can only measure the impedance at this frequency. Hence performance at this frequency not only eases the comparison with available literature values but it also creates a platform for fast analysis at conditions where the attention is to screen the resistances trend with varying the potential. The generated impedance response in Figure 4.12 d) belongs to the porous electrode with electrolyte in the pores that is potentially modelled by the transmission line circuit [10, 158]. This circuit model arrangement creates a -45° phase angle incline at lower frequency range which is shown by a Warburg element. The Warburg element is denoted as (W) on the circuit and is usually used to model diffusion related behaviours. The Warburg element itself contains two components of diffusion related capacitance and resistance [10] where both are dependent to $\sqrt{\omega}$. Hence the Warburg element could potentially replace the transmission line circuit components, i.e. a series of parallel-arranged RC circuits. By doing so, the overall model circuit is over-simplified. This makes the model more practical and robust for many users with broader application. Randle's circuit, shown in Figure 4.12 e), provides an overall demonstration of the impedance response of an ideal EDLC system. In this representation a semicircle at high frequency is obtained and followed by an incline at 45° angle as described and a vertical line in the imaginary axis direction at the low frequency region. As stated, the vertical response corresponds to ideal EDLC system where the electrodes are ideally polarizable. It is worth highlighting that most electrodes, including the produced electrodes for this study, are not ideally polarizable and contain porosity and some degrees of additives or impurities depending on the carbon production routes. Accordingly in EDLCs incorporating porous electrodes, the response at the low frequency region deviates away from ideal case scenarios.

In the course of this work, the Randle's circuit was used to fit the impedance data and ascertain characteristics.

5 Experimental

5.1 Activated carbon preparation

The activated Xerogel carbons are produced via two main steps of carbonization of produced aerogel and activation of the carbonized products at elevated temperatures. In this chapter, a description of the gel synthesis along with the detailed reaction mechanism is provided. Also there are several well-known factors recognized to influence the gel properties and the characteristics of the post-activation carbons. Among these factors the type of the precursors, nature of the activating agent and processing conditions are important and will be discussed in this chapter.

5.1.1 Resorcinol-Formaldehyde gel synthesis

A large portion of the literature study on activated carbons is based on the polycondensation of the aqueous solution of resorcinol (R) with formaldehyde (F) in presence of an alkaline catalyst (C) [37, 41, 42, 162]. Also, there are reports on divergent products of the aforementioned precursors, which undergo a fairly similar reaction mechanism [163-167]. However the core utilized components reported in literature is based on the synthesis of the RF gels with no branching. Hence to make pore characteristic comparisons with readily available literature, the precursors with no branching are selected for this study.

In order to produce the RF hydrogel, 0.1 mole of resorcinol [$C_6H_4(OH)_2$, supplied from Sigma-Aldrich at 99% purity], which is equivalent to 11 g, and the desired mass of sodium carbonate anhydrous [Na_2CO_3, supplied from Sigma-Aldrich at >=99.5% purity] were dissolved in 110 cm^3 of deionized water (W) under constant stirring at room temperature. Once the resorcinol completely dissolved, 0.2 mole of formaldehyde [HCHO, supplied from Sigma-Aldrich at 37% solution], which is equivalent to the mass of 16.2 g, were added to the solution under stirring. The stirring carried on until a homogenous solution was obtained. The solution was then sealed to avoid solvent evaporation and kept at 85°C for a period of 72 hours. At this point, it was found that the solution turned into dark reddish solid from a colourless solution. The produced hydrogel was then removed from the oven and cooled at room temperature. It was observed that the hydrogel was saturated with water hence a solvent exchange procedure was performed with approximately 200 cm^3 of acetone [C_3H_6O, supplied from Fluka at 99% purity] for 72 hours on an orbital shaker at 25°C. The reason for choosing acetone as the solution for solvent exchange is that it contains lower surface tension in comparison to water, and hence reduces pore shrinkage.

It is worth mentioning that, polycondensation of (R) and (F) occurs at the molar ratio of 1:2, i.e. R/F = 0.5. This ratio kept constant for all produced carbons to ensure the same mass of precursors is reacting for all aerogels. The ratio of 0.5 is precisely fit within the reported optimum range of $0.34 < x < 0.7$ [168]. Beyond these limits two scenarios occur: either the mesopore structure breaks down or there is not enough formaldehyde in the solution to proceed with the reaction and form proper cross-linked clusters.
Similarly the ratio of resorcinol to deionized water was also kept constant at 0.1 g/cm^3, i.e. R/W = 0.1, to again guarantee the same volume of solute for all RF hydrogels. The selected ratio for R/W is again in the range with the optimum literature value of $0.05 < x < 0.5$ [168]. If RW ratio is less 0.05 the gel structure may not fully develop and vice-versa if the ratio is greater than 0.5 the final product may be a polymer suspension in solution. Hence an accurate selection of R/F and R/W was done with extra care and attention as they can influence the gel structure hindering porosities.

To summarize, by utilizing the above formulation and consideration, four activated carbons were produced where the R/C ratio is only varying at 200, 250, 300 and 350 ratios. R/F and R/W ratios were kept the same for all carbons meaning the amount of catalyst is the only variant, at the stated ratios, with respect to the resorcinol quantity.

5.1.2 Reaction mechanism

Upon dissolving the resorcinol in deionized water, the hydroxyl bond on the resorcinol ring becomes positively charged. This is typically achieved using sodium carbonate catalyst where it promotes electron donation and forms resorcinol anions [169]. At the beginning of this process, although both charged and uncharged resorcinol species are present but their presence proportion is largely in favour of the uncharged species, i.e. about 98%. In spite of the huge disparity between the species proportions, the resorcinol anions are extremely reactive towards formaldehyde compound. With the addition reaction of 1 mole of electron deficient (R) with 2 moles of (F), hydroxymethyl ($-CH_2OH$) derivatives of (R) are produced which are catalysed by H^+ ions that were removed from the present hydroxyl bond in the addition reaction. In fact presence of H^+ ions help to eliminate the $-OH$ bond that is attached to hydroxymethyl derivatives and form a benzyl type cation [169]. Moreover other compounds such as methylene ($-CH_2-$) and methylene ether ($-CH_2OCH_2-$) are produced through condensation polymerization of the formed product of the addition reaction [169]. This is clearly illustrated in Figure 5.1.

This image has been removed due to the copyright

Figure 5.1 The reaction mechanism for sol-gel polymerization. Adapted from [170]

The methylene and methylene ether compounds are commonly known as the bridge compounds. As the name states, they either connect/bridge the benzyl-type cations together or with another benzene ring to form 3D cross-linked clusters through a sequence of electrophilic reactions [169].

The total pore volume and surface area of the aerogel carbon depends upon the pH at which polymerization takes place. At the polymerization stage, the value of pH itself is depends upon the catalyst amount.

As described earlier the addition reaction is catalysed by a basic solution of sodium carbonate where the condensation polymerization is catalysed by H^+ ions, which are acidic. The combination of the two entities together results in creation of various pH values, which influence the pore characteristics. Precipitation or a halt in condensation may occur if the pH is too small or too large, respectively. Hence an optimum PH window of $6.5 < x < 7.5$ is defined to promote reactions without any interference. In fact the value of PH is dictated by the amount of the consumed basic and acidic catalysts in the addition reaction and the condensation polymerization, respectively. Utilization of these catalysts creates a PH window that is directly influenced by the ratio between the resorcinol and the sodium carbonate, i.e. R/C ratio.

Hence the R/C is known to be the most structural-defining influence of the gel network and is selected as the only varying factor for producing our Xerogels.

5.1.3 Carbonization of aerogels

As described in chapter 2.4.1, it is important and necessary to perform the activation step in order to remove residual valences at the surface and introduce porosity in the structure [10, 17]. Due to the nature of the produced Xerogel, physical activation is selected for this study. The physical activation itself is involved with the carbonization of the aerogels followed by the gasification of the carbonized product with an oxidizing gas, such as CO_2, at several varying temperatures.

In order to produce Xerogel carbons, all produced aerogels were dried at 80°C in a vacuum oven and then pulverized using a bench top high-energy Spex SamplePrep 8000M ball-mill at small batches of 5 g. Tungsten carbide vessel and balls were used as non-reacting materials to mill the aerogel. According to a study performed by Sillars [74], 5 minutes milling is proved to be a sufficient duration for this process as further milling causes significant expansion in the surface area and creation of finer and narrower range of particle sizes that could have a detrimental effect on the cell performance when utilized in an EDLC arrangement in combination with IL electrolytes.

The milled gel was then accurately weighed and transferred onto a ceramic crucible. The carbon-containing crucible was then placed in the centre of a Carbolite tubular furnace and sealed from both sides. In order to reduce the chances of combustion the carbonization must be carried in an inert atmosphere. For this reason an argon gas is utilized to enter the tube furnace from one end, flow over the crucible sample and leave the tube from the opposite side. A gas flow rate of 300 ml min^{-1} was selected and the tube was purged for 30 minutes prior to carbonization. For carbonizing the samples, a heating profile similar to [37, 171, 172] Schedule's was used as mapped in Figure 5.2.

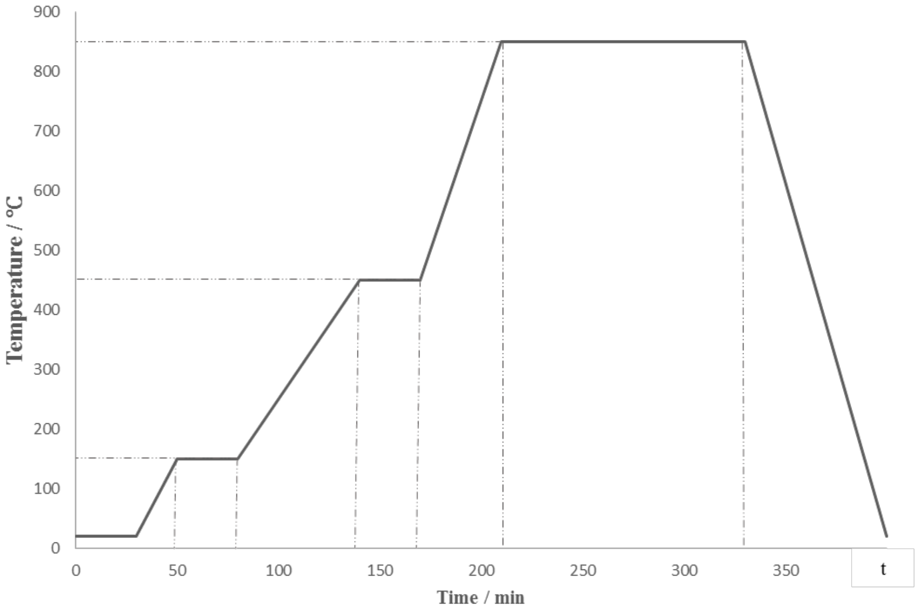

Figure 5.2 Carbonization temperature profile

In this schedule, 3 heating steps are involved. The sample was first heated to 150°C at 5°C min^{-1} increment followed by a hold period of 30 minutes. Afterwards, another heating step is applied to 450°C at the same heating rate followed by another 30 minutes hold period. At the final step, temperature increased to 850°C at the rate of 10°C min^{-1} and maintained for 120 minutes. The maximum carbonization temperature of 850°C allows for complete elimination of volatiles from the aerogel as well as ensuring a maximum surface area at the same time [41, 74, 169, 173, 174]. Once the hold period of the final stage was completed, the flow rate of argon was reduced to 50 ml min^{-1} to allow for slow cooling to room temperature.

It is worth mentioning that through the carbonization process gaseous species contains oxygen and hydrogen are removed from the carbons. After removal, the remaining carbons arrange themselves into sheets of irregular aromatic shaped molecules that are condensed in size and present a partial planar structure. Although the presence of the irregular aromatic ring system causes the introduction of pores into the structure but the vacant pores may become blocked by other disorganized carbon or the decomposition products such as tarry materials [175]. Hence carbons with high porosity cannot be fabricated via carbonization route only. Accordingly another heating procedure known as the activation step comes into action to enhance the pore structure further.

5.1.4 Activation of the carbonized products

Once the crucible sample was cooled to room temperature, it was removed from the furnace and the content was weighed accurately. Afterward, the carbonized material was placed back into the crucible and to the furnace to activate. Both Ar and CO_2 gas were utilized as the heating and oxidizing gases respectively to enhance the pore structure and introduce further porosity. Also it is evident that the activation process affects the pore dimension, hence pores with different shapes and sizes are produced through this step [176]. A heating schedule similar to that used in previous investigations have been utilized [37, 171, 172]

The following heating schedule is used for the activation procedure:

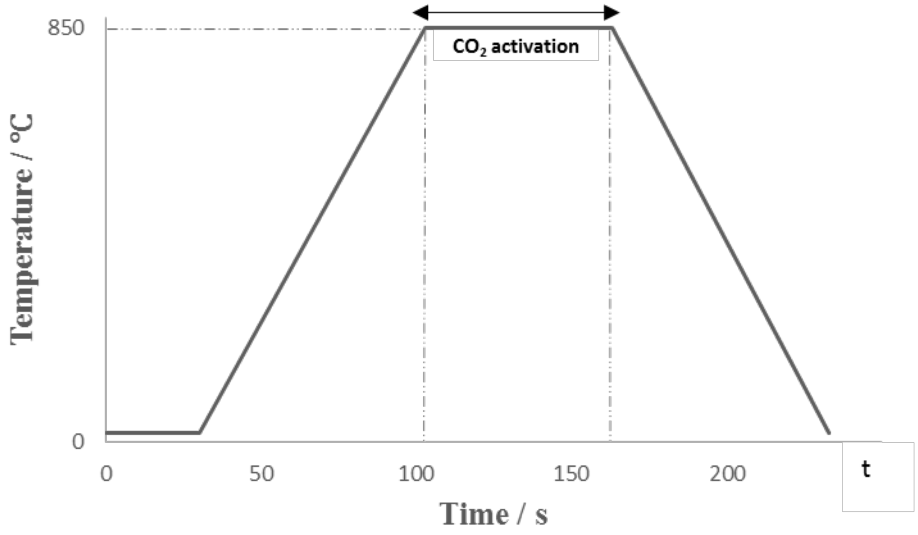

Figure 5.3 Activation temperature profile

Similar to carbonization, the sample kept under flow of argon for 30 minutes prior to the heating procedure. In this schedule however the heating procedure carried at a single step to 850°C at 10°C min^{-1} increments. Argon gas at 300 ml min^{-1} was selected for the heating. Once the temperature reached 850°C, the flow of argon replaced with CO_2. A hold period of 60 minutes at 850°C under flow of CO_2 was then applied which followed by a constant cooling to the room temperature under flow of argon gas at the rate of 50 ml min^{-1}.

It is highly important to apply the same treatment procedures while carbonizing and activating small batches of samples as slightest variation in process conditions and parameters, such as temperature, hold periods, gas flow rate, etc., may influence the surface area and the pore characteristics of the produced Xerogels [35]. Thus, as described in 2.4.1, controlling these parameters opens an opportunity of obtaining carbon materials with a widespread range of porosities suitable for a desired application.

Once all small batches of each Xerogel carbon type were produced, they were the well mixed in separate containers, according to their R/C ratios, to ensure a uniform pore distributions in all produced carbon electrodes.

5.1.5 Xerogel carbon characterization

5.1.5.1 Nitrogen adsorption/desorption

A Micromeritics TriStar II 3020 instrument was used to characterize the produced activated carbons in terms of the surface area, pore volume and pore width.

In order to do this the previously vacuum dried samples were degassed for 10 hrs at 200°C prior to measurements. This step is crucial to the activated carbons as it removes even the traces of volatiles from the structure and ensures the carbon sample is relatively dry. The degassed samples were then transferred to the main chamber and the surface area along with other pore characteristics were generated automatically through utilization of the nitrogen adsorption and desorption isotherms at -196°C.

5.2 Ionic liquid preparations

As described in sections 2.5.3 and 2.6, the cation constituent of an IL can be altered through the alkyl chain length and addition of functional groups in order to vary the stability window, viscosity, conductivity, etc. This statement is tested here through the use of 9 different ionic liquids with Pyrrolidinium, Sulfonium, Ammonium and Phosphonium based cation species. These cations were used in conjugation with a sole anion that kept the same for all cation types. A clear description of the utilized methods to characterize these ILs is given further on in this section.

All utilized ILs, with the exception of Phosphonium based ILs, are commercially available and were supplied from Io-Li-Tec Ltd. The Phosphonium based ILs were synthesized separately at a collaborating group in Universidad de São Paulo and transported here. Preliminary studies on this type of electrolytes are reported and published as a joint work between the same partner university and our group [177]. However a commercially available carbon was utilized to study the performance of the produced cells. Depending on the supplier, commercial carbons are usually containing some degrees of impurities or irregularity in the pore characteristics hindering the optimal performance. Hence all selected electrolytes in this study were tested with every developed activated carbon types creating various combinations. Figure 5.4 signifies the structural differentiation of the utilized cation species with a sole anionic component. Although there are various inorganic anions at available and highest conductivities are attained through conjugation of cations with the smallest anions e.g. BF_4 but small anions are less stable and decompose in lower potentials in comparison to the cations. Hence there is a trade-off between the stability, dimension and conductivity.

A bis(trifluoromethanesulfonyl)imide $[Tf_2N]^-$ anion is selected for use in this study. This selection is mainly made due to the fact that this anion is repeatedly found in ILs with reasonably good transport and electronic properties as well as displaying wide electrochemical stability windows. Provision of the these properties is mainly caused by the presence of a partially delocalized charge on the $[Tf_2N]^-$ anion that weakly interacts with cation species and instigates flexibility in the structure [113].

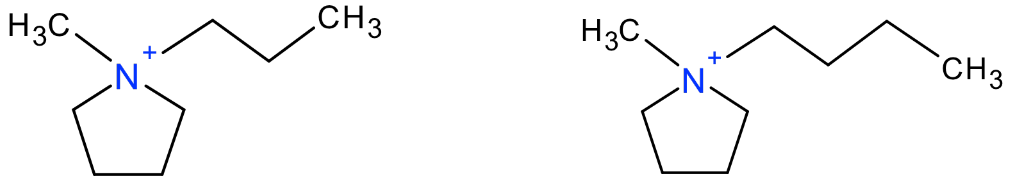

a) [Pyr13] cation b) [Pyr14] cation

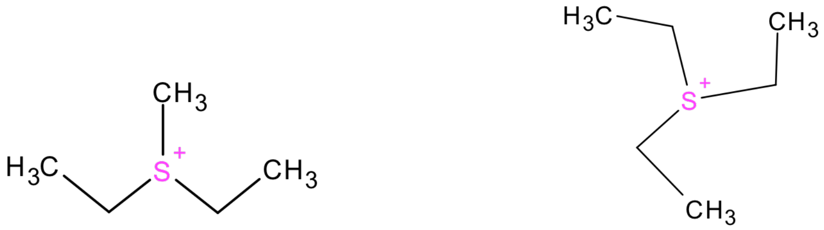

c) [S221] cation d) [S222] cation

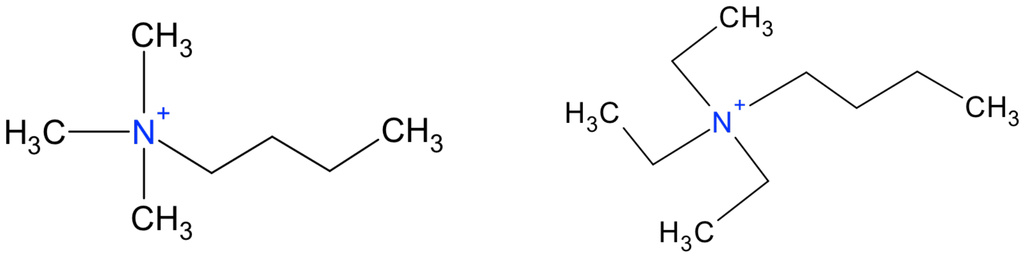

e) [N1114] cation f) [N2224] cation

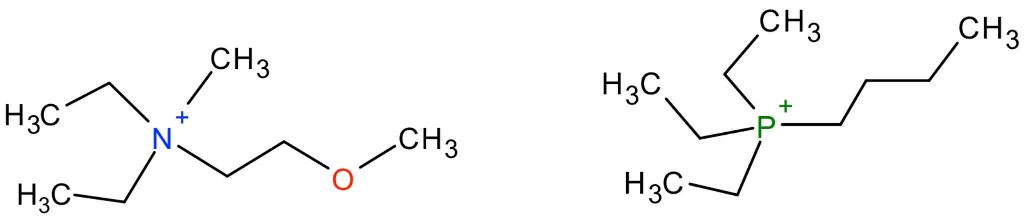

g) [N122(2O1)] cation h) [P2225] cation

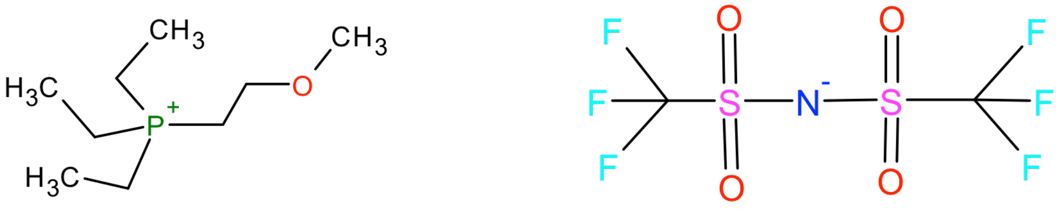

i) [P222(2O1)] cation j) [NTf$_2$] anion

Figure 5.4 Schematic representation of the utilized IL constituents, a) 1-methyl-1-propylpyrrolidinium [Pyr$_{13}$], b) 1-butyl-1-methylpyrrolidinium [Pyr$_{14}$], c) diethylmethyl-sulfonium [S$_{221}$], d) triethylsulfonium [S$_{222}$], e) butyltrimethylammonium [N$_{1114}$], f) butyltriethylammonium [N$_{2224}$], g) N,N-diethyl-N-methyl-N(2methoxyethyl)-ammonium [N$_{122(2O1)}$], h) pentyltriethylphosphonium [P$_{2225}$], i) (2methoxyethyl)triethylphosphonium [P$_{222(2O1)}$] and j) bis(trifluoromethane)sulfonimide [NTf$_2$] anion

As illustrated from above, the Pyrrolidinium based cations are differing from the other cation types as they contain a 5-membered saturated ring structure whereas the rest contain a linear structure with/without ether linkage inclusion.

The Pyrrolidinium based cations comprising of four carbons and a nitrogen atom on their ring. The only factor demarcating the selected Pyrrolidinium based ILs is the presence of an additional CH_2 group in the alkyl chain that is attached to the nitrogen molecule.

The next group of ILs is sulfonium based and as the name states these ILs comprised of a positively charged sulfonium central atom. Two ILs are selected for this category that both are containing alkyl side branching which similar to the pyrrolidinium ILs are differing by absence of a CH_2 group in [S_{221}] cation.

Similar to Pyrrolidinium ILs, the ammonium based ILs are also containing nitrogen in the structure but in a linear arrangement with 7, 10 and 8 carbons for [N_{1114}], [N_{2224}] and [$N_{122(2O1)}$] respectively. The [$N_{122(2O1)}$] cation contains an ether linkage which is incorporated in the structure to investigate its influence on the physiochemical properties of the IL and the overall performance of the cell in comparison to [N_{1114}] and [N_{2224}].

The same approach was applied on the Phosphonium based ILs where an ether linkage is merged in the structure to create [$P_{222(2O1)}$] IL.

All the above cations were combined with a [Tf_2N] anion separately to create nine different ionic liquids with the same anionic component.

5.2.1 IL characterization

In this section a clear and step-by-step description of the utilized methods to characterize the physiochemical properties of the ILs will be given.

Samples were dried at 80°C prior to each measurements hence contained very low moisture content, <7 ppm.

All measurements were performed at replicates of two.

5.2.1.1 Karl-Fischer titration

For water content measurements, 0.3 ml of the dry IL was accurately weighed and injected through a seal rubber into the stirring solution of a KF instrument. The weigh of the sample was then inserted and the water content in the sample is automatically calculated. This is done according to equation 4.6 and equation 4.7 where H_2O and I_2 are consumed when the reaction is complete. By knowing the total mass of the sample and consumed I_2, the amount of moisture in the sample is generated automatically.

5.2.1.2 Conductivity measurements

A pair of platinum electrodes and a clear acrylic cell were used for the purpose of the cell assembly in a way that the electrodes are secured with the PTFE tape at either end of the acrylic cell. The liquid of choice is placed in between the two electrodes and must be airtight and free of any bubbles.

Once the cell is prepared, it was then transferred to a temperature controller chamber connected to a Maccor potentiostat instrument in order to implement the impedance measurements. Temperatures of 4.7, 12.5, 20.5, 25.0, 30.5, 40.0, 49.5, 60.0 and 25.0°C were utilized to carry the measurements. Prior to the impedance measurement for each temperature, an hour of rest step was applied in order to attain the desired temperature.

It is worth mentioning that since acrylic is sensitive to high temperatures and the cell constant may vary at higher temperatures, no further temperature ascent beyond 60°C was implemented.

According to the same reason, prior to each IL conductivity runs, the acrylic cell was calibrated with 0.01M solution of KCl at the conductivity of 1413 $\mu S\ cm^{-1}$. The cell constant, which is given by the length between two platinum electrodes divided by the surface area, was calculated by considering the conductivity of the calibrating solution and the intercept of the impedance plot with the axis. The calculated constant cell value from calibrating solution was then applied on the same equation but this time for IL conductivity calculations.

Note: Since above arrangement is used to measure the conductivity of ILs, the electrodes and the cell must be free from any contaminations and moisture contents. Hence extensive cleansing and vacuum drying steps are carried to ensure elimination of the unwanted effects. For instance after each use the acrylic cell and electrodes were washed firstly with soapy water and acetone respectively, followed by water and ethanol cleansing on the same order. Finally the electrodes and the cell were washed with deionized water and another ethanol cleansing correspondingly. After each of these cleansing steps the relevant compartment was positioned in a vessel containing the fresh cleansing solution particular to that step and placed in an ultrasonic bath for a duration of 15 minutes at 25°C. Or similarly for drying the compartments, a 5 minutes vacuuming at 80°C was followed by an overnight vacuuming at 25°C.

5.2.1.3 Rheology

The dynamic viscosity and density analyses for all ILs were performed at Universidad de São Paulo on a bench top SVM 3000 Anton-Paar viscometer. The same temperature range as of ionic conductivity was selected up to 60°C, i.e. 4.7, 12.5, 20.5, 25.0, 30.5, 40.0, 49.5, 60.0, 65.6, 71.8, 80.0, 90.0°C, in order to make comparison easier. The relative and absolute uncertainty for dynamic viscosity and density is ±1% and ±5E-4 g cm^{-3}.

5.2.1.4 Differential Scanning Calorimetry

For the purpose of cell preparation, a weight of 10 -15 mg of the liquid was precisely measured and placed in the centre of the 40μL Aluminium crucible. A pierced Aluminium lid was placed over the crucible, crimped and transferred to the DSC instrument. The punching helps to vent off any volatiles from the samples and also ensures good contact to the DSC atmosphere for the purpose of the heat transfer or removal. Once the sample cell was prepared, it was then transferred to the other side of the instrument's stage and a rate of 10 °C/min was selected for heating and cooling.

A recommended rate of 50 mL/min of Nitrogen gas was utilized as the purged gas for the standard measuring atmosphere. Although Helium and Air could also be employed as purges gases but the main reason for this selection is that the Nitrogen gas remains inert up to the temperature of 600°C.

The selection of heating and cooling profile is arbitrary and entirely dependent on the physiochemical properties of the sample. Although there are few temperature ranges and profiles are reported by different research groups [61, 178, 179] but a range of -80°C to 200°C seems to be a reasonable selection in terms of providing enough temperature range for the desired functionality.

The following temperature profile, displayed in Figure 5.5, was utilized for all electrolyte samples.

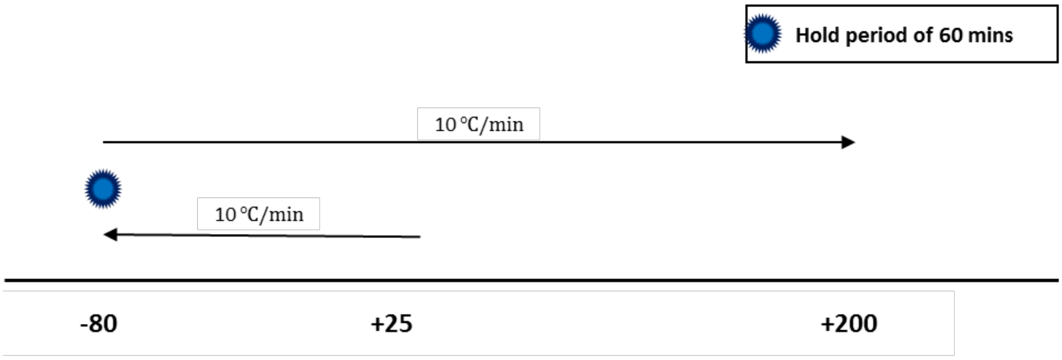

Figure 5.5 Utilized temperature profile for DSC measurements

Liquid Nitrogen was also utilized to reduce the temperature down to -80°C. A temperature of 25°C was selected as the initial temperature for all samples. This was followed by a temperature drop to -80°C at the rate of 10 °C /min and a hold period of 60 minutes to ensure that the sample is not supercooled. Then the temperature increased to 200°C at the same rate of 10 °C/min.

Although other important phase transition properties such as crystallization and glass transition (T_g) could possibly be detected and determined using the above temperature profile, however they are irrelevant to the scope of this project as they are well out with the operating range selected here.

Worth mentioning that all above preparation steps were performed inside a glove-box so the effect of presence of moisture content could be neglected.

5.2.1.5 Operating voltage and Stability Window determination

The operating voltage of the electrolyte was determined through soaking a small disc of glass fibre separator with the electrolyte and arranging it in a Swagelok cell. Linear sweep voltammetry was then performed using a Solartron Analytical 1470E Potentiostat/Galvanostat analyser between 0 and 4.5 V vs. open circuit potential at sweep rates of 50 mV s^{-1}. A cut-off current density of 30 mA cm^{-2} was selected for a 2 mm diameter electrode.

For determining the ESW voltage of an electrolyte, a three-electrode cell arrangement, comprising of a glassy carbon as WE, silver wire as RE and platinum as CE, was utilized. Linear sweep voltammetry was applied in similar manner at a cut-off current density of 40 µA cm^{-2} for a 3mm diameter glassy carbon electrode.

5.3 EDLC fabrication

5.3.1 Electrode preparation

The produced activated carbons, as described in section 5.1, were milled for duration of 60 minutes in a bench top mill using a silicon nitride container and two grinder balls of the same material. The procedure of loading the container was carried out in an oxygen deficient environment as significant amount of heat is generated during milling. Accumulation of trapped heat and increase in temperature of the carbon content in presence of oxygen is hazardous thus the container was filled and sealed in a glovebox. The milled carbons were then transferred to the vacuum oven for drying overnight.

To produce electrode slurries, firstly the dried carbon was mixed with a KynarFlex® 2801 polymer binder at the dry mass ratio of 85:15 on the total basis of 300 mg. Afterwards 3 ml of acetone was added to the dry mixture to create an inky blend. The amount of added acetone is highly arbitrary and it depends on the porosity of the carbon as more porous carbons require more solvent to have the same wettability effect as the carbons with less porosity. However through experimentation, the aforementioned amount is proved to be sufficient for the range of carbon porosities we are interested in.

To encourage impregnation of the pores with the solvent and even distribution of the polymer binder through the solution, the inky mixture was then sealed and positioned inside an ultra-sonic water bath at 30°C for 15 mins. This was followed by medium speed stirring on a magnetic stirrer for the duration of 5-6 hrs.

Once the polymer binder was fully dispersed, the mixture casted over Aluminium foil of 15μm thickness, with the use of a doctor blade spreader.

The spreader itself uses a micrometric adjustable paint applicator that was set at 250 μm. Hence this value is the wet film thickness of the carbon electrode where the solvent is also present. Hence by controlling the thickness, the active mass of substrate is also controlled to some degrees.

This arrangement the Al foil acts as the current collector and the active carbon is utilized as an attached component to the current collector.

Preliminary studies of this work on various types of carbons with imidazolium-based ILs have declared that although more active mass on a given surface area is thought to maximize the cell performance but the actual findings contradicted this hypothesis. This could potentially reasoned by blockage of the pores with narrower range particles resulting in presence of inactive mass that does not contribute to charge storage.

Hence the aforementioned wet film thickness is a reasonable choice for this study and assumed to remain uniform at all points on the sheets of electrodes.

Once the acetone is evaporated from the surface, the produced electrode sheets were then transferred to a vacuum oven at 80°C to fully dry overnight. The dry electrode sheets were then punched into small electrode discs with a diameter of 16mm and placed back into the vacuum oven for further drying overnight.

The completely dried electrode discs were then weighed accurately and matched together as closely as possible to ensure similar mass of active materials are present at both electrodes.

5.3.2 EDLC assembly

The EDLC cell production was performed in an O_2/H_2O deficient glove-box under Argon atmosphere. In this study a coin cell arrangement was used to produce and study the EDLCs. Figure **5.6** illustrates a cross-sectional view of a coin cell arrangement where all cell components were pressed together by a crimping machine into a 20mm diameter coin cell.

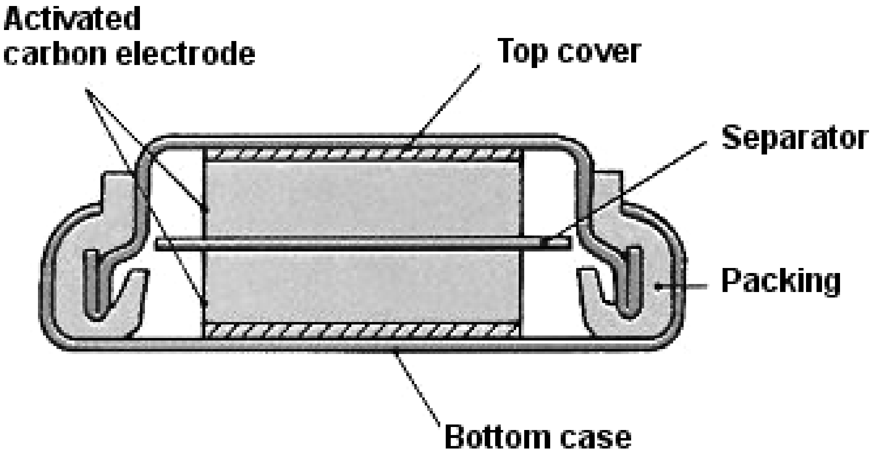

Figure 5.6 Schematic of an EDLC coin cell arrangement

In this arrangement, the previously matched activated carbon electrodes, which were attached to the Al foil, positioned in a way that the Al foils from each electrode faces the top and bottom cases. A 16 mm diameter disc of an ionically conductive separator was placed between the two positive carbon electrodes. Among all potential separators available commercially, both chemically and biologically natured, the chemical separators seem to remain more inert towards the ionic liquids. Due to possible decomposition of the biological natured separators, e.g. cellulose, in contact with ILs [180] their application as separators in energy storage is only limited to the aqueous electrolytes and organic electrolytes to some degree. Hence a common choice of GF3 glass fibre separator, that is an ionically conductive and electronically insulating, was selected and utilized in cell productions.

In order to ensure a good ionic conductivity, presence of excess electrolyte is essential. Hence, all cell components were soaked with drops of electrolyte during construction. The cell was then vacuumed for 5 minutes prior to crimping to maximize the impregnation and filling of the carbon pores with electrolyte. Then, two 0.5 mm thick spacers were placed on the top electrode and sealed close with a crimper. The purpose of inserting the spacers into the arrangement is to increase the contact between the electrodes and the current collector by introducing extra pressure in order to minimize the attainable distance and therefore reduce the resistances [181].

To reduce the internal resistances by eliminating the effect of over pressuring the cell while crimping and also to guarantee comparing cells manufactured under same physical conditions, all cells were crimped up to a certain pressure. This pressure was proven to be sufficient to provide good contact between the cell compartments as well as reducing the internal resistances.

5.3.3 EDLC characterization

All 9 electrolytes were tested in the 4 developed activated porous mediums creating 36 different combinations. These cells were electrochemically characterized by Galvanostatic cycling at different rates and EIS.

For characterizing the temperature elevation runs both methods were utilized.

Worth mentioning that to ensure reproducibility and attaining reliable performances for above chemistries, two cells were produced for each carbon/ electrolyte combinations.

5.3.3.1 Galvanostatic charge/ discharge cycling

The constructed cells were cycled from the open circuit voltage to the operating voltage limit of the selected electrolyte at constant current rates of 0.25, 0.5, 1, 2, 4, 8, 16 and 32 mA. For each constant current charging rate, a total of 20 cycles were implemented and the associated voltage response was recorded at one-second/ -or lower at higher rates- intervals. For each rate, the required values for cell capacitance measurements were extracted at the 15th discharge cycle of the corresponding rate as at this stage the cell has reached a steady state and ions are at equilibrium.

The specific capacitance of a cell can be expressed in various ways including the normalization of the unit mass, area or even volume of the material. However, since our focus here is to study and investigate the materials therefore, the capacitance is normalized according to the mass of active material, i.e. carbon. Hence capacitance was determined using the following expression:

$$C = \frac{It/_{\Delta E}}{W}$$

equation 5.1

Where I is the discharge current in units of A, ΔE is the potential difference from where discharge starts to 1 V, t is the corresponding discharge time to 1 V and W is the mass of the active material. A sample calculation is shown in Appendix 2.
Internal resistance was also measured through introducing 10 short pulses of specific current and recording the response. This step applied right after the potentiostat hold period after charging is complete and before discharging the cell.

5.3.3.2 Electrochemical impedance spectroscopy

The EIS spectras were determined using a 10 mV AC amplitude and 100 mV DC potential at a frequency range of 100 kHz to 10 mHz. The value of capacitance was determined through the use of equation 4.24 at a frequency of 10 mHz and its corresponding imaginary component of impedance.
Various resistances of R_S, R_I and ESR were determined through this method by considering the intercept at coordinate (x=Z', y=Z''=0) in the high frequency region, fitting the equivalent circuit model and isolating resistance at 1 kHz, respectively. Please see Appendix 3 for sample calculations.

5.3.4 Summary

To study the overall performance of a supercapacitor, the individual properties of the constructing components must be altered. Carbon as the porous medium and electrolyte as the conducting medium play an important roles.
To minimize the effect of impurities, the carbon precursors where synthesized, carbonized and activated in-situ with various pore characteristics.
To tackle the high viscosity problem of the ILs, the chain length on the cation is altered and also as an alternative an ether linkage is introduced to the structure.
Temperature elevation at 40°C, 60°C and 80°C was also proposed as a further attempt to reduce the viscosity.

6 Results and discussions

6.1 Physical characterization of ACs

6.1.1 Quantitative investigation of hydrogels

The four activated Xerogel carbon materials were produced using the described procedure in section 5.1 at R/C ratios of 200, 250, 300 and 350. Prior to carbonization a qualitative investigation of the hydrogels were performed by considering the gel colour and its stiffness. As described in the experimental section the full gelation process was completed over a period of 72 hours at 80°C over which a colour change from a colourless solution of precursors to transparent red monoliths was observed. The same colour change was observed for all other hydrogels. However stiffness decreased as the R/C ratio increased. This could be due to the shrinkage of the cross-linked molecules with increase in the R/C ratio [163, 169].

6.1.2 Activated Xerogel carbon characteristics

One of the primary objectives of this study was to investigate the effect of pore size distribution, through altering the R/C ratio, with the cell performance. In order to attain a better understanding of the pore structure of the resultant activated carbons, N_2 adsorption/desorption at 77K was performed on all carbon samples. Through the N_2 adsorption/desorption method the specific surface area of the activated Xerogels was determined with the BET and DFT methods. Albeit both methods are determining the same variable but the DFT model is utilized to ensure the same trend is attained with varying the R/C ratio as with BET for all AC carbons. The pore size distribution, mesopore volume and micropore volume were also determined using the BJH, DFT and t-plot methods, respectively. The pore size distribution attained from BJH was similarly checked with the modal pore width determined from DFT to ensure the accuracy of trends with increasing the R/C ratio. These characteristics are summarized in Table 6.1.

Table 6.1 Pore characteristics of ACs

RC	S_{BET}[a] [m^2g^{-1}]	S_{DFT}[b] [$m^2\,g^{-1}$]	$V_{tot.}$[c] [$cm^3\,g^{-1}$]	$V_{mic.}$[d] [$cm^3\,g^{-1}$]	$V_{meso.}$[e] [$cm^3\,g^{-1}$]	d_{BJH}[f] [nm]	d_{DFT}[g] [nm]
200	670	530	0.48	0.21	0.18	4.3	5.4
250	720	580	0.53	0.22	0.21	5.1	6.3
300	750	620	0.62	0.23	0.27	6.3	7.2
350	790	630	0.67	0.24	0.32	7.5	8.1

[a] specific surface area calculated using the BET method [b]specific surface area determined using DFT model [c]total pore volume calculated at $P/P_0>0.99$ [d] micropore volume determined using the t-plot method [e] mesopore volume from DFT model [f] average modal pore width estimated from BJH pore size. [g]modal pore width estimated from DFT pore size distribution.

From above, it is clear that the determined surface area through both BET and DFT methods exhibit an increasing trend with increase in the R/C molar ratio. Similar trend is attained for the total pore volume with a 28.4% increase from RC200 to RC350. The micropore volume contributes marginally to this trend as no substantial variation is observed. However the total pore volume increases with the R/C ratio resulting in a relative 8% reduction in the micropore volume when compared with the total pore volume for the AC350 and AC200. On the other side is the mesopore volume, which experience an increase influencing the total pore volume the most. This is also reflected in Figure 6.2, which illustrates the pore size distribution determined through the DFT model in the small mesopore region. The attained adsorption/ desorption isotherms for the activated carbons at varying R/C ratios are shown in Figure 6.1. The adsorption/desorption profiles for all carbons display a type IV isothermal curve with combination of H2 and H4 hysteresis loop that are generally obtained for mesoporous materials. The shape of the attained hysteresis loop between the adsorption and desorption isotherms, with gentle and near horizontal desorption profile at relatively high pressures, indicates that the pores are slit shaped or partially wedge-shaped with narrow neck at one end or at both ends if the pore is open [182].

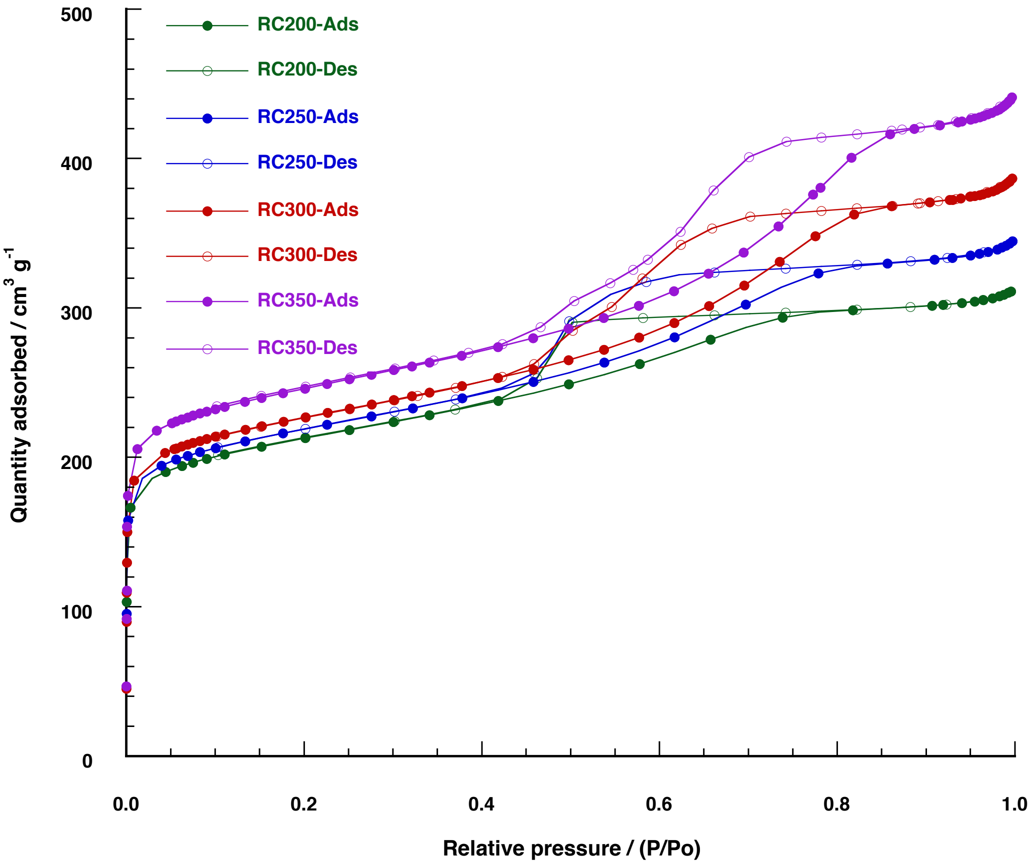

Figure 6.1 Adsorption/desorption isotherms at 77K

As seen in Figure 6.1, the nitrogen uptake maintains an increasing trend with increase in the R/C ratio at all relative pressures with RC200 and RC350 representing the lowest and highest volume of adsorbed nitrogen, respectively. This finding is supported by Figure 6.2, which is related to the available mesopore volume in the sample exhibiting an increasing trend with increase in the R/C ratio. Hence the attained trends for gas uptake at the course of the adsorption and desorption is related to the mesopore volume.

Also as described in section 4.1.1, the quantity of nitrogen adsorbed at low relative pressures is associated with micropore filling which experiences a slight increase with R/C ratio. This agrees well with the summarized micropore volume in Table 6.1. Consequently this is indicative of the fact that mesoporosity has the biggest effect on the pore width.

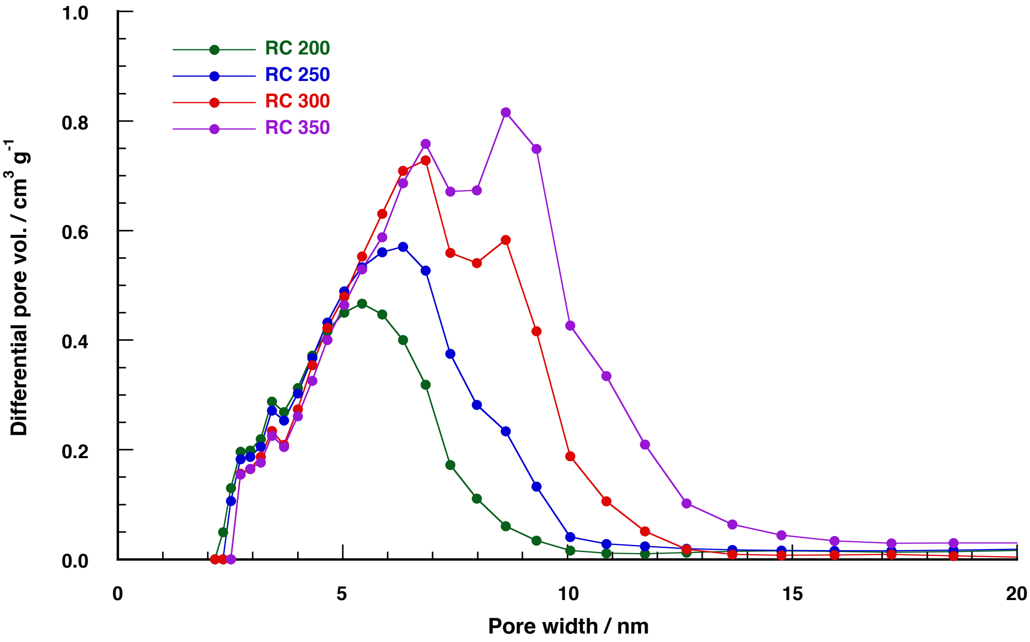

Figure 6.2 Mesopore size distribution of produced ACs

As illustrated in Figure 6.2, with increase in the R/C ratio the mode of the distribution is shifted to larger pore sizes. The estimates of the modal pore width credited to each AC carbon indicate that a 50-unit increase in this region increases the average pore width by approximately 0.9 nm. This trend also exists when the BJH model was applied to the desorption isotherm, as indicated by d_{BJH} shown in Table 6.1.

6.1.3 Burn-off% variation with R/C

The burn-off percentage and the yield at which the precursors are converted to the carbonized and activated carbons are determined using the following relations:

$$Burn\ off\ \% = \frac{W_{original} - W_{final}}{W_{original}} \times 100$$

$$Yield\ \% = 100 - burn\ off$$

These equations are applied to all the small batches of materials and represented in the Table 6.2 as an average with equated standard deviations of 6-8 runs.

Table 6.2 Yield% and Burn-off% of carbonized and activated carbons

AC	Yield %	Burnt-off %
	Carbonization	
RC200	51.6 ± 0.4	48.4 ± 0.4
RC250	50.4 ± 0.4	49.6 ± 0.4
RC300	50.7 ± 0.6	49.3 ± 0.7
RC350	49.6 ± 0.1	50.4 ± 0.1
	Activation	
AC200	87.0 ± 2.2	13.0 ± 2.2
AC250	87.8 ± 0.6	12.2 ± 0.6
AC300	89.7 ± 0.2	10.3 ± 0.2
AC350	90.3 ± 0.4	9.7 ± 0.4

The yield of carbonization for all R/C carbons remains constant at about 50% while an increasing trend is attained when they are activated. Consequently for the activation process the burn-off% is reduced which could be reflected from the possibility that the tarry materials are present and their quantity are varying in a decreasing manner with increase in R/C ratio resulting in smaller weight losses at higher R/C ratios. Moreover, the higher quantity of tar content in smaller AC carbons, may also be due to the trapping of the volatiles by microporosity [183] These findings correlate well with the literature studies [184].

6.2 Physical characterization of ILs

The selected ionic liquids were characterized according to their transport and thermal properties through the techniques described in sections 5.2.1. Previously it was argued that a way forward to tackle the high viscosity problem of the ILs is to operate at elevated temperatures. Hence these properties are measured and investigated at 25°C, 40°C, 60°C and 80°C and presented in sections 6.2.2, 6.2.3, 6.2.4 and 6.2.5. A summary of all physiochemical properties at elevated temperatures is also given in section 6.2.6.

6.2.1 Water content

Prior to any physiochemical characterizations and cell production the moisture content of the selected ILs were determined through three distinct conditions of 1) as received, 2) dried and 3) two weeks after drying. These values are reported in Table 6.3. In the first condition, sealed samples were transferred to an argon-filled glovebox ($O_2 < 0.1$ ppm and $H_2O < 0.1$ ppm) and measurements were followed. A range of 32 – 63 ppm is recorded for the moisture content. In the second condition, the ILs were heated under rapid stirring for 10 hrs inside the same environment to dry. This drying arrangement was set and used for all ILs as an indicator to offer a reasonably dry liquid. The measurement took place immediately after the sample was cooled and typical moisture content of 5 ppm was recorded. In the third condition the ILs were left inside the glovebox for duration of two weeks. Under these conditions the water content rose to a range of 9 – 15 ppm with as large as a nine times approximate increase for $[S_{221}][NTf_2]$ electrolyte. Hence all physiochemical and electrochemical measurements were conducted within a few days of drying the liquids.

Table 6.3 Water content of received, dry and partially dry electrolytes

ILs	**wc.** **$_{\text{As received}}$** **[ppm]**	**wc.** **$_{\text{Dried}}$** **[ppm]**	**wc.** **$_{\text{After 2 weeks}}$** **[ppm]**
[Pyr_{13}][NTf_2]	35.4	3.1	12.3
[Pyr_{14}][NTf_2]	59.1	4.6	15.6
[S_{221}][NTf_2]	59.4	0.9	9.1
[S_{222}][NTf_2]	58.4	4.4	14.3
[N_{1114}][NTf_2]	36.9	2.3	8.9
[N_{2224}][NTf_2]	33.0	1.9	10.4
[$N_{122(2O1)}$][NTf_2]	62.3	3.7	13.9
[P_{2225}][NTf_2]	-	2.8	-
[$P_{222(2O1)}$][NTf_2]	-	4.6	-

Due to insufficient supply of [P_{2225}][NTf_2] and [$P_{222(2O1)}$][NTf_2] batches from USP, only a dry moisture reading was recorded.

It is worth highlighting here that the disparity of some determined physiochemical values with literature might have arisen from the difference in moisture content.

6.2.2 Thermal analysis of ionic liquids

Generally, the thermal stability of ionic liquids is dependent on their structure. The literature on most ILs including the ones utilized in this study has shown excellent thermal stabilities beyond 200°C [185, 186], for instance a thermal stability of 271°C [187] and 300°C [188] is reported for [Pyr_{14}][NTf_2] and [N_{1114}][NTf_2] respectively, determined through the thermogravimetric analysis measurements. However special care must be taken at operating temperatures above 150°C especially for Pyr-ILs where chemistries which yield in impurities are readily observed through increase in fluorescence and coloured impurities at much lower temperatures than previously reported by thermal gravimetric analysis [187]. Accordingly a thermal stability beyond 150°C seems a reasonable value to rely on and is well out of the range of desired operating temperatures for this study, i.e. 25 - 80°C. Hence no thermal stability analysis was performed and determination of the melting point through the DSC technique was only pursued. Figure 6.3 represents the DSC traces of all utilized ILs with the exception of the P-based liquids due to the insufficient synthesized supply. A significant variation in phase behavior is observed for all electrolytes. On heating, all liquids (with exception of [$N_{122(2O1)}$][NTf_2] where a solid line profile was obtained) experience a single or multi solid-solid transition before reaching their melting points. This state manifests itself on the profile as endothermic peak/s before the melting point peak is formed. It is possible for these transition states to consume a large fraction of the enthalpy of melting which may consequently yield in creation of low-energy melting transitions [189]. This is observed for [S_{222}][NTf_2] and [N_{1114}][NTf_2] liquids where multiple solid-solid transition peaks are attained at -32.1, -13.9 and -10.4°C for the former liquid and 9.2°C for the latter one, respectively, lowering the melting energy.

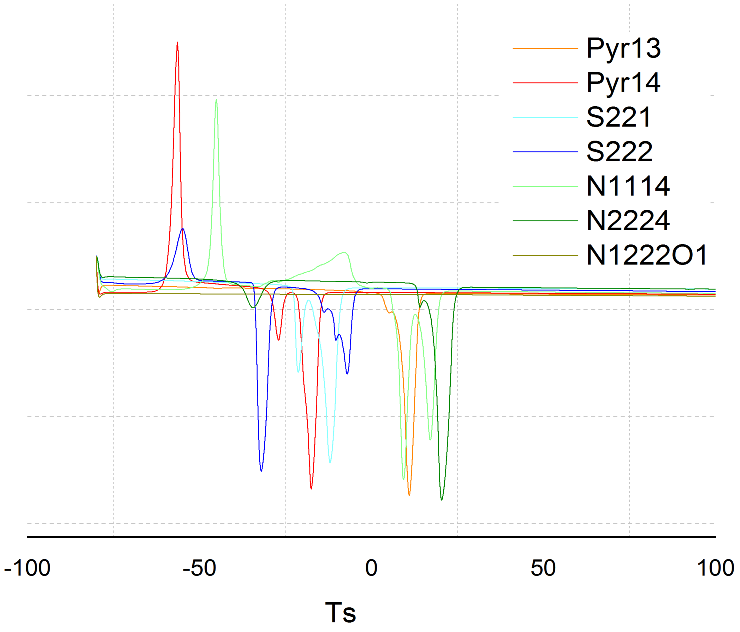

Figure 6.3 DSC traces of all utilized ILs

This work also includes examples where the created solid-solid transition peak/s consume smaller fraction of enthalpy of melting leading to formation of higher energy melting transitions. Examples of this are [Pyr_{13}][NTf_2], [S_{221}][NTf_2] and [N_{2224}][NTf_2] liquids where smaller endothermic peak/s occurred at 4.9, -21.4 and (-34.9 / +13.9)°C, respectively, compared to the melting transition.

While heating, some of the utilized liquids undergo cold crystallization where the occurrence of this phenomenon is associated with development of the exothermic peak/s on the profile. More precisely cold crystallization occurs when the liquid is supercooled at the beginning of the heating procedure, i.e. -80°C. In this condition, the liquid is in the metastable state and addition of the slightest amounts of energy into the system creates cold crystals, which expose themselves as exothermic peak/s on the traces profile. This process is observed for [Pyr$_{14}$][NTf$_2$], [S$_{222}$][NTf$_2$] and [N$_{1114}$][NTf$_2$] liquids first at -59.6, -54.9 and -44.6°C, respectively. With further heating solid-solid transition appears for [Pyr$_{14}$][NTf$_2$] liquid at -32.7°C and for [S$_{222}$][NTf$_2$] liquid at temperatures discussed before. However further heating of [N$_{1114}$][NTf$_2$] from the first cold crystallization peak creates two extra exothermic peaks at -28.7 and -7.5°C, which could be indicative of the fact that this liquid remains in the metastable state as the heating proceeds and several episodes of cold crystallizations are experienced. Through further heating a solid-solid transition is observed at 9.2°C, as already mentioned.

Table 6.4 compares the determined melting points for this study and available literature. The determined melting points here do not follow a clear trend with the length of the linear alkyl substituent and ether linkage.

It is worth noting that the attained profile for [N$_{122(2O1)}$][NTf$_2$] IL is associated with no melting peak and crystallization dips. This can either caused by a melting temperature beyond the utilized temperature range here or can be dedicated to the possibility that [N$_{122(2O1)}$][NTf$_2$] is a non-crystal forming IL. These possibilities can be tested through varying the experimental conditions.

Table 6.4 Melting temperature of utilized ILs vs. literature values

ILs	**Melting point (m_p) [°C] / This study**	**Melting point (m_p) [°C] / From literature**
[Pyr$_{13}$][NTf$_2$]	11.0	
[Pyr$_{14}$][NTf$_2$]	-17.3	-6.5 [186], -6 [177], -18*^{a}
[S$_{221}$][NTf$_2$]	-11.7	-11.7 [186]
[S$_{222}$][NTf$_2$]	-7.0	-17.6 [186], -35.5*^{a}
[N$_{1114}$][NTf$_2$]	17.1	-18*^{a}
[N$_{2224}$][NTf$_2$]	20.9	
[N$_{122(2O1)}$][NTf$_2$]	No peak/s	
[P$_{2225}$][NTf$_2$]	-	16 [177]
[P$_{222(2O1)}$][NTf$_2$]	-	10 [177]

**Denotes m_p values reported on manufacturers website: ^{a} Sigma-Aldrich*

There are also large discrepancies, more than 35°C for some ILs, between the determined melting temperatures and other literature values. This inconsistency is mainly caused by the variation in experimental conditions such as the sample mass, the rate of cooling/ heating, temperature the liquid is held at, duration of the hold period, nitrogen flow rate, moisture content of the sample and purity. Additionally the alkyl substituent on the side chain and the $[NTf_2]^-$ anion have many rotational degrees of freedom, influencing the melting point and creating different transitions on the melting profile [189].

To eliminate or reduce the effect of endo/exo peaks on the melting profile pattern, a setup with lower temperature and extended hold period could be explored. However since all determined melting temperatures here and in literature are <25°C, suggesting that operation between 25 and 80°C can be permitted for all ILs and is acceptable.

6.2.3 Viscosity of ionic liquids

Figure 6.4 demonstrates the Arrhenius-like plot of viscosity for all utilized electrolytes at various temperatures. It is clear that a descending trend for viscosity is attained with increase in temperature regardless of the electrolyte type. This is a common and well expected trend for temperature elevation scenarios and is supported by not only similar studies [117, 177, 190] but with studies utilizing different cations and anions other than the selected ones here [101, 191-193]. The sulfonium-based ILs display the lowest viscosity whereas the ammonium-based ILs, with the exception of $[N_{122(2O1)}][NTf_2]$ electrolyte, exhibit the highest viscosities at all temperatures in the order of $[N_{2224}][NTf_2]$ >> $[N_{1114}][NTf_2]$ >>> $[S_{221}][NTf_2]$ > $[S_{222}][NTf_2]$. The difference between the two extremes is roughly one order of magnitude and is supported by other literature studies [136, 194]. The variation of viscosity for all other electrolytes with temperature lie between the attained profiles for these two extremes in the order of $[P_{222(2O1)}][NTf_2]$ > $[Pyr_{13}][NTf_2]$ > $[N_{122(2O1)}]$ $[NTf_2]$ > $[Pyr_{14}][NTf_2]$ and $[P_{2225}][NTf_2]$.

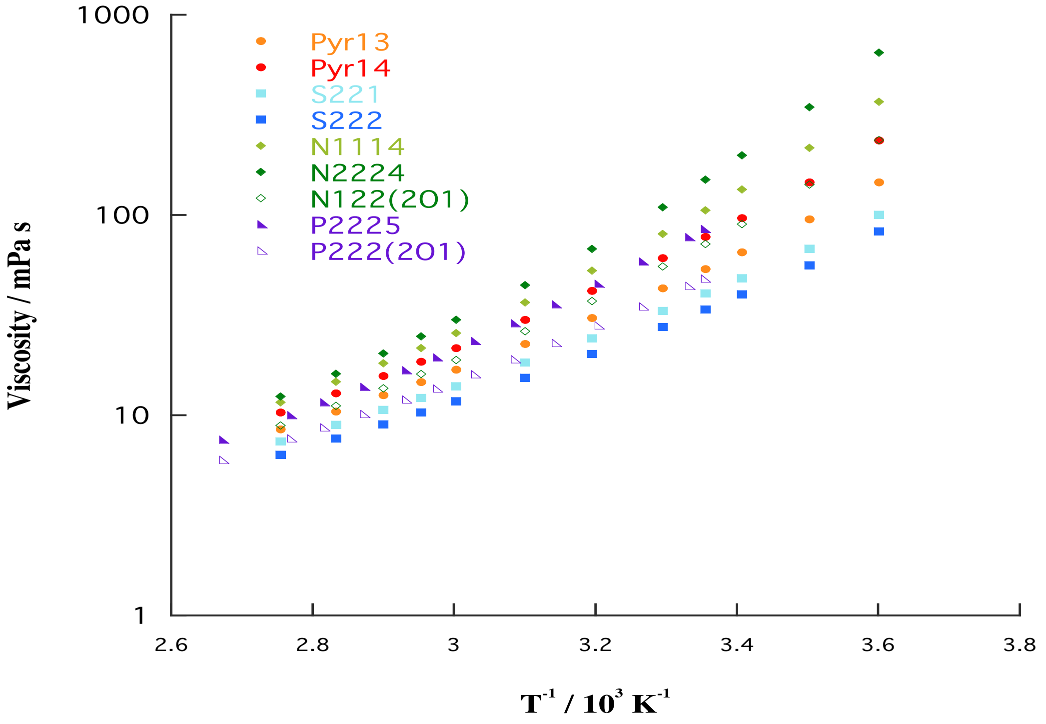

Figure 6.4 Arrhenius plot of viscosity

As illustrated from Figure 6.4 when the alkyl chain length on a particular cation is extended, the viscosity increases at that particular temperature. For instance, the replacement of the present proton on the alkyl side chain of $[Pyr_{13}][NTf_2]$ and $[S_{221}][NTf_2]$ electrolytes with a methyl group creates $[Pyr_{14}][NTf_2]$ and $[S_{221}][NTf_2]$ electrolytes, respectively that both are bigger in size. Similar extension approach is used for the non-ether ammonium ILs but instead of a methyl group, three are added to each alkyl branching chains of $[N_{1114}][NTf_2]$ producing $[N_{2224}][NTf_2]$, which is again bigger in size and exhibits the highest value of viscosity. Table 6.5 compares the cation volumes. A larger cation restricts the mobility and movement of the electrolyte leading to higher viscosity. This holds true for the $[Pyr_{14}][NTf_2]$ and $[N_{2224}][NTf_2]$ electrolytes in comparison to their unextended constituents, i.e. $[Pyr_{13}][NTf_2]$ and $[N_{1114}][NTf_2]$, but not the $[S_{222}][NTf_2]$. Although the $[S_{222}][NTf_2]$ does not follow this relation but there are some literature reports that supports the findings here [194-198].

Table 6.5 Molecular weight and volume of the selected cations

ILs	**Molecular weight of cations (Mwt_c) M [g mol^{-1}]**	**Molecular volume of cations (V_c) [Å^3]**
[Pyr_{13}][NTf_2]	128.2	225
[Pyr_{14}][NTf_2]	142.3	253
[S_{221}][NTf_2]	105.2	179
[S_{222}][NTf_2]	119.2	207
[N_{1114}][NTf_2]	116.2	222
[N_{2224}][NTf_2]	158.3	306
[$N_{122(2O1)}$] [NTf_2]	146.3	266
[P_{2225}][NTf_2]	189.3	359
[$P_{222(2O1)}$][NTf_2]	177.3	313

The given properties in this table are calculated from [199]. The Mwt_a and V_a is also determined to be 280.15 and 248 Å^3 respectively.

In the case of [$N_{122(2O1)}$][NTf_2] and [$P_{222(2O1)}$][NTf_2] electrolytes, the incorporation of an ether linkage into the alkyl side chain roughly halves the viscosity at 298K for both electrolytes when compared against the most similar structure without the ether linkage, i.e. [N_{2224}][NTf_2] and [P_{2225}][NTf_2] respectively. The significant diminution of viscosity is thought to be due to the electron donation property of the oxygen present in the ether linkage resulting in a reduced charge density on the central atom, i.e. N^+ and P^+, and weaker cation-anion electrostatic interactions [200]. Moreover presence of the ether linkage on the alkyl side chain enhances cation flexibility allowing for greater ion mobility and lower viscosity.

Further reduction of viscosity is observed at 40°C, 60°C and 80°C, however the aforementioned trend becomes less significant when comparing the viscosity of the electrolytes with and without the ether linkage at high temperature.

Although as stated earlier, most of the attained curves are characterized to produce an Arrhenius-like behaviour but slight degree of curvature is also observed for some ILs, especially the N-based ones, which is influenced by the structure of the ions. In fact ILs comprising of asymmetric cation structure or mostly absence of any functional groups, obey the Arrhenius law [117]. In contrast, presence of functional groups may lead to the formation of extra hydrogen bonds [201] resulting in additional cation-anion or even cation-cation hydrogen bonding interactions. The illustrated minor deviation from linearity may also be due to chain tangling or even the associated molar mass effects with the alkyl groups on the nitrogen central atom of the ammonium based ILs.

6.2.4 Density of ionic liquids

The density measurements were performed over the same temperature range as the viscosity measurements shown in Figure 6.5. Table 6.6, Table 6.7, Table 6.8 and Table 6.9 also report the corresponding values at 25°C, 40°C, 60°C and 80°C. A linear dependency of density with temperature is observed for all electrolyte systems. More precisely the density decreases as the temperature increases, i.e. more free spaces available between the ions and therefore the IL becomes less ordered at higher temperatures.

The sulfonium based ILs present the highest densities followed by the $[Pyr_{13}][NTf_2]$ > $[N_{122(2O1)}][NTf_2]$ > $[Pyr_{14}][NTf_2]$ > $[N_{1114}][NTf_2]$ > $[P_{222(2O1)}][NTf_2]$ > $[N_{2224}][NTf_2]$ and $[P_{2225}][NTf_2]$ electrolyte with the lowest density at all temperatures. The relatively high density of the S-based ILs in comparison to $[N_{2224}][NTf_2]$ and $[P_{2225}][NTf_2]$ electrolytes in spite of their lower alkyl chains counts is mainly triggered by the greater density of the central atom of these electrolytes.

From Figure 6.5 it is seen that the density decreases with increase in cation size meaning that the expansion of alkyl chain length reduces the density regardless of the fact that the larger ion sizes usually comprise greater mass.

For instance at 25°C, the $[S_{222}][NTf_2]$, $[Pyr_{14}][NTf_2]$ and $[N_{2224}][NTf_2]$ electrolytes encompass densities 2.7%, 5.8% and 3.8 % greater than $[S_{221}][NTf_2]$, $[Pyr_{13}][NTf_2]$ and $[N_{1114}][NTf_2]$ electrolytes, respectively. These trends are in good agreement with literature studies [194, 198, 202].

At 40°C the density of $[S_{222}][NTf_2]$ and $[N_{2224}][NTf_2]$ electrolytes experiences the same degree of increase as 25°C with respect to $[S_{221}][NTf_2]$ and $[N_{1114}][NTf_2]$ constituents (i.e. a further 2.7% and 3.8% respectively) whereas a 2.3% increase is reported for the ring of $[Pyr_{14}][NTf_2]$ compared to the $[Pyr_{13}][NTf_2]$ electrolyte. This trend remains the same for the aforementioned electrolytes at 60°C and 80°C runs. Hence, the larger cation imposes greater densities and this is regardless of the corresponding central IL atom on the cation and operating temperature.

The density of the ILs, i.e. $[N_{122(2O1)}][NTf_2]$ and $[P_{222(2O1)}][NTf_2]$ is significantly greater than their most similar ILs structures, i.e. $[N_{2224}][NTf_2]$ and $[N_{2225}][NTf_2]$, due to the incorporation of the ether linkage

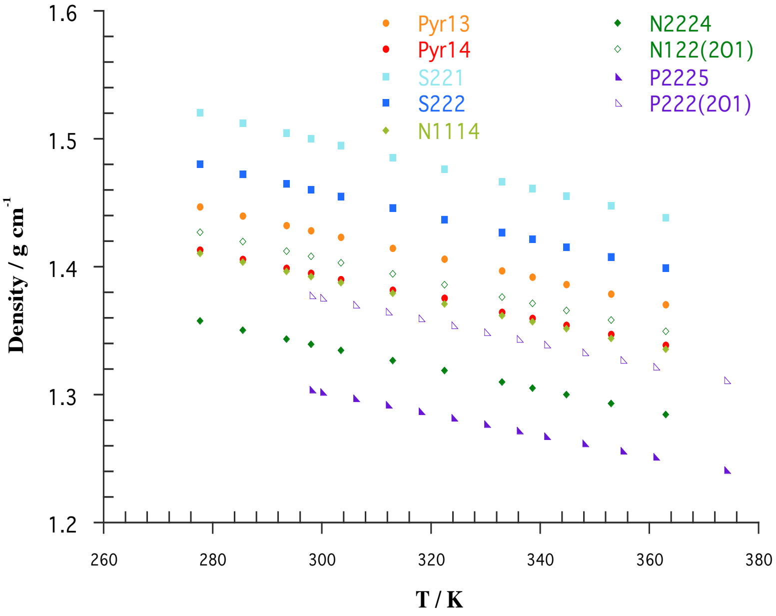

Figure 6.5 Variation of density with temperature

6.2.5 Conductivity of ionic liquids

The variation of conductivity with temperature is illustrated in Figure 6.6. As anticipated from the viscosity measurements when temperature is increasing an ascending trend for conductivity is observed that is mainly attributed to the untangling of chains and improved transport properties with temperature.

As already been discussed, conductivity and viscosity have inverse proportionality meaning that at higher temperatures the reduction in viscosity allows for greater ion mobility leading to an increase in conductivity. Figure 6.7 illustrates the relationship between the molar ionic conductivity and the fluidity (that is inverse of viscosity). All ILs exhibited an almost linear relationship between the molar ionic conductivity and fluidity confirming that the increase in ionic conductivity is directly related to decrease in viscosity.

From literature the cation and anion size also recognized to influence the electrical conductivity. In fact the conductivity is reduced as the alkyl chain length on the cation becomes longer. This observation is most likely caused by limited mobility and motion of the cation with increase in its dimension considering the anionic component is maintained the same for all ILs. In other words a long alkyl chain difficult the movement or hopping of the cations and therefore contribute lower to the electrical conductivity.

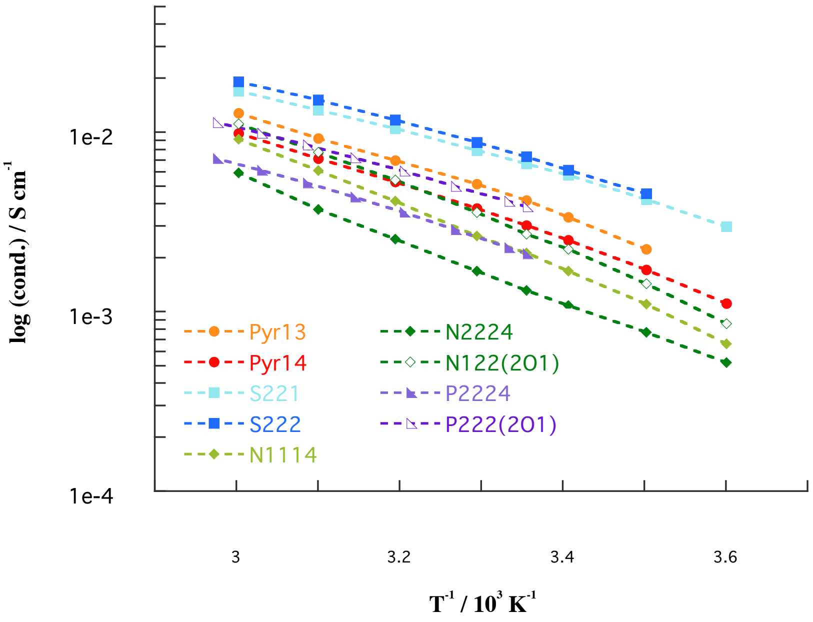

Figure 6.6 Arrhenius plot of ionic conductivity

For further discussion on the viscosity behaviour with temperature, the plot of molar conductivity against the inverse viscosity, so called Walden plot, is used as observed in Figure 6.8. An ideal Walden line was drawn through using a diluted aqueous solution of potassium chloride (KCl) since the slope must be a unity without any ion-ion interactions. From the plot, it is clear that all the data were lying below the ideal line indicating that major deviation from this line is indicative of the stronger interactions among the cations and the [Tf_2N] anion.

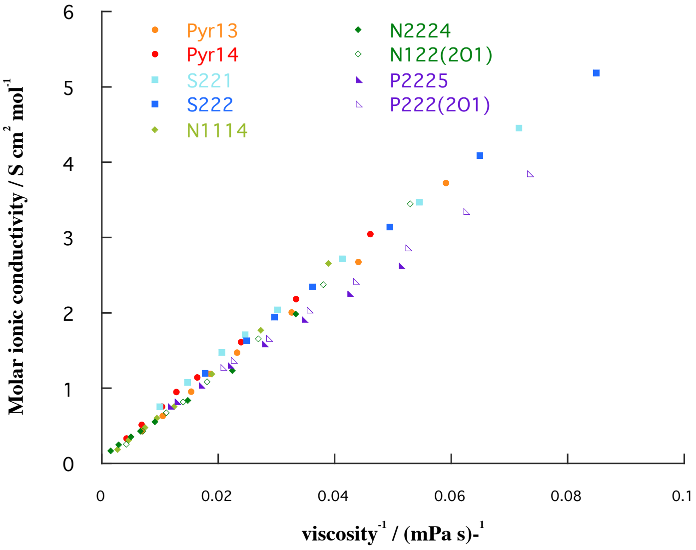

Figure 6.7 Molar ionic conductivity variation with fluidity

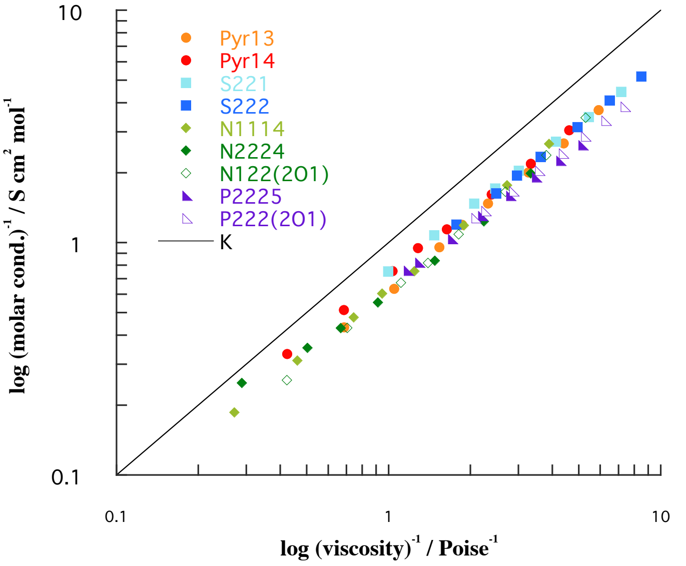

Figure 6.8 Walden plot

6.2.6 Physiochemical properties of ILs at elevated temperatures [A summary]

As shown previously, reported values of viscosity for pyrrolidinium, sulfonium, ammonium and phosphonium based ILs are in broad agreements with the literature values at 25°C. The following tables summaries the physiochemical properties at selected operating temperatures of 25°C, 40°C, 60°C and 80°C.

Table 6.6 Summary of physiochemical properties at 25°C

ILs	**Viscosity (η) [mPa.s]**	**Density (δ) [g cm^{-3}]**	**Conductivity (σ) [mS cm^{-1}]**	**Molar ionic conductivity (Λ) [S cm^{2} mol^{-1}]**
[Pyr$_{13}$][NTf$_2$]	53.7	1.43	4.87	1.19
[Pyr$_{14}$][NTf$_2$]	78.0	1.40	3.02	0.95
[S$_{221}$][NTf$_2$]	40.6	1.50	6.65	1.71
[S$_{222}$][NTf$_2$]	33.7	1.46	7.30	1.94
[N$_{1114}$][NTf$_2$]	105.6	1.39	2.11	0.60
[N$_{2224}$][NTf$_2$]	150.0	1.34	1.31	0.43
[N$_{122(2O1)}$] [NTf$_2$]	71.6	1.41	2.90	0.82
[P$_{2225}$][NTf$_2$]	85.3	1.30	2.10	0.76
[P$_{222(2O1)}$][NTf$_2$]	48.1	1.38	3.84	1.27

Table 6.7 Summary of physiochemical properties at 40°C

ILs	**Viscosity (η) [mPa.s]**	**Density (δ) [g cm^{-3}]**	**Conductivity (σ) [mS cm^{-1}]**	**Molar ionic conductivity (Λ) [S cm^{2} mol^{-1}]**
[Pyr$_{13}$][NTf$_2$]	30.7	1.41	9.25	2.01
[Pyr$_{14}$][NTf$_2$]	41.8	1.38	5.27	1.61
[S$_{221}$][NTf$_2$]	24.2	1.48	10.47	2.72
[S$_{222}$][NTf$_2$]	20.2	1.45	11.68	3.14
[N$_{1114}$][NTf$_2$]	52.8	1.38	4.73	1.19
[N$_{2224}$][NTf$_2$]	67.6	1.33	2.53	0.84
[N$_{122(2O1)}$] [NTf$_2$]	37.2	1.39	6.81	1.65
[P$_{2225}$][NTf$_2$]	43.8	1.29	3.71	1.30
[P$_{222(2O1)}$][NTf$_2$]	27.2	1.36	6.26	2.04

Table 6.8 Summary of physiochemical properties at 60°C

ILs	**Viscosity (η) [mPa.s]**	**Density (δ) [g cm^{-3}]**	**Conductivity (σ) [mS cm^{-1}]**	**Molar ionic conductivity (Λ) [S cm^{2} mol^{-1}]**
[Pyr$_{13}$][NTf$_2$]	16.9	1.40	16.74	3.73
[Pyr$_{14}$][NTf$_2$]	21.7	1.36	9.84	3.05
[S$_{221}$][NTf$_2$]	14.0	1.47	16.94	4.45
[S$_{222}$][NTf$_2$]	11.8	1.43	19.04	5.18
[N$_{1114}$][NTf$_2$]	25.7	1.36	12.73	2.66
[N$_{2224}$][NTf$_2$]	30.0	1.31	5.93	1.98
[N$_{122(2O1)}$] [NTf$_2$]	18.9	1.38	18.33	3.45
[P$_{2225}$][NTf$_2$]	21.5	1.27	6.61	2.43
[P$_{222(2O1)}$][NTf$_2$]	14.8	1.35	10.58	3.60

Table 6.9 Summary of physiochemical properties at 80°C

ILs	**Viscosity (η) [mPa.s]**	**Density (δ) [g cm^{-3}]**	**Conductivity (σ) [mS cm^{-1}]**	**Molar ionic conductivity (Λ) [S cm^{2} mol^{-1}]**
[Pyr$_{13}$][NTf$_2$]	10.4	1.38	-	-
[Pyr$_{14}$][NTf$_2$]	12.9	1.35	-	-
[S$_{221}$][NTf$_2$]	9.0	1.45	-	-
[S$_{222}$][NTf$_2$]	7.6	1.41	-	-
[N$_{1114}$][NTf$_2$]	14.7	1.34	-	-
[N$_{2224}$][NTf$_2$]	16.1	1.29	-	-
[N$_{122(2O1)}$] [NTf$_2$]	11.1	1.36	-	-
[P$_{2225}$][NTf$_2$]	12.2	1.26	10.13	-
[P$_{222(2O1)}$][NTf$_2$]	9.1	1.33	16.00	-

6.3 Electrochemical characterization of ILs

The electrochemical stability window and the operating potential of the utilized ILs are extremely sensitive to the environment and conditions used to determine them. For instance, determination of the cut-off current density is fairly arbitrary and is mainly designated when the current density deemed large enough to signify possible electrolyte decompositions. For determination of the ESW in this work, a cut-off current density of 40 μA cm^{-2} was selected which is rather a conservative choice and results in provision of narrower ESWs when compared against majority of literature values.

On the other hand, utilization of a symmetrical cell arrangement helps to determine a reasonably more accurate value of the operating potential.

In a symmetrical arrangement as of EDLCs, the operating potential was used to determine the electrolyte's decomposition potential. Table 6.10 compares the ESW and the operating potentials in an asymmetric and symmetric cell arrangements as outlined in the experimental chapter.

Table 6.10 ESW and operating voltage of utilised ionic liquids

ILs	**ESW [V]**	**Operating potential [V]**
$[Pyr_{13}][NTf_2]$	4.6	2.92
$[Pyr_{14}][NTf_2]$	4.8	3.07
$[S_{221}][NTf_2]$	3.8	2.67
$[S_{222}][NTf_2]$	2.8	2.57
$[N_{1114}][NTf_2]$	5.2	3.59
$[N_{2224}][NTf_2]$	3.9	3.28
$[N_{122(2O1)}]$ $[NTf_2]$	4.7	3.01
$[P_{2225}][NTf_2]$	4.9	3.42
$[P_{222(2O1)}][NTf_2]$	4.1	2.73
$TEABF_4$ in PC	4.0	2.1

A clear dissimilarity between the above reported values is that the ESW is substantially higher than the operating voltage. In fact the degradation of all electrolytes initiates at the weakest covalent bonds at both methods. As already stated, the difference between the attained values is mainly caused by the ESW tendency to be asymmetric with respect to the OCP of a symmetric cell, hence the operating potential value that can be utilized without appreciable electrolyte decomposition is considerably lower than the ESW.

Since a symmetrical arrangement is utilized to study the electrochemical performance of the produced EDLCs, it is understandable to select the operating potential determined in the similar manner. This selection is taken in spite of the fact that lower operating potential, influences the cell performance contrariwise. However, in this approach the possibility of the surface area being rendered inactive by electrolytes decomposition products is minimized. Figure 6.9 demonstrates the operating potential of each electrolyte up to a cut-off potential of 5V. The large increase in current is associated with the breakdown potential. A simple comparison between the attained operating potential profile for the organic solution of $TEABF_4$ in PC with other ILs demonstrates less stability at elevated potentials. Hence utilization of ionic liquids allow for not only more stability but also must improve energy density when incorporated as electrolytes into a supercapacitor cell.

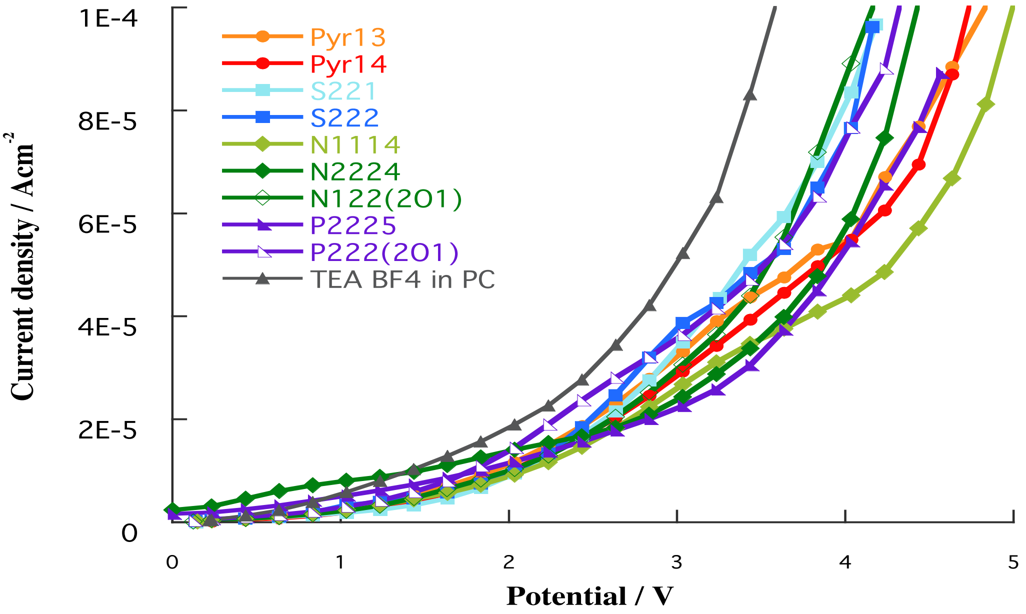

Figure 6.9 The operating potential of utilized ILs

According to Figure 6.9 and Table 6.10, the S-based ILs present the lowest operating potentials with little difference between them and $[N_{1114}][NTf_2]$ and $[P_{2225}][NTf_2]$ electrolytes present the highest with values of 3.5 V and 3.4 V, respectively. More precisely $[S_{221}][NTf_2]$ electrolyte is slightly more stable than the relative $[S_{222}][NTf_2]$ constituent in both 2e and 3e arrangements which may be caused by the influence of the smaller cation on the charge density of the ion leading to marginally higher ion-ion interactions. This trend is also observed for the N-based $[N_{1114}][NTf_2]$ and $[N_{2224}][NTf_2]$ ILs with 3.5 V and 3.2 V of operating potential, respectively. However the Pyr-based ILs do not follow this trend which may be due to the saturated ring structure exhibiting greater influence over the central charge density.

On the other hand, incorporation of the methoxyethyl linkage on the $[N_{122(2O1)}][NTf_2]$ and $[P_{222(2O1)}][NTf_2]$ in the side chain decreases the operating potential. This is mainly attributed to the reduced positive charge density at the ammonium and phosphonium centre atoms. This trend also exists for the 3e method ESW measurement of $[P_{222(2O1)}][NTf_2]$ but not the $[N_{122(2O1)}][NTf_2]$. A ESW value of 4.7 V is recorded for $[N_{122(2O1)}][NTf_2]$ which is considerably higher when compared against the 3.9 V of $[N_{2224}][NTf_2]$. The contradiction here may arise from the fact that possible ionic coordination alteration leading to enhanced stability of the IL.

6.4 Electrochemical analysis of EDLCs

The electrochemical analysis of manufactured supercapacitor cells is mainly based on the information generated during Galvanostatic charge-discharge cycling (GC) and electrochemical impedance spectroscopy [EIS] techniques. GC is generally used for measuring the amount of stored energy whereas EIS provides more details about the capacitance and equivalent series resistances.

In section 6.4.1 a brief overview of the calculated capacitance values, resistances (particularly internal resistance and iR drop) and their relation together is presented using the GC method. Section 6.4.2 provides a brief summary of determined capacitances and various resistances through the EIS method. A more in depth investigation of rate capability and attained resistances with varying temperature is followed in sections 6.4.3, 6.4.4, 6.4.5, 6.4.6 for each of the Pyr-based, S-based, N-based and P-based categories distinctively. Finally section 6.4.7 compares the best performing AC-IL combinations together at room and elevated temperatures.

6.4.1 Galvanostatic cycling and iR drop

Figure 6.10 and Figure 6.11 illustrate Galvanostatic charge-discharge profile for the [Pyr$_{13}$][NTf$_2$] electrolyte at constant current rate of 0.5 mA and at operating temperature of 25°C and (40°C, 60°C and 80°C) for all ACs, respectively. This IL is solely selected for the purpose of demonstration as a representative of all other AC-IL combinations. Table 6.11 summarizes the capacitance and internal resistances determined at current rates of 0.25, 0.5, 1.0, 2.0, 4.0, 8.0, 16.0, 32.0, 64.0 and 100 mA for the same electrolyte at the aforementioned temperatures. Corresponding tables for all AC-IL combinations at 25°C, 40°C, 60°C and 80°C can be found in Appendix 4.

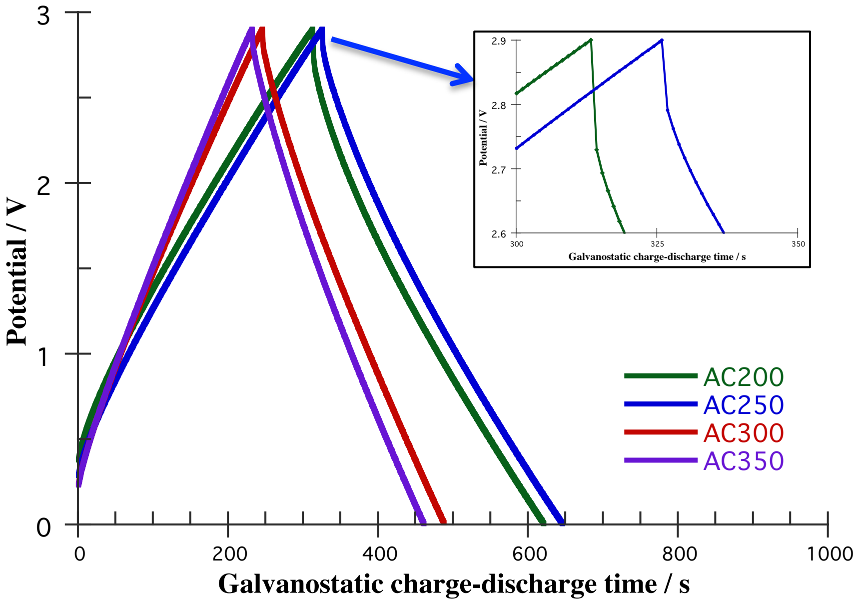

Figure 6.10 Galvanostatic cycling profile for [Pyr13][NTf2] at 25°C

For all test cells a potential drop is detected at the beginning of the discharge profile as indicated from the inset of Figure 6.10. This is usually referred to as the iR drop and is observed for all AC-IL combinations at every discharge current with the distinction that at higher current rates the total impedance of the cell yield in a marginally higher voltage drop. Hence a very small value or no capacitance is attained at high current densities particularly due to inability of the ions to transfer from the bulk solution to the porous structure quick enough to create a double layer of charge. In other words the iR drop becomes greater than the operating potential of the IL. Please see Table 6.11.

As shown in Figure 6.10 for $[Pyr_{13}][NTf_2]$ electrolyte at 25°C, it is apparent that there are no consistent correlation between ACs and constant current charging-discharging partially due to variation in presence of active materials, i.e. data could be normalized on basis of mass. However a faster charge discharge manner is observed for AC300 and AC350 in comparison to the AC200 and AC250, which may be due to better accessibility of the ions to the larger pore volumes. This trend also holds for the aforementioned AC-IL combination at 40°C and 60°C. However, at 80°C a major shift occurs in attaining shorter charge-discharge profiles and higher internal resistance values recorded in comparison to 40°C and 60°C operation temperatures, which is mainly the result of accumulation of all resistances induced on the cell and reduced viscosity, respectively, as a result of temperature elevation.

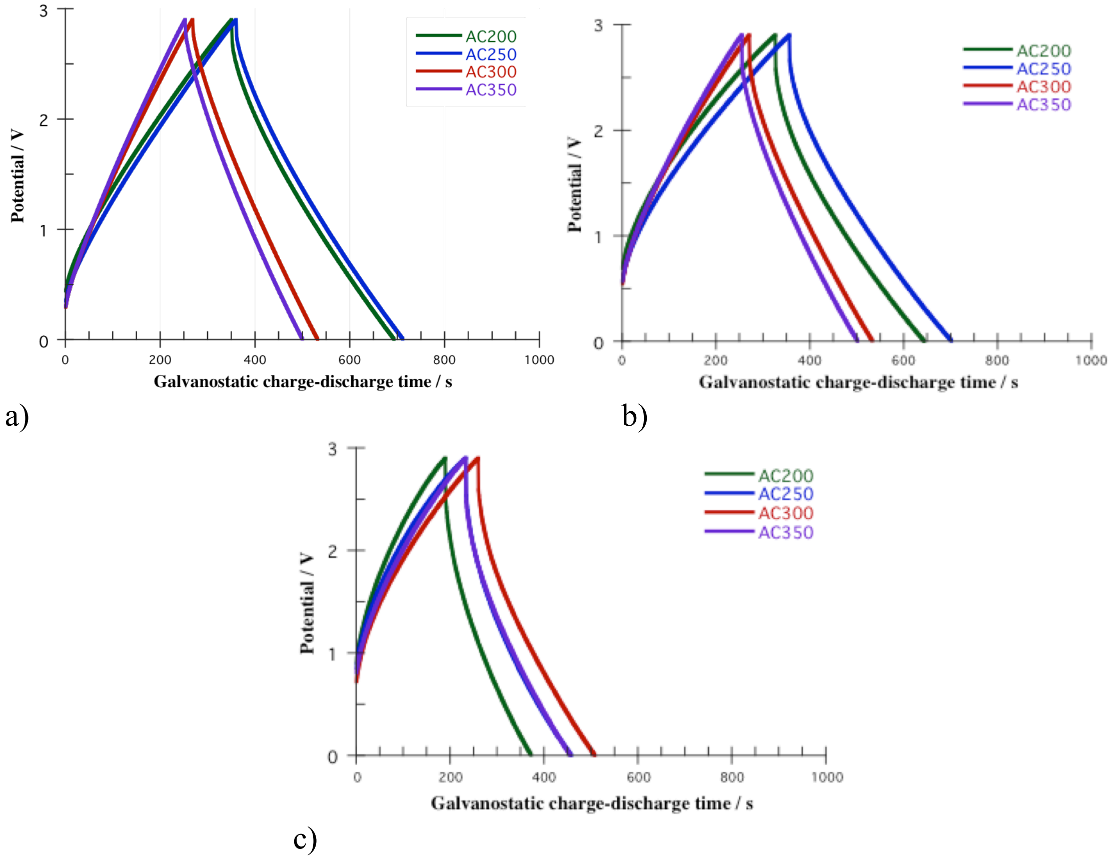

a)

b)

c)

Figure 6.11 Galvanostatic cycling profile for $[Pyr_{13}][NTf_2]$ at a) 40°C, b) 60°C and c) 80°C

Table 6.11 Calculated capacitance [C_s] and internal resistance [iR] at varying current densities and temperatures for [Pyr_{13}][NTf_2]

CC	AC200		AC250		AC300		AC350	
mAcm^{-2}	C_S [Fg^{-1}]	iR[Ω]	C_S [Fg^{-1}]	iR[Ω]	C_S [Fg^{-1}]	iR[Ω]	C_S [Fg^{-1}]	iR[Ω]
At 25℃								
0.25	27.6	76.1	28.7	62.8	24.5	51.7	25.7	52.9
0.5	24.6	78.4	26.2	63.1	23.3	51.2	24.3	53
1	21.4	79.8	23.7	63.6	22	51.7	23	53.3
2	17.8	79.5	20.8	63.7	20.8	51.6	21.4	53.4
4	13.8	77.8	17.1	62.9	18.1	51.5	19.4	52.8
8	7.8	73.7	11.4	60.6	11.3	50.5	15.2	50.7
16	-	-	7.7	53.5	10.3	45.5	12.7	46.4
32	-	-	-	-	3.3	40.4	14.5	44.4
At 40℃								
0.25	31.6	88	32.4	83.9	27	52.5	28.3	75
0.5	27.1	92.3	28.7	93.5	24.8	53.2	26	76.8
1	22.3	94	25	84.9	22.6	53.8	23.8	77.6
2	16.9	94.2	20.6	84.2	19.7	53.9	20.8	77.5
4	12.6	92.5	15.5	84.7	18.5	53.3	17.5	75.7
8	5.6	88	9.3	78.2	12.5	51.1	11.1	70.9
16	-	-	5.4	66.4	15	44.7	-	-
At 60℃								
0.25	33.1	113	35.2	107	29.7	97.5	31.6	118
0.5	24.2	118	27.5	113	24.5	104	26.2	126
1	16.2	119	19.2	114	18.7	106	20.4	128
2	11.1	119	13	113	12.5	105	14.5	127
4	-	-	9.5	110	9.5	103	10.4	124
8	-	-	5.1	103	-	-	-	-
At 80℃								
0.25	21.4	125	27.4	121	30.6	106	32.2	132
0.5	13.3	128	16.5	124	21.7	114	22.6	137
1	9.3	129	11.2	125	13.6	115	15	137
2	6.8	129	7.8	123	9.4	115	9.9	137
4	-	-	-	-	7.5	114	-	-

6.4.2 Electrochemical impedance spectroscopy

The EIS resistance measurements and calculation of cell capacitance was performed as previously outlined. The solution resistance (R_s) was determined using the intersect of the spectra with the real component of impedance, i.e. Z' axis. The ionic resistance (R_i) was estimated through fitting a semi-circle function and a Randle's circuit model to the spectra at the high frequency region in order to determine the diameter. The equivalent series resistance (ESR) was estimated at the frequency of 1 kHz and is the addition of different resistance contributions induced on the cell including the AC material resistance, polymer resistance, IL resistance and the resistance at the AC/current collector interface.

The cell capacitance values were determined at a frequency of 0.01 Hz and normalized against the mass of the active materials present in one electrode. Therefore the value of capacitance is expressed on a basis of 3-electrodes.

It is worth noting that safe operation is only permitted up to the maximum temperature of 60°C.

6.4.3 EDLC performance – Pyr-based ILs

6.4.3.1 EIS measurements

The behaviour of the assembled cells using five-membered ring pyrrolidinium based ILs is considered first where the volume of the cations are 225 Å^3 and 253 Å^3 for [Pyr$_{13}$][NTf$_2$] and [Pyr$_{14}$][NTf$_2$] electrolytes, respectively. It is worth recalling that the [Pyr$_{13}$]$^+$ is smaller in dimension when compared against its paired anion, i.e. 248 Å^3 [NTf$_2$]$^-$. Incorporation of a CH$_2$ group into the side chain of the [Pyr$_{13}$]$^+$ increases the volume of the new cation, that is [Pyr$_{14}$]$^+$, by 11% which is marginally greater than its conjugating anion.

Figure 6.12 illustrates the produced Nyquist plots for each of ACs combined with [Pyr$_{13}$][NTf$_2$] and [Pyr$_{14}$][NTf$_2$] ILs at 25°C, 40°C and 60°C. From the low frequency response region at all temperatures, it is apparent that none of the cells exhibit ideal capacitor behaviour, mainly due to the presence of porosity in the electrodes. However the response in this region can be characterized as approaching ideal when the Pyr-ILs are paired with AC300 and AC350 where pore volume and pore width are greater compared to the AC200 and AC250. In fact according to Table 6.12 there is a clear correlation between increase in the angle of the capacitive component of Nyquist plot and increase in the R/C ratio of carbons for both electrolytes which is caused either by inhomogeneity in the double layer or low conductivity of the utilized ILs.

This condition also holds for other EIS temperature elevation runs. However the phase angle tends to decrease when considering a specific AC-IL combination at different temperatures. For instance the attained capacitive angles for the AC200-[Pyr$_{13}$][NTf$_2$] combination at 25°C, 40°C and 60°C are -52.5, -46.1 and -42.9, respectively. This trend also observed for both ILs paired with wider pores, which indicates a larger deviation from the ideal vertical response as a result of inhomogeneity of the double layer since the conductivity increases with temperature and can be eliminated as an influencing factor at high temperatures.

The inset of Figure 6.12 elucidates a magnified section of high frequency region where a slight variation in the series resistance, R$_s$, is observed with the utilized carbon. Although the variation of R_s does not follow a clear trend with increase in the pore size at a specific temperature but it tends to decrease when the temperature increases, which again is reflected by increase in conductivity. For instance R_s values of 6.3 Ω, 3.5 Ω and 2.4 Ω are recorded for AC200-[Pyr_{13}][NTf_2] combination at 25°C, 40°C and 60°C, respectively. This relation is also holds precisely for other AC-[Pyr_{13}][NTf_2] and AC-[Pyr_{14}][NTf_2] combinations and is attributed to the higher conductivity of the liquids as a result of reduced viscosity at temperature elevation conditions. However when comparing an specific AC-[Pyr_{13}][NTf_2] to the same AC in combination with [Pyr_{14}][NTf_2] of the same temperature, the value of the solution resistance (R_s) tends to increase due to the presence of an extra methyl group in [Pyr_{14}][NTf_2] IL in comparison to [Pyr_{13}][NTf_2] restricting ion mobility. This trend is observed between the Pyr-based ILs regardless of the operating temperature.

From the inset of the high frequency region in Figure 6.12 and the calculated resistances presented in Table 6.12 it is evident that at 25°C, there is a reduction in the ionic resistance (R_i) and ESR with increase in the R/C molar ratio of the activated carbons. In other words with increasing the pore width from RC200 to RC350 at the aforementioned operating temperature, the ionic resistance and ESR for both Pyr-based ILs is decreasing.

With increasing the operating temperature to 40°C the ACs-[Pyr_{13}][NTf_2] combinations obey the same relation as described for AC-IL combinations at 25°C, while this does no longer hold for ACs-[Pyr_{14}][NTf_2] combinations at 40°C. In fact the AC300-[Pyr_{14}][NTf_2] combination provides the lowest ionic and ESR resistances in comparison to other AC-[Pyr_{14}][NTf_2] combinations at the operating temperature of 40°C. However the associated resistances at this combination are still higher compared to the AC300-[Pyr_{13}][NTf_2] at the same temperature due to presence of an extra methyl group in [Pyr_{14}][NTf_2] but the capacitive component is higher allowing for higher capacitance outputs. This property could be attributed to presence of a more localized charge on the [Pyr_{14}] cation causing in a more favourable molecular orientation with AC300 and therefore allowing a higher concentration of ions to be adsorbed to the surface and pore walls. However by increasing the temperature further to 60°C, some inconsistent variations are observed in the ionic resistance and the ESR with increase in the pore width which is mainly due to the increased energy of the system and accumulation of resistances, especially the ionic resistances.

It is worth noting that the value of R_i for all AC-IL combinations, which is the indication of the interaction between the conducting and porous mediums, experience a huge increase compared to the same combination at colder temperature run. This trend contradicts with the previously described expectation that at higher operating temperatures the mobility of the IL increases and therefore the IL can reach the least accessible pores to create a double layer of charge and hence leading in improved performance. The contradiction here could be explained through a possible reduction in the optimum operating potential of the IL when used in the cell configuration as a result of increase in the system energy at elevated temperatures.

Table 6.12 EIS characteristics of pyr-ILs paired with controlled porosity ACs at various temperatures

ILs	**ACs**	**C_{eis} [Fg^{-1}]**	**R_s [Ω]**	**R_i [Ω]**	**ESR [Ω]**	**ϕ [°]**
			At 25°C			
[Pyr_{13}][NTf_2]	200	17.8	6.3	84.6	50.6	-52.5
	250	19.9	5.7	51.5	43.4	-59.8
	300	17.4	5.8	36.3	35.1	-66.7
	350	18.9	5.2	33.4	32.3	-71.1
[Pyr_{14}[NTf_2]	200	19.2	7.7	69.3	51.6	-58.0
	250	19.9	6.9	62.6	48.5	-54.2
	300	20.1	8.0	52.7	43.1	-64.1
	350	20.5	9.4	41.1	42.5	-66.6
			At 40°C			
[Pyr_{13}][NTf_2]	200	16.8	3.5	122.8	49.5	-46.1
	250	19.7	3.5	76.1	48.1	-52.8
	300	17.2	3.3	57.4	42.2	-58.4
	350	19.2	3.2	51.3	39.9	-62.8
[Pyr_{14}][NTf_2]	200	19.4	4.7	133.9	55.4	-45.2
	250	18.2	5.2	78.9	51.0	-49.1
	300	20.1	4.5	58.4	44.2	-61.2
	350	19.9	4.3	63.1	47.1	-57.2
			At 60°C			
[Pyr_{13}][NTf_2]	200	13.6	2.4	160.1	45.2	-42.9
	250	17.8	2.4	126.2	46.3	-47.9
	300	16.5	2.3	112.9	48.5	-48.8
	350	18.3	2.3	103.7	45.3	-52.6
[Pyr_{14}][NTf_2]	200	14.2	3.2	316.8	47.9	-34.5
	250	13.4	2.7	149.7	49.6	-45.6
	300	19.9	3.1	101.3	48.5	-50.6
	350	18.9	3.6	108.7	50.8	-50.7

Where C_{eis} represents the determined specific capacitance through EIS at 0.01Hz, R_s the solution resistance determined at the intercept of x-axis, R_i ionic resistance determined through fitting various functions, ESR equivalent series resistance determined at 1kHz and ϕ capacitive component of the impedance determined at the low frequency region

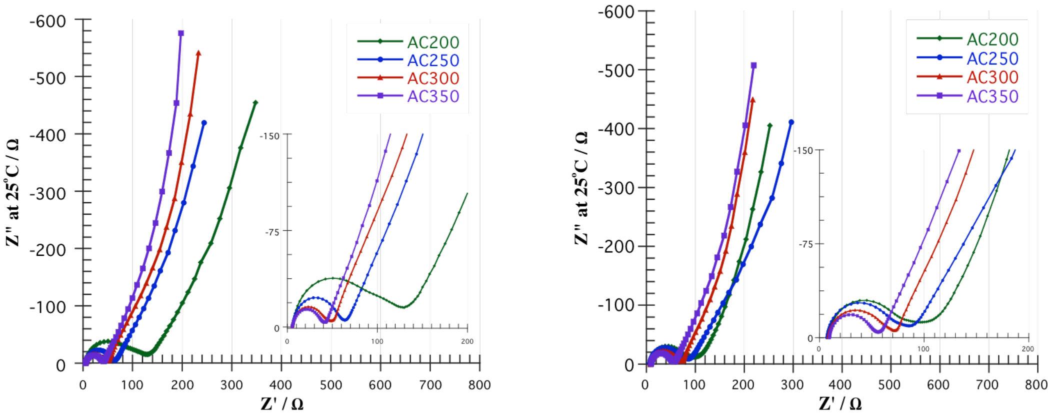

a) [Pyr$_{13}$][NTf$_2$] b) [Pyr$_{14}$][NTf$_2$]

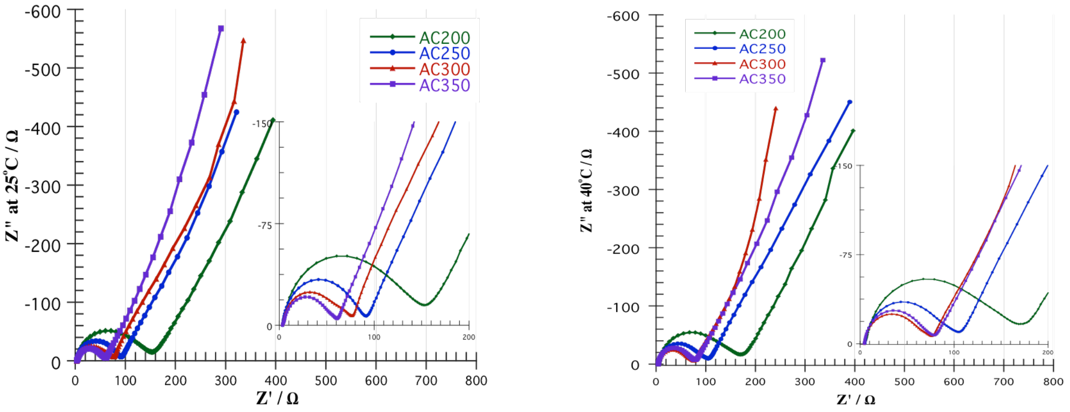

c) [Pyr$_{13}$][NTf$_2$] d) [Pyr$_{14}$][NTf$_2$]

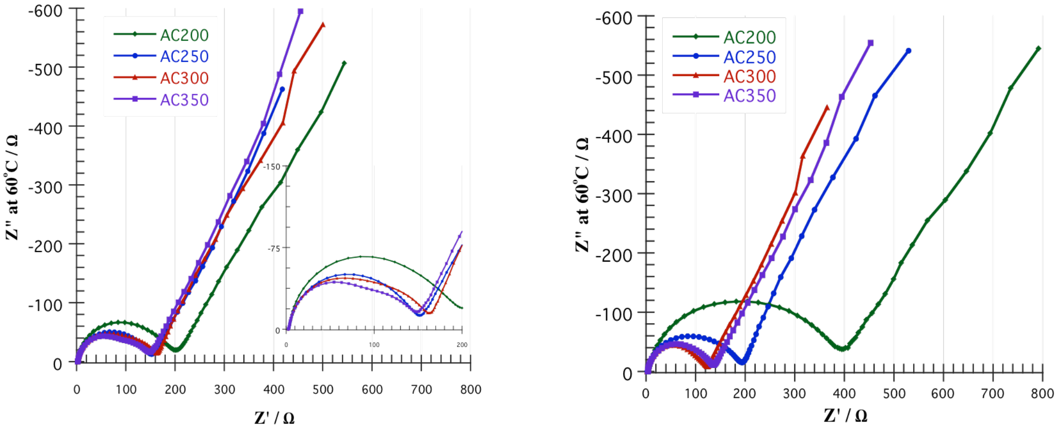

e) [Pyr$_{13}$][NTf$_2$] f) [Pyr$_{14}$][NTf$_2$]

Figure 6.12 EIS plots for a) a) [Pyr$_{13}$][Tf$_2$N], b) [Pyr$_{14}$][Tf$_2$N] at 25°C, c) [Pyr$_{13}$][Tf$_2$N], d) [Pyr$_{14}$][Tf$_2$N] at 40°C and e) [Pyr$_{13}$][Tf$_2$N], f) [Pyr$_{14}$][Tf$_2$N] at 60°C

6.4.3.2 GC measurements

The effect of temperature elevation on resistances, especially for those with smaller pore sizes, through EIS is also evident on the cell performance determined by GC. Figure 6.13 compares the electrochemical performance of [Pyr$_{13}$][NTf$_2$] and [Pyr$_{14}$][NTf$_2$] ILs together with respect to the controlled porosity ACs at temperatures of 25°C, 40°C, 60°C and 80°C.

The curves associated with each of the AC-IL combinations display better performance and improved retention of capacitance with charging rates when combined with ACs with higher pore width, i.e. AC300 and AC350. This is occurring for both pyr-ILs at elevated temperatures, which is also supported by the substantially lower determined resistances through EIS for these pore mediums.

At 25°C operation and at charging rate greater than 2 Ag^{-1} the value of the IR drop tends to be greater than the operating potential of the both pyr-based ILs combined with AC200 as no further cycling beyond this rate was accomplished. This is mainly due to the provision of narrowest pore characteristics of the AC200 carbon. With increasing the pore width by 15% from 4.3 nm to 5.1 nm for AC250, the pyr-based cells provide capacitance at twice the charging rate, i.e. 4 Ag^{-1}. The AC300 and AC350 carbons on the other hand maintain the highest cyclability with the charging rate at this temperature.

The obtained specific capacitances during GC discharge rates of 0.5 and 4.0 mA, i.e. $c_{0.5}$ and $c_{4.0}$, are shown in Table 6.13. This is rather a very narrow selection of discharge densities compared to the whole cycled rate range, however cycling beyond 4 mA for some of the AC-IL combinations at higher temperatures could not be performed. Please refer to Appendix 4.

According to the tabulated data, at the low current density of 0.5 mA, there is an increase in the value of $c_{0.5}$ as the temperature increases to 40°C regardless of the utilized Pyr-IL and AC, which can be attributed to the phenomena of charge redistribution becoming more efficient through improving the mass transport properties by increasing the temperature to 40°C. However with increasing the charging rate to 4.0 mA at temperature of 40°C this trend no longer exists where in fact the self-discharge processes have a greater influence.

It is also evident that at low charging density of 0.5 mA for all AC-IL combinations at room temperature and 40°C the value of capacitance tends to be slightly higher for the ACs with narrower pore width in comparison to the wider pore carbons, with AC250 standing the highest for some combinations. However as the current density increases to 4.0 mA, capacitance retention tends to dramatically fall for the carbons incorporating narrower pores in comparison to wider pore carbons. This is mainly due to the presence of higher percentage of microporosity in AC200 and AC250 carbons, 43% and 41% respectively, compared to the other carbons limiting the mass transfer of the ions as the ions are unable to access the inner surface area of the pores rapidly enough in order to create the double layer at higher rates.

Analogously, the establishment of higher capacitance values for AC200 and AC250 at low current densities at 25°C and 40°C can also be attributed to either the more dominant presence of microporosity getting saturated with ions more rapidly or association of these carbons with lower surface area and lower total pore volumes offering fewer sites in a given geometry for charge storage.

It is worth noting that the aforementioned trend becomes less significant for the $c_{0.5}$ values at operating temperatures of 60°C and 80°C where the energy of the system is higher and narrower pores are influenced by the resistances the most.

No clear trend between the extension of the cation side chain length and the capacitance at the aforementioned rates was observed.

It is worth highlighting that there is a noticeable disparity between these specific capacitances determined through GC method and EIS method. Determination of lower capacitances through EIS is mainly due to the fact that the entire surface available for formation of double layer is not completely used unless very low frequencies are applied. It is possible that at the selected frequency of 0.01 Hz the surface is not fully utilized since the ACs contain a high surface area and high microporosity volume.

As anticipated from electrochemical supercapacitors, a very high coulombic efficiency must have been attained at all discharge rates, usually exceeding 98%. Regardless of the discharge rate, however the attained efficiencies here are noticeably lower than anticipated. The discrepancies here mainly arise due to the experimental design for cycling the cells. A 20 seconds potentiostatic hold period was applied after the cell is fully charged to the operating potential limit of the IL and just before the discharge process starts. This step was applied to allow for charge redistribution inside the pore volume and also to counteract the rate of self-discharge at the same time. During this potentiostatic hold period extra current was added to the system in order to recover the lost potential and maintain the cell at the fully charged state. Therefore the calculated coulombic efficiencies at 0.5 mA and 4.0 mA are not real measures of this quantity at the aforementioned rates. The coulombic efficiency here, which was calculated as a ratio of output charge to the input charge, seems to be greater than 84% at low charging rate of 0.5 mA in all operating temperatures where then significantly reduced with increase in the charging rate to 4.0 mA and increases in temperature. Firstly, at higher charging rates, the cell charges up to the maximum operable potential of the IL much faster when compared against a lower rate since constant current charging was applied. Hence the ions have a shorter time to displace themselves inside the pores accordingly the distribution may taking place unevenly and not to the full capacity of the AC-IL combination. In other words, the current may not reach some of the smaller micropores at higher rates where it leads to participation of smaller fraction of the pores to contribute towards the charge storage and therefore reducing the output capacitance and correspondingly affecting the efficiency. Secondly, as already discussed, with increasing temperature the energy of the system increases leading to accumulation of resistances and occurrence of increased IR drops, even at lower discharge rates. The calculated efficiencies and IR drop values are in good agreement with the determined capacitances, especially at higher rates, as higher efficiencies and lower IR drops are associated with AC350-[Pyr_{13}][NTf_2] and AC300-[Pyr_{14}][NTf_2] combinations for most temperature runs.

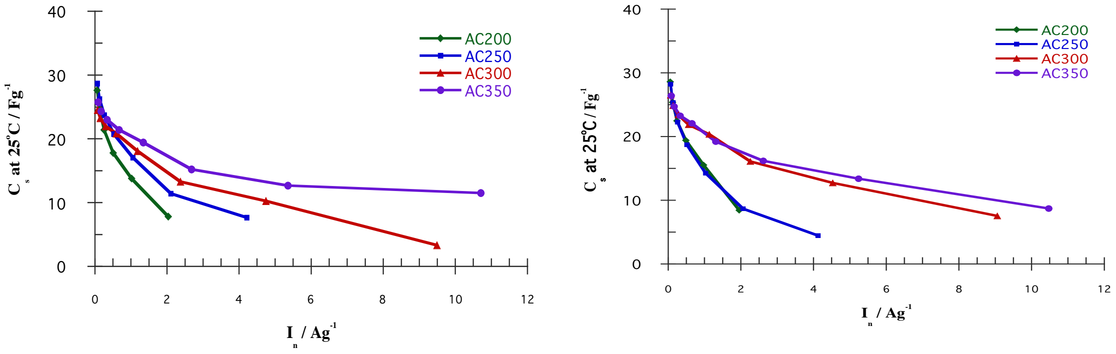

a) [Pyr$_{13}$][NTf$_2$]	b) [Pyr$_{14}$][NTf$_2$]

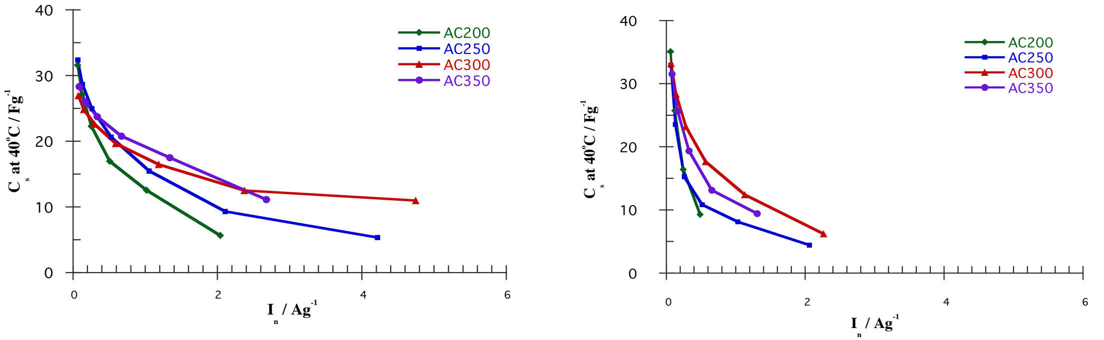

c) [Pyr$_{13}$][NTf$_2$]	d) [Pyr$_{14}$][NTf$_2$]

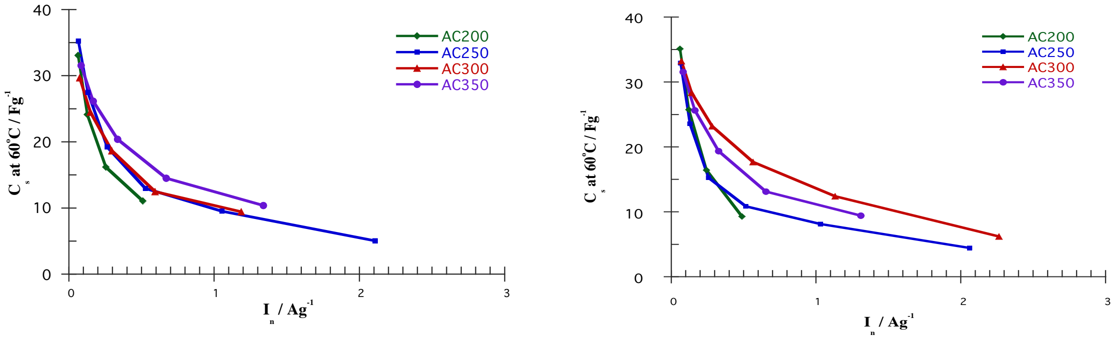

e) [Pyr$_{13}$][NTf$_2$]	f) [Pyr$_{14}$][NTf$_2$]

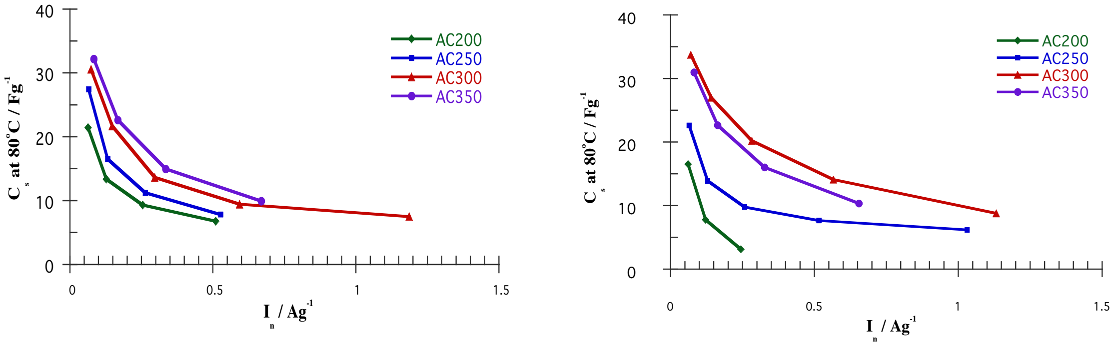

g) [Pyr$_{13}$][NTf$_2$]	h) [Pyr$_{14}$][NTf$_2$]

Figure 6.13 Variation of Specific capacitance with current density for a) [Pyr$_{13}$][Tf$_2$N], b) [Pyr$_{14}$][Tf$_2$N] at 25°C, c) [Pyr$_{13}$][Tf$_2$N], d) [Pyr$_{14}$][Tf$_2$N] at 40°C, e) [Pyr$_{13}$][Tf$_2$N], f) [Pyr$_{14}$][Tf$_2$N] at 60°C and g) [Pyr$_{13}$][Tf$_2$N], h) [Pyr$_{14}$][Tf$_2$N] at 80°C

Table 6.13 GC characteristics of Pyr-ILs paired with controlled porosity ACs at various temperatures

ILs	**AC**	**$c_{0.5}$ [Fg^{-1}]**	**$c_{4.0}$ [Fg^{-1}]**	**$\eta_{0.5}$ [%]**	**$\eta_{4.0}$ [%]**	**IR$_{drop0.5}$ [Ω]**	**IR$_{drop4.0}$ [Ω]**
			At 25°C				
[Pyr$_{13}$][NTf$_2$]	200	24.6	13.8	94.5	67.5	341	263
	250	26.2	17.1	95.1	74.7	217	182
	300	23.3	18.1	95.6	79.0	180	150
	350	24.3	19.4	95.5	80.0	176	146
[Pyr$_{14}$][NTf$_2$]	200	25.4	15.5	95.1	70.9	321	257
	250	25.4	14.3	94.7	70.0	273	227
	300	24.9	20.3	95.5	81.3	173	140
	350	24.7	19.2	95.1	79.1	185	154
			At 40°C				
[Pyr$_{13}$][NTf$_2$]	200	27.1	12.6	93.9	61.7	407	315
	250	28.7	15.5	94.4	70.0	290	227
	300	24.8	18.5	94.5	74.5	221	179
	350	26.0	17.5	94.2	73.3	245	198
[Pyr$_{14}$][NTf$_2$]	200	28.9	15.8	94.1	67.9	361	290
	250	27.4	12.2	93.7	65.9	320	260
	300	26.9	18.1	94.0	74.0	258	205
	350	26.3	17.3	93.5	72.8	231	187
			At 60°C				
[Pyr$_{13}$][NTf$_2$]	200	24.2	-	92.5	45.8	647	445
	250	27.5	9.5	93.3	55.5	478	353
	300	24.5	9.5	92.4	54.6	485	355
	350	26.2	10.4	92.1	51.1	576	408
[Pyr$_{14}$][NTf$_2$]	200	25.7	-	91.5	32.8	890	580
	250	23.6	8.1	91.4	55.2	512	358
	300	28.3	12.4	91.4	59.8	490	352
	350	25.6	9.4	90.6	49.9	579	412
			At 80°C				
[Pyr$_{13}$][NTf$_2$]	200	13.3	-	88.5	34.1	827	529
	250	16.5	-	90.3	40.7	728	482
	300	21.7	7.5	90.3	45.0	622	435
	350	22.6	-	89.8	32.8	847	556
[Pyr$_{14}$][NTf$_2$]	200	7.8	-	84.6	-	2120	-
	250	13.9	6.2	88.1	45.5	729	450
	300	27.0	8.8	88.7	50.3	633	421
	350	22.7	-	87.9	40.6	758	499

6.4.4 EDLC performance – S-based ILs

6.4.4.1 EIS measurements

In this section, the behaviour of the assembled cells using sulfonium based ILs were considered where volume of the cations are 179 $Å^3$ and 207 $Å^3$ for $[S_{221}][NTf_2]$ and $[S_{222}][NTf_2]$, respectively. These cation volumes are markedly lower than their conjugating anion, that is $[NTf_2]^-$ at the volume of 248 $Å^3$, leading to creation of the smallest IL dimensions utilized in this study. The S-based ILs are differing from one another through inclusion of an extra methyl group into the side chain of $[S_{221}]^+$ that contains the lowest number of constituents on its branch, creating $[S_{222}]^+$.

Figure 6.16 shows the produced Nyquist plots for $[S_{221}][NTf_2]$ and $[S_{222}][NTf_2]$ ILs paired with controlled porosity activated carbons at the temperatures of 25°C, 40°C and 60°C. The attained spectra illustrate that, similar to AC-pyr combinations, the AC-S cells do not behave as ideal capacitors at any of the operating temperatures since there are no vertical responses associated with the low frequency region of these plots. The angle of the capacitive components here does not follow a consistent trend with increasing the pore width from AC200 to AC350 or cation size at a specific temperature. However through increasing the temperature, the response deviates further from the ideal behaviour when compared to the previous temperature. This is perhaps caused by presence of some inhomogeneity in the double layer produced as a result of present porosities or uneven electrode thicknesses.

As described in the experimental section, the low frequency impedance is also correlated to capacitance. It is seen that the calculated capacitance values of $[S_{221}][NTf_2]$ IL are markedly higher combined with every controlled porosity ACs in comparison to AC-$[S_{222}][NTf_2]$ combinations. This trend is observed for all operation temperatures and contradicts with the expectation as the least viscous and most conductive IL, i.e. $[S_{222}][NTf_2]$, is expected to perform better.

With the exception of AC200-$[S_{222}][NTf_2]$ and AC350-$[S_{222}][NTf_2]$ combinations where a marginal increase in c_{eis} occurs at 40°C, all other combinations experience a sharp decrease in c_{eis} when the temperature increases as result of resistances build up inside the cells.

Regarding the resistances determined from the magnified section of high frequency region shown in Figure 6.16, in spite of the small cation dimensions, the narrowest pore width AC200 remains the most resistive porous medium in terms of providing insufficient room for ions to form double layers for both ILs at all temperatures. The highest value of ionic resistance and ESR is associated with this carbon in all operating temperatures. The least resistive pore medium, however, tend to vary with the cation size at different temperatures. In fact there are no consistent trend between (R_s, R_i, ESR) and ion size, pore width and temperature. However, similar to AC-pyr combinations the ionic resistance increases with temperature.

The most capacitive behaviour at 25°C is observed for AC300-[S_{221}][NTf_2] and AC350-[S_{222}][NTf_2]. Although this is reflected on c_{eis} for the former combination but the latter combination is associated with the provision of the lowest c_{eis} at the aforementioned temperature as the solution resistance is relatively high at 4.1 Ω compared to other combinations at this temperature.

AC250-[S_{221}][NTf_2] combination at this temperature is seem to equally compete with AC300 paired with the same IL. However the marginally higher R_i and ESR resistances and lower phase angle indicate that the pore width provided by AC250 may be slightly small for the optimum ion adsorption.

It is worth noting that for the value of R_i and ESR tends to be at the minimum for AC350-[S_{221}][NTf_2] at 25°C. However the c_{eis} tends to be the second lowest standing after AC200-[S_{221}][NTf_2] combination at 38.5 Fg^{-1}. This indicates that the provided pore width from AC350 are too large for ions adsorption and it may be the case that the unabsorbed ions compete with the existing absorbed ones in the same pore to form a double layer of charge as this carbon provides the widest pathways for the ion diffusion so no empty pore volume is available in this carbon and perhaps excess electrolyte is present, i.e. pore flooding takes place. This condition is generally associated with a substantial increase in the double layer thickness or a decrease in the IL's dielectric constant and shown in Figure 6.14. Alternatively the mechanism of ion pairing takes place where the attraction between the adsorbed and competing ions becomes lower with the pore walls than ions carrying opposite charge resulting in ion pairing and higher concentration of neutral ion pairs [37]. This behaviour is also observed through further increase in the temperature to 40°C and 60°C for this AC-IL combination.

These finding supports the idea that the performance of IL based supercapacitors can only be improved through careful selection of carbon materials [203]

This image has been removed due to the copyright

Figure 6.14 Pore flooding mechanism resulting in: a) ion exchange and b) ion pairing. Adapted from [37]

In a closer investigation of AC-[S_{222}][NTf_2] combinations at 25°C, only a marginal variation in the c_{eis} is observed for AC200/250/300-[S_{222}][NTf_2] with AC300 standing the highest as discussed. However the resistances are more significant with the narrower pore width ACs causing disparities with the shape of the spectra as shown in Figure 6.15 b). The disparity in the shape of the spectra remains with raising the temperature to 40°C, although interestingly the AC200-[S_{222}][NTf_2] combination provides the highest resistances but also provides the highest capacitance which was followed by AC300>AC350>AC250 respectively. Similar to 25°C operation, AC300-[S_{221}][NTf_2] provides better performances and capacitive behaviour compared to its relative [S_{221}][NTf_2] combinations at 40°C.

Through further increase of temperature to 60°C, AC300-[S_{221}][NTf_2] combination provides the markedly higher capacitance compared to others but R_s and ESR resistances are also among the highest.

The discrepancies between the resistances and determined c_{eis} values with the shape of the spectras for [S_{222}][NTf_2] combinations also remain at this temperature. However the wider pore carbons, i.e. AC300 and AC350, tend to provide better capacitances.

Table 6.14 EIS characteristics of S-ILs paired with controlled porosity ACs at various temperatures

ILs	**ACs**	**C_{eis} [Fg^{-1}]**	**R_s [Ω]**	**R_i [Ω]**	**ESR [Ω]**	**ϕ [°]**
At 25°C						
$[S_{221}][NTf_2]$	200	36.4	3.6	74.4	37.8	-47.2
	250	41.4	3.1	15.5	17.8	-59.5
	300	44.7	4.0	14.4	17.7	-66.8
	350	38.5	3.8	9.8	13.4	-64.6
$[S_{222}][NTf_2]$	200	29.7	3.4	43.7	36.5	-49.6
	250	28.9	3.2	38.5	34.7	-55.9
	300	29.8	3.18	20.7	22.2	-58.0
	350	25.7	4.1	9.5	13.4	-70.2
At 40°C						
$[S_{221}][NTf_2]$	200	35.5	4.0	71.7	43.2	-45.1
	250	35.9	3.4	36.2	31.3	-49.9
	300	37.4	2.3	27.8	25.7	-51.1
	350	34.9	2.4	22.4	22.3	-55.6
$[S_{222}][NTf_2]$	200	30.1	3.3	74.1	43.7	-44.7
	250	24.4	2.1	35.8	30.5	-49.9
	300	28.2	2.4	56.4	38.9	-48.2
	350	25.9	2.1	19.8	19.9	-58.3
At 60°C						
$[S_{221}][NTf_2]$	200	23.3	1.8	144.2	35.9	-39.0
	250	23.5	1.7	61.9	35.7	-46.8
	300	31.5	5.1	73.1	40.0	-45.4
	350	23.1	2.2	55.5	36.7	-50.4
$[S_{222}][NTf_2]$	200	19.7	3.2	144.8	43.4	-40.2
	250	19.1	1.5	59.5	39.4	-49.5
	300	23.2	3.4	129.8	46.0	-40.7
	350	22.0	3.1	45.5	36.9	-50.4

Where C_{eis} represents the determined specific capacitance through EIS at 0.01Hz, R_s the solution resistance determined at the intercept of x-axis, R_i ionic resistance determined through fitting various functions, ESR equivalent series resistance determined at 1kHz and ϕ capacitive component of the impedance determined at the low frequency region

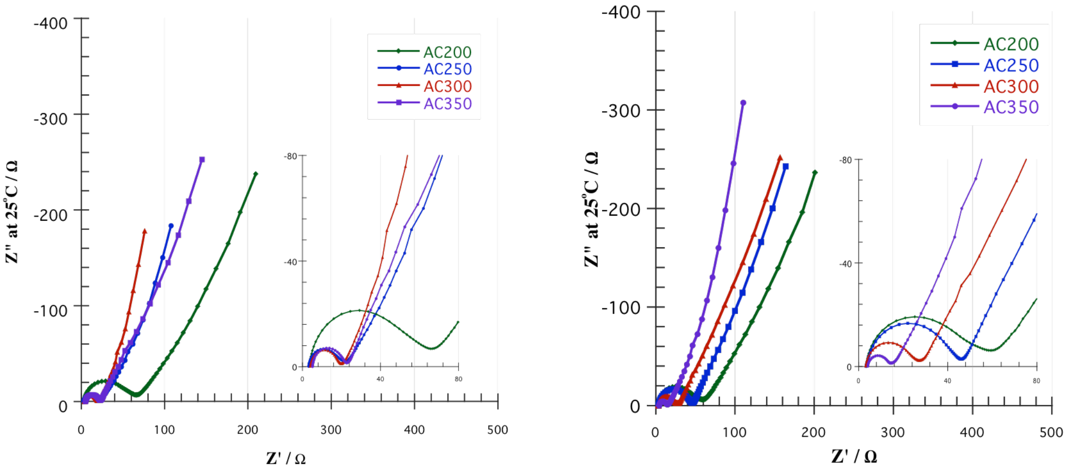

a) $[S_{221}][NTf_2]$ b) $[S_{222}][NTf_2]$

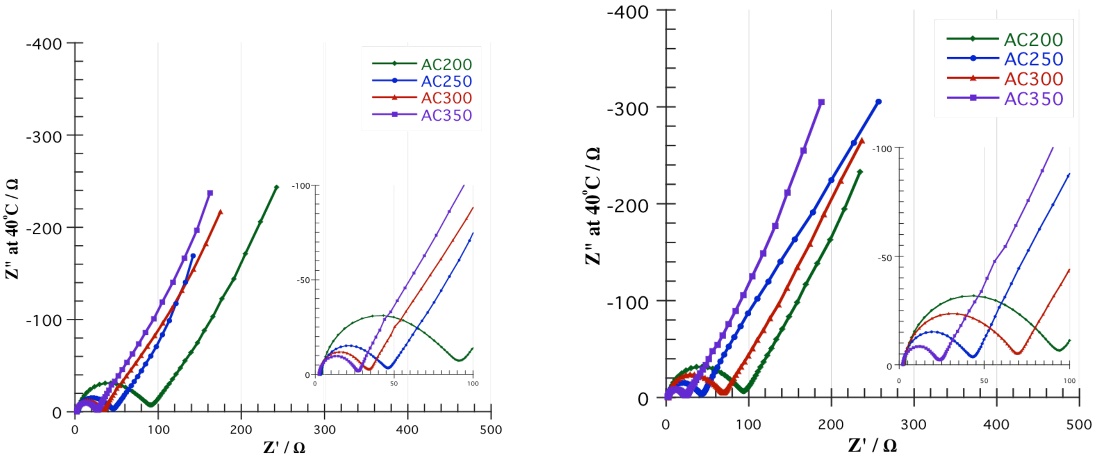

c) $[S_{221}][NTf_2]$ d) $[S_{222}][NTf_2]$

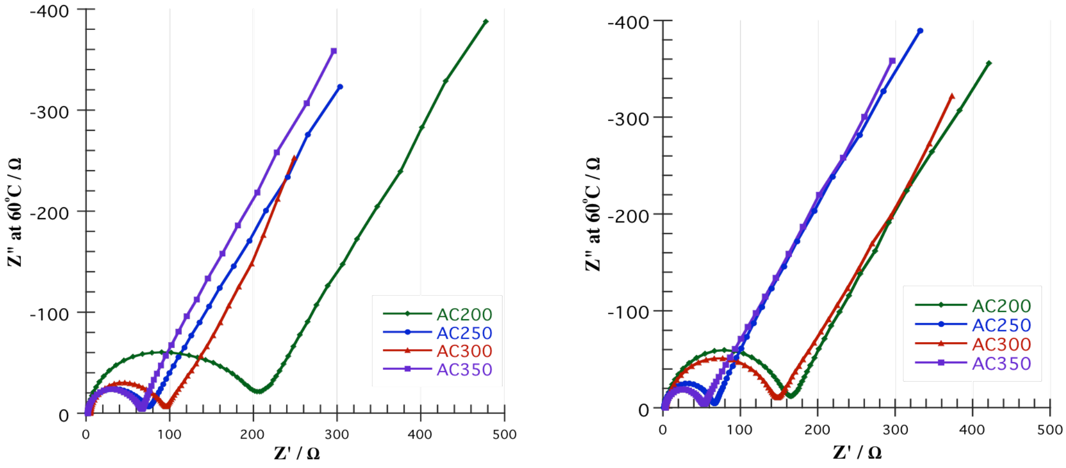

e) $[S_{221}][NTf_2]$ f) $[S_{222}][NTf_2]$

Figure 6.15 EIS plots for a) $[S_{221}][Tf_2N]$, b) $[S_{222}][Tf_2N]$ at 25°C, c) $[S_{221}][Tf_2N]$, d) $[S_{222}][Tf_2N]$ at 40°C and e) $[S_{221}][Tf_2N]$, f) $[S_{222}][Tf_2N]$ at 60°C

6.4.4.2 GC measurements

Figure 6.16 compares the electrochemical performance, determined by GC, of [S_{221}][NTf_2] and [S_{222}][NTf_2] ILs when paired with controlled porosity carbons at 25°C, 40°C, 60°C and 80°C. Table 6.15 compares these combinations with respect to the attained capacitances, efficiencies and IR drop values at the discharge rates of 0.5 and 4.0 mA at the aforementioned temperatures.

Analogous to the determined capacitances using the low frequency impedance, when comparing the characteristics of [S_{221}][NTf_2] cells with those using [S_{222}][NTf_2] there are markedly higher values of $c_{0.5}$ and $c_{4.0}$ are associated with [S_{221}][NTf_2] for each of the ACs, which again contradicts with our expectation due to provision of better conductive and transport properties of [S_{222}][NTf_2] IL. This can be attributed to 3 major reasons of: 1) the absence of a CH_2 in [S_{221}][NTf_2] IL allowing for better accessibility to the surface i.e. greater fraction of pores being utilized, 2) much denser packing of [S_{221}][NTf_2] IL may occur at the electrode surface due to their smaller cation dimension and 3) absence of a methyl group in [S_{221}][NTf_2] can also led to a reduction in distance between the central charged atom of the adsorbed cation with the AC surface transferring greater amount of charge to the porous surface [204].

At 25°C and 40°C runs, the AC200 carbon paired with both S-ILs produce the poorest performance in terms of the ability of the cells to cycle at higher rates. Correspondingly the voltage drop at higher rates is more significant when compared to the operating potential of the IL, in addition, the IR drop is at its maximum for the aforementioned combinations at all temperatures indicating that provided pore width by AC200 is insufficient for optimum charge storage.

With increasing the temperature further to 60°C and 80°C, a sharp drop in capacitance is observed for all AC-ILs perhaps due to a greater degree of self-discharge as a result of improved transport properties. In other words, the better electronic and transport properties for S-ILs at elevated temperatures aids the formation of the double layer, however at the same time the self discharge is also encouraged due to the same reason, i.e. better electronic and transport properties.

This effect is much higher and more noticeable for S-based ILs in comparison to the other ILs due to the smaller size of the cations and provision of the lowest viscosities.

Albeit, analogous to the determined capacitances through EIS, the obtained GC capacitances experience a reduction with higher temperatures but according to the tabulated data, an increase in $c_{0.5}$ is observed for AC200/300/350 at 40°C for both $[S_{221}][NTf_2]$ and $[S_{222}][NTf_2]$ ILs when compared against the same combinations at the same rate at 25°C. This is mainly due to the reason that at this temperature accumulation of resistances are not as significant as 60°C and 80°C runs where the energy of the system increases. This perhaps is in favour with creation of double layer at smallest pores due to improved properties and not in a compromise with self-discharge processes. Also the small size S-cations can perhaps provide better orientation with the surface at this temperature.
However when increasing the discharge density to 4.0 mA, the trend disappears as at higher densities, the cell charges up to the operating potential of the incorporated IL in a shorter time period when compared against lower densities hindering the charge displacement inside the pores. This means that there is insufficient time available for optimum charge storage; therefore lower values were calculated for $c_{4.0}$.

Similar to the presented EIS data, at the operating temperatures of 25°C, 40°C and 60°C the AC300-$[S_{221}][NTf_2]$ combination provides the highest values of $c_{0.5}$ and $c_{4.0}$ at the most stable manner. However the AC200-$[S_{222}][NTf_2]$ combination tends to provide marginally higher $c_{0.5}$ at the operating temperatures of 25°C and 40°C with AC300-$[S_{222}][NTf_2]$ combination standing the second highest. At 60°C, AC300-$[S_{222}][NTf_2]$ combination still provides the second highest value of $c_{0.5}$ with a marginal difference with AC350-$[S_{222}][NTf_2]$ combination standing at the highest. However the $c_{4.0}$ performance seems to remain at the highest for AC350-$[S_{222}][NTf_2]$ combination compared to the other ACs paired with $[S_{222}][NTf_2]$ at all temperatures. In other words, AC350-$[S_{222}][NTf_2]$ combination show better capacitance retention properties with the increased charge density where the association of relatively lower $c_{0.5}$ values of this combination in comparison to other AC-[S_{222}][NTf_2] could be linked to presence of relatively higher percentage of wider mesoporosity in the AC350 carbon than microprosity.

Accordingly the coulombic efficiencies at the discharge rate of 4.0 mA tend to be at the highest for AC300-[S_{221}][NTf_2] and AC350-[S_{222}][NTf_2] combinations at 25°C, 40°C and 60°C runs. Similarly the IR drop values for these combinations are substantially lower in comparison to other controlled porosity carbons at the studied temperatures. Hence the highest efficiencies are achieved with combinations that the IR drop is at the minimum or fairly low, which then result in provision of highest capacitances.

It is also evident that the attained efficiencies at 4.0 mA discharge rates are significantly lower when compared against the corresponding efficiency at 0.5mA of the same combination. As described in section 6.4.3, this is mainly due to the experimental procedure employed as a 20 seconds potentiostatic step was applied at the fully charged state to assist the ions to arrange themselves inside the porous medium in order to minimize the effect of self-discharge processes. Hence extra current was added at this stage to compensate for the potential decay and maintain the cell at the fully charged state. Accordingly when discharge density increases, this current becomes more influencing, as less time is available to the ions to migrate while charging the cell. It is worth noting that a correction for this current is not possible due to the instrument limitation.

Value of the IR drop is also reduced with increase in the discharge density where a relatively bigger potential drop is recorded due to the same mentioned reason.

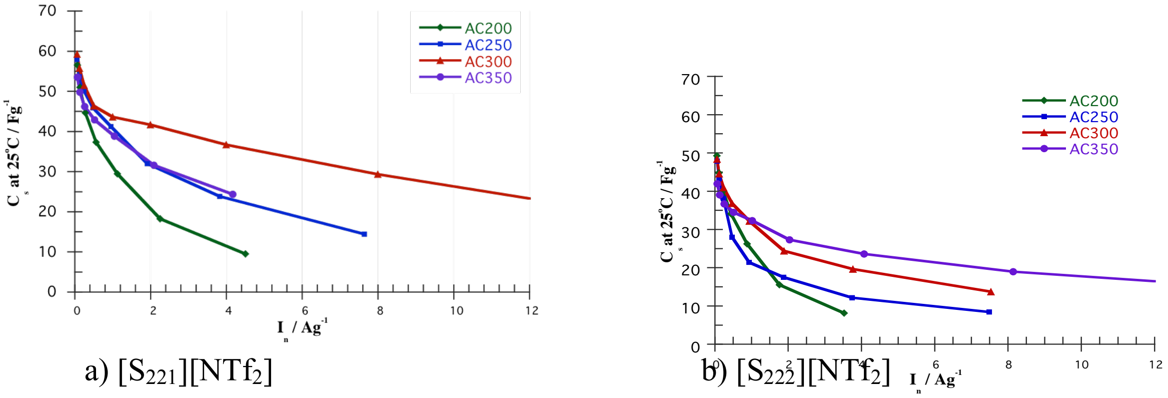

a) $[S_{221}][NTf_2]$ b) $[S_{222}][NTf_2]$

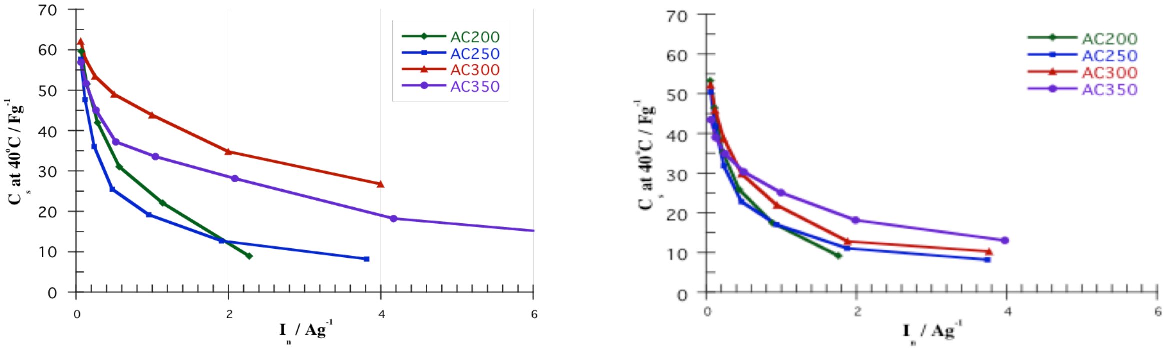

c) $[S_{221}][NTf_2]$ d) $[S_{222}][NTf_2]$

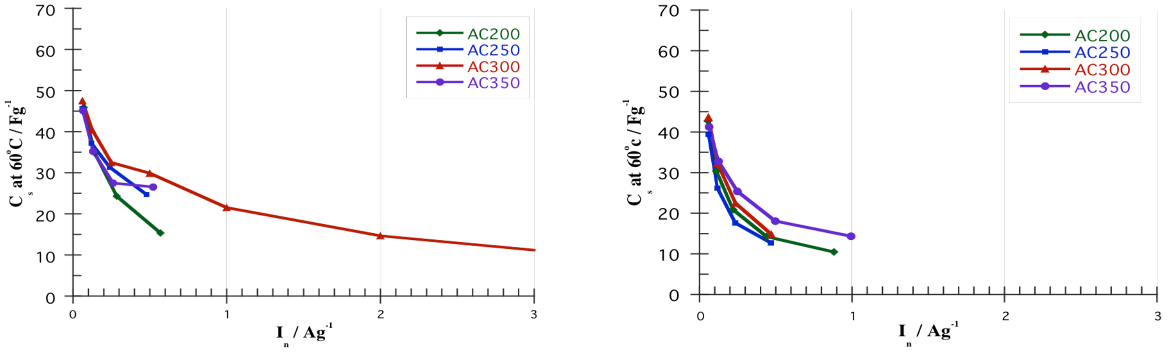

e) $[S_{221}][NTf_2]$ f) $[S_{222}][NTf_2]$

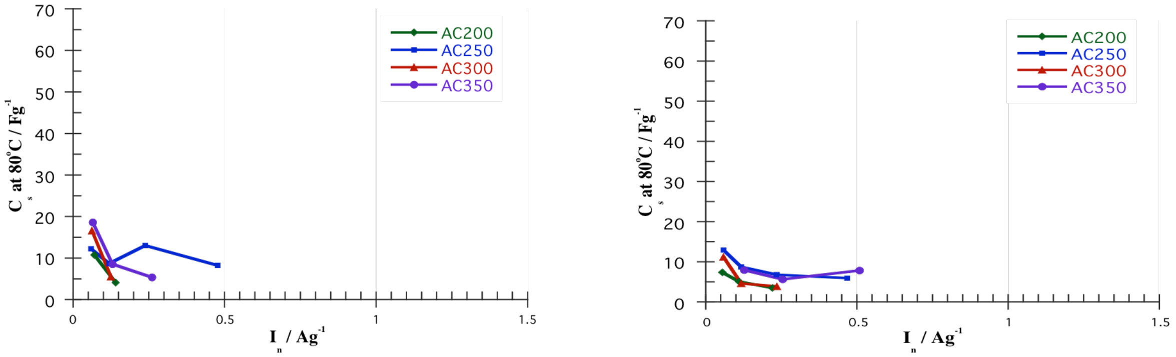

g) $[S_{221}][NTf_2]$ h) $[S_{222}][NTf_2]$

Figure 6.16 Variation of Specific capacitance with current density for a) $[S_{221}][Tf_2N]$, b) $[S_{222}][Tf_2N]$ at 25°C, c) $[S_{221}][Tf_2N]$, d) $[S_{222}][Tf_2N]$ at 40°C, e) $[S_{221}][Tf_2N]$, f) $[S_{222}][Tf_2N]$ at 60°C, $[S_{221}][Tf_2N]$ and h) $[S_{222}][Tf_2N]$ at 80°C

Table 6.15 GC characteristics of S-ILs paired with controlled porosity ACs at various temperatures

ILs	AC	$c_{0.5}$ [Fg^{-1}]	$c_{4.0}$ [Fg^{-1}]	$\eta_{0.5}$ [%]	$\eta_{4.0}$ [%]	$IR_{drop0.5}$ [Ω]	$IR_{drop4.0}$ [Ω]
			At 25°C				
[S$_{221}$][NTf$_2$]	200	51.0	29.4	96.9	77.1	187	169
	250	53.7	41.3	97.4	86.7	139	91
	300	55.8	42.6	98.0	91.9	52	46
	350	49.8	38.8	97.5	87.3	92	78
[S$_{222}$][NTf$_2$]	200	44.8	26.2	97.1	79.3	176	145
	250	43.3	21.4	97.1	74.1	143	190
	300	44.6	32.2	97.4	85.9	84	74
	350	36.2	29.4	96.8	87.3	82	67
			At 40°C				
[S$_{221}$][NTf$_2$]	200	51.5	22.1	95.0	66.8	336	276
	250	47.7	19.1	95.5	75.1	174	149
	300	57.7	43.8	96.4	86.9	95	84
	350	51.7	33.6	96.0	84.1	102	90.6
[S$_{222}$][NTf$_2$]	200	46.4	17.5	96.1	69.1	247	215
	250	41.8	17.1	96.1	72.3	187	157
	300	45.9	21.9	96.1	75.0	198	174
	350	39.0	25.1	96.0	81.5	120	103
			At 60°C				
[S$_{221}$][NTf$_2$]	200	34.8	-	87.0	44.9	572	410
	250	37.2	-	81.3	67.7	243	195
	300	40.5	21.5	85.0	73.1	219	174
	350	35.2	-	85.8	67.1	252	193
[S$_{222}$][NTf$_2$]	200	30.4	10.5	87.2	56.0	401	301
	250	26.2	-	87.2	62.6	288	210
	300	32.3	-	90.2	52.5	406	342
	350	32.8	14.3	91.0	69.3	228	176
			At 80°C				
[S$_{221}$][NTf$_2$]	200	4.1	-	59.7	-	2233	-
	250	8.7	-	74.0	30.9	2487	475
	300	5.6	-	61.8	-	1942	-
	350	8.6	-	63.7	-	1235	-
[S$_{222}$][NTf$_2$]	200	5.1	-	68.8	8.8	1889	-
	250	8.7	-	73.6	33.9	1545	435
	300	4.6	-	43.1	6.8	1531	-
	350	-	-	-	-	-	-

6.4.5 EDLC performance – N-based ILs

6.4.5.1 EIS measurements

Next, the behaviour of the assembled cells containing ammonium based ILs were considered where the volume of one of the cations is smaller and the others are greater than the $[NTf_2]^-$ anion, that is 248 Å^3. The volume of the cations are in the order of 222 Å^3, 306 Å^3 and 266 Å^3 for $[N_{1114}]^+$, $[N_{2224}]^+$ and $[N_{122(2O1)}]^+$ species, respectively. Here the effect of chain length is investigated differently were three CH_2 groups are added to the side chains of $[N_{1114}]^+$ cation in order to produce $[N_{2224}]^+$ whereas formerly addition of only one CH_2 group into the structure was investigated. The incorporation of an ether linkage into the structure and its effect on performance was also considered.

Figure 6.17 demonstrates the produced Nyquist plots for $[N_{1114}][NTf_2]$, $[N_{2224}][NTf_2]$ and $[N_{122(2O1)}][NTf_2]$ ILs in combination with controlled porosity ACs at 25°C, 40°C and 60°C. Analogous to the previously attained spectra for AC-pyr and AC-S at varying operating temperatures, the cells comprised of N-ILs do not exhibit any ideal capacitive behaviour as the low frequency response is not vertical. However as observed from Table 6.16 the capacitive response is approaching ideal behaviour for most combinations with carbons containing higher percentage of pore width and pore volume, i.e. AC300 and AC350.

In fact a clear consistency is observed between increase in the R/C ratio and increase in the capacitive component angle for AC-$[N_{1114}][NTf_2]$ and AC-$[N_{2224}][NTf_2]$ combinations at 25°C and 40°C which then disappears through further temperature increase to 60°C.

On the other side is the ether incorporated $[N_{122(2O1)}][NTf_2]$ IL which shows no consistent correlations with increase in the pore width and capacitive behaviour at various temperature runs. The inconsistency at low temperature run is perhaps caused by high viscosity and low conductivity of this IL even in presence of the ether linkage.

Although no consistent correlations observed for the capacitive component for all ILs paired with controlled porosity carbons at specific temperatures but as the temperature increases a clear deviation from the ideal behaviour is attained for all combinations as a result of inhomogeneity in double layer.

The required data for calculation of c_{eis} for different combinations are also extracted from the low frequency response region where the relative resistances presented in Table 6.16 are attained from the high frequency region.

At 25°C it is seen that there are a marginal increase in the value of calculated capacitances for AC-$[N_{2224}][NTf_2]$ combinations when compared against unextend $[N_{1114}][NTf_2]$ and ether incorporated $[N_{122(2O1)}][NTf_2]$ ILs paired with controlled porosity ACs. This trend in particular is unanticipated as the longer chain IL, that is $[N_{2224}][NTf_2]$, is expected to produce lowest c_{eis} due to the extended chain length limiting the IL mobility and correspondingly lowering the transport properties. Although this may seem as an unexpected result at the first glance, but from the DSC spectras, melting temperatures of 17.1°C and 20.9°C are determined for $[N_{1114}][NTf_2]$ and $[N_{2224}][NTf_2]$ ILs, respectively. Clearly, these melting temperatures are very close to the 25°C operating temperature and the hypothesis is that these N-ILs may still contain some solid crystals in their structure influencing the performance.

It is also evident that at this operating temperature, the solution resistances for different AC-N combinations are in the order of $[N_{2224}][NTf_2]$> $[N_{1114}][NTf_2]$> $[N_{122(2O1)}][NTf_2]$ where a little variation in R_s is observed with $[N_{1114}][NTf_2]$ and $[N_{2224}][NTf_2]$ ILs paired with controlled porosity carbons. This finding supports the original hypothesis about presence of solid crystals in the IL as no significant variation is observed when pore width is increasing. In other words the influence of the cation size and pore width can be treated as negligible for the aforementioned combinations at 25°C.

In the case of $[N_{122(2O1)}][NTf_2]$ IL, presence of the methoxyethyl linkage leads to lower degrees of interactions between the cation and the pore walls of the negatively charged electrode. It is also worth recalling that although incorporation of an ether linkage adds extra flexibility into the chain and reduces viscosity, it also impedes the potential range at which the IL remains stable. Hence the ether-incorporated cells charge up to a lower potential limit at each cycle, reducing the amount of displaced charge in the electrode.

At 25°C, AC350-$[N_{1114}][NTf_2]$ and AC350-$[N_{122(2O1)}][NTf_2]$ combinations provide the highest c_{eis} at 21.9 and 20.8 Fg^{-1}, respectively, in comparison to other AC combinations paired with the same N-based IL at the same temperature. According to the resistances extracted from the high frequency region, there is a minimum R_i and ESR that coincide well with peak values of c_{eis}. These combinations are also associated with the maximum phase angle attained from the low frequency impedance that again is in good agreement with attaining highest c_{eis} capacitances.

The above characteristics of minimum R_i, minimum ESR and maximum phase angle are hold for the AC350-$[N_{2224}][NTf_2]$ combination at the same operating temperature, however a specific capacitance of 21.4 Fg^{-1} is calculated for this combination, which is marginally lower than AC300-$[N_{2224}][NTf_2]$ combination of 22.3 Fg^{-1}. The contradiction here may perhaps arise from the fact the near mp temperature of this IL to the operating temperature may result in the creation of some solid crystals that consequently causes blockage.

The same trend is also observed at 40°C. The contradiction here is no longer linked to the melting of the $[N_{2224}][NTf_2]$ IL as the temperature is increasing, viscosity is reducing and a bigger variation of R_s is recorded with the ACs. Thus the inconsistency here could perhaps be linked to greater degree of ionic coordination of this IL with AC300 leading to denser packing of the ions on the electrode surface and displacing more charge.

An increase in c_{eis} is experienced for all AC-N combinations when increasing the temperature to 40°C. This trend tends to be more significant for the narrower pore width AC200 and AC250 where a greater percentage of microporosity is available for charge storage in comparison to AC300 and AC350. Through further temperature increase to 60°C, a minor reduction in capacitance is experienced for most AC-N combinations due to the increase in the system energy. However the AC250-$[N_{2224}][NTf_2]$ and AC200-$[N_{122(2O1)}][NTf_2]$ combinations are excepted from this trend where a higher value of c_{eis} is produced compared to the previous operating temperature. In fact the aforementioned combinations provide the highest value of c_{eis} when compared against other AC combinations of the same category. These combinations are also associated with higher values of Ri, ESR and lower ϕ than AC300-$[N_{2224}][NTf_2]$ and AC350-$[N_{122(2O1)}][NTf_2]$ combinations, as previously discussed, indicating that this variation is most likely caused by impedance limitation in determining the capacitance in the low frequency region rather than having any physical meaning.

It is also worth noting that at 25°C, the R_i and ESR resistances are at their maximum when the N-ILs are paired with AC200 indicating that a large fraction of microporosity in this carbon is inaccessible to the ions. Although by increasing the temperature to 40°C and 60°C, Ri and ESR resistances increase but the trend for AC200 no longer exists due to the build up of the system energy.

Not to forget that the allowable operating potential window at 25°C was utilized for all temperature operations, which may stand as too wide when dealing with high temperature runs. Although this account as a primary reason for build up of resistances but the c_{eis} variation with temperature is not as extreme as other previously studied systems indicating that the selected operating potentials of N-ILs at 25°C are relatively a conservative choice for potential limit.

Table 6.16 EIS characteristics of N-ILs paired with controlled porosity ACs at various temperatures

ILs	AC	C_{eis} [Fg^{-1}]	R_s [Ω]	R_i [Ω]	ESR [Ω]	ϕ [°]
			At 25°C			
[N$_{1114}$][NTf$_2$]	200	16.1	11.2	71.2	49.1	-51.9
	250	18.1	10.4	39.4	36.8	-57.3
	300	20.8	10.9	49.9	44.1	-68.3
	350	21.9	11.8	18.9	27.6	-74.6
[N$_{2224}$][NTf$_2$]	200	20.4	15.8	66.7	54.2	-57.9
	250	20.0	16.1	51.3	45.5	-58.4
	300	22.3	15.6	41.5	40.5	-61.6
	350	21.4	15.2	30.5	33.5	-69.5
[N$_{122(2O1)}$][NTf$_2$]	200	17.8	11.5	89.5	58.0	-62.3
	250	19.7	9.3	46.3	43.4	-57.2
	300	20.1	8.6	43.7	43.1	-73.3
	350	20.8	7.2	34.9	34.1	-74.7
			At 40°C			
[N$_{1114}$][NTf$_2$]	200	19.7	6.7	148.7	55.3	-47.1
	250	20.7	6.3	54.2	44.2	-49.6
	300	22.2	9.9	107.7	59.7	-55.5
	350	22.6	7.4	43.2	40.4	-64.3
[N$_{2224}$][NTf$_2$]	200	23.6	9.0	104.5	60.4	-52.7
	250	22.1	11.1	106.3	50.9	-54.2
	300	24.2	8.7	42.4	39.1	-64.4
	350	22.3	7.8	41.3	33.5	-62.3
[N$_{122(2O1)}$][NTf$_2$]	200	21.4	5.3	118.1	51.7	-62.8
	250	15.3	5.4	125.9	52.1	-45.3
	300	20.5	4.5	131.8	53.6	-59.3
	350	21.8	4.6	89.5	52.3	-64.3
			At 60°C			
[N$_{1114}$][NTf$_2$]	200	14.5	2.9	178.6	58.4	-42.1
	250	20.4	5.8	74.9	49.3	-48.3
	300	21.2	9.0	168.9	56.5	-44.9
	350	21.7	3.8	72.1	46.3	-54.0
[N$_{2224}$][NTf$_2$]	200	22.4	4.8	158.8	55.1	-40.9
	250	23.0	5.7	112.7	52.4	-48.9
	300	22.0	4.9	99.4	48.9	-46.1
	350	20.6	4.7	62.1	45.1	-52.9
[N$_{122(2O1)}$][NTf$_2$]	200	23.0	3.1	202.8	41.6	-48.0
	250	14.2	3.5	133.2	48.4	-46.1
	300	20.2	2.9	190.1	49.7	-51.5
	350	21.5	4.4	136.8	48.3	-52.7

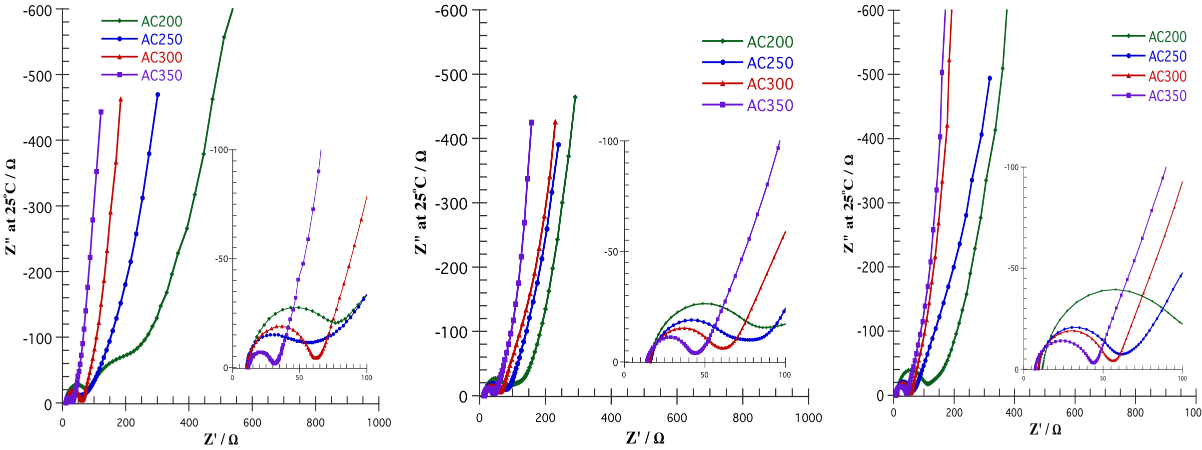

a) $[\mathrm{N}_{1114}][\mathrm{NTf}_2]$ b) $[\mathrm{N}_{2224}][\mathrm{NTf}_2]$ c) $[\mathrm{N}_{122(2O1)}][\mathrm{NTf}_2]$

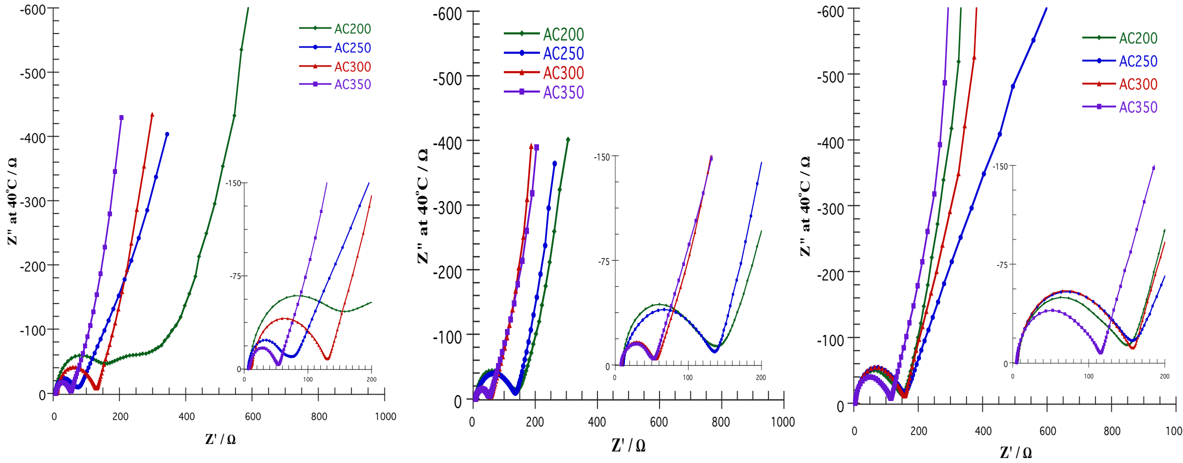

d) $[\mathrm{N}_{1114}][\mathrm{NTf}_2]$ e) $[\mathrm{N}_{2224}][\mathrm{NTf}_2]$ f) $[\mathrm{N}_{122(2O1)}][\mathrm{NTf}_2]$

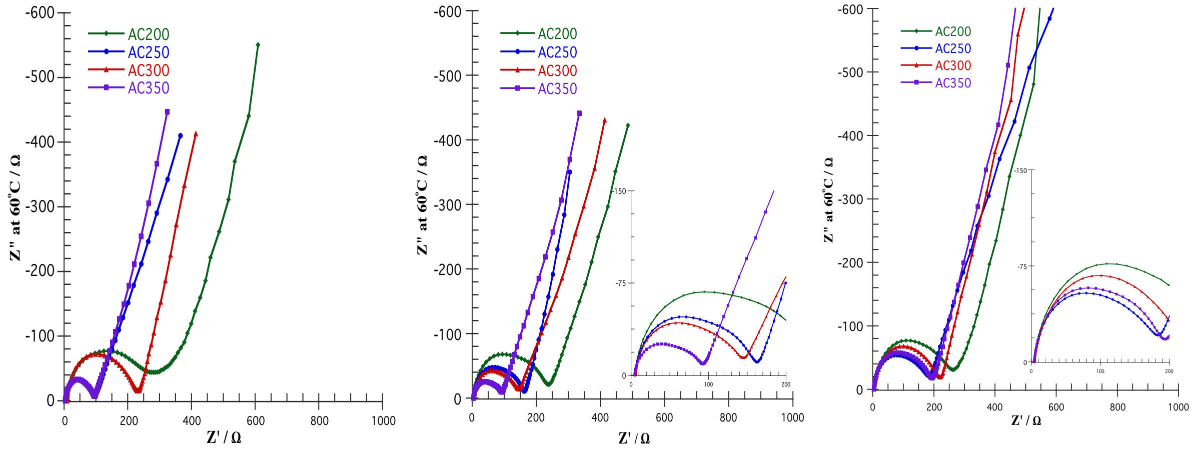

g) $[\mathrm{N}_{1114}][\mathrm{NTf}_2]$ h) $[\mathrm{N}_{2224}][\mathrm{NTf}_2]$ i) $[\mathrm{N}_{122(2O1)}][\mathrm{NTf}_2]$

Figure 6.17 EIS plots for a) $[\mathrm{N}_{1114}][\mathrm{NTf}_2]$, b) $[\mathrm{N}_{2224}][\mathrm{NTf}_2]$, c) $[\mathrm{N}_{122(2O1)}][\mathrm{NTf}_2]$ at 25°C, d) $[\mathrm{N}_{1114}][\mathrm{NTf}_2]$, e) $[\mathrm{N}_{2224}][\mathrm{NTf}_2]$, f) $[\mathrm{N}_{122(2O1)}][\mathrm{NTf}_2]$ at 40°C and g) $[\mathrm{N}_{1114}][\mathrm{NTf}_2]$, h) $[\mathrm{N}_{2224}][\mathrm{NTf}_2]$, i) $[\mathrm{N}_{122(2O1)}][\mathrm{NTf}_2]$ at 60°C

6.4.5.2 GC measurements

Similar to the previously studied ILs, the electrochemical performance of the N-based ILs was also investigated through the Galvanostatic cycling. Figure 6.18 illustrates the produced spectras of the $[N_{1114}][NTf_2]$, $[N_{2224}][NTf_2]$ and $[N_{122(2O1)}][NTf_2]$ ILs paired with controlled porosity activated carbons at 25°C, 40°C 60°C and 80°C. The relative capacitances, coulombic efficiencies and IR drop values of these combinations are also calculated at the discharge rates of 0.5 mA and 4.0 mA at all temperatures. These values are presented in Table 6.17.

At 25°C, the associated curves for the N-ILs combined with AC300 and AC350 display better performance and higher capacitance retention with increasing the discharge rates when compared against narrower pore ACs.

A noticeable similarity in the profile of AC300-$[N_{2224}][NTf_2]$ with AC350-$[N_{2224}][NTf_2]$ and AC200-$[N_{2224}][NTf_2]$ with AC250-$[N_{2224}][NTf_2]$ is also observed. The same similarity is seen for $[N_{122(2O1)}][NTf_2]$ paired with wider pores and narrower pores ACs.

It is also evident that a marginal variation is observed when AC300/AC350-$[N_{2224}][NTf_2]$ are compared against AC300/AC350-$[N_{122(2O1)}][NTf_2]$ combinations with the slightly higher performance of the latter profiles due to the incorporation of ether linkage introducing extra flexibility to the structure and lowering viscosity. Attaining almost the same profiles with two different ILs at the same pore mediums with marginal variation could either be dedicated to similarity in physiochemical properties or the cation constituent volume since the anion remains unchanged. The influence of viscosity and conductivity can be disregarded here as the attained values are fairly apart at 150 mPa.s / 1.31 $mScm^{-1}$ and 71.6 mPa.s / 2.9 $mScm^{-1}$ for $[N_{2224}][NTf_2]$ and $[N_{122(2O1)}][NTf_2]$, respectively, at 25°C. Hence the volume of the cation should have a greater influence. In this case both ILs contain relatively larger size cation constituents in comparison to the $[NTf_2]$ anion so the hypothesis here is that the cations may considered as too large even for the dealing wider pore mediums, i.e. AC300 and AC350. A possibility opens here that the provided surface area and pore volume by these carbons are not fully available to the bigger size cations due to their dimension, accordingly a greater portion of the stored charge is perhaps coming from the creation of the double layer with the anion at the positive electrode. As a result, little performance variation is observed between the narrower and wider pores when paired with two different N-based ILs offering significantly different physiochemical properties.

Hence ACs with greater pore width must be explored to observe whether the stated proposition is the influencing factor.

At the low discharge density of 0.5 mA, there is no consistent correlation between the $c_{0.5}$ values, increase in chain length, incorporation of ether linkage and increase in the pore width. However relatively higher values of $c_{0.5}$ are obtained when the N-based ILs are paired with AC250 in comparison to other ACs in the same category which then changes to AC200 at operating temperature greater than 40°C. These carbons are associated with a higher degree of microporosity indicating that at the low discharge rate of 0.5 mA there are sufficient time available for the current to reach the smaller micropores hence the microporosity is more involved in the storage. Moreover according to the earlier discussed argument, this trend is most likely related to the anion and its dimension directly where these species have sufficient time to create the double layer at smallest micropores and participate in storage. Overall these findings indicate that at the lower charge densities the narrower pore width carbons are the optimum medium choice among the studied carbons here.

By increasing the discharge rate to 4.0 mA, AC350 is a better choice for the N-ILs as the level of microporosity is reduced and mesoporosity increases. In fact, similar to the determined c_{eis} values, the AC350-[N_{1114}][NTf_2], AC300-[N_{2224}][NTf_2] and AC350-[$N_{122(2O1)}$][NTf_2] provide the highest $c_{4.0}$ capacitances which are associated with high efficiencies and low IR drops.

As previously discussed, the reason for selection of 4.0 mA rate as a comparison point to low discharge rate of 0.5 mA is purely due to inability of most combinations to undergo GC cycling beyond this rate at higher temperature operations as the voltage drop due to resistances are significant.

In the case of the AC300-[N_{2224}][NTf_2] combination at 25°C and 40°C operation, it is seen that AC350 paired with the same IL perform better at slightly greater rates than 4.0 mA which is interrelated with the rate of about 1 Ag^{-1} on the GC plots. Hence at the aforementioned temperatures, AC350-$[N_{2224}][NTf_2]$ combination provides better performances with increases in the rate in comparison with AC300-$[N_{2224}][NTf_2]$ combination. This finding is supported by provision of the highest efficiencies and lowest IR drop for this combination at 25°C and 40°C. In fact both wider pore combinations are associated with higher efficiencies and lower IR drops compared to narrower pore ACs at all temperatures.

According to the tabulated data and GC plots, through further temperature increase to 60°C and 80°C, wider pore ACs still provide better performances with increase in the discharge rate at a more stable manner in comparison to narrower pore ACs. However unlike at 25°C and 40°C, the effect of pore characteristics is less apparent when operating at higher temperatures especially for AC250/300/350-$[N_{1114}][NTf_2]$ combinations perhaps due to buildup of resistances and blockage of pores as a result of overcharging decomposition or melting of the polymer due to temperature. At the same time, the mentioned combinations provide the highest $c_{0.5}$ and $c_{4.0}$ at all temperatures when compared against other N-ILs in the same operating temperature indicating a greater contribution of the cation constituent to charge storage, as its smaller in size, in comparison to other ILs in the same category. On the other side are the extended $[N_{2224}][NTf_2]$ and ether incorporated $[N_{122(2O1)}][NTf_2]$ ILs where the extension of the side chains of the former IL limits the ion mobility and increases the viscosity in comparison to $[N_{1114}][NTf_2]$ whereas in the case of $[N_{122(2O1)}][NTf_2]$ although incorporation of the ether linkage improves the viscosity due to the reduced positive charged charge density at the central ammonium atom but a trade-off with maximum operating potential is created which results in lower performance.

As a general trend, AC300 and AC350 deliver better efficiencies and lower potential drops due to resistances at most temperatures regardless of the utilized N-IL. It is also evident that the attained efficiencies at 4.0 mA discharge rates are significantly lower when compared against the corresponding efficiency at 0.5mA of the same combination. As described in section 6.4.3, this is mainly due to the experimental procedure defect.

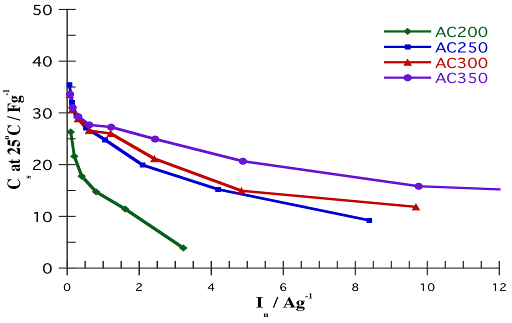

a) $[N_{1114}][NTf_2]$

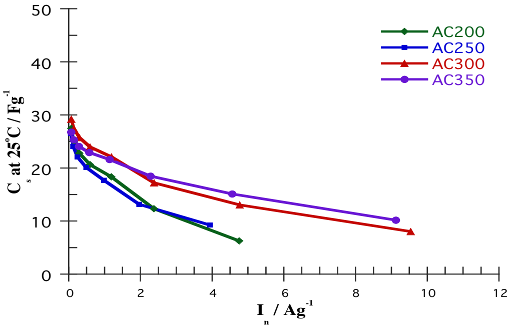

b) $[N_{2224}][NTf_2]$

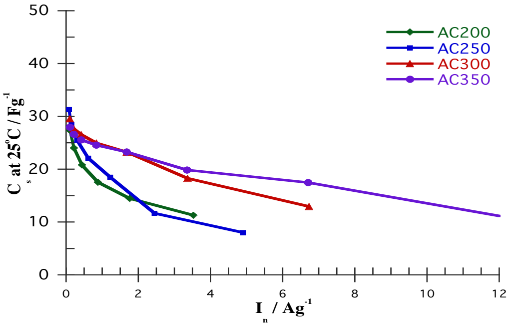

c) $[N_{122(2O1)}][NTf_2]$

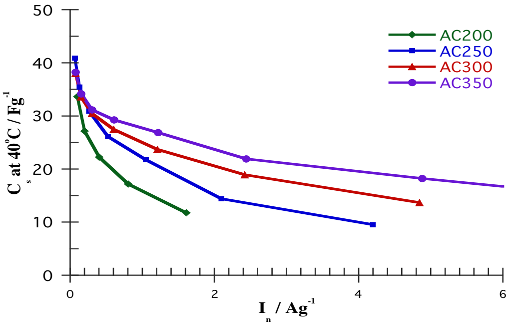

d) $[N_{1114}][NTf_2]$

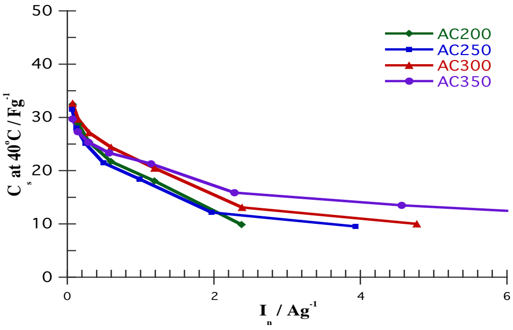

e) $[N_{2224}][NTf_2]$

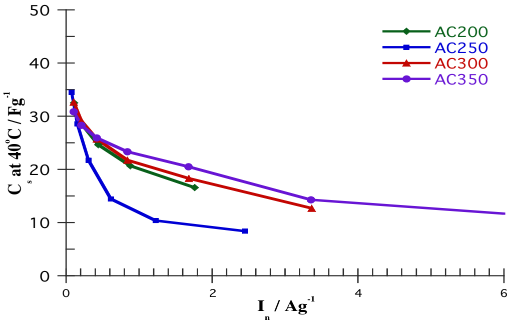

f) $[N_{122(2O1)}][NTf_2]$

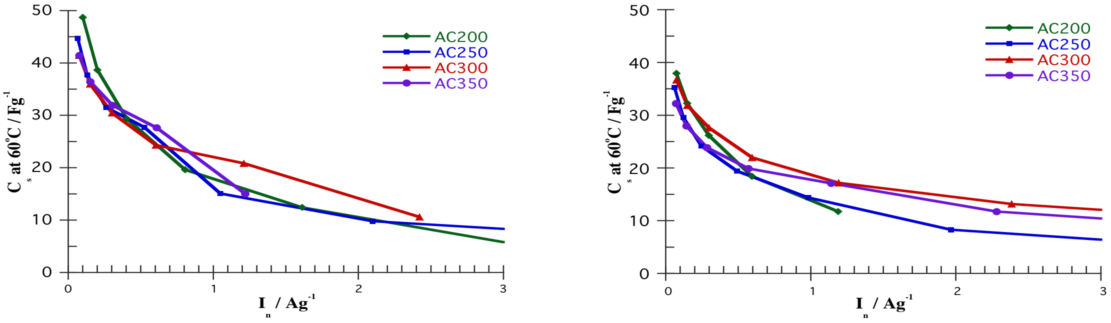

g) [N_{1114}][NTf_2] h) [N_{2224}][NTf_2]

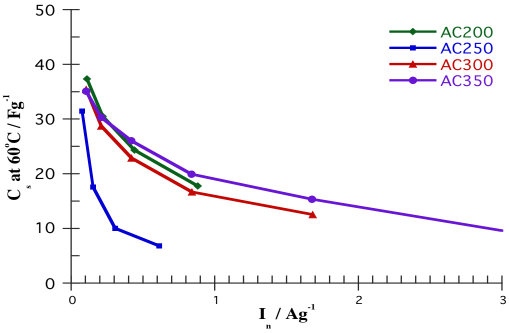

i) [$N_{122(2O1)}$][NTf_2]

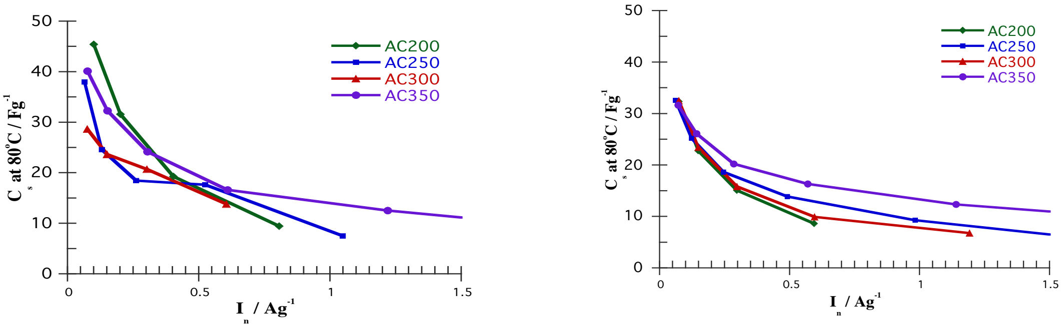

j) [N_{1114}][NTf_2] k) [N_{2224}][NTf_2]

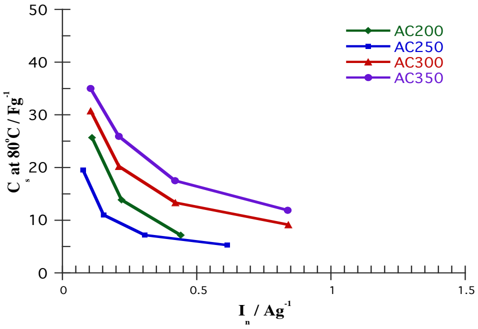

l) [$N_{122(2O1)}$][NTf_2]

Figure 6.18 Variation of specific capacitance with current density for a) [N_{1114}][NTf_2], b) [N_{2224}][NTf_2], c) [$N_{122(2O1)}$][NTf_2] at 25°C, d) [N_{1114}][NTf_2] , e) [N_{2224}][NTf_2], f) [$N_{122(2O1)}$][NTf_2] at 40°C, g) [N_{1114}][NTf_2] , h) [N_{2224}][NTf_2], i) [$N_{122(2O1)}$][NTf_2] at 60°C and j) [N_{1114}][NTf_2] , k) [N_{2224}][NTf_2], l) [$N_{122(2O1)}$][NTf_2] at 80°C

Table 6.17 GC characteristics of N-ILs paired with controlled porosity ACs at various temperatures

ILs	AC	$c_{0.5}$ [Fg^{-1}]	$c_{4.0}$ [Fg^{-1}]	$\eta_{0.5}$ [%]	$\eta_{4.0}$ [%]	$IR_{drop0.5}$ [Ω]	$IR_{drop4.0}$ [Ω]
			At 25°C				
[N$_{1114}$][NTf$_2$]	200	21.6	11.4	92.9	54.1	780	477
	250	32.1	24.8	96.1	84.2	175	139
	300	30.7	26.0	95.9	83.6	189	137
	350	31.1	27.3	96.5	89.7	111	89
[N$_{2224}$][NTf$_2$]	200	25.0	18.3	95.8	75.7	279	218
	250	24.0	17.7	95.0	74.2	615	219
	300	27.4	22.1	95.8	80.0	166	138
	350	25.3	21.6	96.8	86.2	138	113
[N$_{122(2O1)}$][NTf$_2$]	200	24.0	14.4	93.9	63.7	413	313
	250	28.5	18.5	95.5	75.0	212	175
	300	27.7	23.3	95.7	83.5	157	129
	350	26.6	23.3	96.1	86.1	143	118
			At 40°C				
[N$_{1114}$][NTf$_2$]	200	27.1	11.8	93.3	49.0	891	541
	250	35.4	24.8	94.7	78.2	245	194
	300	33.6	23.7	94.6	79.3	246	194
	350	34.2	26.9	94.9	84.7	160	130
[N$_{2224}$][NTf$_2$]	200	28.8	18.1	95.0	68.8	386	294
	250	28.0	18.5	95.2	77.1	263	195
	300	29.7	20.5	95.0	77.8	221	171
	350	27.3	21.3	95.2	81.9	185	141
[N$_{122(2O1)}$][NTf$_2$]	200	28.4	16.6	92.9	54.4	567	403
	250	28.6	10.4	94.2	57.8	396	321
	300	29.1	18.3	93.2	67.9	339	261
	350	28.3	20.5	94.0	70.8	281	218
			At 60°C				
[N$_{1114}$][NTf$_2$]	200	38.6	12.4	92.8	51.8	843	480
	250	37.7	15.1	91.3	72.2	368	268
	300	36.0	20.8	91.8	68.3	457	341
	350	36.4	15.0	91.6	76.2	295	224
[N$_{2224}$][NTf$_2$]	200	32.2	11.7	93.7	53.6	635	451
	250	29.6	14.4	93.0	70.0	373	267
	300	31.8	17.2	92.8	70.4	323	249
	350	28.0	17.1	92.8	71.1	325	242
[N$_{122(2O1)}$][NTf$_2$]	200	30.5	-	91.9	45.6	613	466
	250	17.6	-	91.2	39.8	798	503
	300	28.7	12.5	89.8	49.4	662	443
	350	30.3	15.4	91.5	57.0	512	377

			At 80°C				
[N$_{1114}$][NTf$_2$]	200	31.6	-	88.8	20.7	1545	767
	250	24.6	7.5	86.1	45.0	864	543
	300	23.6	-	88.0	32.3	2877	694
	350	32.3	12.5	85.8	57.9	621	421
[N$_{2224}$][NTf$_2$]	200	22.8	-	89.6	25.7	1221	678
	250	25.2	9.3	88.7	56.1	593	389
	300	23.4	6.8	88.2	45.3	719	456
	350	26.1	12.4	89.0	64.0	403	278
[N$_{122(2O1)}$][NTf$_2$]	200	13.9	-	83.4	6.1	1533	-
	250	11.0	-	85.5	27.5	1087	628
	300	20.2	-	85.4	25.2	1087	636
	350	25.9	-	87.9	33.7	808	549

6.4.6 EDLC performance – P-based ILs

6.4.6.1 EIS measurements

Finally, the behavior of the produced cells using phosphonium ILs was considered and their response with increase in the temperature was investigated. The selected P-ILs for this study were synthesized and supplied from a partner university at a limited quantity. These ILs contain a relatively larger volume of the [P_{2225}] and [$P_{222(2O1)}$] cation constituents at 359 Å^3 and 313 Å^3, respectively, in comparison with the paired [NTf_2] anionic component at the volume of 248 Å^3,

The produced Nyquist plots for [P_{2225}][NTf_2] and [$P_{222(2O1)}$][NTf_2] ILs paired with controlled porosity ACs at 25°C, 40°C and 60°C operating temperatures and the relative resistances at these temperatures are displayed in Figure 6.19 and Table 6.18, respectively.

From the low frequency region it is seen that, with the exception of AC200 carbon paired with [P_{2225}][NTf_2] and [$P_{222(2O1)}$][NTf_2] ILs at all temperatures, there is a clear consistency or trend between the type of the IL and the angle of the capacitive component of the Nyquist plot at specific temperature operations. For instance, considering AC250-[P_{2225}][NTf_2] and AC250-[$P_{222(2O1)}$][NTf_2] combinations at 25°C where the angle of the capacitive components are determined to be -69.5° and -63.7°, respectively. Hence the former combination is behaving more ideally in comparison to the latter combination. Through increasing the temperature to 40°C and 60°C this trend is maintained for the aforementioned combinations and all other ACs paired with P-ILs, except AC200 where perhaps presence of a greater percentage of microporosity in AC200 compared to the other ACs is favouring the smaller cation, i.e. [$P_{222(2O1)}$][NTf_2], the most. In other words a better degree of coordination is perhaps preserved for AC200-[$P_{222(2O1)}$][NTf_2] combination leading to a higher values of phase angle. It is also evident that wider pore ACs have an increasing effect on the capacitive component of the Nyquist plot especially at 25°C and 40°C operations where the influence of system energy and encountered resistances are less significant.

Additionally the inhomogeneity in the double layer is also confirmed for the P-ILs as the low frequency response tend to deviate further away from the ideal response when temperature rises.

As discussed previously, incorporation of the methoxyethyl linkage into the structure introduces extra flexibility in the structure. As a result [$P_{222(2O1)}$][NTf_2] IL, display better transport properties and conductivities at all temperature operations when comparing this IL with its non-ether constituent, i.e. [P_{2225}][NTf_2]. This is clearly demonstrated through attaining relatively higher solution resistances and lower c_{eis} for [P_{2225}][NTf_2] IL paired with different ACs at varying operating temperatures.

At the same time, inclusion of methoxyethyl into the structure introduces a trade-off with the maximum operating potential range that the IL could remain stable mainly as a result of reduced positive charge density on the central phosphonium atom. Although the operating potential of the [$P_{222(2O1)}$][NTf_2] determined to be relatively lower at 2.7V when compared to the [P_{2225}][NTf_2] IL at 3.4V but marginally higher c_{eis} values were attained for the former IL combined with controlled porosity carbons.

This can be explained through two possibilities. The first possibility is that a very small electronegative region is introduced by the methoxyethyl-incorporated link into the cation structure, due to presence of oxygen in the link, that facilitates a denser packing of the [$P_{222(2O1)}$] cation on the AC surface allowing a greater charge displacement over the electrode surface. Second possibility is that, similar to N-based ILs, a great portion of the available pore volume is not accessible to the [P_{2225}][NTf_2] cation constituent due to the high volume of the cation blocking the pores, meaning that these species are perhaps have minimal or low contribution to the charge storage.

Additionally [P_{2225}][NTf_2]-based combinations are associated with lower ionic and ESR resistances at all temperatures when compared against [$P_{222(2O1)}$][NTf_2] combinations. This trend is in contradiction with the fact that the larger volume cation, i.e. [P_{2225}]$^+$, limits the cation mobility and results in higher induced resistances. At the same time this trend favours the earlier discussed possibility that large cation $[P_{2225}]^+$ have minimal or low contribution towards charge storage when paired with the produced ACs displaying lower ionic and ESR resistances. Hence an AC with a larger pore volume and pore width must be considered to ensure that the aforementioned reasoning holds true for the $[P_{2225}][NTf_2]$ based combinations.

It is worth noting that a clear reduction in solution resistance is established for the AC-$[P_{222(2O1)}][NTf_2]$ combinations in comparison to the AC-$[P_{2225}][NTf_2]$ combinations at a specific temperature operation indicating that ether incorporation into the structure improves the transport properties and lowers the R_s. However no correlation is attained between this resistance and varying the ACs at a specific temperature due to the large volume of both utilized phosphonium cations applying minimum effect on the selected pore mediums.

A reduction in R_s is also observed as a result of reduced viscosity while the operating temperature increases to 40°C and 60°C.

At the same time, it is also evident that with increasing the temperature to 40°C, the calculated c_{eis} values for both IL paired with different ACs increases in comparison to 25°C operation. Though at a further temperature elevation to 60°C, an additional improvement in the value of capacitance is attained for AC-$[P_{2225}][NTf_2]$ combinations while the ether incorporated combinations experiences a marginal reduction in the c_{eis} value and substantial increase in the ionic resistances. The increase in the R_i resistances of the aforementioned combinations could be a result of accumulation of the system energy and possibly the decomposition of the $[P_{222(2O1)}][NTf_2]$ IL and introduction of some degrees of self-discharge in the system. Within the described trends, mostly the ACs with wider pores and higher pore volumes, i.e. AC300 and AC350, provide the highest capacitances.

Table 6.18 EIS characteristics of P-ILs paired with controlled porosity ACs at various temperatures

ILs	AC	C_{eis} $[Fg^{-1}]$	R_s [Ω]	R_i [Ω]	ESR [Ω]	ϕ [°]
			At 25°C			
$[P_{2225}][NTf_2]$	200	14.2	10.7	54.9	43.1	-58.7
	250	12.7	11.1	63.2	42.9	-69.5
	300	16.1	10.7	33.0	32.9	-72.6
	350	18.7	11.7	44.6	38.6	-70.1
$[P_{222(2O1)}][NTf_2]$	200	15.1	6.1	114.2	54.9	-61.8
	250	15.5	6.1	77.8	49.2	-63.7
	300	18.2	6.1	38.7	37.3	-67.9
	350	19.1	5.6	48.6	47.6	-66.0
			At 40°C			
$[P_{2225}][NTf_2]$	200	16.1	6.0	67.3	43.8	-55.2
	250	14.4	6.8	64.4	45.3	-65.6
	300	17.2	6.6	55.9	36.4	-66.3
	350	19.7	6.7	50.7	34.8	-66.4
$[P_{222(2O1)}][NTf_2]$	200	16.6	4.7	99.0	49.9	-63.6
	250	15.8	3.8	102.9	48.4	-56.8
	300	18.3	3.7	68.6	46.4	-58.7
	350	20.0	3.8	67.3	46.3	-60.4
			At 60°C			
$[P_{2225}][NTf_2]$	200	18.8	3.5	68.5	45.9	-49.1
	250	15.1	3.7	86.7	48.6	-58.2
	300	18.1	4.9	77.1	36.0	-61.1
	350	20.1	4.2	85.4	37.4	-58.3
$[P_{222(2O1)}][NTf_2]$	200	16.1	2.6	167.6	46.2	-47.7
	250	14.8	2.7	118.5	48.2	-49.1
	300	16.9	2.4	141.1	46.9	-45.9
	350	19.4	2.3	108.4	47.0	-50.2

Where C_{eis} represents the determined specific capacitance through EIS at 0.01Hz, R_s the solution resistance determined at the intercept of x-axis, R_i ionic resistance determined through fitting various functions, ESR equivalent series resistance determined at 1kHz and ϕ capacitive component of the impedance determined at the low frequency region

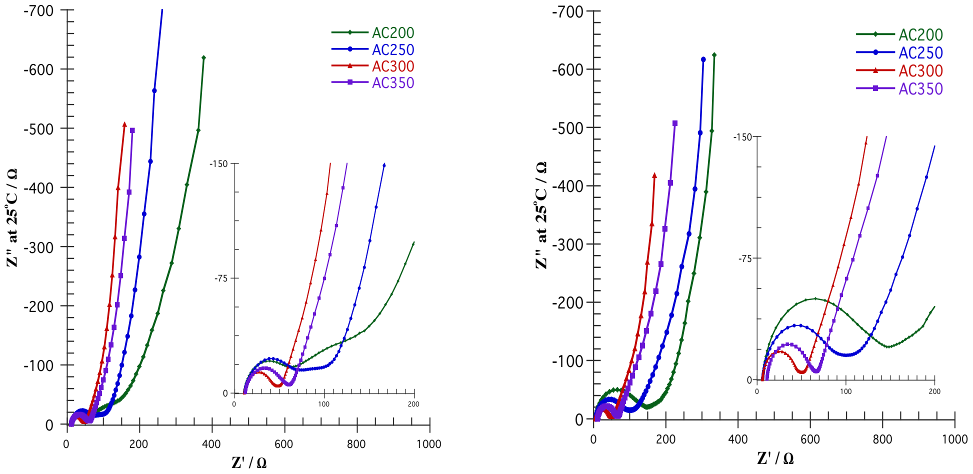

a) $[P_{2225}][NTf_2]$ b) $[P_{222(2O1)}][NTf_2]$

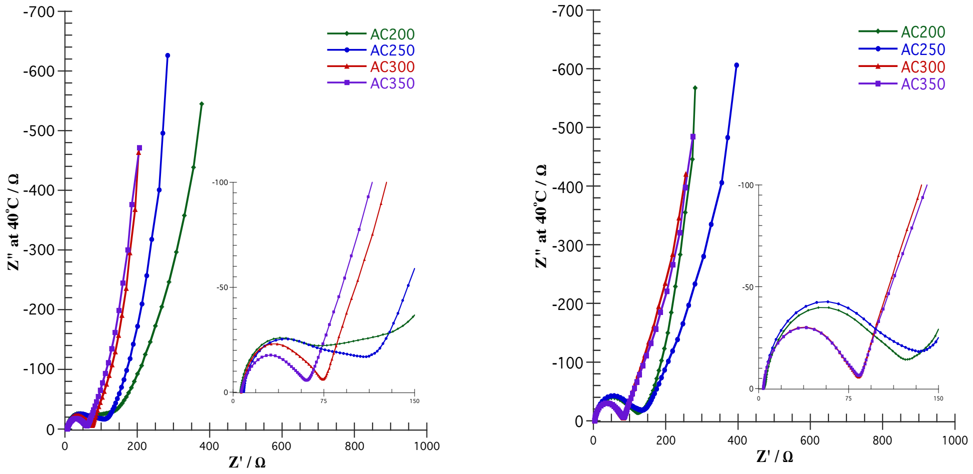

c) $[P_{2225}][NTf_2]$ d) $[P_{222(2O1)}][NTf_2]$

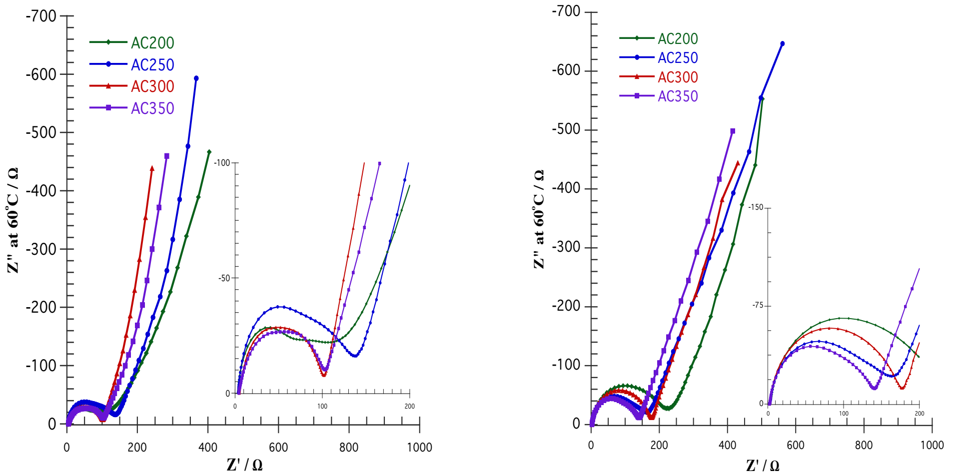

e) $[P_{2225}][NTf_2]$ f) $[P_{222(2O1)}][NTf_2]$

Figure 6.19 EIS plots for a) $[P_{2224}][NTf_2]$, b) $[P_{222(2O1)}][NTf_2]$ at 25°C, c) $[P_{2224}][NTf_2]$, d) $[P_{222(2O1)}][NTf_2]$ at 40°C and e) $[P_{2224}][NTf_2]$, f) $[P_{222(2O1)}][NTf_2]$ at 60°C

6.4.6.2 GC measurements

The influence of temperature elevation on the $[P_{2225}][NTf_2]$ and $[P_{222(2O1)}][NTf_2]$ containing cells paired with controlled porosity carbon was also studied using the GC method.

Figure **6.20** illustrates and compares the electrochemical performance of these P-IL cells at the operating temperatures of 25°C, 40°C, 60°C and 80°C. Table 6.19 summarizes the calculated specific capacitances, efficiencies and IR drop resistances at the discharge rates of 0.5 and 4.0 mA at the stated operating temperatures.

Unlike the attained capacitances from the EIS method, where a marginally higher c_{eis} values were recorded for $[P_{222(2O1)}][NTf_2]$ containing cells at 25°C and 40°C, AC-$[P_{2225}][NTf_2]$ combinations display a reasonably higher $c_{0.5}$ and $c_{4.0}$ values at all operating temperatures in comparison to AC-$[P_{222(2O1)}][NTf_2]$ combinations when using the GC method. The discrepancy in the trends here is mainly due to the selection of 0.01Hz frequency in determining the c_{eis} values, which may classify as slightly high when dealing with high surface area carbons. Additionally the variation in micro and mesoporosity in each of the produced ACs in this study is only varying slightly with increasing the RC ratio of each AC. This means that there are no substantial variations in the pore characteristics. Accordingly the inconsistency in the capacitance trends is more logical especially at high temperature operations when the system energy is increasing and self-discharge processes are encouraged as a result of resistances accumulation. Additionally, the operating potential of the $[P_{2225}][NTf_2]$ IL is higher than the $[P_{222(2O1)}][NTf_2]$ IL indicating that more charge can be displaced on the surface providing higher capacitances.

In spite the provision of higher capacitances for cells containing $[P_{2225}][NTf_2]$ IL, notably higher capacitances at low discharge density of 0.5 mA are also attained in comparison to a higher discharge density, i.e. of 4.0 mA. This is mainly attributed to the fact that at low charge density, a longer period of time is required to charge up the cell to its corresponding operating potential than when utilizing a higher charging current. As a result, longer charging times assist a more efficient ion transfer and charge distribution in a greater fraction of the available pore volume.

Within this trend it is also evident that there are no consistent correlation between the attained $c_{0.5}$ and $c_{4.0}$ capacitances and increase in the pore width at different temperatures. Although there are no consistency but as supported from the EIS data wider pores ACs provide higher $c_{0.5}$ and $c_{4.0}$ capacitances for most P-IL combinations in comparison to narrower pores ACs, i.e. AC200 and AC250, at all operating temperatures. Association of higher efficiencies and lower IR drops with wider pore ACs, i.e. AC300 and AC350, at all operating temperatures also supports these findings.

According to the tabulated data, the calculated capacitance values at the low discharge density of 0.5 mA for both $[P_{2225}][NTf_2]$ and $[P_{222(2O1)}][NTf_2]$ ILs combined with different ACs are improving as the operation temperature increases to 40°C. This trend is mainly accredited to the enhanced transport and electronic properties of both ILs with temperature.

Through a further increase in temperature to 60°C and 80°C, it is seen that $c_{0.5}$ capacitance still improving for AC-$[P_{2225}][NTf_2]$ combinations whereas a marginal variation in this value is experienced for ether incorporated AC-$[P_{222(2O1)}][NTf_2]$ combinations at 60°C followed by a substantial decay at 80°C operation where the system energy increasing and the IR drop is shooting up massively.

As observed from

Figure 6.20 at high temperature operations especially 60°C and 80°C, the AC-$[P_{2225}][NTf_2]$ combinations remain stable at higher charge densities in comparison to AC-$[P_{222(2O1)}][NTf_2]$ combinations with little variation in the IR drops at different current densities with temperature. This finding is supported by the EIS measurements which could again be linked to the original discussion point about larger cations having minimum contribution to charge storage meaning that even the largest studied pore volume, i.e. AC350, is characterized as too narrow for this IL.

Similar to the previously studied IL systems, the attained efficiencies are noticeably lower than anticipated for EDLC systems, that is >98%. As described in section 6.4.3, this is mainly due to the experimental procedure defect as a 20 seconds potentiostatic step was applied at the fully charged state to assist the ions to arrange themselves inside the porous medium in order to minimize the effect of self-discharge processes. Hence extra charge was added at this stage to compensate for the potential decay and maintain the cell at the fully charged state. Accordingly when discharge current density increases, this current becomes more influencing, as less time is available to the ions to place themselves inside the pores while charging the cell. It is worth noting that again a correction for this current is not possible due to the data collection limitations. Accordingly the determined efficiencies at various charging rates cannot be a real measure of this quantity.

Also a major variation is observed between the efficiencies determined at 0.5 mA and 4.0 mA current densities at every operating temperature, which increases substantially as the temperature rises. Since a constant current charging is utilized, at high charging rates the cell charges up to the maximum operating potential of the IL much quicker in comparison to lower charging currents. Therefore the ion transfer takes place over a shorter time scale leading to uneven or incomplete ion displacement over a given surface area. In other words a fraction of pores do not participate towards charge storage, as some of the smaller pores may remain uninfluenced by the applied charging current.

With respect to the variation as a result of temperature elevation, a bigger voltage drops is experienced which according to the Ohm’s law resulting in bigger IR drop readings even at smaller charging currents in comparison to the previous temperature run.

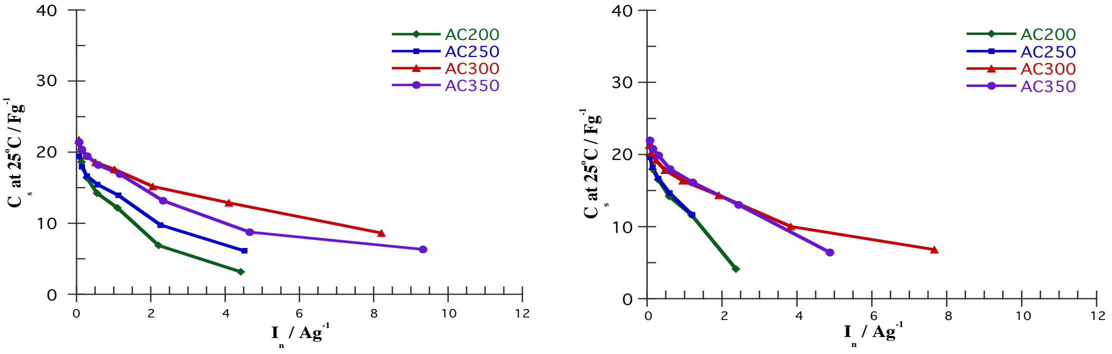

a) [P_{2225}][NTf_2] b) [$P_{222(2O1)}$][NTf_2]

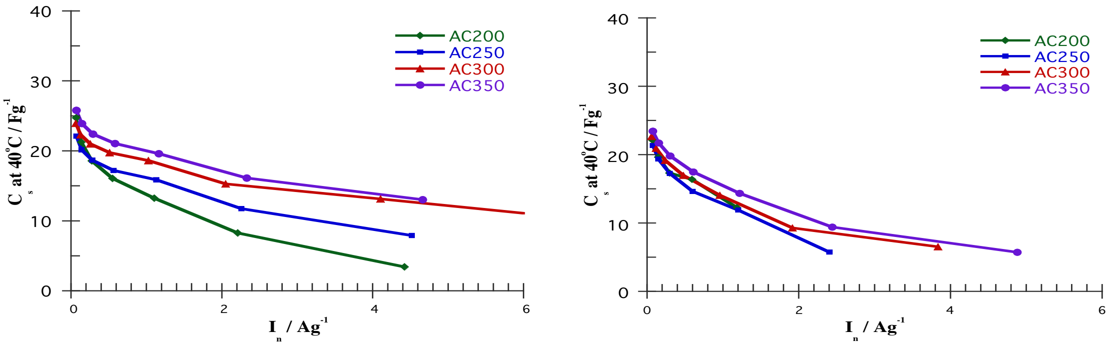

c) [P_{2225}][NTf_2] d) [$P_{222(2O1)}$][NTf_2]

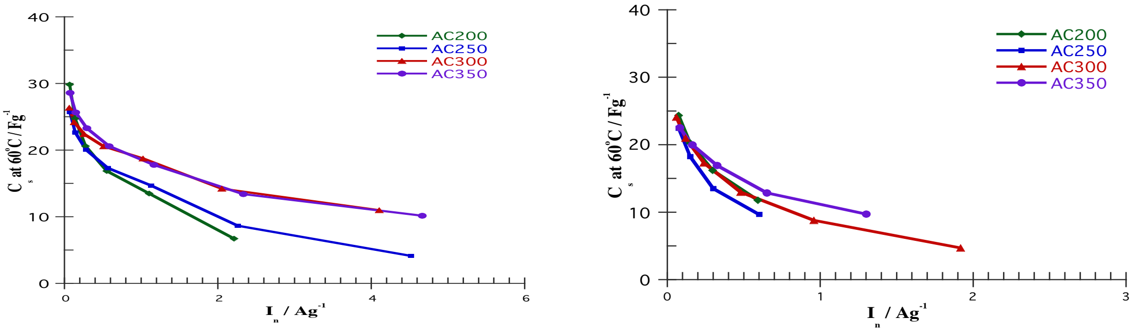

e) [P_{2225}][NTf_2] f) [$P_{222(2O1)}$][NTf_2]

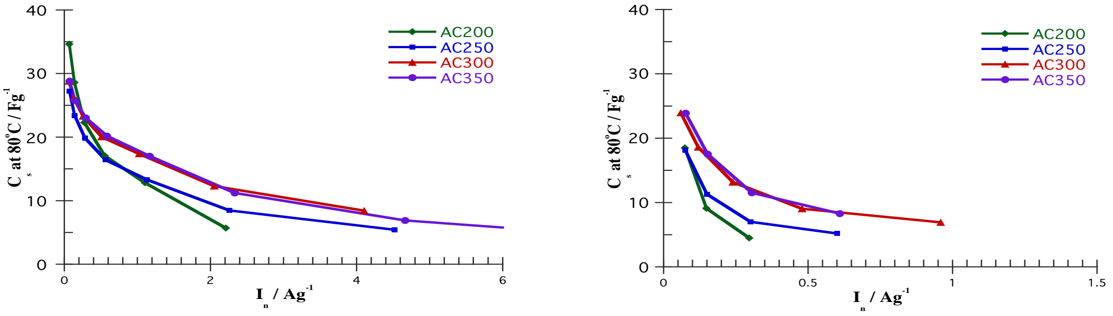

g) [P_{2225}][NTf_2] h) [$P_{222(2O1)}$][NTf_2]

Figure 6.20 Variation of specific capacitance with current density for a) [P_{2225}][NTf_2], b) [$P_{222(2O1)}$][NTf_2] at 25°C, c) [P_{2225}][NTf_2], d) [$P_{222(2O1)}$][NTf_2] at 40°C, e) [P_{2225}][NTf_2], f) [$P_{222(2O1)}$][NTf_2] at 60°C and g) [P_{2225}][NTf_2], h) [$P_{222(2O1)}$][NTf_2] at 80°C

Table 6.19 GC characteristics of P-ILs paired with controlled porosity ACs at various temperatures

ILs	AC	$c_{0.5}$ [Fg^{-1}]	$c_{4.0}$ [Fg^{-1}]	$\eta_{0.5}$ [%]	$\eta_{4.0}$ [%]	$IR_{drop0.5}$ [Ω]	$IR_{drop4.0}$ [Ω]
At 25°C							
$[P_{2225}][NTf_2]$	200	18.6	12.2	94.4	83.2	369	312
	250	18.2	13.9	94.9	86.7	279	237
	300	20.5	17.6	95.7	91.2	161	136
	350	20.9	16.9	95.8	89.9	177	156
$[P_{222(2O1)}][NTf_2]$	200	18.0	11.6	93.7	61.0	400	303
	250	18.2	11.7	94.2	65.4	295	245
	300	20.3	16.4	96.2	81.2	150	127
	350	20.8	16.1	95.1	77.3	179	154
At 40°C							
$[P_{2225}][NTf_2]$	200	21.2	13.2	93.4	70.1	390	283
	250	20.2	15.9	93.8	77.5	276	213
	300	22.3	18.6	94.1	83.9	181	135
	350	23.9	19.6	94.4	81.6	193	148
$[P_{222(2O1)}][NTf_2]$	200	19.6	12.3	93.1	57.9	464	333
	250	19.4	11.9	93.4	61.0	337	274
	300	20.9	14.1	95.1	74.3	208	173
	350	21.7	14.4	94.0	70.6	236	197
At 60°C							
$[P_{2225}][NTf_2]$	200	24.7	13.5	90.9	64.5	553	353
	250	22.7	14.7	90.2	68.4	432	304
	300	24.2	18.7	89.6	79.0	260	184
	350	25.7	19.8	90.8	75.3	324	227
$[P_{222(2O1)}][NTf_2]$	200	20.3	-	91.5	37.7	708	486
	250	18.2	-	91.3	44.4	575	410
	300	21.0	8.8	93.1	57.5	387	299
	350	21.5	9.1	91.5	49.0	513	378
At 80°C							
$[P_{2225}][NTf_2]$	200	28.6	12.8	88.6	60.9	672	384
	250	23.4	13.3	84.0	67.0	417	289
	300	26.2	17.4	84.0	73.5	359	246
	350	25.8	17.0	85.1	70.7	450	284
$[P_{222(2O1)}][NTf_2]$	200	9.1	-	84.5	5.7	1434	-
	250	11.3	-	86.7	33.1	800	513
	300	18.6	6.9	91.2	50.4	486	355
	350	17.5	-	88.7	36.8	695	471

6.4.7 EDLC performance: A comparison

In order to make relatively easy comparisons between different ILs at varying operating temperatures, the best performing AC is selected at 25°C. The selected best forming combinations were then investigated at higher temperatures. As discussed previously the widest pore AC350 provides the highest GC performance with increase in the discharge density along with higher cycle efficiencies and lower IR drops when paired with all the utilized ILs, except [Pyr$_{14}$][NTf$_2$] and [S$_{221}$][NTf$_2$] ILs where AC300 is shown to provide the aforementioned characteristics in place of the AC350 mostly due to the cation orientation and the size of these ILs.

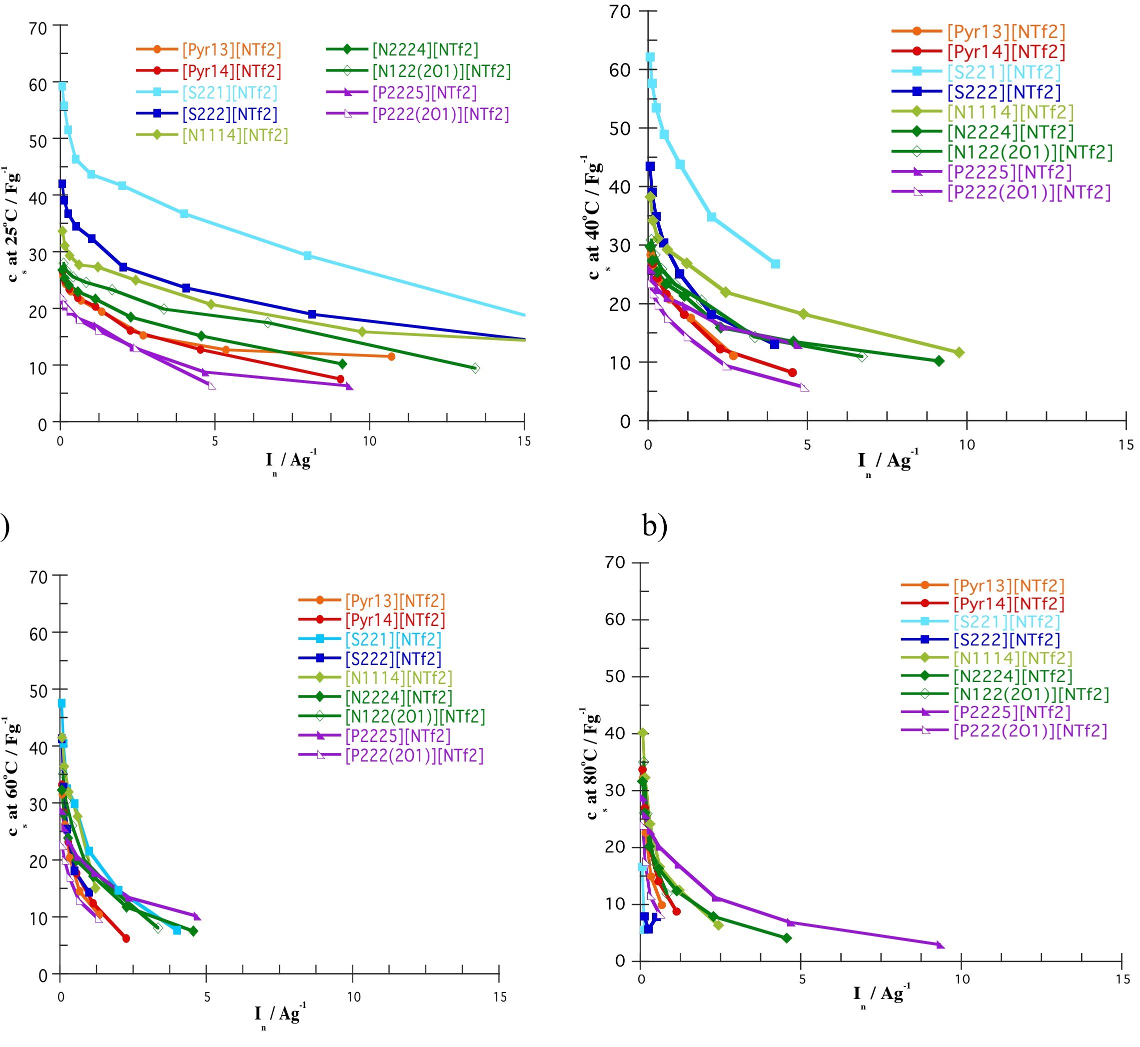

a)

b)

c)

d)

Figure 6.21 Specific capacitance variation of all utilized ILs with current density at a) 25°C, b) 40°C, c) 60°C and d) 80°C

Figure 6.21 compares the best performing ACs paired with each of the ILs at varying temperatures. At 25°C operation a clear performance deterioration is exhibited with increasing the charge densities for the utilized electrolytes in the order of S-ILs > N-ILs > Pyr-ILs > P-ILs, respectively.

This trend is most anticipated for the S-ILs where highest transport and electronic properties are determined for this IL at all temperatures.

Although there are no common agreement about the credibility of specific capacitances through experimental data, but some of the similar experimental settings were selected and presented here for comparison purposes.

In a similar study at normal operation conditions, $[S_{221}][NTf_2]$ and $[S_{222}][NTf_2]$ ILs were utilized with an activated microporous carbon electrode with surface area of 2120 m^2 g^{-1}. It was observed that $[S_{221}][NTf_2]$ IL also results in greater specific capacitances than $[S_{222}][NTf_2]$ IL at all charging rates. However a relatively lower specific capacitances of 22.0 Fg^{-1} and 9.7 Fg^{-1} were reported for $[S_{221}][NTf_2]$ and $[S_{222}][NTf_2]$, respectively [186] in comparison to the most microporous AC200 utilized in the current study (with much lower surface area of 670 m^2 g^{-1}) paired with the same ILs, i.e. 36.4 Fg^{-1} and 29.7 Fg^{-1}. This variation in attained specific capacitances with literature mainly caused by the choice of microporous carbon electrodes providing narrow pathways for ion migration.

In another study on a different sulfonium based ionic liquid, i.e. $[S_{111}][NTf_2]$, with a microporous carbon electrode, it was found that despite the relatively high melting temperature of 45.5°C, a reasonably high specific capacitance of 140 Fg^{-1} was attained at 50°C [205]. The smaller cation size of this electrolyte allows for easier ion migration at the microporous medium and therefore greater packing density of ions at the electrodes pores surfaces. Hence depending on the operation temperature, a careful selection of the pore medium must be considered.

There are other studies about optimizing the specific capacitance claiming that lower pore volumes and higher surface area are only achievable through the use of microporosity [65, 77, 79, 206-208]. This holds true for scenarios where low current densities of 0.1- 3 Fg^{-1} were used. It is also worth noting that variation of specific capacitances with a range of current densities was not reported. Accordingly any possible limitation due to slow mass transfer in micropores would not be apparent. In other words, the small micropores that cause ion distortion or distortion may not necessarily allow for charge and discharge at higher rates [207].

The non-ether N-based constituents are shown to display higher viscosities and lower conductivities compared to the Pyr-ILs while still providing higher performance. As discussed before, ammonium based constituents are seen to provide higher cathodic stabilities towards reduction than the aromatic Pyr-ILs. This is mainly dedicated to the low energy level of LUMO orbital of aromatic pyrrolidinium cations making these ILs more vulnerable towards reductions [209-211]. The susceptibility of these ILs with reduction, reduces the maximum operating potential at which the IL remain stable, hence a lower performance is observed in comparison to N-ILs.

A study on $[Pyr_{14}][NTf_2]$ IL based supercapacitors, containing composite electrodes with >2000 m^2 g^{-1} surface area, reveals a stable GC charge-discharge behaviour of over 16,000 cycles with average specific capacitance of 50 and 100 Fg^{-1} at the operating temperature of 60°C [212]. However these capacitances are reported for a very low charging rate of 10 mA cm^{-2} for charging between 1.5 V and 3.6 V and no information on other charging rates are provided. In another study performed by Rennie and colleagues [177] on the same electrolyte but combined with a mesoporous carbon electrode containing surface area of 1270 m^2 g^{-1} and average pore size of 7 nm, a specific capacitance values in the range of about 80- 90 Fg^{-1} of active material was reported for 0.1- 30 Ag^{-1} discharge currents at room temperature [177]. This value is of course about 3x higher than the attained values in the current work for the selected IL, i.e. 25 Fg^{-1}, considering that the carbon producing this capacitance has also contain an average pore width of 7.5 nm. This variation in capacitance can be dedicated to the much lower surface area of 790 m^2g^{-1} of this carbon in as well as not utilizing carbon black as conductivity enhancer.

The least performance at 25°C operation is observed for P-based ILs with marginal variation between the utilized ILs in this category. Although ether-bond

incorporation into the $[P_{222(2O1)}][NTf_2]$ IL improves the transport and electronic properties by almost two fold, but both P-based cations contain relatively large cation volumes. In fact the largest calculated cation volumes belongs to P-ILs indicating that these cations are perhaps not completely displaced in the given provided pore volume, therefore having minimum contribution to charge storage.
In the same study carried by Rennie and colleagues [177], the same phosphonium based liquids, i.e. $[P_{2225}][NTf_2]$ and $[P_{222(2O1)}][NTf_2]$ ILs, were also used in combination with the mesoporous electrodes with surface area of 1270 m^2 g^{-1} and average pore size of 7 nm. About 50 F g^{-1} increase was reported for the specific capacitance attained by $[P_{222(2O1)}][NTf_2]$ IL, i.e. 82.7 F g^{-1}, in comparison to $[P_{2225}][NTf_2]$ incorporated cell comprising only 30.5 F g^{-1}. This is indicative of the fact that best performing carbon electrode in the current work, i.e. AC350 with surface area of 790 m^2 g^{-1} and average pore size of 7.5 nm, is yet too narrow for both phosphonium liquids in order to reach the full potential of the ILs in terms of specific capacitance. In fact the marginal increase in capacitance between $[P_{2225}][NTf_2]$ incorporated cells of current work and this literature study is a further indication that a carbon electrode with much higher surface area than 1270 m^2 g^{-1} and possibly higher average pore size of 7 nm must be explored.

As a comparison, there are various conductivities reported in literature for a commonly used organic electrolyte of tetraalkyl ammonium salt in propylene carbonate ($TEABF_4$ in PC) depending on the molar concentration. For instance conductivities of 10.6 mS/cm and 8.3 mS/cm are reported for 0.65M and 0.5M solutions, respectively. Comparatively for a 1M solution of this electrolyte a value of 13 mS/cm is reported. Propylene carbonate contains a very large dielectric constant (ε= 64) and therefore a high value of viscosity leading to detrimental effects on ions migration and charge storage especially with mesoporous electrodes. When this electrolyte is paired with an activated carbon, a capacitance of 29 Fg^{-1} is attained at Galvanostatic charging at the rate of 5 mA/cm^2 [213]. It is worth noting that there is no detailed information provided on the carbon characteristics or about the normalization method of the capacitance.

Regardless of the nature and physiochemical properties of the ILs, it is evident that at 25°C operation most combinations allow for charging beyond 8 Ag^{-1} where then a dramatic fall is experienced as the temperature rises.

In fact with increase in temperature, the orderly decay of performance disappears as result of an increase in the system energy. At the same time a marginal increase in capacitance is observed for all combinations as a result of improved transport and electrical properties. On a molecular level, this observation could also be linked to chain untangling at 40°C and results in slightly better performance, which then with further temperature increase to 60°C and 80°C resistances are building up due to the considerations in selecting the operating potentials of the ILs. Accumulation of resistances with temperature reduces the potential range at which the IL remains stable. As discussed previously although a relatively conservative operating potential was selected at 25°C for use at all temperatures with the aim to be applied to all operating temperature runs but this selection is most likely causing the decomposition of some of the ILs containing small cations fallowed by short circuiting and dramatic capacitance loss at high temperatures, e.g. S-ILs.

The effect of temperature on the double layer properties was reflected by large number of experimental [147, 214-219] and simulation works [220-223]. However there are no commonly accepted opinion or a general rule about this.

Among these experimental studies, a positive dependency of capacitance with temperature was attained for different electrodes [81, 146, 147, 215, 216, 218, 219] which was supported but simulation works [221, 222] where the interface of an imidazolium based liquid and graphite was modelled at 27- 127°C temperature range.

At the same time, there are other experimental studies reporting a negative dependency of capacitance with temperature [214, 223-225] similar to the observation in the current study. For instance, Druschler and colleague [214] recently reported a substantial decay in capacitance for an extremely pure $[Pyr_{14}][FAP]$ electrolyte with Au(111) electrode when temperature rises from 30°C to 90°C. In another study the temperature dependence of multi-layering at the free surface of a phosphonium based liquids (trihexyltetradecylphosphonium bis(nonafluorobutanesulfonyl)imide) was investigated and shown to possess negative dependency [224]. However in a further attempt on a different liquid (trioctylmethylammonium bis(nonafluorobutanesulfonyl)imide) a small increase was observed with temperature indicating that the capacitance dependence on temperature is strongly influenced by the molecular structure. The negative dependence of capacitance on temperature was also supported by simulation studies [223] where a combination of $[Pyr_{14}][Tf_2N]$ IL with graphite electrode was studied. The negative dependency was explained through melting of the double layer at neutral graphite interface at elevated temperatures [225]

6.5 Variation of performance with pore characteristics

6.5.1 Capacitance VS surface area

According to the traditional capacitor theory described in section 2.1, the obtained capacitance of the produced cells should display a linear proportionality with increase in the surface area of the carbons if the thickness of the double layer remains constant. As described earlier, with increasing the R/C ratio the BET surface area increases and according to its linear relationship with capacitance, the capacitance is anticipated to follow an increasing trend. However as seen previously and illustrated in Figure 6.22, variation of specific capacitance with the BET surface area of the utilized ACs does not follow the traditional capacitor theory, i.e. the anticipated trend did not emerge. It is worth noting that the traditional capacitor theory is used to describe the interactions from the planar electrode and the electrolyte. Hence it is explicable when fails as dealing with a 3D net of porosity that are interconnected.

Additionally, the traditional capacitor theory assumes that the thickness of the double layer is constant which may not hold valid for bimodal pore samples where the right size pores for the ions create a smaller double layer thickness in comparison to the smaller pores that remain vacant.

The contradiction here can also be explained through the work of Huang and colleagues where a theoretical model is developed to investigate the deviation from the traditional theory by realizing the effect of pore curvature. The model utilizes a selective experimental data from other investigations involving micropore and mesopore carbons and concludes that the traditional model only holds for the macroporous carbons with the pore diameter exceeding 50 nm where the effect of pore curvature is insignificant.

They also proposed new models for carbons with microprosity and mesoporosity distinctively. However these models assume a unimodal pore distribution and cylindrical shape pores, which do not hold valid for the utilized bimodal ACs used in this study containing both microprosity and mesoporosity. Hence this accounts for the deviation from the anticipated linear relation.

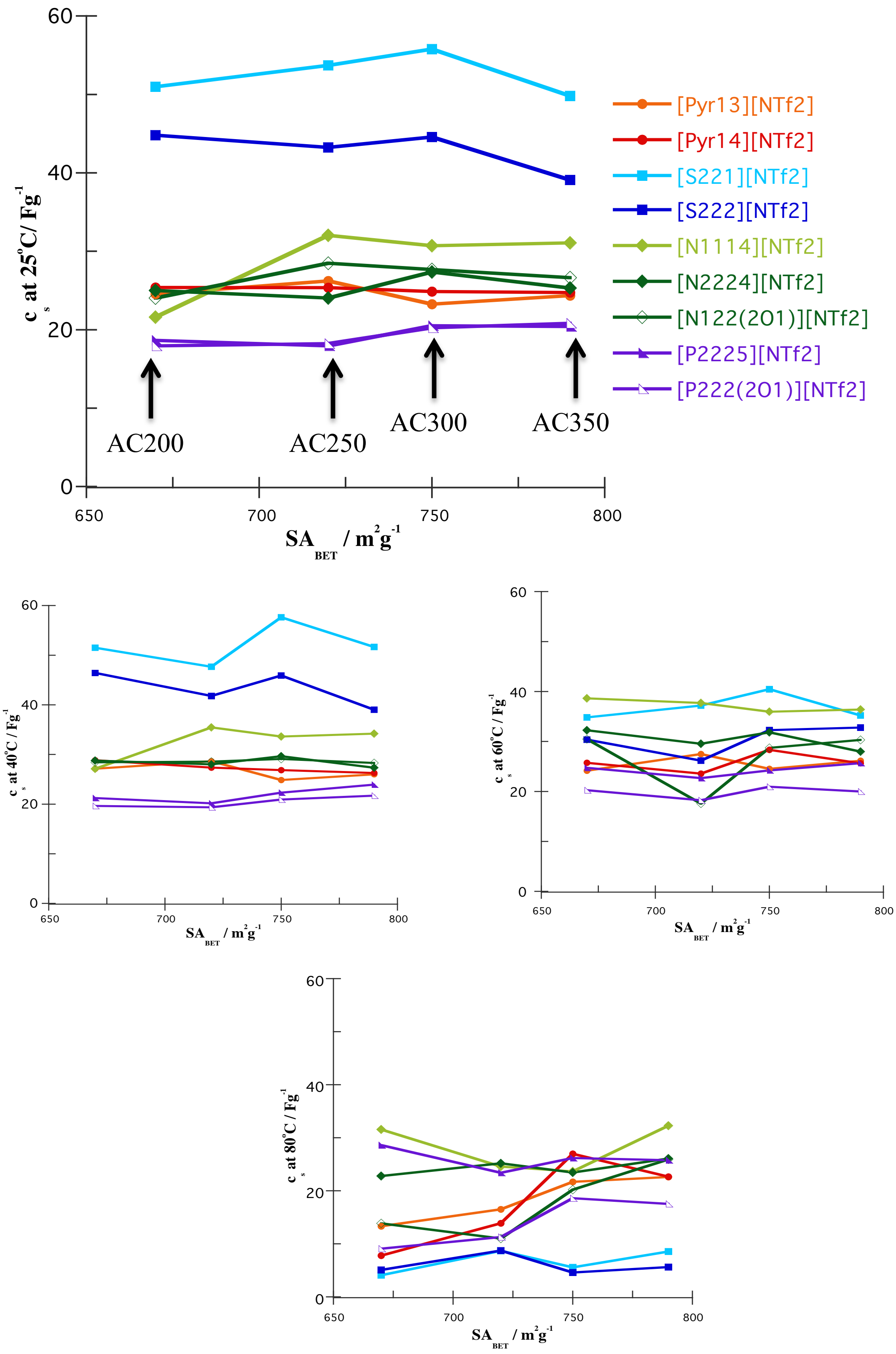

Figure 6.22 Variation of specific capacitance with BET surface area

6.5.2 Capacitance VS pore size

Optimization of the pore size distribution is an important consideration to improve the EDLC performance as this characteristic of the carbon is directly related to the accessible surface for formation of the double layer. Studies on carbon microprosity indicate that ILs are generally considered as too viscous to enter into these pores whereas other studies indicate that microprosity is important to maximize the capacitance. On the other side are studies focused on mesoporosity indicating that such pores are important in provision of wider pathways for ion transfer into smaller pores, hence reducing the resistance and increasing the accessible surface area at the same time by allowing ion diffusion into smaller pores. It is also assumed that increasing the pore size would have an increasing effect on the performance, as wider pathways are available ion transfer, if surface area remains unchanged.

As shown in section 6.1, produced AC200, AC250, AC300 and AC350 carbons exhibiting 43%, 41%, 37% and 35% microporosity. Since these carbons are bimodal and no macroporosity behaviour is exhibited from the adsorption and desorption profiles, then the remainder must be mesoporosity. Although variation of mesoporosity are only 8% apart between the most and least mesoporous carbons, i.e. AC200 and AC350, but as observed for most combinations this small increase resulted in an improvement in capacitance.

Figure 6.23 illustrates the variation of capacitance with increasing the pore size distribution of the ACs at various operating temperature where clear increase in the value of normalized capacitance is observed with AC350 standing the highest. However the highest capacitance for $[S_{221}][NTf_2]$ and $[Pyr_{14}][NTf_2]$ ILs are shown to occur when these ILs are combined with AC300 due to the smaller cation size of the former IL and better coordination of the latter with this carbon. Additionally a decrease in the normalized capacitance value is observed at AC250 in combination with $[S_{222}][NTf_2]$, $[N_{2224}][NTf_2]$ and $[Pyr_{14}][NTf_2]$ ILs, which is mainly caused by the selection of this value at the high charging current of 4.0 mA. This decay is then disappears through charging at higher current densities.

Accordingly the earlier assumption about provision of wider ion transfer pathways due to presence of greater percentage of mesoporosity from AC200 to

AC350 fits well with the findings here. It is worth noting that the BET surface area is also increasing in the order of 670, 720, 750 and 790 m^2g^{-1} for AC200, AC250, AC300 and AC350 carbons, respectively. This indicates that not only wider pathways are available for ion diffusion but also at the same time a greater surface for double layer formation is present, hence these properties are interlinked.

In other words AC300 paired with $[S_{221}][NTf_2]$ and $[Pyr_{14}][NTf_2]$ ILs and AC350 combined with all other ILs provide the optimum capacitance performance indicating that a greater percentage of the surface area and available porosity are being utilized for double layer formation. In the case $[S_{221}][NTf_2]$ IL, AC250 and AC350 exhibit lower performance than the optimum recorded as a result of provision of too narrow pore width from the AC250 with lower surface area than required for optimum performance, which is logical, and too much void volume resulting in excess electrolyte entering the pores of AC350 encouraging pore flooding or ion pairing. Pore flooding in turn may result in ion pairing where the anion-cation interactions are stronger than interaction of the species with the pore wall for double layer formation resulting in presence of greater concentration of neutral anion-cation pairs in the pores. As discussed, pore flooding can also lead to a situation where the non-adsorbed ions are constantly competing with the adsorbed species to participate in the double layer and charge storage. Hence the strength of the double layer is reduced. In terms of the overall cell performance, both conditions result in reduced performance indicating that there must be an optimum carbon with specific characteristics for every IL. A further observation of this occurs in AC250-$[N_{1114}][NTf_2]$ combination where a major increase in performance is obtained in comparison to AC200 paired with the same IL with only a 0.8 nm increase in the pore size distribution.

However for every other investigated ILs in this study, this optimum performance occurred at the widest pore AC, i.e. AC350. Hence it is desirable to explore wider pore ACs in order to test whether the optimum performance is occurring at AC350 or at a wider pore AC than this carbon.

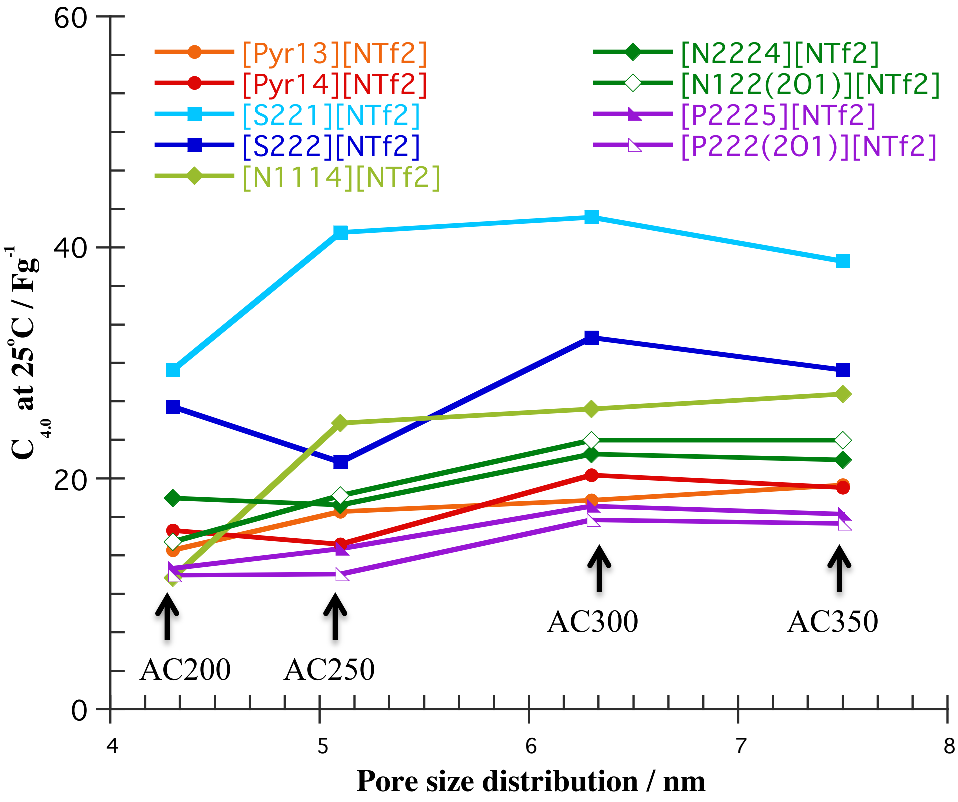

Figure 6.23 Variation of normalized capacitance with average pore size distribution

6.6 Variation of performance with IL characteristics

Figure 6.24 and Figure 6.25 illustrate the variation of capacitance with the viscosity and conductivity, respectively, at 25°C.

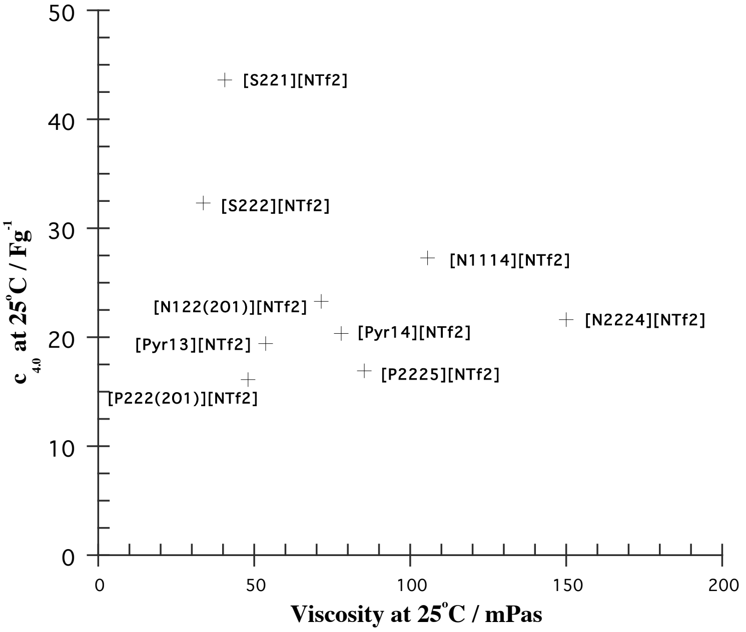

Figure 6.24 Variation of normalized capacitance with IL viscosity

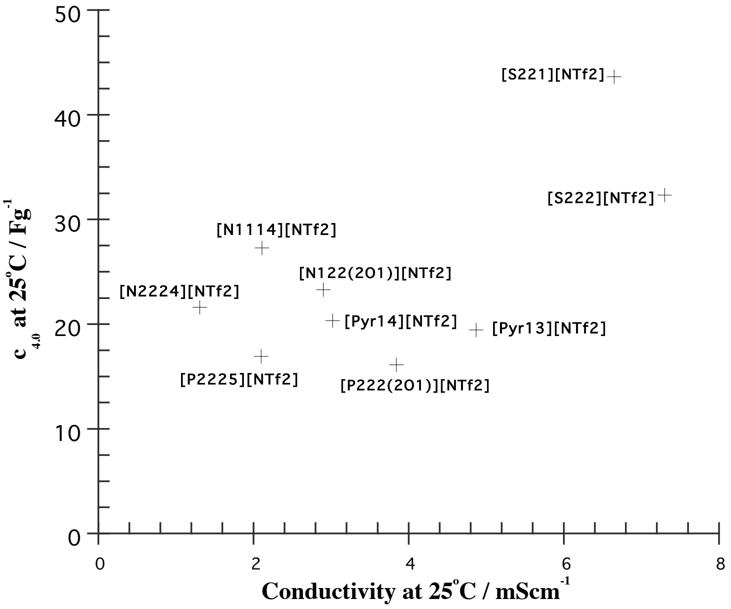

Figure 6.25 Variation of capacitance with IL conductivity

From these figures it can be seen that, S-based ILs are the least viscous and most conductive liquids among the utilized electrolytes in this study and are producing the highest capacitances. Although the effect of reduced viscosity and higher conductivity is clearly demonstrated on the performance of the S-ILs but this trend cannot be generalized and assumed to have the same effect on other classes of electrolytes of the similar viscosity but with different central atoms. For example the least viscosity after S-ILs is displayed for ether incorporated $[P_{222(2O1)}][NTf_2]$ electrolyte at 25°C. However the conductivity of this IL is not laying in the same order after S-ILs, but close enough to characterize it as a relatively good conducting IL. However when the $[P_{222(2O1)}][NTf_2]$ IL used in an EDLC configuration it produces a much lower capacitance in comparison to the S-ILs considering the operating potentials are relatively similar with 0.1 V difference. Theoretically the charge displacement for double layer formation for both cases must be similar, hence another factor must influence the reduced capacitance of this combination in comparison to S-ILs. As discussed earlier, $[P_{222(2O1)}][NTf_2]$ IL comprised of a second largest cation constituent among the other ILs. This property of the $[P_{222(2O1)}][NTf_2]$ IL is most likely blocking the ion transfer pathways and pores limiting the cation access to a great percentage of the pore volume for double layer formation. As a consequence a significant reduction in capacitance is observed. In other words viscosity and conductivity are not the sole determinant or influencing factors in achieving high capacitances.

Variation of capacitance with different cation volumes is shown in Figure 6.26. According to this plot a clear descending trend is observed for capacitance when comparing the ILs comprised of the smallest and largest cation volumes together, i.e. S-ILs and P-ILs respectively. These findings for the two extreme cation volumes, obeys a study performed by Ania *et al.* [77] on four different ionic liquids containing various cation constituent sizes ranging from 0.8 to 2 nm paired with a 80% microporous carbon sample. They confirmed a linear relation between the pore size distribution and size of the ions.

Since all the utilized ILs in the following figure are paired with a best performing AC, that is AC300 and AC350, therefore the available pore volume for ion transfer and cation access is fixed. Moreover all utilized ILs in this study comprised of the same anion constituent indicating that there is a possibility that the same fraction of pores is being utilized for double layer formation with the anion. Hence the determinant factor for identifying the accessible pore volume for ion transfer must be influenced by the cations dimensions or volumes.

Additionally [P_{2225}][NTf_2] IL display a substantially higher operating potential at 3.4 V in comparison to [$P_{222(2O1)}$][NTf_2] IL and S-ILs when considering the two extreme classes of ILs containing the largest and smallest cations. However due to the large volume of this cation the entire pore area is not participating in charge storage hindering the output capacitance. However as the volume of the cation is decreasing better capacitances are attained but the trend with the cation volume no longer exists. Pyr-ILs are unpredictably seen to produce the lowest capacitances at the specified discharge density after P-ILs as the associated cation volumes are relatively small and display reasonably good transport properties, comparable to S-ILs. This is mainly attributed to the strong cation-anion interactions of Pyr-IL constituents as a result of stronger charge located on the N-atom hindering the output capacitance.

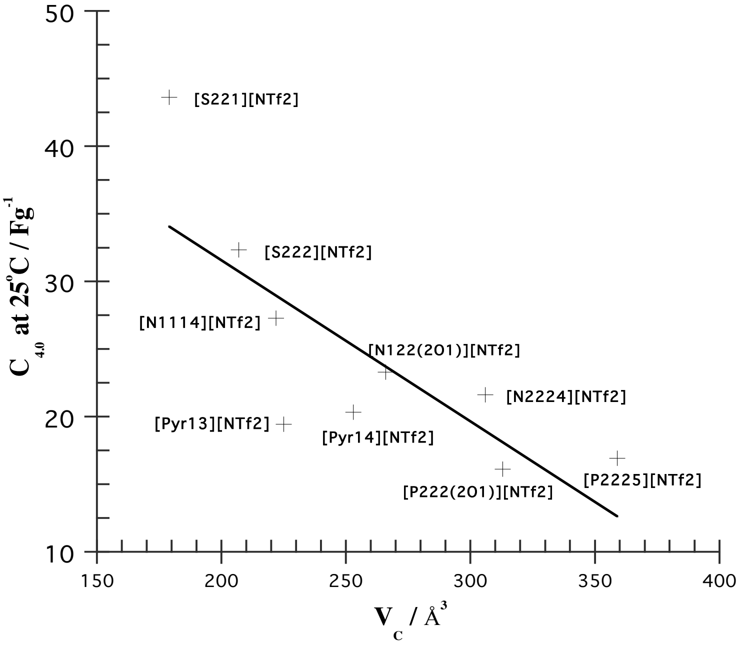

Figure 6.26 Variation of capacitance with cation volume

6.7 Specific energy and specific power

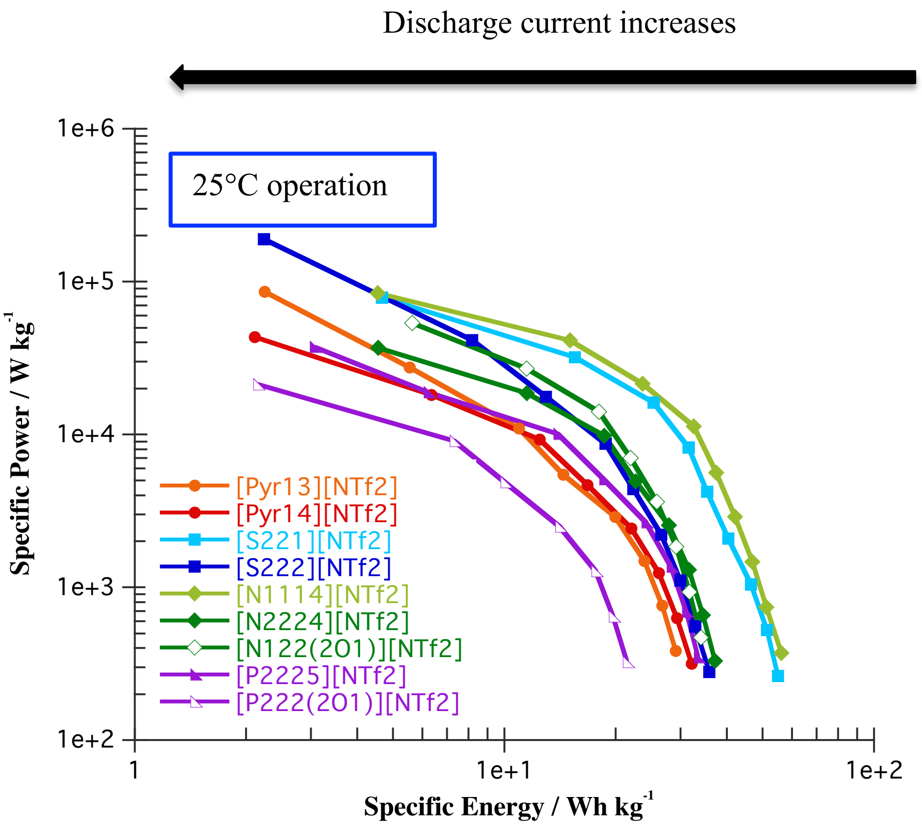

(a)

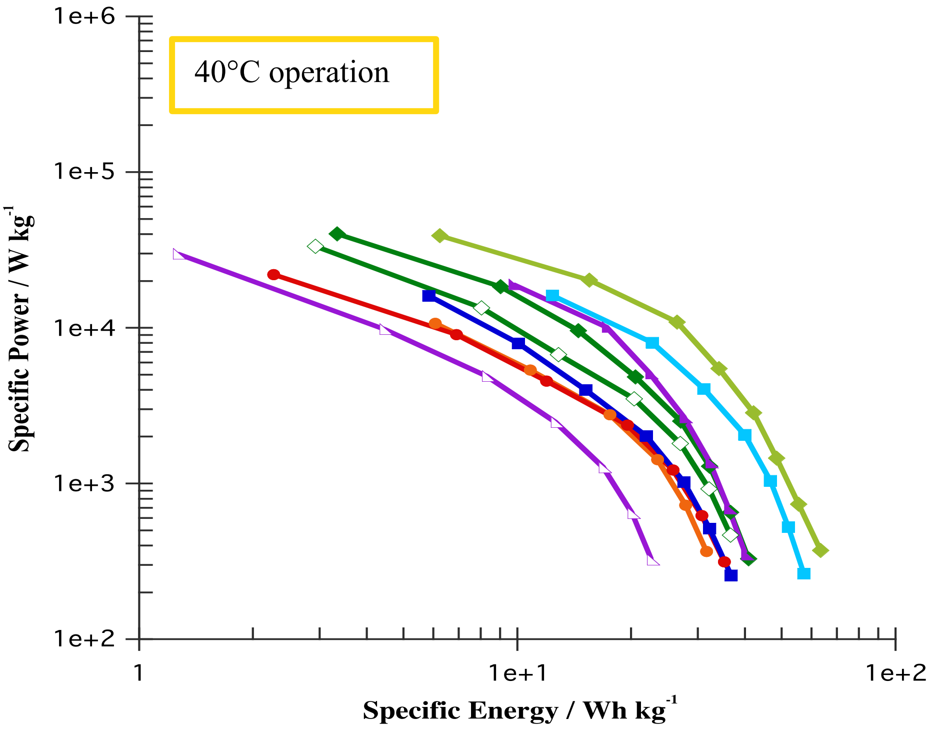

(b)

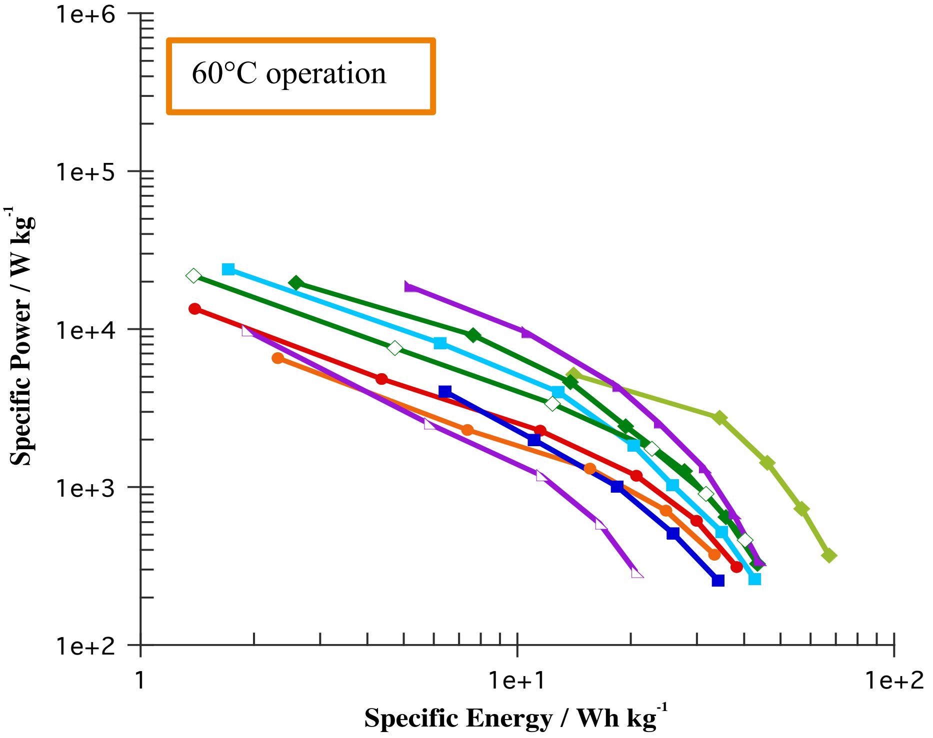

(c)

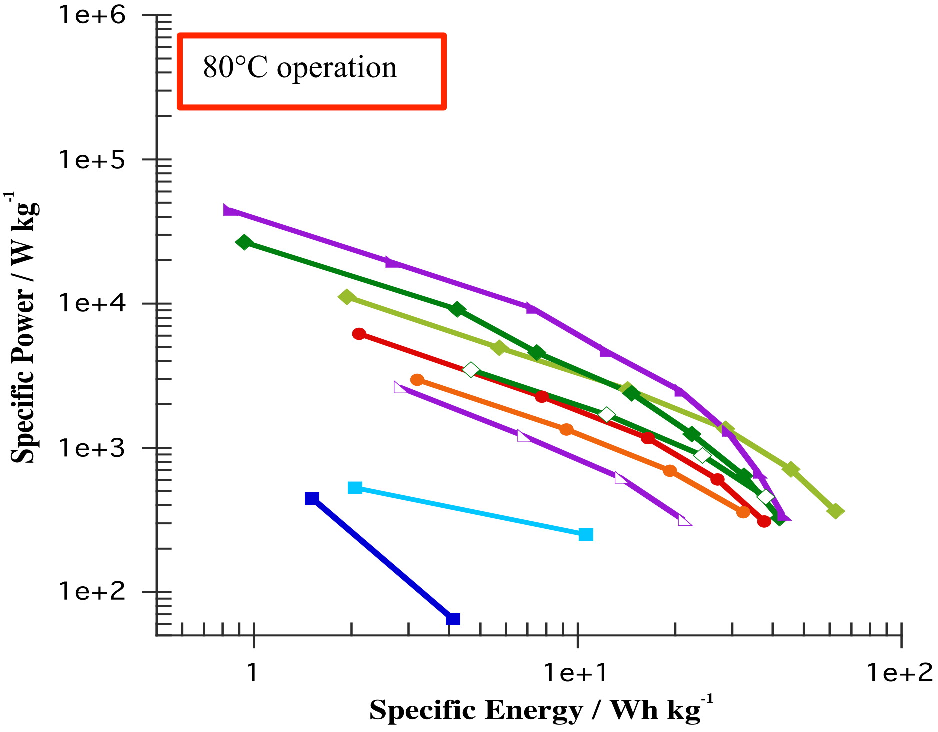

(d)

Figure 6.27 Ragone plot of average power density and average energy density at varying temperatures

Figure 6.27 illustrates the specific energy (E_{ave}) and specific power (P_{ave}) of only the cells delivering the highest capacitance at different temperature operations. See Appendix 5 for demonstration on calculation approach.

Regardless of the operating temperature, it can be seen that the maximum specific energy and maximum value of specific power of all ILs are determined to be at the highest and lowest, respectively, at low discharge currents, which then switches gradually as the discharge current is increasing.

At the operating temperature of 25°C, it can also be seen that the maximum energy and power output is derived from the combinations containing $[N_{1114}][NTf_2]$ and $[S_{221}][NTf_2]$ ILs at low and reasonably high discharge currents. This is mainly attributed to the relatively good transport properties and small cation volumes of these ILs. In fact at this temperature, a clear shift in specific energy is demonstrated for S-ILs and N-ILs, distinctively, as the cation volume of these classes are decreasing. This trend confirms a higher interaction of ILs comprising of small cations with the pores for double layer formation. With increasing the temperature to 40°C this trend is still maintained but the attained specific energies at low current discharges are tend to marginally decrease compared to 25°C operation as these curves are stretched towards the specific power axis. The ILs stabilities with increasing the discharge density is slightly influenced at increased temperature, hence no appreciable storage occurred at these current densities. This influence becomes more significant as the temperature increases to 60°C and 80°C

However as seen for other studied ILs at 25°C operation, the trend of increased energy density with reducing the cation size is mainly reversed for Pyr-ILs and P-ILs at most discharge currents indicating that energy density is also influenced greatly by operating potential of the IL where 0.1 V and 0.7 V increase is demonstrated for the operating potentials of $[Pyr_{14}][NTf_2]$ and $[P_{2225}][NTf_2]$ in comparison to $[Pyr_{13}][NTf_2]$ and $[P_{222(2O1)}][NTf_2]$ constituent.

Additionally at the operating temperatures of 40°C, 60°C and 80°C the specific power of the cells is subject to a decrease in comparison to 25°C operation which becomes more significant at higher temperature runs. This drop is attributed to the increased potential drop and reduced discharge time at temperature elevation runs where system energy is high and the resistances are accumulating on the cell.

It is also demonstrated that at high temperature operations, i.e. 60°C and 80°C, the best performing $[N_{1114}][NTf_2]$ IL containing combination in terms of the energy density tends to change places with $[P_{2225}][NTf_2]$ combination at higher discharge densities. This can be related to the earlier discussion point about the cation volume of $[P_{2225}][NTf_2]$ IL being too large to access the full surface area of the given AC. Interestingly the large volume $[N_{2224}][NTf_2]$ IL is also seen to exhibit a similar results, however the specific energy density gap between the large cation P-ILs still remains due to the much higher operating potential of the non-ether constituent.

7 Conclusions and Further recommendations

From the literature studies presented in chapters 1 and 2, the importance of divergence from fossil fuels was highlighted with the aim to reduce the impact of greenhouse gases on the environment. As an attempt to limit the use of fossil fuels, different robust and relible energy storage systems must be emerged to balance the supply of enegy with the demand for it. Supercapacitors or EDLCs are the system of choice for this study as they bridge the gap between the the tranditional capacitors and batteries in terms of the specific power and energy densities.

As mentioned in chapter 2, EDLCs can either be classified according to the utilized carbons or the electrolytes. The choice of materials here are directly linked to the performance characteristics of the produced cells. For instance, current commercialized EDLCs are based on aqueous electrolytes where relatively high power densities are generated at the expense of the energy density that is mainly manifested as a result of low operating potential of this electrolyte due to presence of water. Comparatively organic electrolytes and ionic liquids are other classes of electrolytes that accompanied by much higher operating potentials in comparison to the aqueous electrolytes. Thus they are expected to increase the energy density when used in an EDLC configuration. However due to the negligible vapour pressure and safer operations at elevated temperatures ionic liquids are selected as the electrolyte material for this study. Aditionally the ionic liquids exhibit very low melting temperatures due to the asymmetric structure, allowing for operation at a wide range of temperatures. However these liquids are substantially more viscous in comparison to the other electrolytes, consequently accompanied by higher values of equivalent series resistances hindering power output.

The choice of carbon material is equally important with respect to performance characteristics. RF xerogels are selected for this study as it has been confirmed that by varying the amount of precursors through adjusting the R/C molar ratio and controlling the processing conditions, the average pore size and surface area of the produced activated carbons can be altered.

One of the primary objectives of this study was to investigate the effect of chain length and incorporation of linkages into the structure on the physiochemical characteristics, operating potentials of the ILs and electrochemical performance of the cells. Hence a systematic study of nine ionic liquids from different classes of pyrrolidinium, sulphonium, ammonium and phosphonium ILs was performed.
The alkyl chain length was altered through incorporation of CH_2 group/s into the side chains of the pyrrolidinium, sulfonium and ammonium ILs. Also the effect of presence of linkages on the physiochemical properties and overall performance was studied through incorporation of methoxyethyl group in the side chain of ammonium and phosphonium ILs. Another objective of this study was to investigate the influence of pore size and optimize the performance through pairing each selected electrolyte with carbons with different average pore sizes. Hence activated carbons at different R/C molar ratios were produced.
As already mentioned high viscosity of ionic liquids results in higher values of equivalent series resistances hindering the output power. Accordingly temperature elevation approach at 40°C, 60°C and 80°C was used as a further attempt to improve the transport properties of the ILs and overall performance of the cells.

To optimize the capacitance and study the influence of pore characteristics on performance, AC xerogels were produced at the R/C molar ratios of 200, 250, 300 and 350 by maintaining R/F and R/W molar ratios constant. Although this selection of R/C ratios is rather a narrow choice, but carbonization and activation of precursors has shown a 15% increase in the BET surface area and 28% increase in the total pore volume from AC200 to AC350. An 8% increase in the mesopore volume is also experienced when comparing AC200 and AC350 together. Comparatively these ACs experiencing an 8% reduction of micropore volume as the R/C molar ratio increases, since the carbons exhibit a bimodal pore size distribution. Correspondingly AC200, AC250, AC300 and AC350 samples are 43%, 41%, 37% and 35% microporous, respectively, indicating that the remainder must be mesoporosity. A 3.2 nm increase in the BJH pore size distributions is also observed as the R/C molar ratios are increasing for AC200 – AC350 in the orders of 4.3, 5.1, 6.3 and 7.5 nm, respectively.

From the adsorption and desorption isotherms profiles, it has been identified the pores are slit-shaped or partially wedge-shaped with a narrow neck at one end or at both ends if the pore is open.

Results determined that the characteristics of the controlled porosity ACs exhibit a reasonably decent platform for attaining optimum capacitance performance when paired with different ILs comprising of different side chain lengths and linkages. The utilized IL cations in this study are 1-methyl-1-propylpyrrolidinium [Pyr_{13}], 1-butyl-1-methylpyrrolidinium [Pyr_{14}], diethylmethylsulfonium [S_{221}], triethyl-sulfonium [S_{222}], butyltrimethylammonium [N_{1114}], butyltriethylammonium [N_{2224}], N,N-diethyl-N-methyl-N(2methoxyethyl)ammonium [$N_{122(2O1)}$], pentyl-triethylphosphonium [P_{2225}] and (2methoxyethyl)-triethylphosphonium [$P_{222(2O1)}$] paired with bis(trifluoromethane)sulfonimide [NTf_2] anion as very high stabilities up to 6 V is reported for this anion. Additionally this anion displays reasonably good transport and electronic properties due to the presence of a partially delocalized charge. The volume of the cations are shown to increase in the order of 179, 207, 222, 225, 253, 266, 306, 313 and 359 $Å^3$ for [S_{221}], [S_{222}], [N_{1114}], [Pyr_{13}], [Pyr_{14}], [$N_{122(2O1)}$], [N_{2224}], [$P_{222(2O1)}$] and [P_{2225}] cations paired with [NTf_2] anion at the volume of 248 $Å^3$.

The water content measurements confirmed a moisture content reading of less than 5 ppm for all studied ILs after drying indicating that only traces amounts of moisture is present in the IL samples. Hence possible diminution in capacitance performance cannot be linked to the moisture content.

From the differential scanning calorimetry traces, melting points below 21°C were recorded for all utilized ILs designating that liquids should remain in the liquid state at the selected operating temperatures for this study, i.e. 25°C, 40°C, 60°C and 80°C. However [N_{1114}][NTf_2] and [N_{2224}][NTf_2] ILs displayed melting temperatures of 17.1°C and 20.9°C, respectively, indicating that melting crystals may partially remain in the solution at 25°C operations influencing the capacitance performance.

From the viscosity measurements, $[N_{1114}][NTf_2]$ and $[N_{2224}][NTf_2]$ ILs are shown to display the highest viscosities at 105.6 and 150 mPa.s at 25°C operation whereas S-ILs exhibit the lowest viscosities at 40.6 and 33.7 mPa.s at the same operating temperature. At 40°C although the viscosity of aforementioned N-ILs drops significantly below half the original stated values but still stands the highest among other ILs at that operating temperature with S-ILs still standing the lowest. In fact this trend is maintained for 60°C and 80°C operations. An Arrhenius-like behaviour was displayed for most ILs with a slight curvature for the mentioned N-ILs, which could be explained through two possibilities of extra hydrogen bond formation influencing the cation-anion or even cation-cation interactions or the chain tangling. A 1.5x increase in the value of viscosity was also observed as the alkyl side chain length is expanding for the $[Pyr_{14}][NTf_2]$ and $[N_{2224}][NTf_2]$ in comparison to the unextended constituents at 25°C. However extended S-IL, i.e. $[S_{222}][NTf_2]$, is not following this trend when compared against $[S_{221}][NTf_2]$ due to the shielding effect of an extra incorporated CH_2 molecule weakening the interactions between the central atom and the anion. A massive reduction in viscosity readings was also recorded for methoxyethyl incorporated $[N_{122(2O1)}]$-$[NTf_2]$ and $[P_{222(2O1)}][NTf_2]$ ILs in comparison to non-ether constituents due to the presence of an electronegative region adding extra flexibility into the structure.

A linear dependency of density with temperature was observed for all studied ILs. The variation of density with temperature for different ILs was mainly triggered by the density of the central atom and confirmed to be independent of the individual species dimensions or volumes as the highest densities were displayed for S-ILs that are associated with the smallest cation volumes.

From the conductivity measurements an inverse proportionality with viscosity is claimed when temperature increases. This means that at higher temperatures the reduced viscosity of the IL allows for greater degree of ion mobility and increase in conductivity. Accordingly the conductivity and viscosity properties are interlinked. Also longer chain $[Pyr_{14}][NTf_2]$ and $[N_{2224}][NTf_2]$ ILs are seen to difficult the cation movement and demonstrated to display relatively lower conductivities compared to their unextended [Pyr_{13}] and [N_{1114}] constituents at all temperatures. Up to two fold increase in the conductivity values were recorded for the methoxyethyl containing [$P_{222(2O1)}$][NTf_2] and [$N_{122(2O1)}$][NTf_2] ILs with respect to the corresponding non-ether constituents.

From the electrochemical stability measurements at the cut-off current density of 40 μA cm^{-2}, following operating potentials were determined: [Pyr_{13}][NTf_2] – 2.9 V, [Pyr_{14}][NTf_2] – 3.0 V, [S_{221}][NTf_2] – 2.6 V, [S_{222}][NTf_2] – 2.5 V, [N_{1114}][NTf_2] – 3.5 V, [N_{2224}][NTf_2] – 3.2 V, [$N_{122(2O1)}$]- [NTf_2] – 3.0 V, [P_{2225}][NTf_2] – 3.4 V and [$P_{222(2O1)}$][NTf_2] – 2.7 V. A comparison made with a commonly used organic electrolyte, 1M solution of $TEABF_4$ in PC – 2.71 V, indicated that provision of higher operating potentials from most of the ILs in comparison to this electrolyte improves the specific energy performance. No clear consistency was attained between the increased alkyl chain length and operating potentials of Pyr-ILs, S-ILs and N-ILs. However a 0.2 V and 0.7 V reduction in operating potential was demonstrated for methoxyethyl incorporated [$N_{122(2O1)}$][NTf_2] and [$P_{222(2O1)}$]-[NTf_2] ILs, respectively, in comparison to their non-ether constituents indicating that improved transport and electronic properties are achieved at the expense of lowered operating potential.

As mentioned, one of the primary objectives of this study was to assess the influence of pore characteristics on the ion migration and capacitance performance, thus Galvanostatic cycling was used at different discharge densities. The AC with the widest average pore size (AC350) was found to exhibit the optimum capacitance performance with increase in the discharge current for all studied ILs, with the exception of [S_{221}][NTf_2] and [Pyr_{14}][NTf_2] ILs where AC300 produces the best capacitance performing combinations and accounts as the optimum pore size for the mentioned liquids. The reduction in capacitance performance for AC350-[S_{221}][NTf_2] combination, where the cation constituent is smallest among other studied cations at a molecular volume of 179 $Å^3$, is caused by pore flooding mechanism as the double layer thickness increases. However below this optimum average pore size, the presented porosity from AC250 considered as too small for ion transfer to take place inside the pores for double layer formation. For the [Pyr_{14}][NTf_2] IL although the cationic volume is significantly larger than the [S_{221}] constituent at 253 Å^3 but a better ionic coordination of [Pyr_{14}][NTf_2] with AC300 held responsible for the higher capacitance performance in comparison to other ACs above and below the optimum pore size. Accordingly below and above this optimum average pore size for [Pyr_{14}][NTf_2] IL, ACs are accounted as too small for double layer formation hence diminishing the capacitance performance.

The EIS method was also used to determine the capacitance performance and identify the magnitude of involved resistances for all produced combination. General findings here is that the highest ionic and equivalent series resistances along with the lowest phase angles are attained for combinations with narrowest average pore sizes, i.e. AC200 and AC250, at all operating temperatures. On the other hand AC350 exhibited the lowest resistances for most combinations with the exception of [Pyr_{14}][NTf_2] and [S_{122}][NTf_2] ILs, due to previously stated reasons, where wider pathways are available for ion migration and charge storage. However the best performing ACs determined through this method did not exactly match those determined from GC method. This was attributed to the selection of 0.01 Hz at the low frequency response region being recognized as slightly high for accessing the entire surface area, hence a lower frequency must be selected for future studies. Accordingly no consistent correlations were attained between the capacitance performance of the cells determined through the GC and EIS methods.

The best performing combinations determined from the GC method are generally associated with relatively low ionic and equivalent series resistances at higher phase angles determined from the EIS method. The findings about wide pore AC300 and AC350 presenting the best capacitance performance supports the idea that there is an optimum pore size for every IL which is seen here for ACs containing wider pathways for ion transport for double layer formation. AC350 displays the highest BET surface area and pore volume of 790 m^2 g^{-1} and 7.5 nm, respectively, among the studied ACs here indicating that although this carbon produces the best performance capacitance when paired with most ILs but may not be the optimum pore medium for that specific IL. Hence ACs containing higher R/C molar ratios must be considered in order to determine the peak specific capacitance performance especially for the ILs comprising of larger size cations, i.e. $[N_{2224}][NTf_2]$, $[P_{222(2O1)}][NTf_2]$ and $[P_{2225}][NTf_2]$, requiring wider pores and pathways for double layer formation at all sites.

Temperature elevation was utilized as an approach to reduce the viscosity of the electrolytes and anticipated to improve the performance vastly through provision of higher ionic conductivities with increasing the temperature. Although the increase in ionic conductivity with temperature was confirmed by a reduction in solution resistance (R_s), but it was demonstrated that the R_i and ESR resistances were increasing with temperature. The severe increase in ionic resistance and variation in series resistances for most combinations with temperature were mainly attributed to accumulation of resistances as a result of overcharging the cells due to selection of the attained operating potential at 25°C for all operation temperatures. This is initially thought to be a sensible and beneficial selection for all runs as firstly a conservative operating potential at a reasonably low cut-off current was utilized at 25°C and secondly all AC combinations of the same IL at all temperatures would charge up to a uniform potential allowing direct comparisons between runs. However overcharging at higher temperatures, is likely to encouraged IL decomposition and perhaps causes corrosion towards cell species. It is also likely that at the high temperature and overcharged conditions the polymer binder begins to melt blocking pores or ion diffusion pathways reducing the available surface area for charge storage, which then would lead to short-circuiting, self-discharge and reduced performance.

At 25°C a neat capacitance performance deterioration was established with charge density in the order of S-ILs > N-ILs > Pyr-ILs > P-ILs which is most anticipated for S-ILs and $[N_{1114}][NTf_2]$ IL containing cells due to provision of higher transport and electronic properties, as discussed. However $[N_{2224}][NTf_2]$ and $[N_{122(2O1)}][NTf_2]$ based cells displayed higher capacitance performance compared to the Pyr-ILs which contradicts with the attained physiochemical properties at this temperature, which was attributed to the higher operating potential of the mentioned N-ILs. P-ILs on the other side exhibited lowest capacitance performance in comparison to the other studied ILs even though $[P_{222(2O1)}][NTf_2]$ displays the second lowest viscosity after S-ILs and very good electronic conductivity. Low capacitance performance of these ILs accredited to the large cation volume of P-ILs being unable to access the entire surface of the provided pore volume for double layer formation. Hence the effect of methoxyethyl linkage for $[P_{222(2O1)}][NTf_2]$ IL did not encountered any interesting observation with respect to its non-ether constituent.

A concluding remark can be made here that incorporation of an ether functionalization in an IL improves the transport properties while the hydrophilicity, polarity and capability of such ILs to bind with hydrogen increases at the cost of lower operating potential [201, 226]. However the cation volume influences the capacitance in a fixed pore volume as an increase in capacitance performance was attained for $[N_{122(2O1)}][NTf_2]$ IL in comparison to its non-ether constituent confirming that the cation volume is equally a determining factor for attaining optimum capacitances as well as pore size and physiochemical properties of the liquids.

At 40°C operation an increase in capacitance was recorded for all AC-IL combinations mainly due to chain untangling at this temperature. Unlike 25°C operation, the orderly increase in capacitance variation no longer exists due to the build up of resistances. Beyond this point and through further temperature elevation to 60°C and 80°C different responses were recorded for different ILs classes. However a sharp reduction in capacitance performance was demonstrated for smaller size S-ILs whereas a substantial increase was experienced for $[N_{1114}][NTf_2]$, $[N_{2224}][NTf_2]$ and $[P_{2225}][NTf_2]$ incorporated cells.

From the specific energy and specific power data, it is demonstrated that at the operating temperature of 25°C the small cation $[N_{1114}][NTf_2]$ and $[S_{221}][NTf_2]$ ILs display the highest performance in comparison to their extended constituents at all discharge currents. For instance, at the low discharge current of 0.5 mA, a specific power value of 740 and 526 W kg^{-1} are attained for $[N_{1114}][NTf_2]$ and $[S_{221}][NTf_2]$ incorporating cells with little variation of specific energy at 51.17 and 51.31 Wh

kg^{-1}, respectively. However as the discharge current increases to 32 mA, specific power shoots up to values in the orders of thousands, i.e. 41 and 32 kW kg^{-1} respectively, where specific energy of both liquids drops by about 70% to 15 and 15.5 Wh kg^{-1}. The attained trend for these ILs is irrespective of the operating potentials of the liquids. However as seen with larger cation $[Pyr_{14}][NTf_2]$ and $[P_{2225}][NTf_2]$ ILs, as the cation volume increases the operating potential becomes more influencing where more charge can be displaced on the surface thus improving the energy density. The methoxyethyl incorporation into the chain demonstrated different behaviours for $[N_{122(2O1)}][NTf_2]$ and $[P_{222(2O1)}][NTf_2]$ ILs where a 23% improvement and 29% diminution in energy density was displayed for these ILs, respectively, in comparison to their non-ether constituents at high discharge current of 32 mA.

At elevated temperature runs, a decrease in specific energy and power was attained for most combinations indicating that total impedance of the cell leads to bigger IR and voltage drops. However $[P_{2225}][NTf_2]$ IL is exempted from this observation where in fact this IL is seen to change place with the best energy and power performing $[N_{1114}][NTf_2]$ IL due to the significantly larger volume of the cation at higher temperatures providing limited access to the pores, hence lower resistances are present therefore the significant reduction in energy and power performance did not occur.

Future work and further recommendations

- Perform X-ray Diffraction analysis before carbon activation step for phase identification of the crystalline material
- Use spectroscopy techniques before and after activation step to screen the development of the porous structure
- Use spectroscopy techniques in place of thermal gravimetric analysis to minimise the chance of electrolytes decomposition and attain a reliable and stable operating temperature range
- Use a control sample or a commonly used organic electrolyte for more efficient comparisons between different electrolyte classes
- Produce a wider range of carbons comprising higher surface areas and possibly slightly large average pore diameters especially for liquids containing larger cations
- Produce carbons with higher percentage of mesoporosity
- Identify suitable operating potentials for various operating temperature runs

8 Appendices

8.1 Appendix 1: Maximum power density [10]

The maximum deliverable power from an EDLC can be determined using an equivalent circuit containing a resistor and a capacitor in series arrangement. Presence of a resistor signifies the equivalent series resistances in the cell, i.e. ESR. In this arrangement the initial potential, V_1, is reduced across the circuit by the product of discharge current and equivalent series resistance, as shown in equation A1.E1. And the corresponding power to this discharge step is given by A1.E2. This power is known to be at the maximum when the derivative of power with respect to current is zero as demonstrated in A1.E3.

$$V = V_1 - (I \times ESR)$$

A1.E1

$$P = IV_1 - (I^2 \times ESR)$$

A1.E2

$$\frac{dP}{dI} = V_1 - (2I \times ESR) = 0$$

A1.E3

Hence when the cell is at the maximum power state, the discharge current can be rearranged as illustrated in A1.E4. Accordingly the potential at maximum power is halved in comparison to the initial voltage as shown in A1.E5. The product of current and potential at maximum power yields in the value of maximum power as shown in A1.E6.

$$I = \frac{V_1}{2ESR}$$

A1.E4

$$V = V_1 - (I \times ESR) = V_1 - \left(\left(\frac{V_1}{2ESR}\right) \times ESR\right) = \frac{V_1}{2}$$

A1.E5

$$P_{max} = V \times I = \left(\frac{V_1}{2ESR}\right)\left(\frac{V_1}{2}\right) = \frac{{V_1}^2}{4ESR}$$

A1.E6

8.2 Appendix 2: Sample calculation for C_s using GC method

The specific capacitance, C_s, from the galvanostatic cycling method was determined using the discharge data generated from an Arbin instrument at various charge and discharge rates. Data from the discharge rate of 0.001A for AC300-[S_{221}][NTf_2] combination at 25°C is selected and shown in the following table for demonstration purposes.

Table 8.1 Discharge data at 0.001 A

Discharge time (t_d) / s	Discharge potential (E_d) / V	Discharge current (I_d) / A	Internal resistance (iR) / Ω
1.02956388	2.5496614	0.00099989	15.4637194
2.05912584	2.52991891	0.00099989	15.4637194
…	…	…	…
162.580973	1.01203609	0.00099989	15.4637194
163.610543	1.00436747	0.00099989	15.4637194

As described previously in section 6.4.1, the potential at the beginning of the discharge step is used to determine the potential or voltage drop of the cell at that specific rate. This was determined using the potential difference between the final voltage of the charge step that is the operating potential of the IL, i.e. 2.6 V for this electrolyte, and the initial potential at the discharge step. The value of the IR_{drop} was calculated using the difference in operating potential of ionic liquid and the initial potential at the discharge step divided by the discharge current.

While charging the cells at constant current density, the potential difference across the plates increases with time in a linear manner as the charges accumulate across the interface over a time interval. This is shown through following equations:

$$C = \frac{\Delta q}{\Delta E}$$

equation 4.10

$$\Delta q = \int I \, dt$$

equation 4.11

$$C = \int \frac{I}{\Delta V} dt = \frac{I.\Delta t}{\Delta E}$$

equation 4.12

As previously stated, to determine the capacitance at the specified rate, equation 5.1 was used where I is the discharge current at 0.00099989 A, ΔE is the potential difference from where discharge starts to 1 V at 1.54529393 V, t is the corresponding discharge time to 1 V at 162.580979 and W is the mass of the active material since capacitance is normalized against mass of active materials.

$$C = \frac{I.\Delta t / \Delta E}{W}$$

equation 5.1

Mass of the active material was determined using the lowest electrode mass, i.e. 0.01311 g for the selected combination, minus the current collector mass of 0.008404 g multiply by 0.85 since a mass ratio of 85:15 of carbon to polymer was used. It is worth noting that above capacitance calculation is determined for one electrode and must be doubled to account for both present electrodes.

8.3 Appendix 3: Sample calculation for C_{eis} using EIS method

As previously discussed, utilization of impedance spectroscopy method allows for determination of capacitance as well as various resistances present in the cell including solution resistance, ionic resistance and equivalent series resistance where these evaluations become important for device design and optimization of power density.

Interpretation of the attained resistance data from EIS was carried out through fitting the frequency response of 100 kHz to 10 mHz to the equivalent circuit model described in detail in section 4.2.4.

Table 8.2 illustrates a brief representation of EIS output data for AC300-$[S_{221}][NTf_2]$ combination at 25°C where used for capacitance calculations. This was done by incorporating the value of imaginary impedance at the lowest frequency value of 0.01 Hz using the relationship in equation 4.24. The determined capacitance was then normalized against the active mass of the carbon as described in Appendix 2. It is also worth noting that the capacitance calculation using this method is only for one electrode and must be doubled to account for both present electrodes.

Table 8.2 Generated data from EIS

Frequency (ω) / Hz	-Z'$_{real}$ / Ω	Z''$_{imaginary}$ / Ω	Phase angle / °
100000	4.2329	-0.95097	-12.662
77426	4.322	-1.2709	-16.386
…	…	…	…
0.0129155	68.704	-143.17	-64.365
0.01	76.26	-178	-66.808

$$C_{eis} = \frac{1}{2\pi\omega Z''_{im}}$$

equation 4.24

8.4 Appendix 4: Variation of Cs with rate at different temperatures

Table 8.3 Variation of capacitance with discharge rate at 25°C

CC	**AC200**		**AC250**		**AC300**		**AC350**	
mAcm-2	C$_S$ [Fg^{-1}]	iR[Ω]	C$_S$ [Fg^{-1}]	iR[Ω]	C$_S$ [Fg^{-1}]	iR[Ω]	C$_S$ [Fg^{-1}]	iR[Ω]
[Pyr$_{13}$][Tf$_2$N]								
0.25	27.6	76.1	28.7	62.8	24.5	51.7	25.7	52.9
0.5	24.6	78.4	26.2	63.1	23.3	51.2	24.3	53.0
1	21.4	79.8	23.7	63.6	22.0	51.7	23.0	53.3
2	17.8	79.5	20.8	63.7	20.8	51.6	21.4	53.4
4	13.8	77.8	17.1	62.9	18.1	51.5	19.4	52.8
8	7.8	73.7	11.4	60.6	11.3	50.5	15.2	50.7
16	-	-	7.7	53.5	10.3	45.5	12.7	46.4
32	-	-	-	-	3.3	40.4	14.5	44.4
[Pyr$_{14}$][Tf$_2$N]								
0.25	28.6	77.9	28.2	67.8	26.5	52.5	26.4	55.6
0.5	25.4	78.9	25.4	69.3	24.9	53.5	24.7	56.9
1	22.5	80.0	22.3	70.3	23.4	53.7	23.3	57.2
2	19.4	80.1	18.7	70.5	21.9	53.7	22.1	57.2
4	15.5	78.9	14.3	69.7	20.3	52.9	19.2	57.1
8	8.4	75.2	8.7	67.6	16.1	50.6	16.2	56.1
16	-	-	4.5	58.6	12.7	44.7	13.4	50.7
32	-	-	-	-	7.5	42.3	8.7	45.2
[S$_{221}$][Tf$_2$N]								
0.25	56.5	64.4	58.0	59.9	59.3	14.4	53.6	30.8
0.5	51.0	59.6	53.7	61.7	55.8	15.1	49.8	30.6
1	44.7	67.2	50.2	41.8	51.5	15.5	46.2	31.0
2	37.3	60.6	45.9	40.2	46.4	15.4	42.9	31.2
4	29.4	60.4	41.3	40.1	42.6	15.6	38.8	31.1
8	18.3	58.6	32.0	39.3	41.7	15.7	31.6	30.7
16	9.5	50.6	23.9	30.6	36.7	15.4	24.3	26.8
32	-	-	14.5	22.2	29.3	15.5	16.5	17.8
64	-	-	-	-	17.3	16.2	11.8	17.2
[S$_{222}$][Tf$_2$N]								
0.25	49.3	65.7	47.9	46.3	48.4	18.4	38.6	17.7
0.5	44.8	62.2	43.3	44.7	44.6	18.7	36.2	17.5
1	40.1	51.2	38.1	44.2	40.9	18.9	34.0	17.8
2	34.1	51.7	28.0	126.3	36.8	19.1	31.7	17.8
4	26.2	51.5	21.4	87.4	32.2	19.2	29.4	17.9
8	15.5	50.9	15.5	49.3	24.4	19.2	25.2	17.9
16	8.1	44.4	12.2	34.1	19.6	18.1	21.3	17.2
32	-	-	8.4	27.1	13.8	17.8	14.8	16.6
64	-	-	-	-	-	-	7.7	15.5
[N$_{1114}$][Tf$_2$N]								
0.25	26.3	69.7	35.4	32.7	33.5	63.3	33.6	25.6

0.5	21.6	72.0	32.1	33.4	30.7	64.4	31.1	25.1
1	17.8	72.5	29.5	33.9	28.9	64.2	29.3	25.7
2	14.7	72.8	27.1	34.0	26.6	63.6	27.7	25.9
4	11.4	71.9	24.8	34.0	26.0	56.6	27.3	25.9
8	3.9	68.9	19.9	33.6	21.1	55.3	25.0	25.8
16	-	-	15.2	29.8	14.9	49.7	20.7	24.8
32	-	-	9.2	29.4	11.8	46.5	15.9	24.4
64	-	-	-	-	-	-	13.1	23.6
[N$_{2224}$][Tf$_2$N]								
0.25	27.5	60.0	26.5	300.6	29.2	44.4	26.8	36.2
0.5	25.0	60.5	24.0	298.4	27.4	45.4	25.3	36.4
1	22.8	61.0	22.1	176.0	25.7	45.4	24.1	36.0
2	20.6	61.5	20.1	135.1	24.0	45.7	22.9	36.3
4	18.3	61.0	17.7	97.0	22.1	45.7	21.6	36.1
8	12.3	59.1	13.1	75.4	17.2	45.3	18.5	35.7
16	6.3	52.0	9.2	59.6	13.0	40.8	15.1	32.8
32	-	-	-	-	8.0	39.8	10.2	32.0
[N$_{122(2O1)}$][Tf$_2$N]								
0.25	27.3	71.0	31.3	44.1	29.5	39.2	28.0	32.9
0.5	24.0	73.8	28.5	45.7	27.7	40.5	26.6	34.2
1	20.8	75.5	25.5	46.1	26.5	41.3	25.6	34.4
2	17.5	76.3	22.1	46.4	25.0	41.6	24.6	34.8
4	14.5	76.0	18.5	46.4	23.3	41.7	23.3	34.9
8	11.3	73.6	11.7	45.9	18.3	41.3	19.8	34.4
16	-	-	8.0	40.7	13.0	38.2	17.5	31.9
32	-	-	-	-	-	-	9.4	30.9
[P$_{2225}$][Tf$_2$N]								
0.25	21.2	59.1	19.4	63.4	21.8	40.1	21.4	33.3
0.5	18.6	59.5	18.0	63.0	20.5	41.2	20.4	33.6
1	16.4	60.2	16.7	63.3	19.5	41.1	19.4	33.8
2	14.2	60.1	15.5	63.3	18.6	41.2	18.2	33.9
4	12.2	59.5	13.9	62.2	17.6	40.9	16.9	33.9
8	6.9	56.8	9.8	58.6	15.2	39.6	13.2	33.5
16	3.2	49.2	6.1	50.0	12.9	35.2	8.8	30.8
32	-	-	-	-	8.6	33.7	6.3	39.1
[P$_{222(2O1)}$][Tf$_2$N]								
0.25	19.8	100.8	19.6	75.3	21.3	43.3	22.0	53.5
0.5	18.0	101.3	18.2	76.0	20.3	43.9	20.8	53.1
1	16.5	101.4	16.7	76.2	19.2	44.3	19.9	53.4
2	14.2	100.8	14.7	75.5	17.9	44.3	18.0	53.3
4	11.6	97.1	11.7	74.9	16.4	44.0	16.1	53.0
8	4.1	89.7	-	-	12.3	43.1	14.0	51.2
16	-	-	-	-	10.0	39.2	6.4	46.3
32	-	-	-	-	6.8	38.1	-	-

Table 8.4 Variation of capacitance with discharge rate at 40°C

CC	**AC200**		**AC250**		**AC300**		**AC350**	
mAcm^{-2}	C_S [Fg^{-1}]	iR[Ω]	C_S [Fg^{-1}]	iR[Ω]	C_S [Fg^{-1}]	iR[Ω]	C_S [Fg^{-1}]	iR[Ω]
[Pyr$_{13}$][Tf$_2$N]								
0.25	31.6	88.0	32.4	83.9	27.0	52.5	28.3	75.0
0.5	27.1	92.3	28.7	93.5	24.8	53.2	26.0	76.8
1	22.3	94.0	25.0	84.9	22.6	53.8	23.8	77.6
2	16.9	94.2	20.6	84.2	19.7	53.9	20.8	77.5
4	12.6	92.5	15.5	84.7	18.5	53.3	17.5	75.7
8	5.6	88.0	9.3	78.2	12.5	51.1	11.1	70.9
16	-	-	5.4	66.4	15.0	44.7	-	-
[Pyr$_{14}$][Tf$_2$N]								
0.25	33.4	88.2	31.9	78.0	29.6	79.3	29.0	55.9
0.5	28.9	93.4	27.4	83.5	26.9	75.3	26.3	58.4
1	24.6	96.2	22.8	81.0	24.4	75.9	23.8	59.1
2	20.3	96.8	17.5	79.6	21.6	75.7	21.4	59.4
4	15.8	95.1	12.2	79.7	18.1	74.6	17.3	58.8
8	7.3	90.0	7.1	76.0	12.3	72.4	12.8	56.6
16	-	-	-	-	8.2	61.1	-	-
[S$_{221}$][Tf$_2$N]								
0.25	59.6	97.2	57.7	42.9	62.1	33.0	56.9	22.9
0.5	51.5	99.8	47.7	43.3	57.7	34.4	51.7	24.7
1	41.9	100.9	36.1	44.0	53.4	34.7	45.1	24.9
2	31.0	100.3	25.5	44.2	48.9	35.2	37.2	25.0
4	22.1	97.0	19.1	44.3	43.8	35.1	33.6	25.0
8	8.9	90.0	12.7	43.6	34.8	34.3	33.2	24.6
16	-	-	8.2	39.5	26.8	31.3	18.2	22.9
32	-	-	-	-	-	-	11.3	22.3
[S$_{222}$][Tf$_2$N]								
0.25	53.2	72.1	50.5	50.8	52.2	66.0	43.5	23.9
0.5	46.4	75.0	41.8	51.2	45.9	66.6	39.0	24.2
1	35.2	76.1	31.8	51.9	38.7	66.7	34.9	25.1
2	25.8	76.3	22.8	52.0	29.8	66.3	30.4	24.9
4	17.5	74.2	17.1	52.0	21.9	65.3	25.1	25.0
8	9.1	70.0	11.1	51.5	12.8	62.6	18.2	24.8
16	-	-	8.2	42.4	10.2	55.1	13.0	22.7
[N$_{1114}$][Tf$_2$N]								
0.25	33.6	109.3	40.9	44.0	38.0	71.3	38.2	40.6
0.5	27.1	112.8	35.4	46.3	33.6	75.2	34.2	41.4
1	22.2	113.7	30.9	47.1	30.5	76.8	31.1	43.8
2	17.2	112.2	26.1	47.4	27.5	77.0	29.2	44.4
4	11.8	108.2	24.8	47.3	23.7	76.1	26.9	44.2
8	-	-	14.4	46.2	18.9	72.1	21.9	43.4
16	-	-	9.5	40.6	13.7	61.6	18.2	39.9

32	-	-	-	-	-	-	11.6	38.8
[N$_{2224}$][Tf$_2$N]								
0.25	32.5	95.3	31.5	60.8	32.7	49.3	29.7	41.5
0.5	28.8	97.8	28.0	62.7	29.7	50.2	27.3	42.2
1	25.4	99.3	25.1	63.1	27.1	50.7	25.3	42.6
2	21.7	99.8	21.5	63.0	24.4	50.9	23.4	42.4
4	18.1	98.0	18.5	61.9	20.5	50.7	21.3	42.1
8	9.9	92.1	12.2	59.1	13.1	49.4	15.9	46.3
16	-	-	9.5	49.4	10.0	43.0	13.5	35.9
32	-	-	-	-	-	-	10.2	35.9
[N$_{122(2O1)}$][Tf$_2$N]								
0.25	32.5	130.5	34.5	100.7	32.6	96.6	30.9	82.2
0.5	28.4	133.1	28.6	100.2	29.1	101.1	28.3	84.0
1	24.6	134.6	21.7	103.2	25.7	102.9	25.9	85.1
2	20.7	133.4	14.5	107.2	21.7	102.8	23.3	85.5
4	16.6	127.0	10.4	105.3	18.3	99.6	20.5	83.7
8	-	-	8.4	98.3	12.7	92.1	14.3	78.8
16	-	-	-	-	-	-	11.0	66.7
[P$_{2225}$][Tf$_2$N]								
0.25	24.7	58.6	22.1	59.7	23.9	42.4	25.8	50.2
0.5	21.2	60.8	20.2	61.2	22.3	43.9	23.9	50.6
1	18.6	61.6	18.7	62.5	21.0	44.1	22.4	50.6
2	16.1	61.6	17.2	63.1	19.8	44.1	21.1	50.4
4	13.2	60.7	15.9	62.6	18.6	43.3	19.6	49.6
8	8.3	58.2	11.8	59.7	15.3	41.9	16.1	47.2
16	3.4	49.0	7.9	49.8	13.1	36.0	13.0	39.7
32	-	-	-	-	8.7	33.7	-	-
64	-	-	-	-	5.4	28.7	-	-
[P$_{222(2O1)}$][Tf$_2$N]								
0.25	22.1	112.0	21.4	87.1	22.7	60.1	23.4	71.7
0.5	19.6	114.0	19.4	88.3	20.9	61.2	21.7	71.5
1	17.3	114.3	17.3	89.1	19.2	61.5	19.8	72.5
2	16.4	113.6	14.6	88.5	17.0	61.7	17.5	71.9
4	12.3	109.5	11.9	86.4	14.1	60.7	14.4	70.7
8	-	-	5.8	81.1	9.3	58.0	9.4	66.7
16	-	-	-	-	6.5	50.8	5.7	58.5

Table 8.5 Variation of capacitance with discharge rate at 60°C

CC	**AC200**		**AC250**		**AC300**		**AC350**	
mAcm^{-2}	C_S [Fg^{-1}]	iR [Ω]	C_S [Fg^{-1}]	iR [Ω]	C_S [Fg^{-1}]	iR[Ω]	C_S [Fg^{-1}]	iR[Ω]
[Pyr_{13}][Tf_2N]								
0.25	33.1	113.0	35.2	107.4	29.7	97.5	31.6	118.3
0.5	24.2	118.0	27.5	113.8	24.5	104.0	26.2	126.4
1	16.2	119.6	19.2	114.6	18.7	106.2	20.4	128.2
2	11.1	119.2	13.0	113.6	12.5	105.7	14.5	127.4
4	-	-	9.5	110.7	9.5	103.9	10.4	124.3
8	-	-	5.1	103.4	-	-	-	-
[Pyr_{14}][Tf_2N]								
0.25	35.1	144.8	32.9	99.9	33.2	99.0	31.5	159.0
0.5	25.7	150.9	23.6	106.8	28.3	106.7	25.6	167.2
1	16.4	151.1	15.3	108.3	23.2	108.1	19.4	168.0
2	9.3	149.3	10.8	107.5	17.7	107.8	13.1	166.1
4	-	-	8.1	104.5	12.4	105.7	9.4	152.0
8	-	-	4.4	98.5	6.2	100.1	-	-
[S_{221}][Tf_2N]								
0.25	45.8	109.2	45.6	58.4	47.5	57.4	45.1	65.0
0.5	34.8	113.3	37.2	60.6	40.5	60.2	35.2	65.9
1	24.3	115.1	31.4	61.9	32.5	64.1	27.5	66.3
2	15.3	113.9	24.7	61.8	32.9	60.9	26.5	66.1
4	-	-	-	-	21.5	60.0	-	65.3
8	-	-	-	-	14.7	57.2	-	-
16	-	-	-	-	7.6	47.2	-	-
[S_{222}][Tf_2N]								
0.25	42.7	94.5	39.4	67.8	43.7	104.6	41.3	47.2
0.5	30.4	100.3	26.2	70.1	32.3	107.6	32.8	48.2
1	20.9	101.9	17.6	70.6	22.5	122.2	25.4	48.6
2	14.2	102.4	12.7	70.7	14.8	131.2	18.1	48.8
4	10.5	100.7	-	-	-	-	14.3	48.2
[N_{1114}][Tf_2N]								
0.25	48.7	93.4	44.7	68.6	41.5	112.5	41.4	73.3
0.5	38.6	96.7	37.7	74.2	36.0	119.2	36.4	76.5
1	29.4	95.2	31.5	74.6	30.5	120.5	31.9	77.2
2	19.6	93.7	27.7	74.0	24.3	119.1	27.6	77.3
4	12.4	91.8	15.1	72.5	20.8	116.1	15.0	76.2
8	4.7	87.1	9.8	69.2	10.6	108.8	-	-
16	-	-	6.4	58.5	-	-	-	-
[N_{2224}][Tf_2N]								
0.25	37.9	119.1	35.3	75.4	36.7	73.3	32.2	63.2
0.5	32.2	136.8	29.6	80.6	31.8	77.3	28.0	66.9
1	26.2	140.6	24.2	81.2	27.6	78.4	23.8	67.9
2	18.4	140.1	19.4	80.0	22.0	78.4	19.9	67.9

4	11.7	135.3	14.4	77.4	17.2	77.0	17.1	66.7
8	-	-	8.3	73.3	13.2	73.6	11.7	63.1
16	-	-	4.7	60.9	8.9	66.6	7.5	51.9
$[N_{122(2O1)}][Tf_2N]$								
0.25	37.3	113.9	31.5	127.7	35.4	132.8	35.1	112.2
0.5	30.5	122.4	17.6	134.4	28.7	138.6	30.3	121.9
1	24.3	124.7	10.0	135.0	22.9	138.8	26.0	124.7
2	17.8	124.2	6.8	134.2	16.7	137.3	19.9	125.2
4	-	-	-	-	12.5	133.2	15.4	121.5
8	-	-	-	-	-	-	8.0	114.8
$[P_{2225}][Tf_2N]$								
0.25	29.8	78.1	25.7	81.5	26.4	59.2	28.6	69.9
0.5	24.7	83.9	22.7	86.0	24.2	60.3	25.7	71.3
1	20.6	83.8	20.1	87.0	22.4	60.8	23.3	71.4
2	16.9	82.2	17.3	86.6	20.6	60.8	20.6	70.7
4	13.5	78.8	14.7	85.1	18.7	59.3	19.8	69.0
8	6.7	74.6	8.6	79.8	14.2	55.1	13.4	64.8
16	-	-	4.1	64.1	11.0	45.0	10.2	49.8
$[P_{222(2O1)}][Tf_2N]$								
0.25	24.3	128.7	22.4	116.1	24.1	99.3	24.8	118.7
0.5	20.3	131.9	18.2	118.6	21.0	102.7	21.5	123.7
1	16.2	131.7	13.5	118.9	17.3	103.3	17.5	124.7
2	11.8	130.4	9.7	117.0	13.0	102.8	12.6	123.6
4	-	-	-	-	8.8	100.2	9.1	119.6
8	-	-	-	-	4.7	94.0	-	-

Table 8.6 Variation of capacitance with discharge rate at 80°C

CC	**AC200**		**AC250**		**AC300**		**AC350**	
mAcm^{-2}	C_S [Fg^{-1}]	iR [Ω]	C_S [Fg^{-1}]	iR [Ω]	C_S [Fg^{-1}]	iR [Ω]	C_S [Fg^{-1}]	iR [Ω]
[Pyr_{13}][Tf_2N]								
0.25	21.4	125.1	27.4	121.2	30.6	106.4	32.2	132.3
0.5	13.3	128.0	16.5	124.8	21.7	114.0	22.6	137.3
1	9.3	129.0	11.2	125.0	13.6	115.0	15.0	137.9
2	6.8	129.0	7.8	123.6	9.4	115.2	9.9	137.1
4	-	-	-	-	7.5	114.1	-	-
[Pyr_{14}][Tf_2N]								
0.25	16.5	165.5	22.6	123.0	33.7	121.6	31.0	136.8
0.5	7.8	166.0	13.9	125.3	27.0	125.4	22.7	141.2
1	3.1	165.1	9.8	126.0	20.2	125.5	16.0	141.6
2	-	-	7.6	116.0	14.1	123.0	10.4	140.8
4	-	-	6.2	115.9	8.8	119.6	-	-
[S_{221}][Tf_2N]								
0.25	10.8	179.6	12.2	426.5	16.6	175.5	18.6	161.2
0.5	4.1	177.5	8.7	211.8	5.6	194.2	8.6	167.8
1	-	-	13.0	32.9	-	-	5.3	166.0
2	-	-	8.2	31.8	-	-	-	-
[S_{222}][Tf_2N]								
0.25	7.3	-	12.9	-	11.2	120.1	-	-
0.5	5.1	551.0	8.7	627.6	4.6	24.9	-	-
1	3.5	375.6	6.8	359.3	3.9	27.2	-	-
2	-	-	5.9	233.4	-	-	-	-
[N_{1114}][Tf_2N]								
0.25	45.4	171.1	38.0	137.8	28.6	442.7	40.1	115.5
0.5	31.6	176.8	24.6	145.2	23.6	1436	32.3	129.0
1	19.2	167.0	18.4	144.4	20.7	420.5	24.2	130.6
2	9.4	155.2	17.6	140.6	13.8	252.6	16.6	128.0
4	-	-	7.5	135.0	-	-	12.5	123.4
8	-	-	-	-	-	-	6.3	114.8
[N_{2224}][Tf_2N]								
0.25	32.3	155.7	32.6	100.0	32.5	115.5	31.6	78.8
0.5	22.8	163.9	25.2	100.9	23.4	118.3	26.1	80.9
1	15.1	164.2	18.6	102.1	15.8	118.2	20.2	81.0
2	8.6	160.8	13.9	99.4	9.9	116.7	16.3	80.6
4	-	-	9.3	97.0	6.8	114.6	12.4	79.4
8	-	-	4.0	93.1	-	-	7.9	76.1
16	-	-	-	-	-	-	4.1	62.1
[$N_{122(2O1)}$][Tf_2N]								
0.25	25.7	139.1	19.5	143.6	30.8	149.4	35.0	133.4
0.5	13.9	143.1	11.0	145.5	20.2	155.5	25.9	138.5
1	7.2	143.0	7.2	145.1	13.3	154.6	17.5	138.6

2	-	-	5.3	143.1	9.1	152.9	11.9	137.3
$[P_{2225}][Tf_2N]$								
0.25	34.6	105.4	27.2	79.6	28.8	71.1	28.8	75.0
0.5	28.6	103.4	23.4	78.7	26.2	77.1	25.8	72.9
1	22.3	99.7	19.9	78.1	23.3	79.5	23.0	72.9
2	17.1	94.0	16.4	77.4	20.0	80.6	20.2	72.9
4	12.8	87.1	13.3	76.1	17.4	79.6	17.0	72.1
8	5.7	82.4	8.5	73.1	12.3	75.3	11.2	68.6
16	-	-	5.4	58.6	8.4	60.3	6.9	51.5
32	-	-	-	-	-	-	3.0	46.0
$[P_{222(2O1)}][Tf_2N]$								
0.25	18.5	144.1	18.2	121.3	23.9	104.0	23.9	126.2
0.5	9.1	145.0	11.3	124.2	18.6	108.4	17.5	130.2
1	4.5	143.3	7.0	124.2	13.2	109.5	11.5	130.1
2	-	-	5.2	123.1	9.0	109.0	8.3	128.7
4	-	-	-	-	6.9	107.0	-	-

8.5 Appendix 5: Sample calculations for energy and power density

The average specific energy and power densities are derived from the GC runs performed at different discharge currents, I_d, and calculated from the following equations:

$$E_{ave} = I_d . \int \frac{V_d}{3.6m} . dt_d$$

A5.E1

$$P_{ave} = \frac{E_{ave} . 3600}{t_d}$$

A5.E2

Where m is the mass of active materials in both electrodes in units of grams, V_d is the potential at which the discharge begins, i.e. the effect of IR drop is considered, and t_d is the discharge time in seconds. According to equation A5.E1, the quantity of the electrical energy carried in 1 second by the applied current of 1 ampere is known as 1 coulomb. It is also known that 1 joule corresponds to the required work to move an electric charge of 1 coulomb through an electric potential difference field of 1 V and 1 watt is equivalent to the flow of 1 joule per second. 3.6 is representing the conversion factor of discharge time in seconds to hours as well as the mass of active materials of both electrodes in grams to kilogram. Hence the unit of average specific energy is Wh kg^{-1}.

It is worth noting that this method of analysis was selected as the traditional equations for power and energy densities, defined in chapter 2, are measures of the maximum volumetric values and not an actual/real measure of these characteristics where the losses are occurring.

9 References

1. Stocker, T.F., *Climate Change 2013: The Physical Science Basis. Working Group 1 (WG1) Contribution to the Intergovernmental Panel on Climate Change (IPCC)* 2013, Cambridge University Press.
2. IEA, *Transport, Energy and CO2; moving towards sustainablity*, 2009.
3. *Linking population, poverty and development*. Available from: http://www.unfpa.org/pds/trends.htm.
4. *International agreements and instruments*. Available from: http://www.environmentlaw.org.uk/rte.asp?id=54.
5. *The European Strategic Energy Technology Plan*. Available from: http://www.eera-set.eu.
6. *How the UK will meet CO2 emissions targets*. 2009 [cited 2012 October the 6th]; Available from: http://www.direct.gov.uk/en/Nl1/Newsroom/DG_179190.
7. *International action on climate change*. [cited 2012 October the 6th]; Available from: http://www.direct.gov.uk/en/Environmentandgreenerliving/Thewiderenvironment/Climatechange/DG_072978.
8. Running, S.W., *Ecosystem Disturbance, Carbon, and Climate.* Science, 2008. **321**(5889): p. 652-653.
9. Wee, H.-M., et al., *Renewable energy supply chains, performance, application barriers, and strategies for further development.* Renewable and Sustainable Energy Reviews, 2012. **16**(8): p. 5451-5465.
10. Conway, B.E., *Electrochemical Supercapacitors: Scientific Fundamentals and Technological Applications*1999: Springer.
11. *Superconducting Magnetic Energy Storage (SMES)*. Available from: http://www.superpower-inc.com/content/superconducting-magnetic-energy-storage-smes.
12. *Flywheel technology*. Available from: http://www.activepower.com/UKen/flywheel-technology/.
13. *Battery and energy technologies*. 2005 [cited 2012 November the 18th]; Available from: http://www.mpoweruk.com/energy_efficiency.htm.
14. Flach, B., K. Bendz, and S. Lieberz, *GAIN Report (NL4025): EU Biofuels Annual 2014*, 2014, USDA Foreign Agricultural Service.
15. Wei, W., et al., *Manganese oxide-based materials as electrochemical supercapacitor electrodes.* Chemical Society Reviews, 2011. **40**(3): p. 1697-1721.
16. circuitstoday. *Capacitors – Invention History and the Story of Leyden Jar*. 2013 [cited 2014 August 3rd]; Available from: http://www.circuitstoday.com/capacitors-invention-history-and-the-story-of-leyden-jar.
17. Hall, P.J., et al., *Energy storage in electrochemical capacitors: designing functional materials to improve performance.* Energy & Environmental Science, 2010. **3**(9): p. 1238-1251.

18. Miller, J.R. and A.F. Burke, *Electrochemical capacitors: Challenges and opportunities for real-world applications.* Electrochemical Society Interface, 2008. **17**(1): p. 53-57.
19. Long, J.W., *Opportunities foe Electrochemical Capacitors as Energy-storage Solutions in Present and Future Navy and Marine Corps Missions*, 2009, Naval Research Laboratory Washington DC.
20. Carter, R., et al., *An Improved Lead Acid Battery Pack Model for Use in Power Simulations of Electric Vehicles.* Energy Conversion, IEEE Transactions on, 2012. **27**(1): p. 21-28.
21. Carter, R., A. Cruden, and P.J. Hall, *Optimizing for Efficiency or Battery Life in a Battery/Supercapacitor Electric Vehicle.* Vehicular Technology, IEEE Transactions on, 2012. **61**(4): p. 1526-1533.
22. Lailler, P., et al., *Study of the softening of the positive active-mass in valve-regulated lead-acid batteries for electric-vehicle applications.* Journal of Power Sources, 1999. **78**(1,Äì2): p. 204-213.
23. Omar, N., et al., *Power and life enhancement of battery-electrical double layer capacitor for hybrid electric and charge-depleting plug-in vehicle applications.* Electrochimica Acta, 2010. **55**(25): p. 7524-7531.
24. Ruetschi, P., *Aging mechanisms and service life of lead,Äìacid batteries.* Journal of Power Sources, 2004. **127**(1,Äì2): p. 33-44.
25. Miller, J.M. and M. Everett. *Ultra-capacitor augmentation of the vehicle electrical system to reset its power budget*. in *Power Electronics in Transportation, 2004*. 2004.
26. Miller, J.R. and P. Simon, *Electrochemical Capacitors for Energy Management.* Science, 2008. **321**(5889): p. 651-652.
27. An, K.H., et al., *Supercapacitors Using Single-Walled Carbon Nanotube Electrodes.* Advanced Materials, 2001. **13**(7): p. 497-500.
28. Du, C.S., J. Yeh, and N. Pan, *High power density supercapacitors using locally aligned carbon nanotube electrodes*, 2005, IOP PUBLISHING LTD.
29. Burke, A., *Ultracapacitors: Why, How, and Where is the Technology*, 2000.
30. Simon, P. and Y. Gogotsi, *Materials for electrochemical capacitors.* Nature materials, 2008. **7**: p. 845-854.
31. Frackowiak, E. and F.o. Beguin, *Carbon materials for the electrochemical storage of energy in capacitors.* Carbon, 2001. **39**(6): p. 937-950.
32. Rennie, A., *Nitrogen-Enriched Carbon Materials for High-Power Electrochemical Capacitors*, in *Department of Chemical & Process Engineering*2011, University of Strathclyde.
33. Kotz, R. and M. Carlen, *Principles and applications of electrochemical capacitors.* Electrochimica Acta, 2000. **45**(15,Äì16): p. 2483-2498.
34. Shi, H., *Activated carbons and double layer capacitance.* Electrochimica Acta, 1996. **41**(10): p. 1633-1639.
35. Bandosz, T.J., *Activated Carbon Surfaces in Environmental Remediation*2006: Elsevier Science & Tech.

36. Qu, D.Y. and H. Shi, *Studies of activated carbons used in double-layer capacitors.* Journal of Power Sources, 1998. **74**(1): p. 99-107.
37. Sillars, F.B., et al., *Effect of activated carbon xerogel pore size on the capacitance performance of ionic liquid electrolytes.* Energy & Environmental Science, 2011. **4**(3): p. 695-706.
38. Arico, A.S., et al., *Nanostructured materials for advanced energy conversion and storage devices.* Nature materials, 2005. **4**(5): p. 366-377.
39. Wang, J., et al., *Morphological effects on the electrical and electrochemical properties of carbon aerogels.* Journal of The Electrochemical Society, 2001. **148**(6): p. D75-D77.
40. Mirzaeian, M. and P.J. Hall, *Characterizing capacity loss of lithium oxygen batteries by impedance spectroscopy.* Journal of Power Sources, 2010. **195**(19): p. 6817-6824.
41. Mirzaeian, M. and P.J. Hall, *The control of porosity at nano scale in resorcinol formaldehyde carbon aerogels.* Journal of Materials Science, 2009. **44**(10): p. 2705-2713.
42. Mirzaeian, M. and P.J. Hall, *Preparation of controlled porosity carbon aerogels for energy storage in rechargeable lithium oxygen batteries.* Electrochimica Acta, 2009. **54**(28): p. 7444-7451.
43. Escribano, S., et al., *Characterization of carbon aerogels.* Eurocarbon, 1998: p. 841-842.
44. McEuen, P.L., M.S. Fuhrer, and P. Hongkun, *Single-walled carbon nanotube electronics.* Nanotechnology, IEEE Transactions on, 2002. **1**(1): p. 78-85.
45. Wen, S., et al., *EDLC characteristics with high specific capacitance of the CNT electrodes grown on nanoporous alumina templates.* Current Applied Physics, 2006. **6**(6): p. 1012-1015.
46. Frackowiak, E., et al., *Supercapacitor electrodes from multiwalled carbon nanotubes.* Applied Physics Letters, 2000. **77**(15): p. 2421-2423.
47. Chen, Q.-L., et al., *Fabrication and electrochemical properties of carbon nanotube array electrode for supercapacitors.* Electrochimica Acta, 2004. **49**(24): p. 4157-4161.
48. Kibi, Y., et al., *Fabrication of high-power electric double-layer capacitors.* Journal of Power Sources, 1996. **60**(2): p. 219-224.
49. Béguin, F. and E. Frąckowiak, *Carbons for Electrochemical Energy Storage and Conversion Systems*2010: CRC PressINC.
50. P. Wasserscheid and T. Welton, *Ionic Liquids in Synthesis*2003, Weinheim: Wiley-VCH.
51. Abbott, A.P., R.C. Harris, and K.S. Ryder, *Application of Hole Theory to Define Ionic Liquids by their Transport Properties,Ä†.* The Journal of Physical Chemistry B, 2007. **111**(18): p. 4910-4913.
52. Widegren, J.A., et al., *Electrolytic conductivity of four imidazolium-based room-temperature ionic liquids and the effect of a water impurity.* The Journal of Chemical Thermodynamics, 2005. **37**(6): p. 569-575.

53. Billard, I., et al., *EuIII Luminescence in a Hygroscopic Ionic Liquid: Effect of Water and Evidence for a Complexation Process.* European Journal of Inorganic Chemistry, 2004. **2004**(6): p. 1190-1197.
54. Jarosik, A., et al., *Conductivity of ionic liquids in mixtures.* Journal of Molecular Liquids, 2006. **123**(1): p. 43-50.
55. Lu, W., et al., *Incorporating ionic liquid electrolytes into polymer gels for solid-state ultracapacitors.* Journal of The Electrochemical Society, 2008. **155**(5): p. A361-A367.
56. MacFarlane, D.R., et al., *Pyrrolidinium Imides: A New Family of Molten Salts and Conductive Plastic Crystal Phases.* The Journal of Physical Chemistry B, 1999. **103**(20): p. 4164-4170.
57. Welton, T., *Room-Temperature Ionic Liquids. Solvents for Synthesis and Catalysis.* Chemical Reviews, 1999. **99**(8): p. 2071-2084.
58. Earle, M.J. and K.R. Seddon, *Ionic Liquids: Green Solvents for the Future* Pure and Applied Chemistry, 2000. **72**: p. 1391-1398.
59. Endres, F., D. MacFarlane, and A. Abbott, *Electrodeposition from Ionic Liquids*2008: Wiley.
60. Tsuda, T. and C.L. Hussey, *Electrochemical applications of room-temperature ionic liquids.* Interface-Electrochemical Society, 2007. **16**(1): p. 42-49.
61. Fletcher, S.I., et al., *Physical Properties of Selected Ionic Liquids for Use as Electrolytes and Other Industrial Applications.* Journal of Chemical and Engineering Data, 2010. **55**(2): p. 778-782.
62. Kandil, M.E., K.N. Marsh, and A.R.H. Goodwin, *Measurement of the viscosity, density, and electrical conductivity of 1-hexyl-3-methylimidazolium bis(trifluorosulfonyl)imide at temperatures between (288 and 433) K and pressures below 50 MPa.* Journal of Chemical and Engineering Data, 2007. **52**(6): p. 2382-2387.
63. Galinski, M., A. Lewandowski, and I. Stępniak, *Ionic liquids as electrolytes.* Electrochimica Acta, 2006. **51**(26): p. 5567-5580.
64. Geller, E., *Encyclopedia of Science and Technology (I-LEV)*. 10 ed. Vol. 9. 2007: McGraw-Hill
65. Largeot, C., et al., *Relation between the Ion Size and Pore Size for an Electric Double-Layer Capacitor.* Journal of the American Chemical Society, 2008. **130**(9): p. 2730-2731.
66. Zech, O., et al., *The Conductivity of Imidazolium-Based Ionic Liquids from (248 to 468) K. B. Variation of the Anion.* Journal of Chemical & Engineering Data, 2010. **55**(5): p. 1774-1778.
67. Abdallah, T., D. Lemordant, and B.n.d. Claude-Montigny, *Are room temperature ionic liquids able to improve the safety of supercapacitors organic electrolytes without degrading the performances?* Journal of Power Sources, 2012. **201**(0): p. 353-359.
68. Xu, W. and C.A. Angell, *Solvent-free electrolytes with aqueous solution - Like conductivities.* Science, 2003. **302**(5644): p. 422-425.
69. Wu, J.-Y., Y.-P. Chen, and C.-S. Su, *Density and Viscosity of Ionic Liquid Binary Mixtures of 1-n-Butyl-3-methylimidazolium Tetrafluoroborate*

with Acetonitrile, N,N-Dimethylacetamide, Methanol, and N-Methyl-2-pyrrolidone. Journal of Solution Chemistry, 2015. **44**(3-4): p. 395-412.
70. Qi, F. and H. Wang, *Application of Prigogine,ÄìFlory,ÄìPatterson theory to excess molar volume of mixtures of 1-butyl-3-methylimidazolium ionic liquids with N-methyl-2-pyrrolidinone.* The Journal of Chemical Thermodynamics, 2009. **41**(2): p. 265-272.
71. Kim, H.-D., I.-C. Hwang, and S.-J. Park, *Isothermal Vapor,Liquid Equilibrium Data at T = 333.15 K and Excess Molar Volumes and Refractive Indices at T = 298.15 K for the Dimethyl Carbonate + Methanol and Isopropanol + Water with Ionic Liquids.* Journal of Chemical & Engineering Data, 2010. **55**(7): p. 2474-2481.
72. Stoppa, A., J. Hunger, and R. Buchner, *Conductivities of Binary Mixtures of Ionic Liquids with Polar Solvents.* Journal of Chemical & Engineering Data, 2009. **54**(2): p. 472-479.
73. Tian, S., et al., *Physical Properties of 1-Butyl-3-methylimidazolium Tetrafluoroborate/N-Methyl-2-pyrrolidone Mixtures and the Solubility of CO2 in the System at Elevated Pressures.* Journal of Chemical & Engineering Data, 2012. **57**(3): p. 756-763.
74. Sillar, F.B., *High Energy Density Electrochemical Double Layer Capacitors: The effect of pore size distribution on the performance of room temperature ionic liquids*, in *Department of Chemical & Process Engineering*2010, University of Strathclyde.
75. Galiński, M., A. Lewandowski, and I. Stępniak, *Ionic liquids as electrolytes.* Electrochimica Acta, 2006. **51**(26): p. 5567-5580.
76. Lewandowski, A. and M. Galinski, *Carbon, Ionic liquid double-layer capacitors.* Journal of Physics and Chemistry of Solids, 2004. **65**(2,Äì3): p. 281-286.
77. Ania, C.O., et al., *Solvent-free ionic liquids as in situ probes for assessing the effect of ion size on the performance of electrical double layer capacitors.* Carbon, 2006. **44**(14): p. 3126-3130.
78. Sun, G.-h., K.-x. Li, and C.-g. Sun, *Application of 1-ethyl-3-methylimidazolium thiocyanate to the electrolyte of electrochemical double layer capacitors.* Journal of Power Sources, 2006. **162**(2): p. 1444-1450.
79. Balducci, A., et al., *High temperature carbon-carbon supercapacitor using ionic liquid as electrolyte.* Journal of Power Sources, 2007. **165**(2): p. 922-927.
80. Arbizzani, C., et al., *Safe, high-energy supercapacitors based on solvent-free ionic liquid electrolytes.* Journal of Power Sources, 2008. **185**(2): p. 1575-1579.
81. Fletcher, S.I., et al., *The effects of temperature on the performance of electrochemical double layer capacitors.* Journal of Power Sources, 2010. **195**(21): p. 7484-7488.
82. Zemaitis Jr, J.F., et al., *Handbook of aqueous electrolyte thermodynamics: Theory & application*2010: John Wiley & Sons.

83. Giernoth, R., *Solvents and Solvent Effects in Organic Chemistry. 4th Ed. By Christian Reichardt and Thomas Welton.* Angewandte Chemie International Edition, 2011. **50**(48): p. 11289-11289.
84. Ab Rani, M.A., et al., *Understanding the polarity of ionic liquids.* Physical Chemistry Chemical Physics, 2011. **13**(37): p. 16831-16840.
85. Weingärtner, H., *Understanding Ionic Liquids at the Molecular Level: Facts, Problems, and Controversies.* Angewandte Chemie International Edition, 2008. **47**(4): p. 654-670.
86. Kobrak, M.N., *Electrostatic Interactions of a Neutral Dipolar Solute with a Fused Salt:,Äâ A New Model for Solvation in Ionic Liquids,Ä†.* The Journal of Physical Chemistry B, 2007. **111**(18): p. 4755-4762.
87. Znamenskiy, V. and M.N. Kobrak, *Molecular Dynamics Study of Polarity in Room-Temperature Ionic Liquids.* The Journal of Physical Chemistry B, 2004. **108**(3): p. 1072-1079.
88. Gonfa, G., et al., *Unique Structure and Solute,ÄìSolvent Interaction in Imidazolium Based Ionic Liquids: A Review.* Asian Trans. Eng, 2011. **1**: p. 24-34.
89. Ito, N. and R. Richert, *Solvation Dynamics and Electric Field Relaxation in an Imidazolium-PF6 Ionic Liquid:,Äâ from Room Temperature to the Glass Transition,Ä†.* The Journal of Physical Chemistry B, 2007. **111**(18): p. 5016-5022.
90. Embs, J.P., et al., *Cation Dynamics in the Pyridinium Based Ionic Liquid 1-N-Butylpyridinium Bis((trifluoromethyl)sulfonyl) As Seen by Quasielastic Neutron Scattering.* The Journal of Physical Chemistry B, 2012. **116**(44): p. 13265-13271.
91. Ito, N., et al., *Solvation Dynamics and Rotation of Coumarin 153 in Alkylphosphonium Ionic Liquids.* The Journal of Physical Chemistry B, 2004. **108**(18): p. 5771-5777.
92. Schroder, C., et al., *Collective rotational dynamics in ionic liquids: A computational and experimental study of 1-butyl-3-methyl-imidazolium tetrafluoroborate.* The Journal of Chemical Physics, 2007. **126**(8): p. 084511.
93. Chathoth, S.M., et al., *Fast diffusion in a room temperature ionic liquid confined in mesoporous carbon.* EPL (Europhysics Letters), 2012. **97**(6): p. 66004.
94. Mamontov, E., *Boiling Temperature As a Scaling Parameter for the Microscopic Relaxation Dynamics in Molecular Liquids.* The Journal of Physical Chemistry B, 2013. **117**(32): p. 9501-9507.
95. Weingartner, H., et al., *The dielectric response of room-temperature ionic liquids: Effect of cation variation.* Journal of Physical Chemistry B, 2007. **111**(18): p. 4775-4780.
96. Shirota, H., et al., *Ultrafast dynamics of pyrrolidinium cation ionic liquids.* The Journal of Chemical Physics, 2005. **122**(18): p. 184512.
97. Ghandi, K., *A Review of Ionic Liquids, Their Limits and Applications.* Green and Sustainable Chemistry, 2014. **4**: p. 44-53.
98. MacFarlane, D.R., et al., *On the concept of ionicity in ionic liquids.* Physical Chemistry Chemical Physics, 2009. **11**(25): p. 4962-4967.

99. Every, H.A., et al., *Transport properties in a family of dialkylimidazolium ionic liquids.* Physical Chemistry Chemical Physics, 2004. **6**(8): p. 1758-1765.
100. Tokuda, H., et al., *Physicochemical Properties and Structures of Room Temperature Ionic Liquids. 1. Variation of Anionic Species.* The Journal of Physical Chemistry B, 2004. **108**(42): p. 16593-16600.
101. Tokuda, H., et al., *Physicochemical Properties and Structures of Room Temperature Ionic Liquids. 2. Variation of Alkyl Chain Length in Imidazolium Cation.* The Journal of Physical Chemistry B, 2005. **109**(13): p. 6103-6110.
102. *Allen J. Bard and Larry R. Faulkner, Electrochemical Methods: Fundamentals and Applications, New York: Wiley, 2001, 2nd ed.* Russian Journal of Electrochemistry, 2002. **38**(12): p. 1364-1365.
103. Brookes, R., et al., *Diffusion Coefficients in Ionic Liquids: Relationship to the Viscosity.* The Journal of Physical Chemistry B, 2005. **109**(14): p. 6485-6490.
104. Barrosse-Antle, L.E., et al., *Voltammetry in Room Temperature Ionic Liquids: Comparisons and Contrasts with Conventional Electrochemical Solvents.* Chemistry – An Asian Journal, 2010. **5**(2): p. 202-230.
105. Barrosse-Antle, L.E., et al., *Electroreduction of Sulfur Dioxide in Some Room-Temperature Ionic Liquids.* The Journal of Physical Chemistry C, 2008. **112**(9): p. 3398-3404.
106. Silvester, D.S., et al., *The electrochemical oxidation of hydrogen at activated platinum electrodes in room temperature ionic liquids as solvents.* Journal of Electroanalytical Chemistry, 2008. **618**(1,Äì2): p. 53-60.
107. Evans, R.G., et al., *Electroreduction of Oxygen in a Series of Room Temperature Ionic Liquids Composed of Group 15-Centered Cations and Anions.* The Journal of Physical Chemistry B, 2004. **108**(23): p. 7878-7886.
108. Chung, S.H., et al., *Nuclear Magnetic Resonance Study of the Dynamics of Imidazolium Ionic Liquids with ,àíCH2Si(CH3)3 vs ,àíCH2C(CH3)3 Substituents,Ä†.* The Journal of Physical Chemistry B, 2007. **111**(18): p. 4885-4893.
109. Vila, J., L.M. Varela, and O. Cabeza, *Cation and anion sizes influence in the temperature dependence of the electrical conductivity in nine imidazolium based ionic liquids.* Electrochimica Acta, 2007. **52**(26): p. 7413-7417.
110. Zoski, C.G., *Preface*, in *Handbook of Electrochemistry*, C.G. Zoski, Editor 2007, Elsevier: Amsterdam. p. v-vi.
111. Vila, J., et al., *Electrical conductivity of aqueous solutions of aluminum salts.* Physical Review E, 2005. **71**(3): p. 031201.
112. Vila, J., et al., *Temperature dependence of the electrical conductivity in EMIM-based ionic liquids: Evidence of Vogel,ÄìTamman,ÄìFulcher behavior.* Fluid Phase Equilibria, 2006. **242**(2): p. 141-146.
113. McFarlane, D.R., et al., *High conductivity molten salts based on the imide ion.* Electrochimica Acta, 2000. **45**(8,Äì9): p. 1271-1278.

114. Nigmatullin, R.R., S.I. Osokin, and G. Smith, *New approach in the description of dielectric relaxation phenomenon: correct deduction and interpretation of the Vogel,ÄìFulcher,ÄìTamman equation.* Journal of Physics: Condensed Matter, 2003. **15**(20): p. 3481.
115. Wang, H., et al., *Electrochemical Study of Dialcarb "Distillable" Room-Temperature Ionic Liquids.* ChemPhysChem, 2009. **10**(2): p. 455-461.
116. Vila, J., et al., *Temperature Behavior of the Electrical Conductivity of Emim-Based Ionic Liquids in Liquid and Solid States.* Portugaliae Electrochimica Acta, 2007. **25**(1): p. 163.
117. Okoturo, O.O. and T.J. VanderNoot, *Temperature dependence of viscosity for room temperature ionic liquids.* Journal of Electroanalytical Chemistry, 2004. **568**(0): p. 167-181.
118. Wang, J., et al., *A volumetric and viscosity study for the mixtures of 1-n-butyl-3-methylimidazolium tetrafluoroborate ionic liquid with acetonitrile, dichloromethane, 2-butanone and N, N - dimethylformamide.* Green Chemistry, 2003. **5**(5): p. 618-622.
119. Zhu, A., et al., *Measurements and correlation of viscosities and conductivities for the mixtures of imidazolium ionic liquids with molecular solutes.* Chemical Engineering Journal, 2009. **147**(1): p. 27-35.
120. Rouquerol, J., et al., *Recommendations for the characterization of porous solids (Technical Report).* Pure and Applied Chemistry, 1994. **66**(8): p. 1739-1758.
121. Riikonen, J., J. Salonen, and V.-P. Lehto, *Utilising thermoporometry to obtain new insights into nanostructured materials, Review Part 1.* Journal of Thermal Analysis and Calorimetry, 2011. **105**(3): p. 811-821.
122. Brunauer, S. and P.H. Emmett, *The Use of Low Temperature van der Waals Adsorption Isotherms in Determining the Surface Areas of Various Adsorbents.* Journal of the American Chemical Society, 1937. **59**(12): p. 2682-2689.
123. Lowell, S. and J.E. Shields, *Powder Surface Area and Porosity*1991: Springer.
124. Brunauer, S., P.H. Emmett, and E. Teller, *Adsorption of Gases in Multimolecular Layers.* Journal of the American Chemical Society, 1938. **60**(2): p. 309-319.
125. Yang, Q., et al., *Pore structure of SWNTs with high hydrogen storage capacity.* Science in China Series E: Technological Science, 2002. **45**(6): p. 561-568.
126. Guo, Y. and D.A. Rockstraw, *Physical and chemical properties of carbons synthesized from xylan, cellulose, and Kraft lignin by H3PO4 activation.* Carbon, 2006. **44**(8): p. 1464-1475.
127. Sing, K.S.W., *Reporting physisorption data for gas/solid systems with special reference to the determination of surface area and porosity (Recommendations 1984)*, in *Pure and Applied Chemistry*1985. p. 603.
128. Fraissard, J.P., *Physical Adsorption: Experiment, Theory, and Applications*. Vol. 491. 1997: Springer Science & Business Media.

129. Sigma-Aldrich. [cited 2015 10th of June]; Available from: http://www.sigmaaldrich.com/analytical-chromatography/titration/hydranal/learning-center/theory.html.
130. Bard, A.J. and L.R. Faulkner, *Fundamentals and applications.* Electrochemical Methods, 2nd ed.; Wiley: New York, 2001.
131. Xu, K., S.P. Ding, and T.R. Jow, *Toward Reliable Values of Electrochemical Stability Limits for Electrolytes.* Journal of The Electrochemical Society, 1999. **146**(11): p. 4172-4178.
132. Sukardi, S.K., et al., *Prospects for a widely applicable reference potential scale in ionic liquids based on ideal reversible reduction of the cobaltocenium cation.* Electrochemistry Communications, 2008. **10**(2): p. 250-254.
133. Ohno, H., *Electrochemical aspects of ionic liquids*2011: John Wiley & Sons.
134. O, Mahony, A.M., et al., *Effect of Water on the Electrochemical Window and Potential Limits of Room-Temperature Ionic Liquids.* Journal of Chemical & Engineering Data, 2008. **53**(12): p. 2884-2891.
135. Ignat'ev, N.V., et al., *New ionic liquids with tris(perfluoroalkyl)trifluorophosphate (FAP) anions.* Journal of Fluorine Chemistry, 2005. **126**(8): p. 1150-1159.
136. Sun, J., M. Forsyth, and D.R. MacFarlane, *Room-Temperature Molten Salts Based on the Quaternary Ammonium Ion.* The Journal of Physical Chemistry B, 1998. **102**(44): p. 8858-8864.
137. Donato, R., et al., *The electrochemical properties of a platinum electrode in functionalized room temperature imidazolium ionic liquids.* Journal of Solid State Electrochemistry, 2007. **11**(11): p. 1481-1487.
138. Nicholson, R.S. and I. Shain, *Theory of Stationary Electrode Polarography. Single Scan and Cyclic Methods Applied to Reversible, Irreversible, and Kinetic Systems.* Analytical Chemistry, 1964. **36**(4): p. 706-723.
139. Nicholson, R.S., *Theory and Application of Cyclic Voltammetry for Measurement of Electrode Reaction Kinetics.* Analytical Chemistry, 1965. **37**(11): p. 1351-1355.
140. Plieth, W., *Electrochemistry for Materials Science*2008: Elsevier Science.
141. Pell, W.G. and B.E. Conway, *Analysis of power limitations at porous supercapacitor electrodes under cyclic voltammetry modulation and dc charge.* Journal of Power Sources, 2001. **96**(1): p. 57-67.
142. Yu, D. and L. Dai, *Self-Assembled Graphene/Carbon Nanotube Hybrid Films for Supercapacitors.* The Journal of Physical Chemistry Letters, 2010. **1**(2): p. 467-470.
143. Tashima, D., et al., *Mesoporous graphitized Ketjenblack as conductive nanofiller for supercapacitors.* Materials Letters, 2013. **110**(0): p. 105-107.
144. Li, Z.J., et al., *Graphene oxide with improved electrical conductivity for supercapacitor electrodes.* Applied Surface Science, 2012. **258**(8): p. 3726-3731.

145. Sun, J., et al., *A simple and controllable nanostructure comprising non-conductive poly(vinylidene fluoride) and graphene nanosheets for supercapacitor.* Frontiers of Materials Science, 2012. **6**(2): p. 149-159.
146. Kotz, R., M. Hahn, and R. Gallay, *Temperature behavior and impedance fundamentals of supercapacitors.* Journal of Power Sources, 2006. **154**(2): p. 550-555.
147. Lockett, V., et al., *Differential Capacitance of the Electrical Double Layer in Imidazolium-Based Ionic Liquids:,Äâ Influence of Potential, Cation Size, and Temperature.* The Journal of Physical Chemistry C, 2008. **112**(19): p. 7486-7495.
148. Li, Z. and J. Chen, *An impedance-based approach to predict the state-of-charge for carbon-based supercapacitors.* Microelectronic Engineering, 2008. **85**(7): p. 1549-1554.
149. Basnayaka, P.A., et al., *Graphene/polypyrrole nanocomposite as electrochemical supercapacitor electrode: electrochemical impedance studies.* 2013.
150. Jurewicz, K., et al., *Supercapacitors from nanotubes/polypyrrole composites.* Chemical Physics Letters, 2001. **347**(1,Äì3): p. 36-40.
151. Kim, T., et al., *Activated Graphene-Based Carbons as Supercapacitor Electrodes with Macro- and Mesopores.* Acs Nano, 2013. **7**(8): p. 6899-6905.
152. Kondrat, S. and A. Kornyshev, *Charging Dynamics and Optimization of Nanoporous Supercapacitors.* The Journal of Physical Chemistry C, 2013. **117**(24): p. 12399-12406.
153. Vatamanu, J., et al., *Molecular Dynamics Simulation Study of the Interfacial Structure and Differential Capacitance of Alkylimidazolium Bis(trifluoromethanesulfonyl)imide [Cnmim][TFSI] Ionic Liquids at Graphite Electrodes.* The Journal of Physical Chemistry C, 2012. **116**(14): p. 7940-7951.
154. Shim, Y. and H.J. Kim, *Nanoporous Carbon Supercapacitors in an Ionic Liquid: A Computer Simulation Study.* Acs Nano, 2010. **4**(4): p. 2345-2355.
155. Lazzari, M., et al., *Role of carbon porosity and ion size in the development of ionic liquid based supercapacitors.* Journal of The Electrochemical Society, 2011. **158**(1): p. A22-A25.
156. Fletcher, S., V. Black, and I. Kirkpatrick, *A universal equivalent circuit for carbon-based supercapacitors.* Journal of Solid State Electrochemistry, 2014. **18**(5): p. 1377-1387.
157. de Levie, R., *On porous electrodes in electrolyte solutions: I. Capacitance effects.* Electrochimica Acta, 1963. **8**(10): p. 751-780.
158. de Levie, R., *On porous electrodes in electrolyte solutions.* Electrochimica Acta, 1964. **9**(9): p. 1231-1245.
159. Taberna, P., P. Simon, and J.-F.o. Fauvarque, *Electrochemical characteristics and impedance spectroscopy studies of carbon-carbon supercapacitors.* Journal of The Electrochemical Society, 2003. **150**(3): p. A292-A300.

160. Fang, B. and L. Binder, *A modified activated carbon aerogel for high-energy storage in electric double layer capacitors.* Journal of Power Sources, 2006. **163**(1): p. 616-622.
161. Orazem, M.E. and B. Tribollet, *Electrochemical impedance spectroscopy*. Vol. 48. 2011: John Wiley & Sons.
162. Liang, C., G. Sha, and S. Guo, *Resorcinol-formaldehyde aerogels prepared by supercritical acetone drying.* Journal of Non-Crystalline Solids, 2000. **271**(1,Äì2): p. 167-170.
163. Pekala, R.W., *Organic aerogels from the polycondensation of resorcinol with formaldehyde.* Journal of Materials Science, 1989. **24**(9): p. 3221-3227.
164. Li, W., G. Reichenauer, and J. Fricke, *Carbon aerogels derived from cresol,Äìresorcinol,Äìformaldehyde for supercapacitors.* Carbon, 2002. **40**(15): p. 2955-2959.
165. Li, W.-C., A.-H. Lu, and S.-C. Guo, *Control of Mesoporous Structure of Aerogels Derived from Cresol,ÄìFormaldehyde.* Journal of Colloid and Interface Science, 2002. **254**(1): p. 153-157.
166. Gu, S., et al., *Polybenzoxazine aerogels with controllable pore structures.* RSC Advances, 2015. **5**(34): p. 26801-26805.
167. Lee, J., G. Gould, and W. Rhine, *Polyurea based aerogel for a high performance thermal insulation material.* Journal of Sol-Gel Science and Technology, 2009. **49**(2): p. 209-220.
168. Tamon, H., et al., *Porous structure of organic and carbon aerogels synthesized by sol-gel polycondensation of resorcinol with formaldehyde.* Carbon, 1997. **35**(6): p. 791-796.
169. Lin, C. and J.A. Ritter, *Effect of synthesis pH on the structure of carbon xerogels.* Carbon, 1997. **35**(9): p. 1271-1278.
170. Al-Muhtaseb, S.A. and J.A. Ritter, *Preparation and Properties of Resorcinol–Formaldehyde Organic and Carbon Gels.* Advanced Materials, 2003. **15**(2): p. 101-114.
171. Sillars, F.B., et al., *Variation of electrochemical capacitor performance with Room Temperature Ionic Liquid electrolyte viscosity and ion size.* Physical chemistry chemical physics : PCCP, 2012. **14**(17): p. 6094-100.
172. Rennie, A.J.R. and P.J. Hall, *Nitrogen-enriched carbon electrodes in electrochemical capacitors: investigating accessible porosity using CM-SANS.* Physical Chemistry Chemical Physics, 2013. **15**(39): p. 16774-16778.
173. Pekala, R.W., et al., *Carbon aerogels for electrochemical applications.* Journal of Non-Crystalline Solids, 1998. **225**: p. 74-80.
174. Kim, S.J., S.W. Hwang, and S.H. Hyun, *Preparation of carbon aerogel electrodes for supercapacitor and their electrochemical characteristics.* Journal of Materials Science. **40**(3): p. 725-731.
175. Edwards, I.A.S. and H. Marsh, *Introduction to carbon science*1989: Butterworths.
176. Freeman, J.J., *Active carbon Edited by R. C. Bansal, J.-B. Donnet and F. Stoeckli. Marcel Dekker, New York, 1988, pp. xiv + 482, US$150.00. ISBN*

0–8247–7842–1. Journal of Chemical Technology & Biotechnology, 1990. **48**(2): p. 240-241.

177. Rennie, A.J.R., et al., *Ether-Bond-Containing Ionic Liquids as Supercapacitor Electrolytes.* The Journal of Physical Chemistry Letters, 2013. **4**(17): p. 2970-2974.
178. Fredlake, C.P., et al., *Thermophysical Properties of Imidazolium-Based Ionic Liquids.* Journal of Chemical & Engineering Data, 2004. **49**(4): p. 954-964.
179. Crosthwaite, J.M., et al., *Phase transition and decomposition temperatures, heat capacities and viscosities of pyridinium ionic liquids.* Journal of Chemical Thermodynamics, 2005. **37**(6): p. 559-568.
180. Swatloski, R.P., et al., *Dissolution of Cellose with Ionic Liquids.* Journal of the American Chemical Society, 2002. **124**(18): p. 4974-4975.
181. Obreja, V.V.N., *On the performance of supercapacitors with electrodes based on carbon nanotubes and carbon activated material, A review.* Physica E: Low-dimensional Systems and Nanostructures, 2008. **40**(7): p. 2596-2605.
182. Dullien, F.A., *Porous media: fluid transport and pore structure*2012: Academic press.
183. Mattson, J.S. and H.B. Mark, *Activated Carbon: Surface Chemistry and Adsorption from Solution*1971: M. Dekker.
184. Tennison, S.R., *Phenolic-resin-derived activated carbons.* Applied Catalysis A: General, 1998. **173**(2): p. 289-311.
185. Tokuda, H., et al., *Physicochemical Properties and Structures of Room-Temperature Ionic Liquids. 3. Variation of Cationic Structures.* The Journal of Physical Chemistry B, 2006. **110**(6): p. 2833-2839.
186. Rennie, A.J.R., et al., *Ionic Liquids Containing Sulfonium Cations as Electrolytes for Electrochemical Double Layer Capacitors.* The Journal of Physical Chemistry C, 2015. **119**(42): p. 23865-23874.
187. Del Sesto, R.E., et al., *Limited thermal stability of imidazolium and pyrrolidinium ionic liquids.* Thermochimica Acta, 2009. **491**(1,Äì2): p. 118-120.
188. Gotz, M., et al., *Evaluation of Organic and Ionic Liquids for Three-Phase Methanation and Biogas Purification Processes.* Energy & Fuels, 2013. **27**(8): p. 4705-4716.
189. Wasserscheid, P. and T. Welton, *Ionic liquids in synthesis*2008: John Wiley & Sons Incorporated.
190. Martins, V.L., et al., *Two phosphonium ionic liquids with high Li+ transport number.* Physical Chemistry Chemical Physics, 2015. **17**(35): p. 23041-23051.
191. Aniya, M., et al., *Development of a Model for Analyzing the Temperature Dependence of the Viscosity of Ion Conducting Polymers and Ionic Liquids.* Arabian Journal for Science and Engineering, 2014. **39**(9): p. 6627-6633.
192. Bazito, F.F.C., Y. Kawano, and R.M. Torresi, *Synthesis and characterization of two ionic liquids with emphasis on their chemical*

stability towards metallic lithium. Electrochimica Acta, 2007. **52**(23): p. 6427-6437.

193. Sanchez-Ramirez, N., et al., *Physicochemical Properties of Three Ionic Liquids Containing a Tetracyanoborate Anion and Their Lithium Salt Mixtures.* The Journal of Physical Chemistry B, 2014. **118**(29): p. 8772-8781.
194. Lee, C.-P., et al., *Trialkylsulfonium and tetraalkylammonium cations-based ionic liquid electrolytes for quasi-solid-state dye-sensitized solar cells.* Electrochimica Acta, 2013. **114**: p. 303-308.
195. Fang, S., et al., *Low-viscosity and low-melting point asymmetric trialkylsulfonium based ionic liquids as potential electrolytes.* Electrochemistry Communications, 2007. **9**(11): p. 2696-2702.
196. Matsumoto, H., T. Matsuda, and Y. Miyazaki, *Room Temperature Molten Salts Based on Trialkylsulfonium Cations and Bis(trifluoromethylsulfonyl)imide.* Chemistry Letters, 2000. **29**(12): p. 1430-1431.
197. Matsumoto, H., H. Sakaebe, and K. Tatsumi, *Preparation of room temperature ionic liquids based on aliphatic onium cations and asymmetric amide anions and their electrochemical properties as a lithium battery electrolyte.* Journal of Power Sources, 2005. **146**(1,Äì2): p. 45-50.
198. Bhattacharjee, A., et al., *Thermophysical properties of sulfonium- and ammonium-based ionic liquids.* Fluid Phase Equilibria, 2014. **381**: p. 36-45.
199. Ye, C. and J.n.M. Shreeve, *Rapid and Accurate Estimation of Densities of Room-Temperature Ionic Liquids and Salts.* The Journal of Physical Chemistry A, 2007. **111**(8): p. 1456-1461.
200. Sato, T., G. Masuda, and K. Takagi, *Electrochemical properties of novel ionic liquids for electric double layer capacitor applications.* Electrochimica Acta, 2004. **49**(21): p. 3603-3611.
201. Bonhate, P., et al., *Hydrophobic, Highly Conductive Ambient-Temperature Molten Salts.* Inorganic Chemistry, 1996. **35**(5): p. 1168-1178.
202. Machanov√° , K., et al., *Thermophysical Properties of Ammonium-Based Bis{(trifluoromethyl)sulfonyl}imide Ionic Liquids: Volumetric and Transport Properties.* Journal of Chemical & Engineering Data, 2012. **57**(8): p. 2227-2235.
203. Sillars, F.B., et al., *Effect of activated carbon xerogel pore size on the capacitance performance of ionic liquid electrolytes.* Energy & Environmental Science, 2011. **4**(3): p. 695.
204. Noofeli, A., P.J. Hall, and A.J.R. Rennie, *Ionic liquid based EDLCs: influence of carbon porosity on electrochemical performance.* Faraday Discussions, 2014. **172**(0): p. 163-177.
205. Anouti, M.r.m., et al., *Sulfonium Bis(trifluorosulfonimide) Plastic Crystal Ionic Liquid as an Electrolyte at Elevated Temperature for High-Energy Supercapacitors.* The Journal of Physical Chemistry C, 2012. **116**(17): p. 9412-9418.

206. Raymundo-Pinero, E., et al., *Relationship between the nanoporous texture of activated carbons and their capacitance properties in different electrolytes.* Carbon, 2006. **44**(12): p. 2498-2507.
207. Chmiola, J., et al., *Anomalous increase in carbon capacitance at pore sizes less than 1 nanometer.* Science, 2006. **313**(5794): p. 1760-1763.
208. Chmiola, J., et al., *Desolvation of ions in subnanometer pores and its effect on capacitance and double-layer theory.* Angewandte Chemie (International ed. in English), 2008. **47**(18): p. 3392-3395.
209. Ong, S.P., et al., *Electrochemical Windows of Room-Temperature Ionic Liquids from Molecular Dynamics and Density Functional Theory Calculations.* Chemistry of Materials, 2011. **23**(11): p. 2979-2986.
210. Zhang, Y., et al., *Refined Method for Predicting Electrochemical Windows of Ionic Liquids and Experimental Validation Studies.* The Journal of Physical Chemistry B, 2014. **118**(23): p. 6250-6255.
211. Mousavi, M.P.S., et al., *Electrochemical Stability of Quaternary Ammonium Cations: An Experimental and Computational Study.* Journal of The Electrochemical Society, 2016. **163**(2): p. H74-H80.
212. Balducci, A., et al., *Cycling stability of a hybrid activated carbon//poly(3-methylthiophene) supercapacitor with N-butyl-N-methylpyrrolidinium bis(trifluoromethanesulfonyl)imide ionic liquid as electrolyte.* Electrochimica Acta, 2005. **50**(11): p. 2233-2237.
213. Delnick, F., *Proceedings of the Symposium on Electrochemical Capacitors II*. Vol. 96-25. Electrochemical Society.
214. Druschler, M., et al., *New insights into the interface between a single-crystalline metal electrode and an extremely pure ionic liquid: slow interfacial processes and the influence of temperature on interfacial dynamics.* Physical Chemistry Chemical Physics, 2012. **14**(15): p. 5090-5099.
215. Ivanistsev, V., et al., *Comparative Impedance Study of Cd (0001) Electrode in EMImBF4 and KI Aqueous Solution at Different Temperatures.* Journal of The Electrochemical Society, 2013. **160**(6): p. H368-H375.
216. Siinor, L., et al., *Influence of temperature on the electrochemical characteristics of Bi(1 1 1)|ionic liquid interface.* Journal of Electroanalytical Chemistry, 2013. **689**: p. 51-56.
217. Lockett, V., et al., *Differential capacitance of the double layer at the electrode/ionic liquids interface.* Physical Chemistry Chemical Physics, 2010. **12**(39): p. 12499-12512.
218. Silva, F., et al., *The electrical double layer at the [BMIM][PF6] ionic liquid/electrode interface ‚Äì Effect of temperature on the differential capacitance.* Journal of Electroanalytical Chemistry, 2008. **622**(2): p. 153-160.
219. Costa, R., C.M. Pereira, and F. Silva, *Double layer in room temperature ionic liquids: influence of temperature and ionic size on the differential capacitance and electrocapillary curves.* Physical Chemistry Chemical Physics, 2010. **12**(36): p. 11125-11132.

220. Mezger, M., et al., *Molecular layering of fluorinated ionic liquids at a charged sapphire (0001) surface.* Science, 2008. **322**(5900): p. 424-428.
221. Kislenko, S.A., R.H. Amirov, and I.S. Samoylov, *Molecular dynamics simulation of the electrical double layer in ionic liquids.* Journal of Physics: Conference Series, 2013. **418**(1): p. 012021.
222. Kislenko, S.A., R.H. Amirov, and I.S. Samoylov, *Influence of temperature on the structure and dynamics of the [BMIM][PF6] ionic liquid/graphite interface.* Physical Chemistry Chemical Physics, 2010. **12**(37): p. 11245-11250.
223. Vatamanu, J., O. Borodin, and G.D. Smith, *Molecular Insights into the Potential and Temperature Dependences of the Differential Capacitance of a Room-Temperature Ionic Liquid at Graphite Electrodes.* Journal of the American Chemical Society, 2010. **132**(42): p. 14825-14833.
224. Nishi, N., et al., *Temperature dependence of multilayering at the free surface of ionic liquids probed by X-ray reflectivity measurements.* Langmuir, 2011. **27**(12): p. 7531-7536.
225. Dou, Q., et al., *Molecular dynamics simulation of the interfacial structure of [C n mim][PF 6] adsorbed on a graphite surface: effects of temperature and alkyl chain length.* Journal of Physics: Condensed Matter, 2011. **23**(17): p. 175001.
226. Compton, R.G. and C.E. Banks, *Understanding voltammetry*2007: World Scientific.